ENERGY RESOLVED PHONON SCATTERING IN GLASSES

ANN CATRINA HANNA

Ph.D.

THE UNIVERSITY OF GLASGOW
DEPARTMENT OF PHYSICS AND ASTRONOMY

FEBRUARY 1987

ProQuest LLC.
789 East Eisenhower Parkway
P.O. Box 1346
Ann Arbor, MI 48106 – 1346

Declaration

The work presented in this thesis is that of the author except where explicitly mentioned in the text when an appropriate reference is given.

Some of the results in this thesis have already been published (A.F. Cattell, A.R. Long, A.C. Hanna and A.M. MacLeod, J. Phys. F 13, 855 (1983) and A.R. Long, A.C. Hanna and A.M. MacLeod, J. Phys. C 19, 467 (1986)) but no part has been submitted previously for a degree at this or any other university.

Acknowledgements

I would like to thank Dr. A. R. Long, my supervisor, for his help, encouragement and advice throughout the period of this work without which these experiments would not have been possible. I would also like to thank the members of the Solid State Physics Group for many helpful discussions.

I would like to express my gratitude to Dr. A. M. MacLeod for writing the programs for the analysis of the data in the Motorola Exorset microcomputer. I wish to thank the technicians of the Solid State Physics Group for their assistance during the period of the experimental work.

Finally I wish to thank my husband for his support particularly during the writing of this thesis.

Table of contents

Summary

Amorphous materials posses low temperature thermal properties which are different from those of crystalline materials but are common to a wide range of disordered materials. The low temperature heat capacity is larger than that of the corresponding crystalline material and below 1K has a linear term in temperature as well as the T^3 term. In this temperature range the thermal conductivity is lower tha ı that of the crystalline material and proportional to T^2. At temperatures between 1 and 10K it is approximately constant. Below 1 K the behaviour of these materials can be understood in terms of the two level system model. However at higher temperatures none of the various theories proposed to account for the observed behaviour have been confirmed experimentally. This is due to the insensitivity of measurements like those of thermal conductivity to the exact form of the energy dependence of the phonon mean free path and to whether the scattering is elastic or inelastic. Thus, to clarify the theoretical picture, a direct determination of the energy dependence of the phonon mean free path as a function of energy is required.

Energy resolved phonon scattering measurements were performed using a heat pulse technique. Two generators were deposited on one face of a sapphire crystal substrate and two phonon detectors were deposited on the opposite face. A thin film of glass was deposited under either one of the generators or one of the detectors. The phonon generators were thin film constantan heaters and the detectors were superconducting tunnelling heterojunctions. The ratio of the currents generated in the detectors by the phonon fluxes with and without the glassy film were calculated at different biases. By comparing these to current ratios calculated from theoretical models the phonon mean free path as a function of energy could be deduced.

The results of these measurements led to the following conclusions.

Thin film constantan heaters produce a phonon spectrum which can be described by a simple acoustic mismatch theory. The phonon scattering in sputtered silicon dioxide is best explained by elastic scattering with a mean free path of 2.2μm at 1meV and varying as E^{-6}. This form of scattering fitted the data measured from three samples. Two of these were under a detector and the third had been deposited under a phonon generator. However inelastic scattering cannot be ruled out. In

evaporated silicon monoxide evidence of two scattering mechanisms was observed. A strong, probably elastic, process which saturated as the phonon input power was increased. At higher powers this gives way to a weaker process. A scattering mechanism with a significant dwell time was observed in sputtered arsenic trisulphide.

1.1 The Low Temperature Specific Heat Capacity and Thermal Conductivity

The specific heat capacity and thermal conductivity were among the first low temperature properties of amorphous materials to be measured. Zeller and Pohl (1971) reported measurements of these properties for several amorphous materials. The range of materials measured was extended by Stephens (1973) The results showed trends which appear to be characteristic of the amorphous state. These results are summarised below.

In all materials the specific heat capacity of the amorphous state is larger than that of the crystalline state. This can be seen in figure 1.1 which shows the specific heat capacity for both amorphous and crystalline silicon dioxide. There is also a linear term present in the amorphous specific heat which does not occur in the crystalline form.

Using the Debye model the specific heat capacity, C_V, for an amorphous material would be expected to take the form:-

$$C_V = c_D T^3 \qquad (1.1)$$

where c_D is calculated from the measured sound velocities. However, the observed temperature dependence of the specific heat capacity is of the form:-

$$C_V = c_1 T + c_3 T^3 \qquad (1.2)$$

where c_3 is larger than c_D typically by a factor of two to five. This T^3 term corresponds to Debye phonons. From their measurements, Pohl et al. (1974) concluded that Debye phonons exist in glasses and are the main carriers of the heat. The T^3 term is anomalously high and is thought to be due to large numbers of low frequency transverse acoustic phonons. These excess modes are characteristic of the amorphous state.

The linear term, $c_1 T$, is found in all amorphous materials. Later measurements by Lasjuanias et al. (1972 and 1975) showed that at very low temperatures ($T<0.1K$)

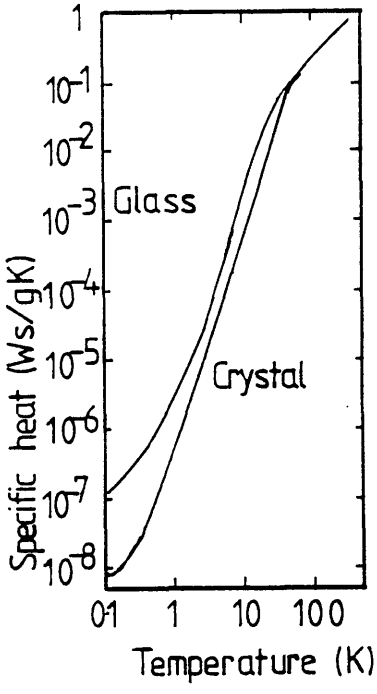

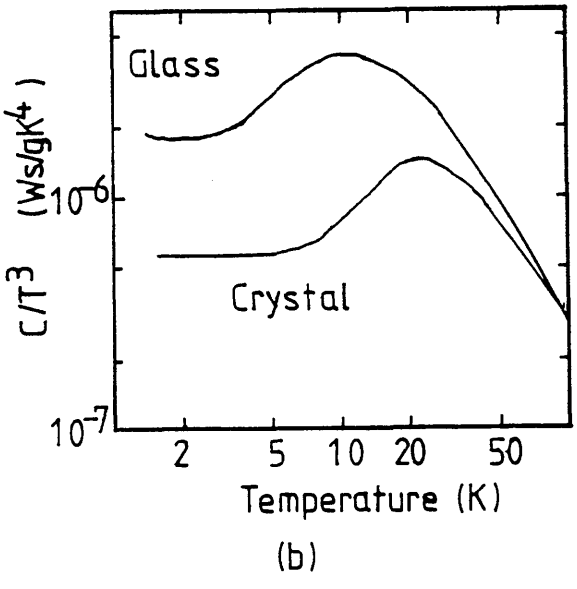

Figure 1.1 (a)The specific heat versus temperature and (b) C/T^3 versus temperature of amorphous and crystalline silicon dioxide (from Zeller and Pohl (1971)).

this term was no longer linear. It took the form of $T^{1+\varepsilon}$ where ε was around 0.2. Stephens (1976) found that by increasing the purity of the material this term can be reduced. However, it does not reduce to zero. This approximately linear term has been attributed to new states characteristic of amorphous systems and its possible origin will be discussed later in this chapter.

At low temperatures the thermal conductivity of the amorphous phase of a material is lower than that of the crystalline phase. Figure 1.2 shows the thermal conductivity as a function of temperature for both amorphous and crystalline silicon dioxide. It is clear form this figure that the temperature dependencies for the two thermal conductivities are different. Below 10K the thermal conductivity is proportional to T^3 and, therefore, increases with increasing temperature. It reaches a peak around 10K then decreases as the temperature increases. The thermal conductivity for the amorphous material increases montonically with increasing temperature. For all materials measured there is a plateau around 10K (see figure 1.3). Below this temperature Zeller and Pohl found that the thermal conductivity varies as T^n, $n \approx 1.8$.

Zeller and Pohl also noted that the thermal conductivity of amorphous materials is almost independent of chemical composition. As can be seen in figure 1.3 there is very little difference in the thermal conductivity of different glasses. This would be understandable if amorphous materials had the lowest possible thermal conductivity. It could then be explained by the diffusion of vibrational energy from one atom to its neighbouring atoms. However viteous silica does not have the lowest possible thermal conductivity. Zeller and Pohl (1971) showed that a crystal of potassium chloride doped with 0.1% cyanide has a lower thermal conductivity than amorphous silicon dioxide at temperatures lower than 5K (see figure 1.2).

All amorphous materials so far investigated have similar features in their specific heat capacity and thermal conductivity. The specific heat capacities all have an approximately linear term. Their thermal conductivities are all about the same order of magnitude, have a plateau around 10K and vary as T^n, $n \approx 1.8$-1.9 below 1K. These features are peculiar to amorphous materials. This leads to the conclusion that these features are consequences of the amorphous structure itself. By considering the amorphous structure it should be possible to produce a model which can explain them.

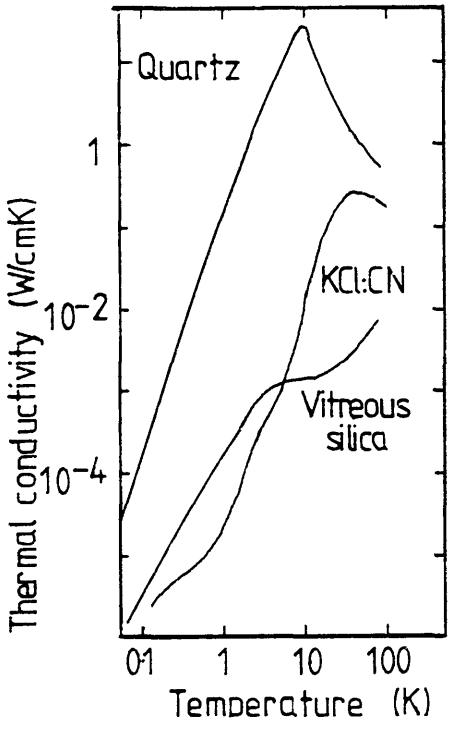

Figure 1.2 The thermal conductivity of crystalline and amorphous silicon dioxide and of KCl doped with 0.1% CN (from Zeller and Pohl (1971)).

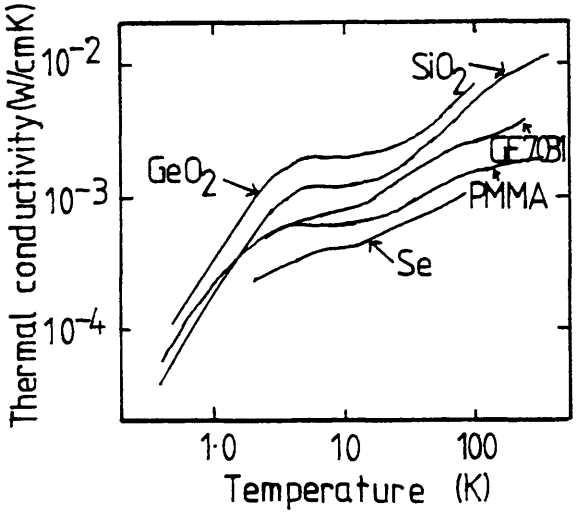

Figure 1.3 The thermal conductivity of various thin film glasses (from Zeller and Pohl (1971)).

There have been several models suggested to explain this behaviour. The majority of these models involve the scattering of the phonons off the structure of the amorphous material. Examples of such models are those proposed by Chang and Jones (1962), Fulde and Wagner (1971), Rosenstock (1971),Takeno and Goda (1972), Baltes (1973), Walton (1974), Morgan and Smith (1974) and Handrich (1983). All of these models explain either the heat capacity or the thermal conductivity. Another model suggested by Anderson et al. (1972) and, independently, by Phillips (1972) can be used to explain both these properties. This model is based on a distribution of localised tunnelling levels. Although it has not been confirmed beyond all doubt the tunnelling model is the one best supported by the experimental evidence.

1.2 The Two-level Model

In a glass there should be atoms or groups of atoms that can sit in two or more equilibrium positions. The energy, E, of the atom or group of atoms will have two local minima which are separated by a barrier. The continuous random network of an amorphous material means that the distribution of atoms corresponding to one minimum is likely to be different from the distribution around the other. Therefore these two minima are likely to have different energies. Figure 1.4 shows the energy as a function of position along a line joining the two localised minima. At low temperatures only the two lowest energy states are important. Thermal excitation of the system is unimportant since, at these temperatures, kT is much less than the barrier height. In order for the atom, or group of atoms, to transfer from one minimum to the other it must tunnel. It can be shown that these two states are separated by an energy ε, where:-

$$\varepsilon^2 = \delta^2 + \delta_o^2 \qquad (1.3)$$

where δ_o is the tunnelling energy, the energy associated with the coupling due to the wavefunctions of the two states overlapping. δ_o is related to the tunnelling probability and is given by:-

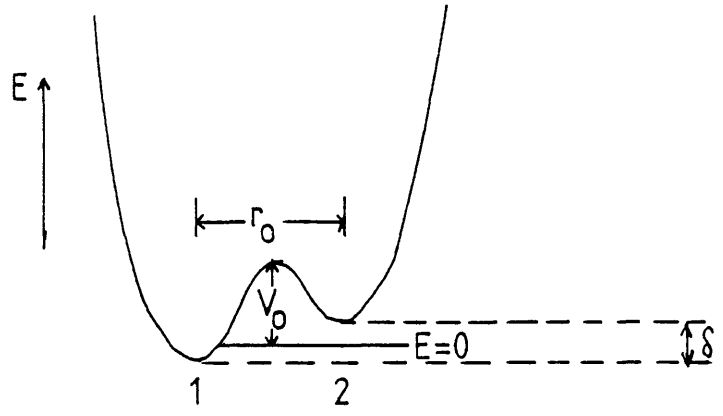

Figure 1.4 The two level system potential energy diagram.

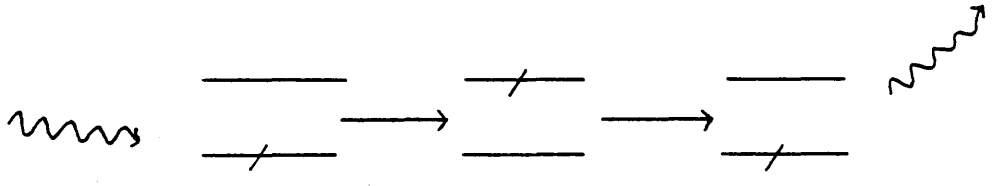

Figure 1.5 The scattering of a phonon by a two level system.

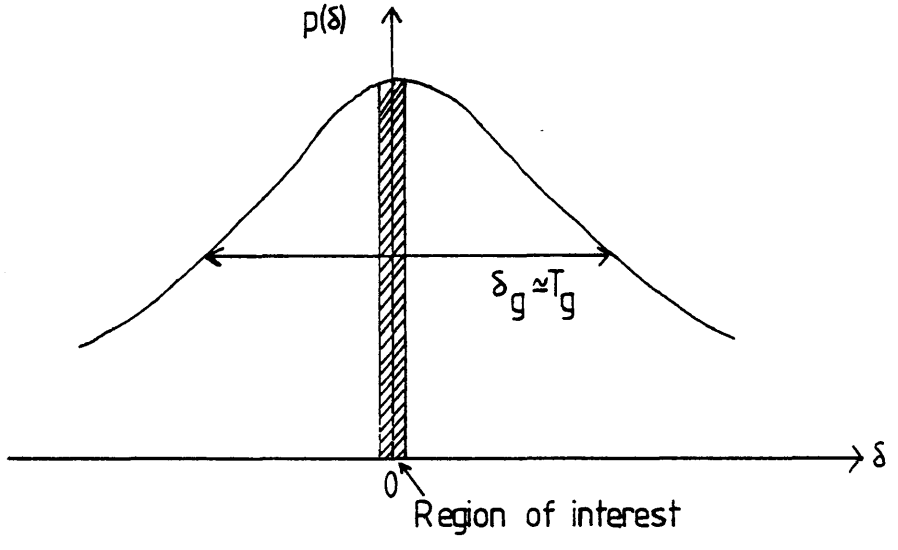

Figure 1.6 The probability density of tunnelling states as a function of δ.

$$\delta_o = \hbar \Omega_o e^{-\lambda} \qquad (1.4)$$

where

$$\lambda = (2mV_o/\hbar^2)^{0.5}.r_o \qquad (1.5)$$

and Ω_o is the frequency of oscillation of the tunelling entity in an individual well, m is the mass of the tunnelling entity, $\hbar$ is Plank's constant divided by 2π, V_o is the height of the barrier between the two wells and r_o is the spatial separation of the two lowest energy states.

If there is sufficient coupling between the two minima an atom in the lowest energy state, the ground state of the system, can absorb a phonon of energy ε and tunnel through the barrier to the other side of the double potential well. The system is now in the excited state. Later, when the system relaxes back to the ground state, a phonon of energy ε is emitted. This process is shown in figure 1.5. This process produces two interesting results. Firstly, the scattering of the phonon by the system leads to thermal resistance. Secondly, the energy can be stored in the two level system and consequently it has a thermal capacity. Both these effects are time dependent.

The disorder is frozen into the glass when it is formed at a temperature T_g. So it is expected that the tunnelling systems have a range of asymmetry energies (δ values) up to the order of $kT_g = \delta_g$. This is typically a few tens of meV. The energy splitting between the two levels is equally likely to be positive or negative with respect to any particular direction, so the energy distribution must be symmetrical about zero. Since we are restricting ourselves to low temperatures, $T \approx 1K$, we are interested in those states for which $\delta \approx kT \approx 10^{-4}eV$. So we are considering only states which lie in a small energy band around zero (see figure 1.6). It is expected that, for a symmetric distribution, the probability density, $p(\delta)$, over this range of energies will be approximately constant. Due to normalisation $p(0)$ will be

approximately δ_g^{-1}.

There is also likely to be a distribution of δ_o about which there is much less information. From equation (1.4) it is known that

$$\delta_o = \hbar\Omega_o e^{-\lambda} \qquad (1.4)$$

This together with equation (1.5) tells us that it is exponentially dependent on $V_o^{0.5}$ and r_o. These variables will probably have a wide range of values. As an approximation it is generally assumed that there is a uniform distribution over the range of λ from o to λ_o. This combined with $p(\delta)$ leads to an expression for the density of tunnelling states:-

The number of tunnelling states in the intervals $d\lambda$ around λ and $d\delta$ around δ per unit volume is

$$n/(\delta_g \lambda_o)\, d\delta\, d\lambda \qquad (1.6)$$

where n is the total number of tunnelling states per unit volume.
Since

$$\varepsilon^2 = \delta^2 + \delta_o^2 \qquad (1.3)$$

we should consider the distribution of tunnelling states as a function of both δ and δ_o. However,in typical cases δ is much larger than δ_o and so we can consider the energy splitting as a single variable $\varepsilon \approx \delta$. So the density of state distribution, $n(\varepsilon)$, in this approximation is a constant and is given by

$$n(\varepsilon)\, d\varepsilon = n_o\, d\varepsilon \qquad (1.7)$$

where

$$n_o = n \cdot \delta_g^{-1} \qquad (1.8)$$

This approximation is the two level system approximation.

Let us now consider the time dependent coupling of the tunnelling states to the thermal phonons. First it is necessary to calculate the transition probability for the spontaneous emission of a phonon by a two level system in the excited state, Γ. Using the "Fermi Golden Rule" it can be shown that

$$\Gamma = (2\pi)^{-1} \cdot M^2 \varepsilon \delta_o^2 \cdot (\hbar^4 \rho v^5)^{-1} \qquad (1.9)$$

Where M is the deformation potential, v is the phonon velocity and ρ is the mass density per unit volume. Summing up for different polarizations gives

$$\Gamma_{tot} = a \varepsilon \delta_o^2 \qquad (1.10)$$

where

$$a = (2\pi\hbar^4\rho)^{-1} \sum M_i^2 v_i^{-5} \qquad (1.11)$$

and where the sum is over modes i.

We can now calculate how a population of tunnelling states all having the same energy splittings δ and δ_o will behave when there is a change in temperature. Normally such a population will be in equilibrium with the phonons. The probability of a transition from the excited state, 2, to the ground state, 1, per unit time is the probability of a spontaneous emission plus that of a stimulated emission, $\Gamma + g_\phi \Gamma$. g_ϕ is the thermal occupancy factor of the phonons of relevant lattice modes of energy ε. It is given by

$$g_\phi = (e^{\varepsilon/kT} - 1)^{-1} \qquad (1.12)$$

Similarly the probability for a transition from the ground state to the excited state is $g_\phi \Gamma$.

Let N_1 and N_2 be the occupancy numbers of the ground and excited states respectively. Using the calculated transition probabilities dynamic equations describing the changes in the occupancy of the tunnelling states can be written

$$\dot{N}_1 = -g_\phi \Gamma N_1 + (g_\phi + 1) \Gamma N_2 = -\dot{N}_2 \qquad (1.13)$$

When the states are in equilibrium with the phonon population there will be no change in the occupancy number of either the excited state or the ground state. Therefore

$$\dot{N}_1 = \dot{N}_2 = 0 \qquad (1.14)$$

So, from substituting equation (1.14) into equation (1.13), the equilibrium occupation numbers of the tunnelling states, N_{10} and N_{20}, are related by

$$N_{20}/N_{10} = g_\phi \cdot (g_\phi + 1)^{-1} \qquad (1.15)$$

If a deviation from equilibrium is generated we can write

$$N_1 = N_{10} + N' e^{-t/\tau} \qquad (1.16a)$$

Similarly

$$N_2 = N_{20} - N' e^{-t/\tau} \qquad (1.16b)$$

By differentiating equation (1.16a) and equating this to equation (1.13), with the expressions for $\dot{N}_1$ and $\dot{N}_2$ substituted in, it can be shown that

$$\tau^{-1} = \Gamma (2g_{\phi} + 1) \qquad (1.17)$$

Substituting for g_{ϕ}, using equation (1.11), gives

$$\tau^{-1} = \Gamma \cdot \coth (\varepsilon/2kT) \qquad (1.18)$$

Using equations (1.4) and (1.10) we can rewrite equation (1.18)

$$\tau^{-1} = a\, \varepsilon\, (\hbar \Omega_o)^2\, e^{-2\lambda} \coth (\varepsilon/2kT) \qquad (1.19)$$

τ^{-1} has a maximum value when λ is a minimum. This occurs when δ_o is a maximum and δ is a minimum, i.e. $\delta_o = \varepsilon$ and $\delta = 0$. Therefore

$$\tau_{min}^{-1} (\varepsilon) = a\, \varepsilon^3 \coth (\varepsilon/2kT) \qquad (1.20)$$

Since the term λ is exponential most of the states which contribute to the population have much longer lifetimes than the minimum value.

To calculate the thermal capacity locked in the two level system let us first go back to equation (1.15)

$$N_{20}/N_{10} = g_{\phi} \cdot (g_{\phi} + 1)^{-1} \qquad (1.15)$$

This can be expressed as the ratio of occupation probabilities

$$p_{20}/p_{10} = N_{20}/N_{10} \qquad (1.21)$$

where p_{10} and p_{20} are the probabilities that the ground state and the excited state, respectively, are occupied. Also, since the tunnelling system must be in either the ground state or the excited state,

$$p_{10} + p_{20} = 1 \qquad (1.22)$$

From statistical mechanics we can write

$$p_{10} = e^{\varepsilon/kT} \cdot (e^{\varepsilon/kT} + 1)^{-1} \qquad (1.23a)$$

and

$$p_{20} = (e^{\varepsilon/kT} + 1)^{-1} \qquad (1.23b)$$

The energy, U, of the tunnelling state can be calculated

$$U = \varepsilon/2 \cdot p_{20} - \varepsilon/2 \cdot p_{10} \qquad (1.24)$$

Substituting for p_{10} and p_{20} using equations 1.23 a and b gives

$$U = -\varepsilon/2 \cdot \tanh(\varepsilon/2kT) \qquad (1.25)$$

From this the thermal capacity for one state, C_s, is given by

$$C_s = \varepsilon^2 (4kT^2)^{-1} \cdot \operatorname{sech}^2(\varepsilon/2kT) \qquad (1.26)$$

The distribution of tunnelling states is given by equation (1.6). So the thermal capacity per unit volume, C_V, is given by

$$C_V = \int_0^{\delta} \int_0^{\lambda} n\, \varepsilon^2 (\delta_g \lambda_o 4kT^2)^{-1} \operatorname{sech}^2(\varepsilon/2kT)\, d\delta\, d\lambda \qquad (1.27)$$

As the integral stands it does not take into account the time dependencies of the states.This is important since only the states with a lifetime, τ, less than the time taken for a measurement , t, can respond and contribute to the thermal capacity. In order to take this into account it is necessary to change the variables of integration

from δ and λ to ε and τ. This gives

$$C_V(t) = \int_0^{\sim\delta} \int_{\tau_{min}}^{t} n\,\varepsilon^2\,(\delta_g\,\lambda_o\,8kT^2)^{-1}\,\mathrm{sech}^2(\varepsilon/2kT) \quad x$$
$$\tau^{-1}\,(1-\tau_{min}/\tau)^{-0.5}\,d\tau\,d\varepsilon \qquad (1.28)$$

When this is integrated it produces

$$C_V(t) = \pi^2\,.\,n\,.(12\,\delta_g\,\lambda_o)^{-1}.\,k^2T.\,\ln(66.3\,a\,(kT)^3\,t) \qquad (1.29)$$

The temperature dependence is dominated by the T term. However, the logarithmic term has some effect. By looking at the temperature power law

$$\partial(\ln C)/\partial(\ln T) = 1 + 3/(\ln(66.3\,a\,(kT)^3\,t)) \qquad (1.30)$$

and substituting in typical values for a ($\approx 200\mu eV^{-3}s^{-1}$), T (=0.1K) and t (=1s) leads to a temperature dependence of $T^{1.19}$. This is close to the temperature dependence found by Lasjuanias et al. (1972) which was discussed in section 1.1. Equation (1.29) also shows a logarithmic dependence on time. This has led to the experimental investigation into the time dependence of the thermal capacities of amorphous materials. The results of these experiments will be discussed in section 1.4.

The thermal conductivity is not as easy to calculate. The resonant scattering of the phonons by the tunnelling states causes a reduction of the mean free path of the phonons and leads to a thermal resistivity. The finite lifetime effects of the tunnelling states and the different phonon modes make this effect difficult to analyse.

Looking at one polarisation, i, for equation (1.12) the rate of "up processes" is given by

$$N_1\,\Gamma_i\,(\delta_o, \varepsilon)\,g_\phi \qquad (1.31)$$

This rate of "up processes" is equal to the rate of phonon absorption by the

tunnelling states.

Consider the phonons in the energy range dε around the energy ε. $N_1\ \Gamma_i$ needs to be averaged over all the states in the energy range dε around ε. As before we wish to express this as a function of ε and τ. So the rate of "up processes" is written as

$$\int_t^{\infty} n\,(\delta_g\ \lambda_o)^{-1}\ .\ p_1(\varepsilon).\ (\tau\ \coth(\varepsilon/2kT))^{-1}.g_\phi\ .d\varepsilon.(2\tau)^{-1}.(1\ -\tau_{min}/\tau)^{-0.5}\ d\tau \qquad (1.32)$$

$$= np_1(\delta_g\ \lambda_o)^{-1}.\ a_i\ \varepsilon^3,\ g_\phi.\ d\varepsilon \int_{\tau_{min}}^{\infty} \tau_{min}\ (2\tau^{\ 2})^{-1}(1-\tau_{min}/\tau)^{-0.5}\ d\tau \qquad (1.33)$$

The integral in expression (1.33) was found to be unity. So the rate of "up processes" is given by

$$n\ p_1\ .\ (\delta_g\ \lambda_o)^{-1}\ .\ a_i\ \varepsilon^3\ g_\phi\ d\varepsilon \qquad (1.34)$$

The rate of absorption of phonons of energy ε in the range dε is

$$n_\phi/\tau_\phi\ .\ d\varepsilon \qquad (1.35)$$

where τ_ϕ is the phonon lifetime and n_ϕ is the number of phonons per unit energy range in thermal equilibrium at temperature T

$$n_\phi\ =\ \omega^2\ g_\phi\ .\ (2\pi^2\ v^3\ \hbar)^{-1} \qquad (1.36)$$

Equating expressions (1.34) and (1.35) produces an equation for the "overall" phonon lifetime

$$\tau_\phi\ =n\ p_1\ (\ \delta_g\ \lambda_o)^{-1}\ .\ a_i\ \varepsilon^3\ g_\phi\ .\ n_\phi^{-1} \qquad (1.37)$$

Simplifying this expression gives

$$\tau_\phi = n\, p_1\, (\delta_g\, \lambda_o)^{-1} \cdot \pi\, M_i^2\, \varepsilon\, (\hbar\, \rho v_i^2)^{-1} \qquad (1.38)$$

This is obtained using equations (1.11) and (1.36) to substitute for a_i and n_ϕ respectively.

It is necessary to make some approximations in order to estimate the thermal conductivity. The first is that we use the dominant phonon approximation. We assume that the phonons with energies of 3.8kT dominate the thermal conductivity. Secondly, we assume that we can use a kinetic model of a phonon gas to calculate the thermal conductivity. From this we can write

$$\kappa = 1/3 \quad C\, v\, l \qquad (1.39)$$

where C is the specific heat per unit volume in a phonon gas. This is proportional to T^3 for Debye phonons. v is the mean velocity of the phonons in the gas and l is the mean free path of the dominant phonons. This equation can also be written as

$$\kappa = 1/3\ C\, v^2\, \tau_{eff} \qquad (1.40)$$

This effective lifetime, τ_{eff}, is not the "overall" τ_ϕ which has been calculated above. The phonon population needs to be randomised by the scattering. The absorption of a phonon followed by stimulated emission does not do this. There is no net scattering in this process. To take account of this the "overall" lifetime needs to be corrected by a factor of the ratio of the spontaneous transition rate to the total transition rate. The effective phonon scattering lifetime is given by

$$\tau_{eff}^{-1} = \tau_\phi^{-1} \cdot (g_\phi + 1)^{-1} \qquad (1.41)$$

Substituting this into equation (1.38) gives

$$\tau_{eff}^{-1} = n\, p_1\, (\delta_g\, \lambda_o)^{-1}\, .\, \pi\, M_i^2\, \varepsilon\, (\hbar\, \rho v_i^2)^{-1}.\, (g_\phi + 1)^{-1} \quad (1.42)$$

Taking the two statistical factors, p_1 and $(g_\phi + 1)^{-1}$, together

$$\tau_{eff}^{-1} = n(\, \delta_g\, \lambda_o)^{-1}\, .\, \pi\, M_i^2\, \varepsilon\, (\, \hbar\, \rho v_i^2)^{-1} \tanh(\varepsilon/2kT) \quad (1.43)$$

Using this along with the dominant phonon approximation and the kinetic phonon gas model leads to

$$\kappa\ \alpha\ C\ v^2\ (\varepsilon \tanh(\varepsilon/2kT))^{-1} \quad (1.44)$$

$$\kappa\ \alpha\ T^3\, .\, T^o\, .\, T^{-1} \quad (1.45)$$

In other words κ is proportional to T^2 . As mentioned in section 1.1 the actual variation is a power slightly below 2. This can be obtained from more accurate calculations.

It is uncertain as to what the tunnelling entities are. The most widely studied glass has been silica therefore most suggestions have been made about the tunnelling states in this material. Jackle et al. (1976) suggested three possibilities, an oxygen atom moving transversely between two bonding silicon atoms, two potential minima for an oxygen atom along the bond direction or the rotation of an SiO_4 tetrahedron. Von Haumeder et al. (1980) and Raychaudhuri and Pohl (1982) suggest that it is a single oxygen atom which is tunnelling. From recent experimental evidence (von Lohneysen et al. (1985), Buchenau (1985), Phillips (1985) and Dianoux et al. (1986)) rotation of SiO_4 tetrahedra is thought more likely. However these experiments only provide indirect evidence on this question and are not conclusive.

Although the two level model can explain many of the thermal properties of amorphous materials it is not without problems. Calculations of n_o from the specific heat capacity produce a value which is an order of magnitude greater than that

calculated from the thermal conductivity. This is possibly due to the thermal conductivity measurement being made over a short time compared to the specific heat. Only two level states with short time constants could participate in the measurement of the thermal conductivity. Another possibility suggested by Hunklinger et al. (1975) and Black and Halperin (1977) is the existence of anomalous levels which have long coupling times with a narrow distribution function. These anomalous states would only participate in the specific heat measurement. The existence of these states has not yet been confirmed experimentally.

1.3 Ultrasonic properties of amorphous materials

The tunnelling model predicts an ultrasonic attenuation which saturates with increasing input acoustic power (Anderson et al. (1972), Jackle (1972), Jackle et al. (1976)). When a sound wave travels through a material with two level systems present energy is absorbed from it by the two level systems. In absorbing this energy the system goes from the ground state to the excited state. At low powers the attenuation is independent of the power. This is because the sound wave does not significantly affect the occupation numbers of the two level systems. At these phonon energies ($\ll kT$) the occupation numbers of the upper and lower levels are approximately equal. High acoustic intensity generates more exactly equal populations so that the probability of an up process is approximately equal to the probability of a stimulated down process. Energy is only lost by spontaneous processes at the same rate as before. Therefore, as the input power is increased the attenuation decreases. Hunklinger et al. (1972) measured the ultrasonic attenuation over five orders of magnitude of intensity and found this nonlinear effect. This was also found by Golding et al.(1973). Further measurements by Hunklinger et al. (1973) showed that the low intensity absorption was proportional to ω^2/T and the saturated attenuation varied as T^3 at low temperatures. This is in agreement with the predictions of the tunnelling model. Jackle et al. (1976) measured the attenuation up to a temperature of 100K and explained their results in terms of resonant tunnelling of two level systems and, at temperatures above 50K, structural relaxation.

Hunklinger et al. (1975) and Hunklinger and Piche (1975) measured the variation in ultrasonic velocity at low input powers. It was found that the change in velocity (Δv) at the lowest temperatures measured was proportional to $\ln(T/T_1)$, where T_1 is some reference temperature less than T. At higher temperatures Δv was proportional to $-\ln(T/T_2)$, again T_2 is a reference temperature. The authors explained this in terms of the interaction of the phonons with two level systems. At low temperatures the phonon interaction is a resonant process causing the tunnelling of the entity in the system. At higher temperatures it is a relaxation process which dominates the interaction. A similar variation of ultrasonic velocity was measured by Piche et al. (1974) at higher pulse powers which saturated the absorption. This negligible effect of the saturation of the absorption on the velocity variation is to be expected. This is because a broad energy range of two level states contribute to the variation in the velocity and only a small part of this energy range will be saturated by the phonons.

Measurements of the ultrasonic attenuation and the variation of the acoustic velocity produce estimates of $n_o M^2$. When these estimates are used to calculate the thermal conductivity of the material on which the measurements were made good agreement with the experimentally measured values of the thermal conductivity is found. Another measurement which links the acoustic and the thermal properties of amorphous materials is that performed by Golding, Graebner and Schutz (1976). They measured the temperature dependence of the mean free path of acoustic phonons in silica at lower temperatures than previously investigated. They were able to attain the $\hbar\omega > kT$ regime and were, therefore, able to measure the resonant decay lengths of the phonons. From this measurement they calculated the thermal conductivity in agreement with the measured value.

Phonon echoes have been detected in glasses (Golding and Graebner (1976) and Graebner and Golding (1979)). They input two phonon pulses of the same frequency into the glass. On looking at the output they detected a third pulse a short time after the detection of the reflection of the input pulses. This third pulse was an echo which can be explained by the coherent emission of phonons by two level states associated with atomic tunnelling. This coherent emission was stimulated by the second pulse.

Golding et al. (1973) and, later, Graebner et al. (1983) measured the recovery time of the two level systems from saturation. To do this they used a two pulse technique, a strong pulse followed a variable time later by a weak pulse. By measuring the attenuation of the second pulse a measure of the recovery time is obtained. They observed a distribution of states with decay times ranging over at least a factor of ten as expected from the two level model. The decay times could be fitted with a distribution function that emphasises the slower asymmetric states.

Arnold and Hunklinger (1975) also performed a two pulse experiment. In their experiment the first pulse, P_1, was of high power and variable frequency. The second pulse, P_2, was a low power, fixed frequency pulse. They swept through the frequency range of P_1 and measured the attenuation of P_2. They found a broad, asymmetric minimum in the attenuation of P_2 where the two pulse frequencies were equal. The minimum was more pronounced when the input power of P_1 was increased. The broadness of the minimum indicated that the pulse P_1 saturated a wide range about its own nominal frequency i.e. that interactions between two level systems of similar frequency are strong. The authors were able to explain the width, asymmetry and temperature dependence of the minimum in terms of direct interaction between two level systems.

Results of ultrasonic measurements support the two level system model. Values of n_0M^2 calculated from these measurements are consistent with the values obtained from the thermal conductivity. Inconsistencies arise when the value of n_0 calculated from the ultrasonic measurements is compared with the value calculated from the specific heat. It is found that the specific heat produces a value that is about an order of magnitude larger than the value from the acoustic measurements, this is a similar result to that obtained when comparing n_0 calculated from the thermal conductivity and the heat capacity (see section 1.2).

1.4 The time dependent specific heat

One of the predictions of the tunnelling states model is that the specific heat has a time dependence at short times. This is caused by the tunnelling states taking a time τ to come into equilibrium with the phonons. Equation (1.19) gives the distribution of τ. If the time of measurement, t, is reduced then a reduced heat capacity should be observed since fewer states have sufficient time to interact with the phonons. From equation (1.29) it can be seen that this time dependence is logarithmic for a uniform energy density of tunnelling states.

The first measurements of the short time heat capacity found no evidence of the expected time dependence (Goubau and Tait (1975) and Kummer et al. (1978)). Black (1978) noted that the measurements of Goubau and Tait (1975) appeared to be inconsistent with measurements of the ultrasonic properties of glasses. Using the standard tunnelling model of Anderson et al. (1972) and Phillips (1972) and parameters of the tunnelling systems calculated from the ultrasonic measurements Black (1978) calculated both the long time and the short time specific heat of vitreous silica. In both cases the theoretical value of the specific heat was smaller than the experimental value. He then introduced anomalous tunnelling states which do not participate in phonon scattering, but only contribute to the specific heat. The theoretical value of the long time specific heat calculated using the standard and the anomalous tunnelling states agreed with the experimental value. However the short time theoretical value in this case was much smaller than that measured by Goubau and Tait (1975). More recent measurements by Meissner and Spitzmann (1981) and Loponen et al. (1982) have revealed a logarithmic time dependence of the specific heat capacity on a time scale of less than 100μs.They found that the short time specific heat below 0.3K around 10μs was considerably smaller than the long time specific heat but larger than the Debye value. Above 0.3K around 10μs the heat capacity is beginning to be dominated by the contribution from the thermal phonons. Loponen et al. (1982) also measured the diffusivity of the samples and found that it did not reveal the reduction of the heat capacity which they observed around 10μs. This result is consistent with the measurements of Kummer et al. (1978) who did not observe the time dependence when they measured the diffusivity of the sample.

Measurements with time scales of 50s to 6000s were performed by Zimmerman

and Weber (1981) and on time scales of 10 to 1000s by Leponen et al. (1982) on amorphous silica. In both these measurements the samples were heated to fixed temperatures and maintained at these temperatures for several hours. They were then allowed to cool through a known thermal link to the temperature of a thermal bath. The cooling curves were compared to theoretical ones which took into account the contributions from the Debye phonons and the tunnelling states. The authors concluded that there was a time dependent contribution from tunnelling states as described by the models of Anderson et al. (1972) and Phillips (1972). The calculated density of states was very similar to that calculated by Black (1978) from ultrasonic measurements.

The time dependent specific heat measurements have revealed a logarithmic time dependence. This is consistent with a tunnelling model based on a uniform density of two level systems.

1.5 The temperature range 1 to 10K

The two level system model explains the thermal and ultrasonic properties of amorphous materials below 1K. Taking relaxation into consideration it can also explain the ultrasonic data at temperatures up to 100K. However the situation for the thermal properties at temperatures between 1 and 10K is less clear. This is in the region of the plateau of the thermal conductivity and the peak in C/T^3. Zeller and Pohl (1971) calculated from the thermal conductivity that the mean free path of the phonons in this temperature range varied approximately as ω^{-4}. As this frequency dependence is the same as that for Rayleigh scattering. The authors proposed an "isotopic scattering" model. The glass was represented by a crystal with every atom displaced and Rayleigh scattering taking place at each of these displaced atoms. Jones et al. (1980) used light scattering data to calculate the strength of the Rayleigh scattering and found it to be too weak by almost two orders of magnitude. Zaitlin and Anderson (1975) used Walton's (1974) structure scattering model to explain their thermal conductivity data. However, Jackle et al. (1976) calculated the scattering strength to be less than that needed to explain the Zaitlin and Anderson (1975) data. Jones et al. (1978) attempted to fit the plateau of the thermal conductivity of silica using a structure scattering model but similarly found that the

structure scattering was not strong enough to explain the data. Recently Handrich (1983) used a structure scattering model to explain the thermal conductivity of amorphous materials at temperatures up to 20K. He found that this model explained the published experimental data.

An extension to the tunnelling model was proposed by Zaitlin and Anderson (1975). This involved introducing an extra quadratic term in the density of states. It is able to explain both the plateau in the thermal conductivity and the heat capacity in excess of the Debye contribution using parameters which are consistent with the acoustic data. This model has been used successfully by other authors (Smith et al. (1978) and Jones et al. (1978)) to explain their data. However, this extension of the tunnelling model is not altogether satisfactory. Jones et al. (1978) criticise it on three points. First there is no natural cut off in the density of states, one has to be introduced arbitrarily. Secondly, when the total number of tunnelling states is integrated up it is only one order of magnitude less than the number of atoms which is unphysical. Finally, the number of variables used in the model makes it easy to fit the data.

Dianoux et al. (1986) using inelastic neutron scattering found vibrational excitations in viteous silica over a wide frequency range above 150GHz. They identified these excitations as the coupled rotations of SiO_4 tetrahedra and determined their density of states. This measured density of states was then used to calculate the excess T^3 term in the specific heat of vitreous silica and was found to agree with the published data. Below 1K the dominant contribution to the specific heat comes from the tunnelling term. The authors are unsure about how these vibrational excitations are related to the tunnelling states.

The thermal data in the temperature range 1 to 10K can be explained using both structure scattering models and an extension to the tunnelling model. Both these types of models have been criticised and there is no clear evidence to support one or the other. The data can be explained by any mechanism which gives a sufficiently rapid increase in the mean free path with phonon frequency.

Two level states are thought to be an intrinsic feature of the structure of amorphous solids. Experiments have been performed in which the structure of the amorphous material has been changed. The effect that this change has had on the two level states has been observed indirectly through the measurement of the thermal and acoustic properties of the material.

Smith et al. (1978) measured the heat capacity, thermal conductivity and variation in acoustic velocity for unirradiated and neutron irradiated silica. They found that the heat capacity decreased and the thermal conductivity and the variation of the phonon velocity increased upon irradiation. Earlier measurement of the thermal conductivity by Cohen (1958) produced similar results. These changes are not due to an increase in the atomic order of the materials. X-ray diffraction measurements by Bale et al. (1978) showed that neutron irradiation makes the structure less ordered. This rules out structure scattering as the cause of the anomalous thermal and acoustic properties of amorphous materials. Smith et al. (1978) calculated that all the changes they observed were consistent with about a 35% decrease in the number of tunnelling states.

Investigations were carried out by Raychaudhuri and Pohl (1982) on the doping of nitrate and silica glasses with water, lithium and nitrite. They measured the low temperature heat capacity of the doped glass and found that this property changed if the dopant changed the glass transition temperature, T_g. The linear part of the specific heat increased as the glass transition temperature decreased. This observation is consistent with a density of two level systems frozen into the glass varying as T_g^{-1}. This conclusion is supported by the studies of von Lohneysen et al. (1985) on the effects of annealing on the low temperature properties of silica. They found a decrease in the heat capacity and an increase in the thermal conductivity when the glass was annealed. Both of these observations indicate a decrease in the density of tunnelling states. The higher the annealing temperature the greater the decrease in n_o, i.e. $n_o \sim T_a^{-1}$. The authors also noted that the largest changes occurred at the peak of C/T^3 versus T (T~3K) and at the plateau in the thermal conductivity which implies that these two features are linked. Their results agree with the

theory developed by Cohen and Grest (1981) and the observations of Raychaudhuri and Pohl (1982). Both von Lohneysen et al. (1985) and Raychaudhuri and Pohl (1982) discuss the neutron irradiation experiments. They attribute the increase in thermal conductivity to an increase in the fictive temperature, T_f, of the glass. The larger the neutron dose the larger the fictive temperature. Von Lohneysen et al. (1985) suggest that a possible mechanism leading to the decrease in the density of tunnelling states as T_a, T_g or T_f increases is the increase in the mass density inhibiting the atomic motion in the material.

Measurements on amorphous selenium and α-Se_{1-x}-Ge_x glasses (Duquesne and Bellessa (1985b) and Jones et al. (1982)) indicate that as the rigidity of the network increases, as the Ge component is increased, the number of tunnelling states decreases. It is thought that the Ge links Se chains and makes the structure more rigid reducing the number of atoms that can tunnel. This effect is also found in amorphous polymers. Matsumoto et al. (1979) measured the low temperature thermal and ultrasonic properties of two similar epoxies which differed in their crosslink densities. The epoxy with the greater crosslink appeared to have the lower density of tunnelling states.

1.7 Dielectric properties

It has been noted that there is a similarity between the acoustic and dielectric properties of amorphous materials (Hunklinger and von Schickfus (1981)). This has lead to the suggestion that the same mechanism is responsible for both dielectric and acoustic losses.

Von Schickfus et al. (1975) measured the change in the dielectric constant of glasses as a function of temperature. He did this by measuring the change in the resosnant frequency of a microwave cavity containing a sample of the glass. A maximum in the velocity at 4K was observed. At temperatures less than 4K the change in the light velocity followed the same logarithmic dependence as the sound velocity. This behaviour could be explained in terms of the dipole moment associated with transitions within the tunnelling systems in analogy to the acoustic properties. A difference was found between the dipole moments of silica and borosilicate glasses.

This suggests that the electrical dipole moment is more sensitive to differences in composition than the elastic dipole moment.

Mon et al. (1975) measured the infrared absorption of silica, germania and PMMA. They found that the absorption was dependent on both the temperature and the frequency. As the temperature of the glass increased the absorption coefficient decreased. The authors explained this in terms of a thermal population dependence of a simple two level model. To explain deviations between their theory and measurements they introduced three level systems into their model. Calculation of the electric dipole moment from this experiment produced good agreement with von Schickfus et al. (1975).

The range of materials and measurements has been extended by other workers. These have produced similar results and conclusions (Hunklinger and von Schickfus (1981)).

1.8 Energy resolved phonon scattering experiments

It is unclear as to whether the thermal conductivity between 1 and 10K is determined by structure scattering or by scattering from a non-constant density of tunnelling states. Also very little is known about the details of the interaction between phonons and tunnelling states at high energies, in particular whether higher order phonon scattering processes are important. One way of throwing light on the problem is to investigate whether the phonon scattering processes are elastic or inelastic by using energy resolving phonon transducers.

Long et al. (1980) measured energy resolved phonon scattering in thin films. They investigated three materials; evaporated silicon monoxide, evaporated germanium and sputtered hydrogenated germanium. They observed that inelastic scattering processes dominated in the amorphous germanium films and elastic processes in the silicon monoxide film. They also found evidence for scattering events with significant dwell times. Measurements were made on amorphous evaporated silicon dioxide by Deitsche and Kinder (1979). In contrast to the results of Long et al. (1980) they interpreted their data as being due to inelastic scattering. The two experiments were very similar. They both used superconducting tunnel

heterojunctions as phonon detectors and thin amorphous films. There were some important differences. Long et al. (1980) held their samples in vacuum and the film being investigated was deposited under the detector, whereas, Deitsche and Kinder (1979) had their samples in a liquid helium bath and the sample was under the heater. The implications of these differences will be discussed in chapter 6.

This project was a continuation of the measurements of Long et al. (1980). The first priority was to establish that the detectors and their energy resolution was as theory predicted and to establish the output of the thin film heaters used in the experiment. The range of materials investigated was then extended and the differences between depositing the sample under the detectors and the heaters were investigated.

Chapter2 The phonon detectors and sources

2.1 Introduction

Superconducting tunnel junctions have been used as phonon generators and detectors since their introduction by Eisenmenger and Dayem (1967). However, they were not used as phonon energy sensitive detectors until Dietsche (1978) introduced this technique. He used an aluminium, lead bismuth (0.85:0.15) tunnel junction. We decided to use these junctions as our detectors since they operate in the energy range of interest. For phonon generation we used one of two sources, either tin-tin superconducting tunnel junctions or constantan thin films. The tunnelling junctions were used because they emit a well known phonon energy spectrum (Berberich and Kinder (1981)) and using this spectrum we can check our matrix analysis scheme. The constantan thin films were used for the majority of the experiments since they emit a wide continuous band of phonon energies and are easy to manufacture.

2.2 D.C. electrical characteristics of superconducting tunnelling junctions

Figure 2.1 shows a density of states versus energy diagram for a junction between identical superconductors. The tunnelling processes are shown. At finite temperatures there is a current due to the tunnelling of thermally excited quasiparticles. This current is fairly constant with voltage after the initial rise and is the dominant current for voltages less than $2\Delta/e$. The current due to the pair-breaking process is zero below $V=2\Delta/e$. The tunnelling electron must have sufficient energy to reach an empty state above the gap, this is the lowest energy at which this occurs. This process produces a sharp rise in the tunnelling current at this voltage. At higher voltages there is a gradual approach to the normal state characteristic. These characteristics are shown in figure 2.2.

Figure 2.3 shows the density of states versus energy diagram and the tunnelling processes for an S_1-S_2 type junction. These processes are similar to those occuring in an S-S junction. Below a voltage of $(\Delta_1-\Delta_2)/e$ there is a tunnelling current due to thermally excited quasiparticles in the aluminium. Quasiparticles of energy greater than a thershold value of Δ_1-eV can contribute to the tunnelling current.

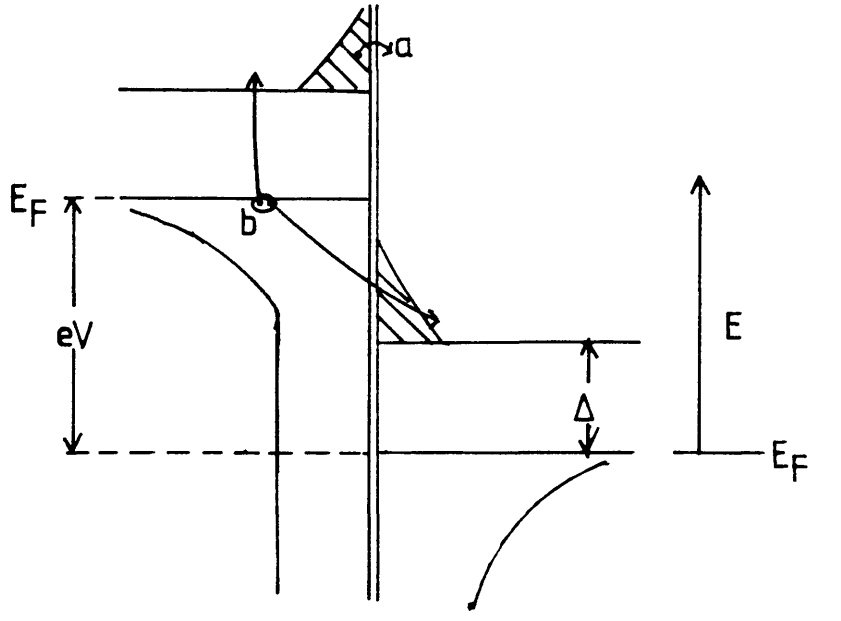

a - quasiparticle tunnelling, b - tunnelling by pair breaking

Figure 2.1 Energy diagram of and tunnelling in a symmetric superconducting tunnel junction.

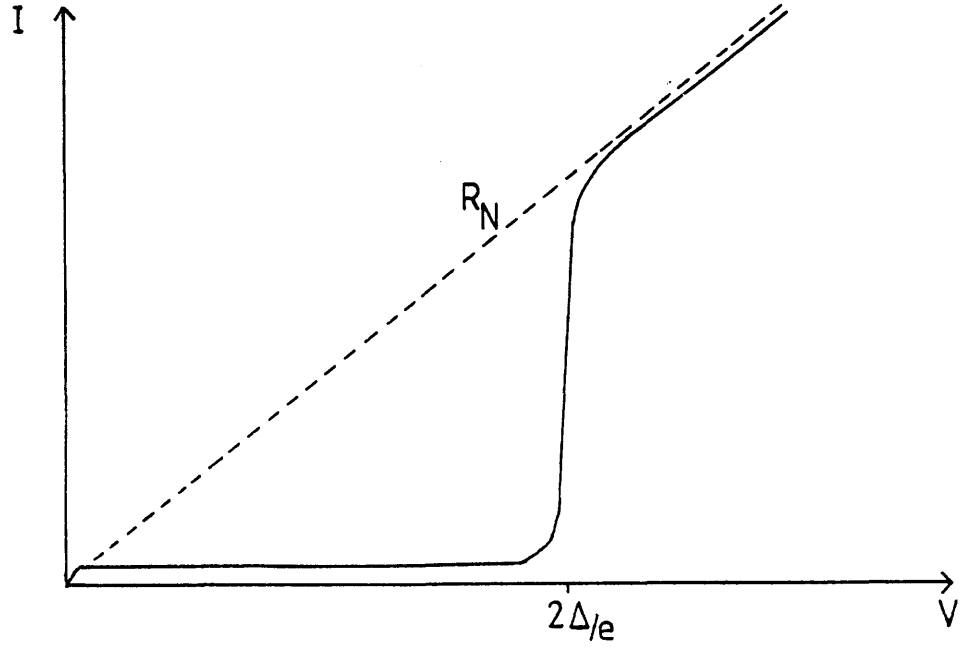

Figure 2.2 Schematic of d.c. electrical characteristics of a symmetric superconducting tunnel junction.

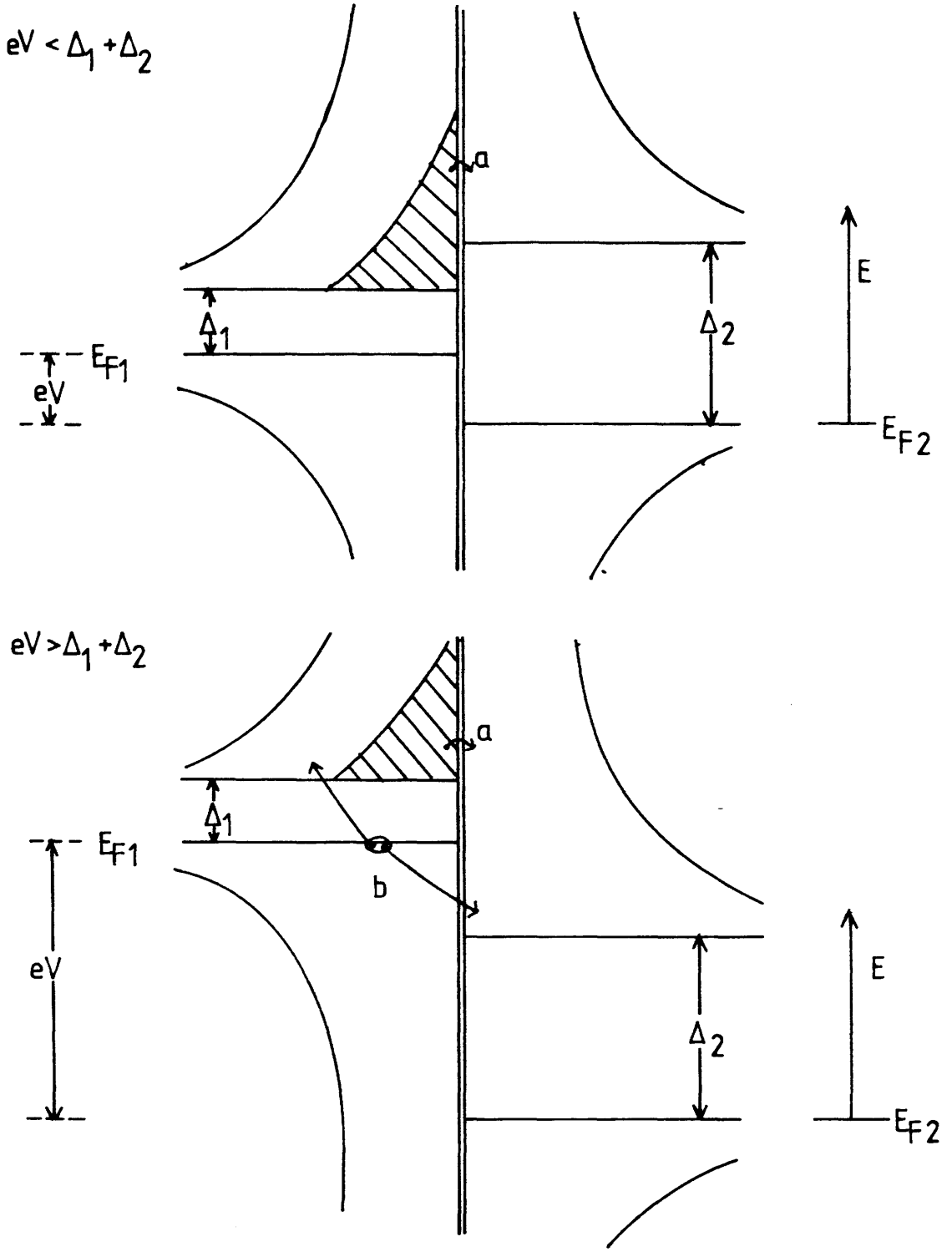

a - quasiparticle tunnelling, b - tunnelling by pair breaking

Figure 2.3 Energy diagram of and tunnelling in a superconducting heterojunction

This current increases at low voltages up to the singularity at $(\Delta_1-\Delta_2)/e$ then decreases as the voltage is increased to $(\Delta_1+\Delta_2)/e$. This is due to the thermally excited quasiparticles in the aluminium being moved up from the singularity in the density of empty states just above the energy gap in the lead-bismuth. The current increases again at $V=(\Delta_1+\Delta_2)/e$ due to tunnelling by the pair breaking process. These current voltage characteristics are shown in figure 2.4 a. In this experiment a current biasing supply was used. The effect of this is that the junction switches at constant current between the voltages of $(\Delta_1-\Delta_2)/e$ and $(\Delta_1+\Delta_2)/e$. The d.c. electrical characteristics obtained from a current source are shown in figure 2.4b.

The junctions were operated as detectors in the region $0 < eV < \Delta_1-\Delta_2$ so the current voltage characteristics in this region should be considered in more detail. In this region the current is dominated by the tunnelling of thermally excited quasiparticles from the aluminium to the lead-bismuth. The reverse current of thermally excited quasiparticles from the lead bismuth to the aluminium is negligible. The number of excited quasiparticles in a superconductor is proportional to $(\exp(\Delta/kT)+1)^{-1}$. For lead bismuth at a temperature of 1K this has a value of $\sim 10^{-8}$ which is negligible compared to that of aluminium ($\sim 10^{-1}$). Following from Giaever and Megerle (1961) it can be shown that the tunnelling current from aluminium to lead bismuth is given by

$$I = K \int_{\Delta_1}^{\infty} N_2(E-eV)\ f(E-eV)\ N_1(E)\ [1-f(E)]\ dE \qquad (2.1)$$

Where $N_i(E)$ is the BCS density of quasiparticle states in material i given by

$$N_i(E) = E/\sqrt{(E^2-\Delta_i^2)} \qquad (2.2)$$

and f(E) is the fermi distribution function given by

$$f(E) = (\exp(E/kT) + 1)^{-1} \qquad (2.3)$$

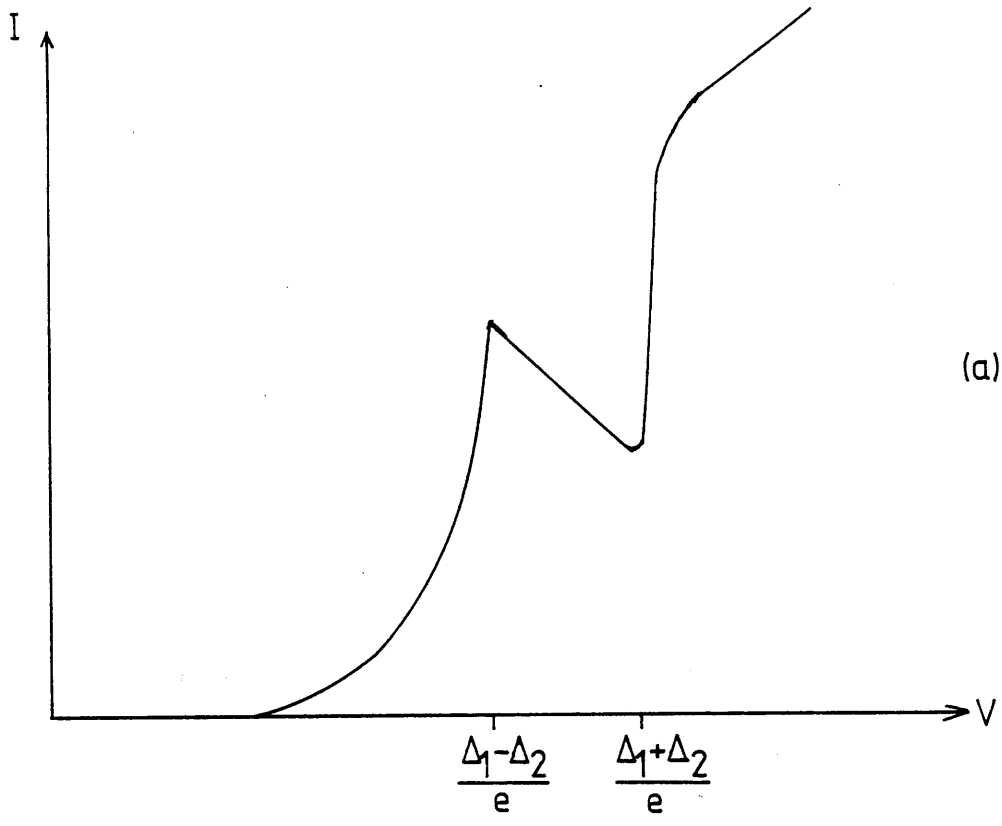

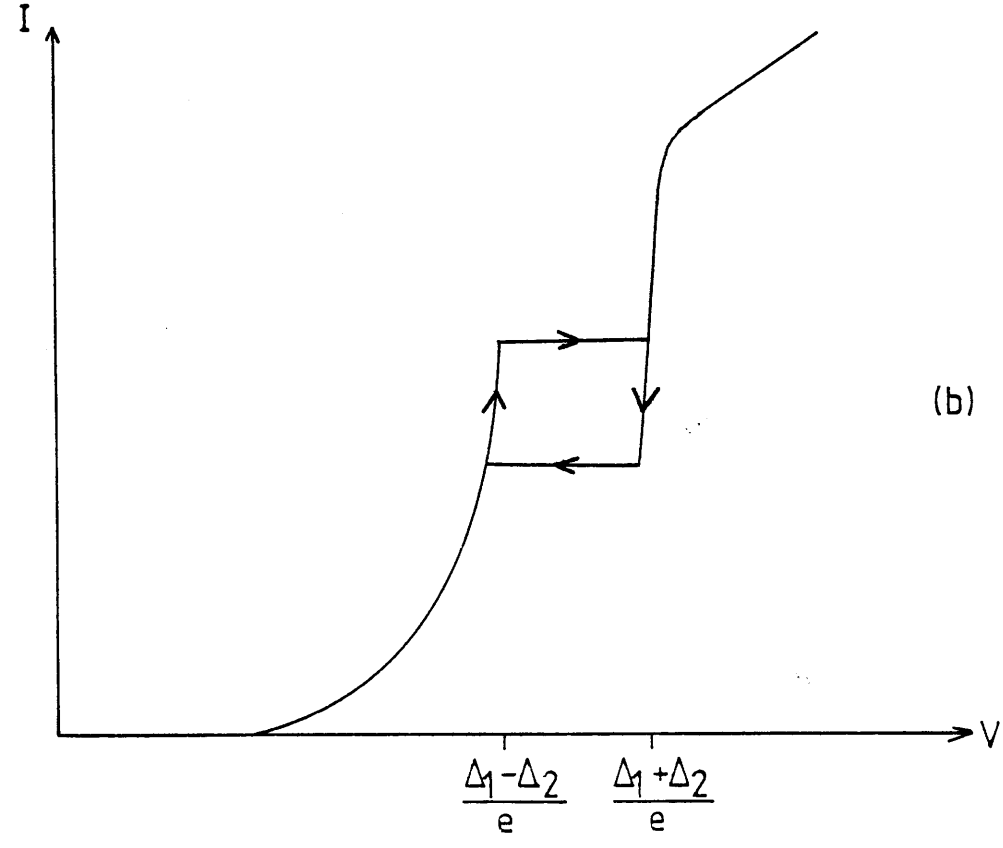

Figure 2.4 Schematic of d.c. electrical characteristics of a superconducting heterojunction,
(a) voltage biasing source, (b) current biasing source

The junctions are used at temperatures below 1K so all but the most significant fermi distribution functions can be approximated by zero. Equation (2.1) now becomes

$$I = K.\int_{\Delta_1}^{\infty} N_2(E-eV)\ f(E-eV)\ N_1(E)\ dE \qquad (2.4)$$

$$= K.\int_{\Delta_1-eV}^{\infty} N_2(E)\ f(E)\ N_1(E+eV)\ dE \qquad (2.5)$$

In the voltage range measured $N_2(E)$ is approximately constant. Substituting this into equation (2.5) along with the expressions for f(E) and $N_1(E+eV)$ gives

$$I = K.\ N_2(\Delta_1-eV).\int_{\Delta_1-eV}^{\infty} (\exp(E/kT)+1)^{-1} \quad x$$
$$(E+eV)\ .\ (\sqrt{((E+eV)^2-\Delta_1{}^2)})^{-1} \qquad (2.6)$$

$$I = K\ .\ N_2(\Delta_1-eV)\ .\ \sqrt{(\Delta_1\pi kT/2)}\ .\ \exp((\Delta_1-eV)/kT) \qquad (2.7)$$

Equation (2.7) is the expression used for the current in the junction in this range.

In practice there are contributions to the tunnelling current at $V < (\Delta_1-\Delta_2)/e$ other than those taken into account when deriving equation (2.7). There is the Josephson tunnelling current. This may reduced to a neglgible level by applying a magnetic field. If the oxide layer is incomplete a short is formed in parallel with the junction. This usually renders the junction useless. A third source of leakage current is a parallel superconducting-normal junction. This occurs when some of the PbBi alloy remains normal. It is unclear why this happens but it appears to be connected with surface roughness on the sapphire substrate. Figure 2.5 shows the density of states versus energy diagram for an S-N junction. The tunnelling current is dominated by the tunnelling of quasiparticles thermally excited to a voltage of Δ/e. There is then a sharp rise in the current due to the pair-breaking process. The current-voltage characteristic is shown in figure 2.6. When an S-N junction is formed in parallel with an S_1-S_2 junction the d.c. characteristic shown in figure

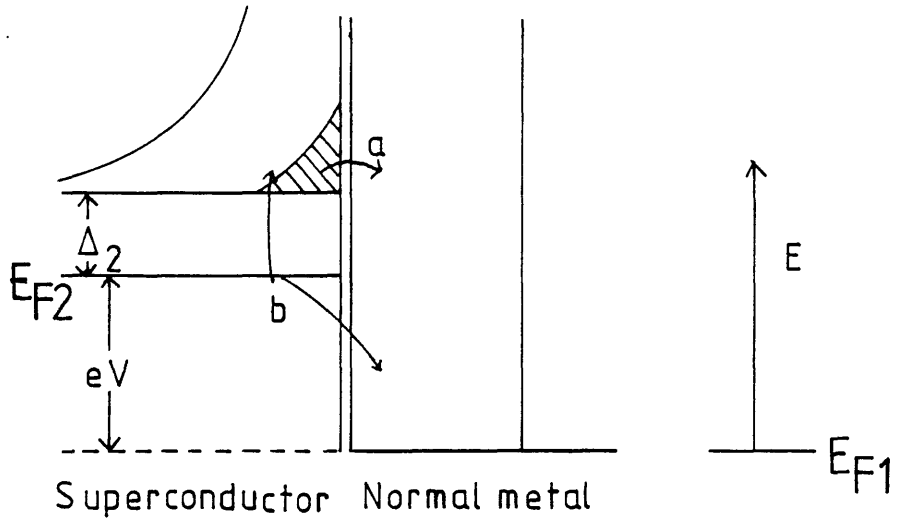

a - quasiparticle tunnelling, b - tunnelling by pair breaking

Figure 2.5 Energy diagram of and tunnelling in a S-N tunnel junction.

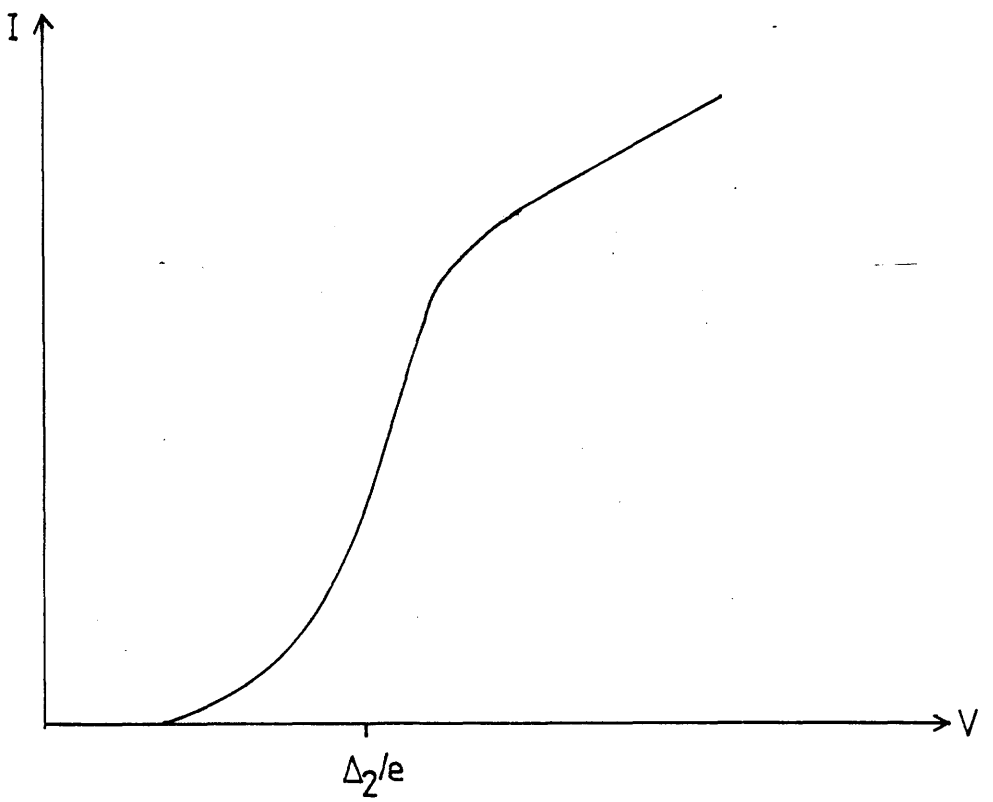

Figure 2.6 Schematic of d.c. electrical characteristics of a S-N tunnel junction.

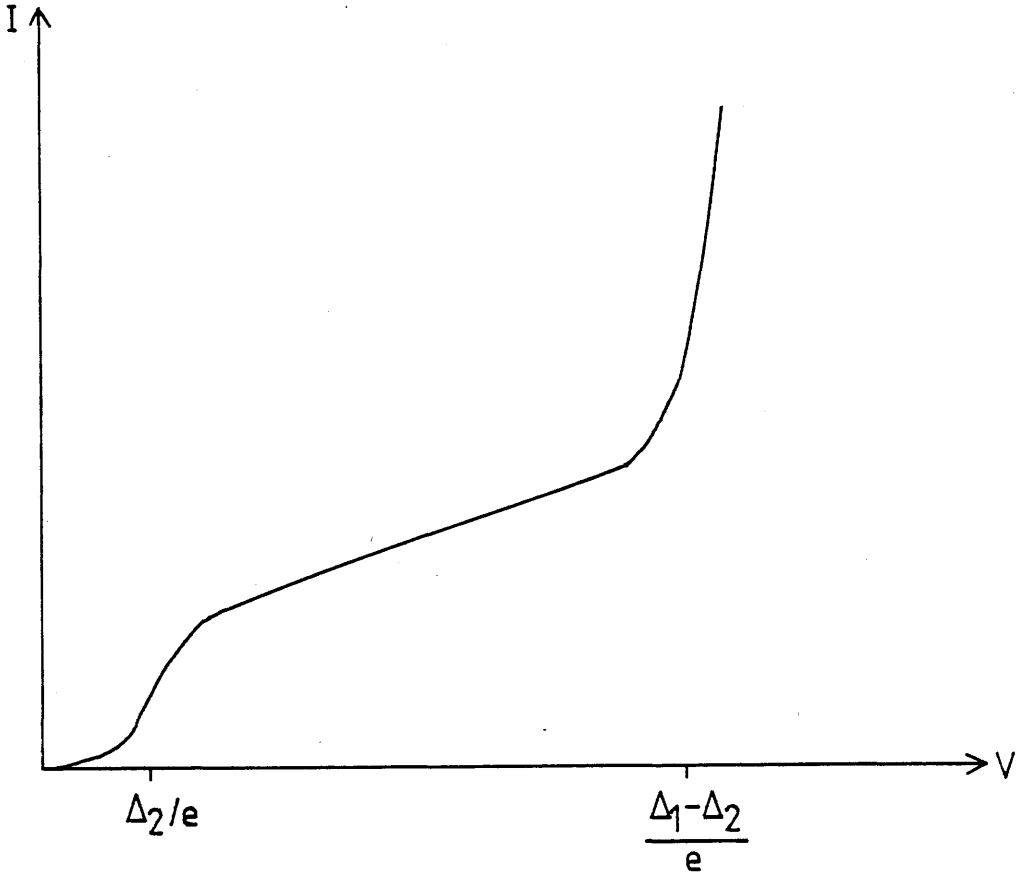

Figure 2.7 Schematic of d.c. electrical characteristics of a superconducting heterojunction in parallel with a S-N junction.

2.7 is obtained. A correction for the perturbing effects of this excess contribution can be made and is discussed in section 2.6.

2.3 Superconducting tunnel junctions as phonon generators

The phonon emission spectrum of superconducting tunnel junctions has been thoroughly investigated and is well known (Eisenmenger and Dynes (1967); Dayem, Miller and Wiegand (1971); Berberich and Kinder (1972)). It is for this reason that they were used to check our analysis scheme. Tin junctions were chosen because the energies of the emitted phonons match the energy range of our detectors.

There are two processes by which phonons are emitted by excited quasiparticles, relaxation and recombination. The quasiparticles are generated above the energy gap by applying a voltage pulse ($V > 2\Delta/e$). The energies (E) of these quasiparticles are in the range $\Delta \leq E \leq eV-\Delta$ (see figure 2.8). Relaxation from a state with energy E_1 to a state of energy E_2 takes place with the emission of a phonon of energy E_1-E_2. Quasiparticles from higher energy states mainly relax into states just above the energy gap. This is because of the large number of empty states at this energy, a consequence of the singularity in the density of states.

From Long and Adkins (1973) the relaxation transition rate is proportional to

$$E_2 \cdot \sqrt{(E_2^2-\Delta^2)^{-1}} \cdot (E_1-E_2)^2 \cdot (1-\Delta^2/E_1E_2) \qquad (2.8)$$

assuming the fermi function to be zero at the low temperature of our experiment.

A phonon of energy E_1+E_2 is emitted when a quasiparticle of energy E_1 recombines with a quasiparticle of energy E_2 to give a Cooper pair.The recombination rate goes as

$$(E_1+E_2)^2 \cdot (1+\Delta^2/E_1E_2) \qquad (2.9)$$

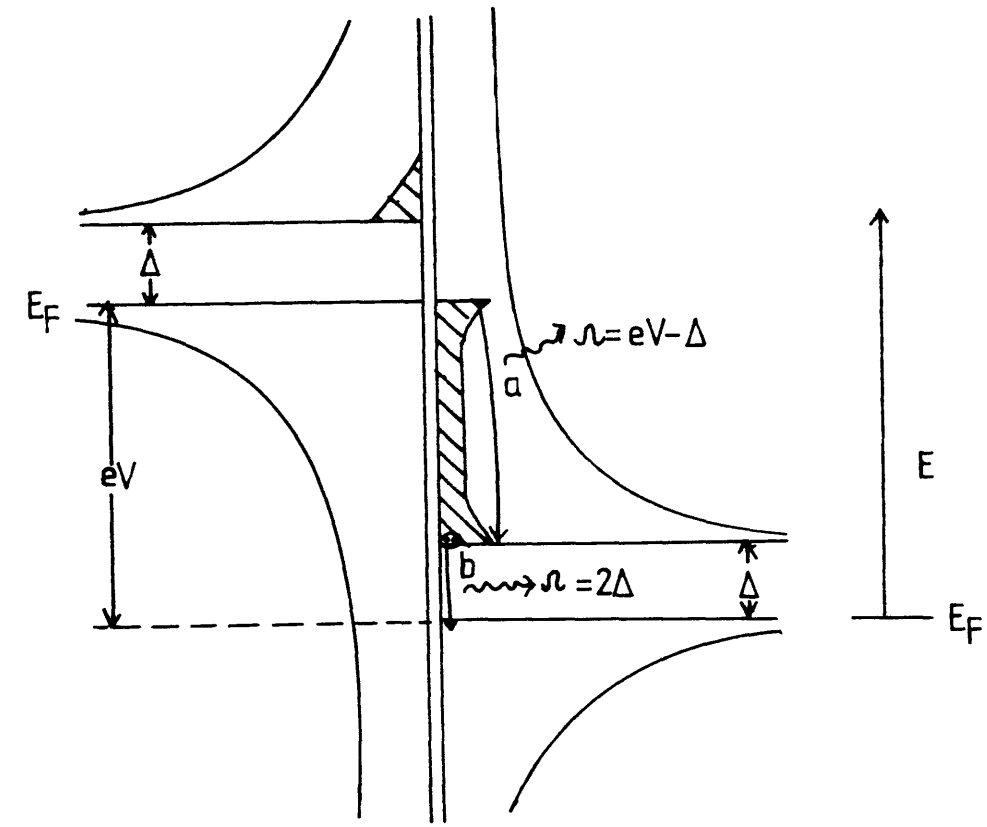

Figure 2.8 Quasiparticle population generated by a voltage pulse in a symmetric superconducting tunnel junction.

a - emission of a phonon by relaxation, b - emission of a phonon by recombination

The calculations of Long and Adkins (1973) show that for superconducting tin at a temperature of 1K the quasiparticles of energy less than 1.2Δ are more likely to recombine than relax.

Long (1973) calculated that a phonon of energy $\Omega > 2\Delta$ will be reabsorbed in tunnel junctions whose thickness is much greater than the phonon mean free path. The quasiparticles which these phonons excite will relax and recombine emitting on average more than one phonon. Therefore very few phonons of energy greater than 2Δ will be emitted due to this reabsororption.

Our experiments were performed at a temperature around 1K using junctions of total thickness 400nm (which is greater than the phonon mean free path (W. Eisenmenger (1976))). The processes which occur in these junctions produce a phonon spectrum which has a peak around 2Δ due to recombination and a continuous background of low energy "bremsstrahlung" phonons from the relaxation process. The 2Δ peak will be shifted slightly higher in energy due to recombination becoming dominant over relaxation at quasiparticle energies of about 1.2Δ. This is the type of spectrum measured by Berberich and Kinder (1981).

2.4 Aluminium - lead bismuth tunnel junctions as phonon detectors

A phonon, energy Ω, incident upon a superconductor can be absorbed in two ways. It can be absorbed by a quasiparticle which has been previously excited to an energy E above the gap. This is highly improbable since at the temperatures of our experiment the density of excited quasiparticles is very small compared with that of Cooper pairs. The alternative is for the phonon to break a Cooper pair into two quasiparticles, one with energy E and one with energy Ω-E. So phonons with energy Ω incident upon a superconductor will produce a distribution of quasiparticles between Δ and Ω-Δ. This distribution can be deduced as follows.

Bobetic (1964) calculated the energy dependence of the pair breaking phonon mean free path. His result for the ratio of the pair breaking absorption coefficient in the

superconducting state to the absorption coefficient in the normal state at low temperatures is

$$\alpha_s/\alpha_n = \Omega^{-1} \int_{\Delta}^{\Omega-\Delta} E.(\Omega-E).\sqrt{[(E^2-\Delta^2)((\Omega-E)^2-\Delta^2)]^{-1}} \times (1+\Delta^2/E(\Omega-E)) \, . \, dE \qquad (2.10)$$

Since α_n is proportional to Ω we can deduce the energy dependence of α_s. The phonon mean free path for pair breaking is inversely proportional to α_s. Also the transition rate for this process varies directly as the phonon speed and inversely as the phonon mean free path. So the transition rate is proportional to

$$\int_{\Delta}^{\Omega-\Delta} E.(\Omega-E).\sqrt{[(E^2-\Delta^2)((\Omega-E)^2-\Delta^2)]^{-1}} \times (1+\Delta^2/E(\Omega-E)) \, . \, dE \qquad (2.11)$$

This is the transition rate for pair breaking phonons of energy Ω producing quasiparticles anywhere between the energies Δ and $\Omega-\Delta$. Therefore the transition rate for a pair breaking phonon producing quasiparticles of energies E_1 and E_2 (= $\Omega-E_1$) is proportional to

$$(E_1+E_2).(E_1/\sqrt{(E_1^2-\Delta^2)}).(E_2/\sqrt{(E_2^2-\Delta^2)}).(1+\Delta^2/E_1E_2) \qquad (2.12)$$

This energy dependent transition rate determines the energy distribution of the quasiparticles. From it we can deduce an occupation probability distribution, $h(\Omega,E)$, which gives the probability that a phonon of energy Ω will produce a quasiparticle of energy E. We obtain

$$h(\Omega,E) = A(\Omega) \, . \, E.(\Omega-E).\sqrt{[(E^2-\Delta^2)((\Omega-E)^2-\Delta^2)]^{-1}} \times (1+\Delta^2/E(\Omega-E)) \qquad (2.13)$$

where $A(\Omega)$ is a normalisation factor and is given by

$$\int_{\Delta}^{\Omega-\Delta} h(\Omega,E) \, . \, dE = 2 \qquad (2.14)$$

since each phonon produces two quasiparticles.

By rearranging equation (2.13) we obtain

$$h(\Omega,E) = A(\Omega) \, . \, (E.(\Omega-E)+\Delta^2) \quad x \quad \sqrt{[(E^2-\Delta^2)((\Omega-E)^2-\Delta^2)]^{-1}} \qquad (2.15)$$

Hence

$$A(\Omega) = 1/2 \, . \int_{\Delta}^{\Omega-\Delta} (E.(\Omega-E)+\Delta^2) \quad x \quad \sqrt{[(E^2-\Delta^2)((\Omega-E)^2-\Delta^2)]^{-1}} \qquad (2.16)$$

This integral has been calculated by Bobetic (1964) and takes the form

$$A(\Omega) = \Omega \; E \sqrt{(1-(2\Delta/\Omega)^2)} \qquad (2.17)$$

where E is the elliptic integral of the second kind.

Assuming that the phonon energy is less than $2\Delta_1$, Δ_1 being the energy gap in the lead bismuth, then the only significant absorption of phonons will occur in the aluminium since the aluminium energy gap, Δ_2, is much smaller than Δ_1 (Δ_1=1.56meV and Δ_2=0.18meV, typically). The density of occupied quasiparicle states produced by this process is shown in figure 2.9. These quasiparicles will produce an extra non-thermal tunnelling current from the aluminium to the lead bismuth. If the junction is biased at a voltage V then only quasiparticles of energy greater than or equal to the threshold energy Ω_0 ($=\Delta_1$-eV) will contribute to this non-thermal tunnelling current. This region is crosshatched in figure 2.9. We assume that the phonons which generate a quasiparticle in this region also generates a quasiparticle at the singularity above the aluminium gap. Therefore, the energy of the absorbed phonon is the sum of the energies of the two quasiparticles,

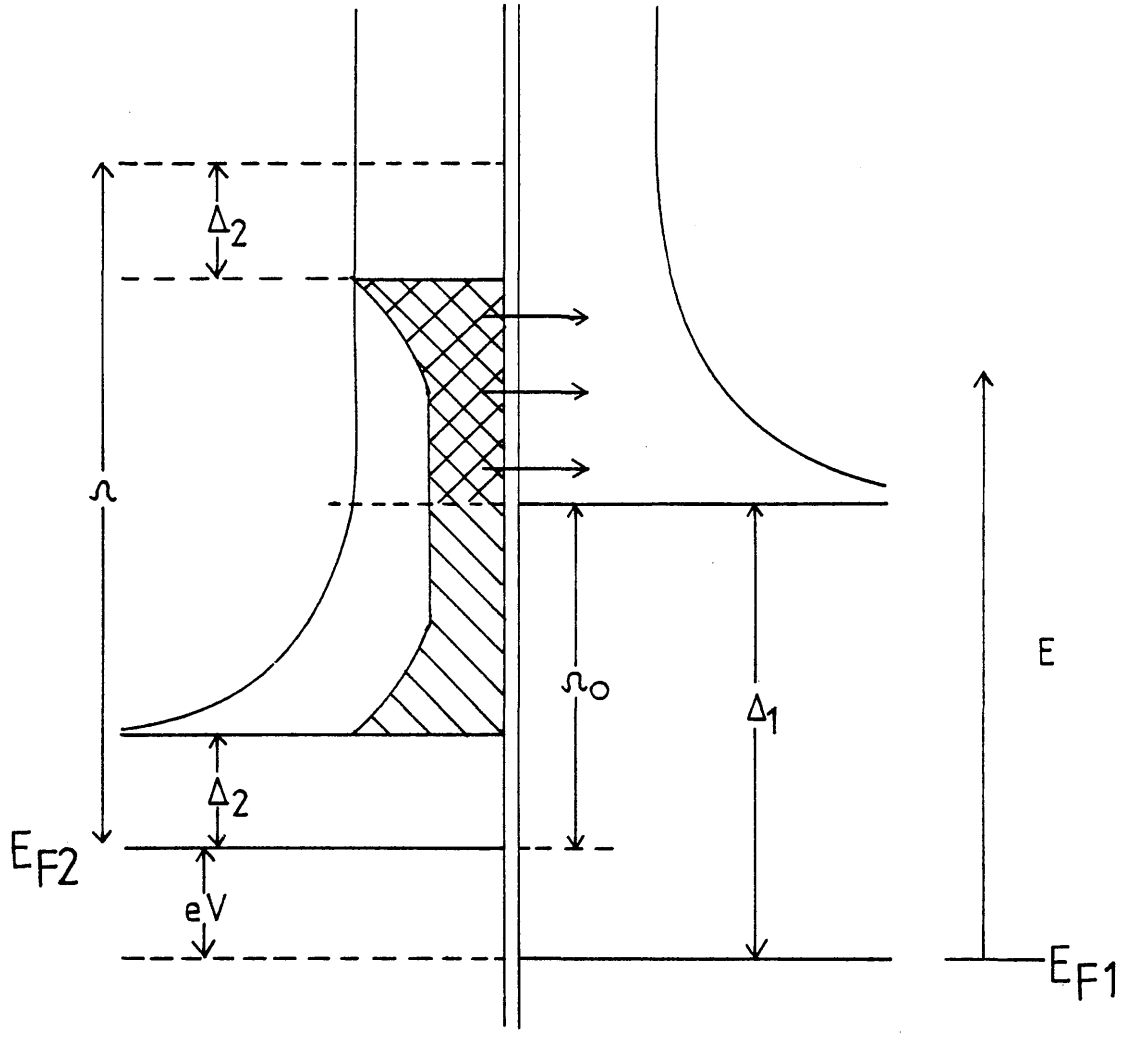

Figure 2.9 Quasiparticle population generated by an absorbed phonon flux of energy Ω.

$\Delta_2+(\geq\Delta_1-eV)$. The number of quasiparticles contributing to the enhanced current is equal to the number of phonons with energy greater than or equal to the thershold energy of $\Delta_1+\Delta_2-eV$ absorbed by the detector. We have limited ourselves to the bias range $0 \leq eV \leq \Delta_1-\Delta_2$ so we can vary the measurement of the phonon enhanced current through the phonon threshold energy range $2\Delta_2$ to $\Delta_1+\Delta_2$.

2.5 Analysis of the phonon induced tunnelling current

We need to calculate the effect that this phonon induced quasiparticle distribution, $h(\Omega,E)$, has upon the tunnelling current, $I(\Omega_o)$, in order to be able to calculate the energy distribution of the absorbed phonon flux from a series of tunnelling current readings at a range of bias values.In order to achieve this a matrix analysis technique was developed (Cattell et al. (1983)).

Assuming that all the states above the energy gap in the lead bismuth are empty we can write the tunnelling current as

$$I(\Omega_o) = K[vol]/e \cdot \int_{\Omega_o}^{\infty} n(E).N_1(E+eV).dE \qquad (2.18)$$

where [vol] is the volume of the junction and n(E) is the number of quasiparticles excited at energy E in the aluminium per unit volume. We need to know how the quasiparticle population responds to a phonon input. If we consider a single phonon input energy, Ω, we can write a differential equation to describe the time-dependent behaviour of the quasiparticle population:

$$dn(E)/dt = G_{th}(E) + I_p(\Omega).h(\Omega,E)/[vol] - n(E)/\tau_{rl}(E) \qquad (2.19)$$

where $G_{th}(E)$ is the rate of thermal excitation of quasiparticles from the gap region per unit time, $I_p(\Omega)$ is the absorbed phonon flux at energy Ω and $\tau_{rl}(E)$ is the thermal relaxation time. This equation neglects recombination and relaxation of

quasiparticles to energy E from higher energies. The calculations of Long and Adkins (1973) show that for aluminium at a temperature of 0.83K, a typical temperature for our experiments, the relaxation process dominates for $E>2.3\Delta_2$. Since we are considering energies above this value then recombination is unlikely to have an important effect. The relaxation process will be considered later.

We assume that the phonon flux is constant or varies very slowly compared to $\tau_{rl}(E)$. For thermal equilibrium we can write $G_{th}(E) = n_o(E) /\tau_{rl}(E)$. Substituting this into equation (2.19) we obtain

$$n(E) = n_o(E) + [I_p(\Omega).h(\Omega,E) .\tau_{rl}(E)]/[vol] \qquad (2.20)$$

Using this n(E) the tunnelling current, $I(\Omega_o)$, can be calculated from equation (2.18).The absolute value of $\tau_{rl}(E)$ is poorly known but its energy dependence is well understood (Tewordt (1962)). It varies assymptotically as E^{-3} so the tunnelling current due to the absorbed phonons at a cut off Ω_o is dominated by quasiparticles of energy $E \approx \Omega_o$. The incident phonon beam contains a distribution of energies so that the resultant quasiparticle distributions overlap. Hence the tunnelling current is determined by all phonons of energy $\Omega \geq \Omega_o+\Delta_2$. By combining equations (2.18) and (2.20) and dropping the thermal background current we obtain

$$\Delta I(\Omega_o) = 2K/e \int_{\Omega_o}^{\infty} \left(\int_{\Omega-\Delta_2}^{\infty} I_p(\Omega).h(\Omega,E).d\Omega\right) x \; \tau_{rl}(E).N_1(E+eV).dE \qquad (2.21)$$

So far we have ignored the relaxation of quasiparticles into our detection range. As a first order correction to the quasiparticle distribution at energy E due to phonons of energy Ω the contribution from the first decay of quasiparticles from energy E' to energy E is added to $h(\Omega,E)$. Therefore we replace $h(\Omega,E)$ by a modified

distribution, $h'(\Omega,E)$, given by

$$h'(\Omega,E) = h(\Omega,E) + \int_{E}^{\Omega-\Delta_1} h(\Omega,E').p(E,E').dE \qquad (2.22)$$

where $p(E,E')$ is the normalised probability of decay from energy E' to energy E, calculated by Tewordt (1962). This correction is for a constant input of phonons of energy Ω but is a good approximation if the phonon input current varies slowly over a time scale $\tau_{rl}(E)$.

In our experiment the data are collected at discrete bias intervals, V_j, which are separated by a constant interval ε/e. Each detector voltage corresponds to a different cut off energy $\Omega_{oj} = \Delta_1 - eV_j$. The energy resolution is limited so we consider phonons in the energy band $\Omega_{oj}+\Delta_2$ to $\Omega_{oj}+\Delta_2+\varepsilon$ together and assign them an average energy $\bar{\Omega}_j = \Omega_{oj}+\Delta_2+\varepsilon/2$. The distribution functions in this scheme have average values given by

$$H(\bar{\Omega}_j,E) = 1/\varepsilon \int_{\bar{\Omega}_j-\varepsilon/2}^{\bar{\Omega}_j+\varepsilon/2} h(\Omega,E).d\Omega \qquad (2.23)$$

and

$$H'(\bar{\Omega}_j,E) = H(\bar{\Omega}_j,E) + \int_{E}^{\bar{\Omega}_j-\Delta_2+\varepsilon/2} H(\bar{\Omega}_j,E').p(E,E').dE' \qquad (2.24)$$

To complete this approximation we divide the phonon input current $I_p(\Omega)$ into discrete contributions I_{pj} at energies $\bar{\Omega}_j$. We also need to assume that no phonons that enter the junction have an energy greater than $\Omega_1 = \Delta_1+\Delta_2-eV+\varepsilon/2$. We can now rewrite equation (2.21) as

$$\Delta I(\Omega_{oi}) = \sum_{j=1}^{i} \Lambda_{ij} I_{pj} \qquad (2.25)$$

where the elements Λ_{ij} of the transfer matrix take the form

$$\Lambda_{ij} = 2K/e \cdot \int_{\Omega_{oi}}^{\bar{\Omega}_j - \Delta_2 + \varepsilon/2} H'(\bar{\Omega}_j, E).\tau_{rl}.N_1(E-eV).dE \qquad (2.26)$$

Apart from the constant factor of the junction conductance K the elements of Λ involve known functions and can be calculated.

In order to keep the analysis tractable we have neglected the reabsorption of phonons which have been produced by recombination and relaxation of quasiparticles in the detector. If such a phonon were reabsorbed it would produce quasiparticles at an average energy of half the phonon energy. The energy of a relaxation phonon would be Ω-$2\Delta_2$ and that of a recombination phonon would be less $\leq 4.6\Delta_2$. Half of either of these energies is likely to be less than the threshold energy of our measurements. This assumption is certainly true for high biases but may breakdown at low biases.

We have assumed that no phonons of energy greater than $\Delta_1+\Delta_2$-eV+ε/2 enter the junction. If this is not the case then we overestimate the phonon current above $\Delta_1+\Delta_2$-eV+ε/2 and this leads to a large negative contribution to the lower energy phonon currents calculated. Also, we have ignored the recombination processes, this will lead to errors in the calculation of phonon currents at lower energies. These two effects will be discussed in more detail in section 4.3.

2.6 The effect of a parallel S-N junction

A parallel S-N short affects the detected signal markedly. The tunnelling current is derived from all the excited quasiparticles in the junction therefore it responds to all the phonons absorbed by the detector. If the S-N shorting resistance is large compared to the differential resistance of the S_1-S_2 junction then the total signal derived from the combined junction is insensitive to changes in the S-N current and therefore to changes in the total number of quasiparticles. At high biases the differential resistances of the S_1-S_2 junction are very small so this condition is

easy to fulfill. However, at low biases, 0.3mV say, the signal from the S_1-S_2 junction due to high energy phonons is weak because of the short quasiparticle relaxation lifetime. The signal from the two sources becomes comparable in magnitude at these biases and the phonon spectrum derived from the tunnelling current can be significantly distorted in the high energy range.

To quantify the effect of the S-N short we need to estimate the change in the total quasiparticle number caused by the arrival of the phonon pulse. We assume that the quasiparticle population remains thermal and that the change in the total number of quasiparticles is characterised by a change in the temperature. We estimate the change in temperature from the change in the aluminium gap which is measured at the current onset at $\Delta_1+\Delta_2$. $d\Delta/dT$ is calculated from the Muhschlegel tabulation (1959) of Δ/Δ_o and T/T_c according to BCS theory. Using the tables of G.B. Donaldson (private communication) we can calculate the current change expected at a fixed bias for the observed temperature change. Donaldson's tables give the relative current, I, as a function of Δ/kT (=A) and eV/Δ (=B). The S-N short current, I_{SN}, is given by

$$I_{SN} = K.\Delta.I(A,B) \qquad (2.27)$$

where K is the conductance of the S-N junction. So the variation of I_{SN} with temperature can be written as

$$K^{-1}.dI_{SN}/dT = d\Delta/dT \; . \; [I + A(\partial I/\partial A)_B - B(\partial I/\partial B)_A] - A.\Delta/T \; . \; (\partial I/\partial A)_B \qquad (2.28)$$

The expected voltage signal from the S-N short, V_{SN}, for a measured gap change δ is given by

$$V_{SN} = K[K^{-1} \; . \; dI_{SN}/dT] \; . \; [d\Delta/dT]^{-1} \; . \; \delta \; . R_{eff} \qquad (2.29)$$

where R_{eff} is the effective resistance of the detection system which is discussed in section 3.5. From a knowledge of δ the S-N signal, V_{SN} can be estimated in a given experimental situation, using equation (2.29), and in principle subtracted from the detected voltage signal.

This calculation is subject to error resulting from the assumptions made in performing it. Particularly susceptible to error is the assumption that the quasiparticle distribution remains thermal when the phonon pulse arrives and, hence, that a temperature change can be calculated from the gap variation. So analysing the high energy phonon signal may be subject to large errors when there is a low resistance parallel S-N junction.

2.7 Constantan thin films as wideband phonon sources

For metallic thin films using the acoustic mismatch theory of Little (1959) we can write

$$W/A = \pi^2 k^4/120\hbar^3 \cdot [e_\ell/c_\ell^2 + 2e_t/c_t^2] \cdot (T^{*4} - T_o^4) \quad (2.30)$$

where W is the power dissapated in the heater, A is the area of contact between the heater and the substrate (5×10^{-7} in our experiments), T^* is the equivalent heater temperature and T_o the base temperature. e_ℓ and e_t are phonon emission coefficients to the substrate and c_ℓ and c_t are the phonon phase velocities. The subscripts ℓ and t refer to the longitudinal and transverse modes respectively. The following values were obtained by Herth and Weis (1970) for transmission from constantan to sapphire:-

$$e_\ell = 0.216, \quad e_t = 0.176, \quad c_\ell = 5.24 \text{kms}^{-1}, \text{ and } c_t = 2.64 \text{kms}^{-1}$$

Substituting these values into equation (2.30) we obtain

$$W = 7.52 \times 10^{-5} \cdot (T^{*4} - T_o^4) \quad (2.31)$$

We are able to measure W and T_o and hence calculate T^*.

It is well known that the number distribution of phonons emitted by such a heater, N(E), can then be calculated from

$$N(E) \alpha E^2 . (\exp(E/kT^*) -1)^{-1} \qquad (2.32)$$

The form of this distribution over the energy range of our detectors is shown in figure 2.10. This is the output expected from the acoustic mismatch model. Since we are dealing with phonon numbers the occupation number distribution is the correct function to use.

Frick et al. (1975) developed a model specifically for constantan heaters which are thin films. In this model the heater was assumed to be weakly coupled to the sapphire substrate. They derived the phonon output to be

$$n_\sigma(E) = \pi A e_\sigma E/(2c_\sigma dh) \quad x$$
$$\text{entier}(2Ed/c_\sigma h) .[f(E,T^*) - f(E,T^o)] \qquad (2.33)$$

where σ is the polarisation of the phonon, and d is the heater thickness and entier(x) is the largest whole number not exceeding x. The form of this function is shown in figure 2.11. Their experimental results support this theory.

In section 4.4 the measured phonon spectra are discussed and compared to these models.

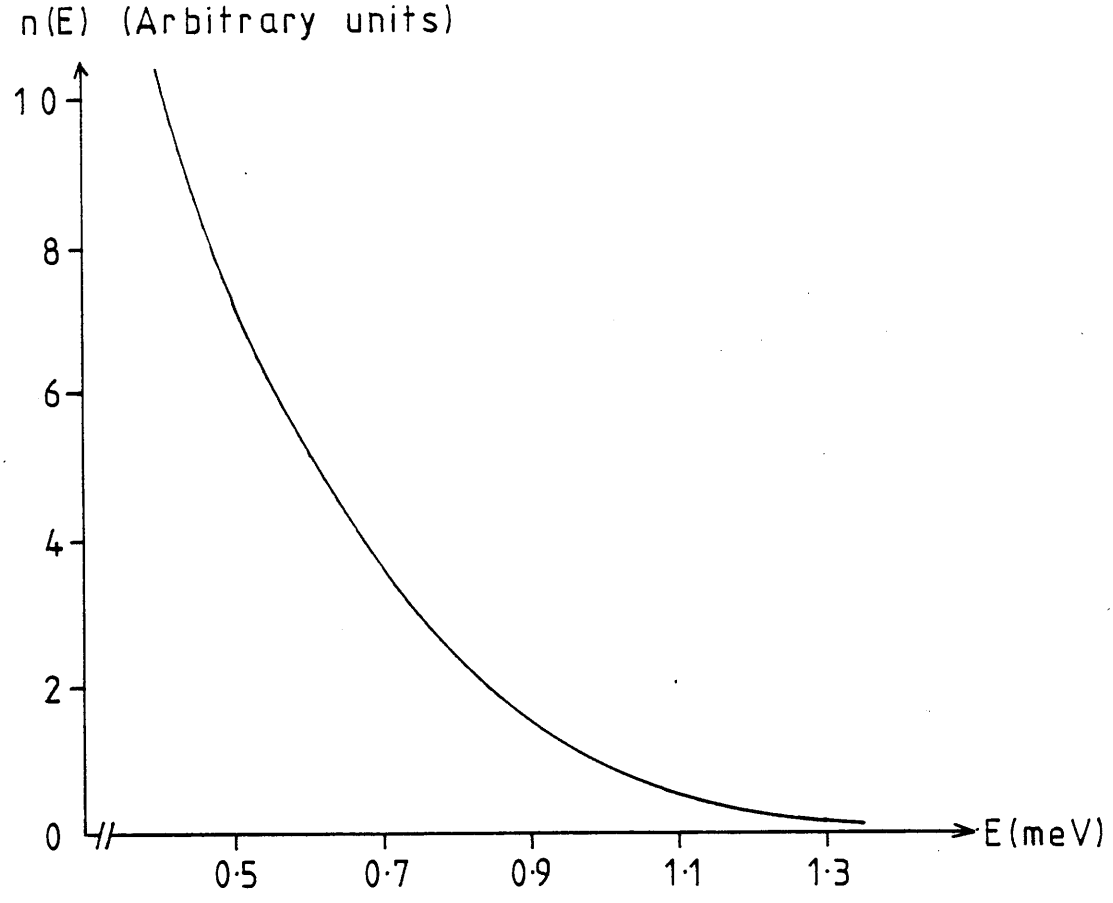

Figure 2.10 The output of a thin film constantan heater over the energy range of our detectors according to the acoustic mismatch theory.
T_o=0.90K, T*=1.65K.

3.1 Introduction

The thin film samples were prepared by thermal evaporation and by radio frequency sputtering. They were then mounted onto an insert and put into a cryostat. This system was then cooled to liquid nitrogen temperature. The samples were stored at this temperature between experiments. When measurements were to be made the system was cooled to less than 1K using liquid helium. For the collection of the data a digital signal averaging technique was used.

In the next section of this chapter the thin film preparation will be described. The third section will discuss the cryostat and the cooling techniques. Finally the data acquisition system will be described.

3.2 Thin Film Preparation and Geometry

The heaters and the tunnelling junctions were prepared by thermal evaporation. The silicon monoxide films were prepared by thermal evaporation. The silicon dioxide films and the arsenic trisulphide films were deposited using r.f. sputtering.

The evaporator used for thermal evaporation is shown in figure 3.1. It had a stainless steel base with ports through which all the necessary electrical and water feedthroughs passed using ultra high vacuum techniques. The ports were sealed with copper gaskets to reduce outgasing which arises from conventioanl O-rings. On top was placed a glass cylinder. The top was a stainless steel plate. The seals between the glass and the stainless steel was made using viton gaskets with an "L" shaped cross section. The system was pumped by a diffusion pump with a water cooled baffle. This was backed by a two stage rotary pump. When samples were being prepared a liquid nitrogen cooled Meissner trap was used to reduce the pressure further. This condensed out reactive gases such as oxygen and water vapour. The Meissner trap was a coil of copper tubing which was supported from the top plate. The base pressure in the system was usually about 10^{-8} torr for the evaporation of the thin films.

The evaporator had been designed so that films of different materials can be deposited on different areas of the substrate without the need to open the evaporator

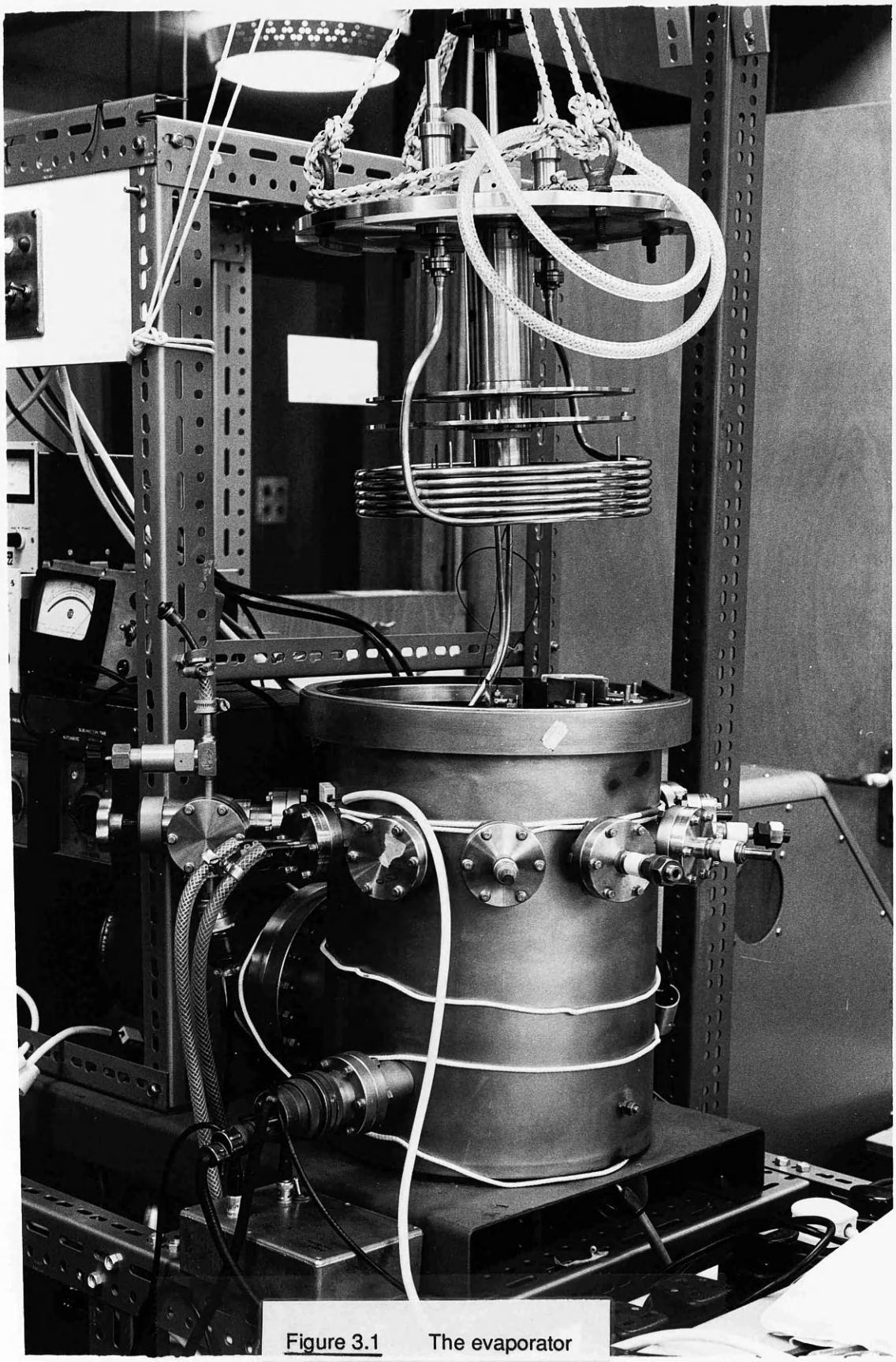

Figure 3.1 The evaporator

to air. The mask changing mechanism was based on a shaft seal supporting rotary and linear motion fixed to the top plate (see figure 3.2). Parallel to the top plate were three stainless steel plates. The top stainless steel plate had six rectangular holes cut in it any one of which could hold the substrate and its holder. The middle stainless steel plate had six smaller holes in which could be placed the copper masks in their holders. There was a single hole on the bottom stainless steel plate . This single aperture was lined up beneath the desired mask by rotating the bottom plate. The plate was then raised until the main locating pin passed through the corresponding hole in the middle plate. Both plates could then be rotated until the mask was lined up with the substrate. At this stage the plates were raised so that the locating pins were all in place and the mask was in contact with the substrate. The contact masking system was used in order to eliminate "shadowing" around the edges of the films.

There were five resistance heated boats arranged on an arc. The centres of the boats were the same distance from the central axis of the system as the apertures on the plates so the substrate and mask could be aligned directly above the boat which contained the material to be evaporated.

A water cooled quartz crystal which was used to monitor the thickness of the material deposited. When a mass, dm, is deposited on a quartz crystal undergoing sheer bulk oscillations the rate of change of the resonant frequency is given by

$$df/dm = -f^2/ah \qquad (3.1)$$

where a is the area of the crystal exposed to the evaporating beam and h is a constant dependent on the type of crystal. Therefore from the change in the reso nant frequency of the crystal the amount of mass deposited on it could be calculated. The crystal was at the same height as the substrate on the central axis of the system so that the geometrical factor was the same no matter which source boat was used. It was initially calibrated by evaporating aluminium onto a substrate and comparing the thickness of the film with the change in the crystal's frequency of vibration. A constant check on the calibration was made by measuring the thicknesses of the thin films after the samples had been used. The thickness measurements were performed using an Angstromscope Multiple Beam Interferometer. The basic principle of the Angstromscope is that the film with its layer of aluminium , which is used as a

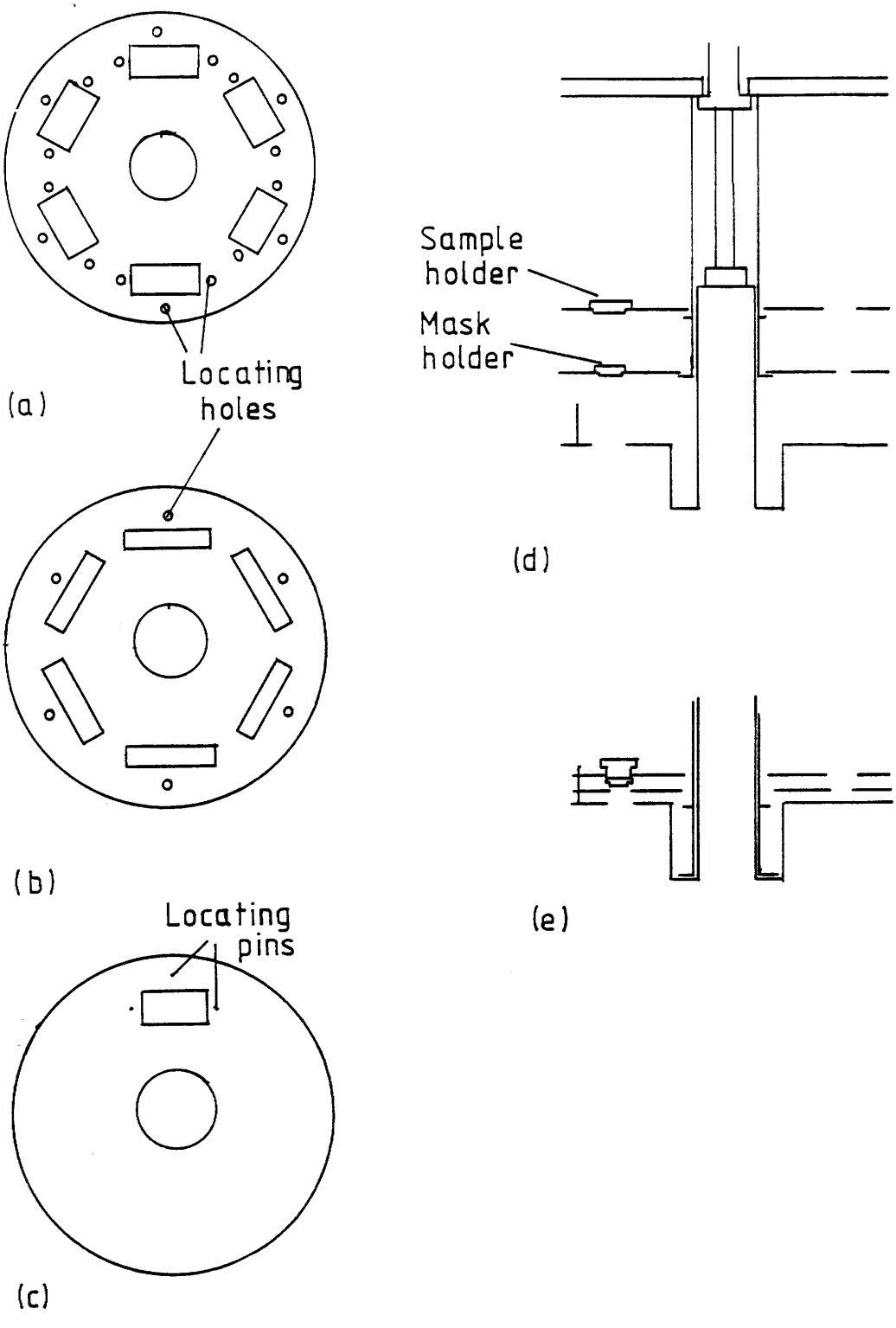

Figure 3.2 The substrate and mask handling system in the evaporator.
(a)top plate, (b) middle plate, (c) bottom plate,
(d) position of plates for selscting mask,
(e) mask in contact with sample

highly reflecting film, is placed into a wedge of glass (see figure 3.3a) and illuminated with monochromatic light. An interference pattern is formed (figure 3.3b) due to the different path lengths of the light reflected from the aluminium and from the glass above. The spacing between the fringes is $\lambda/2$, where λ is the wavelength of the illuminating light. At the step between the substrate and the sample the fringes are offset. The thickness of the sample, d, is given by

$$d = (\text{offset/spacing}) \times (\lambda/2) \qquad (3.2)$$

An accuracy of ±3nm is obtainable with the Angstromscope but the accuracy of the thickness was limited by variations across the samples.

The substrates used were sapphire single crystals in the shape of a cuboid 7mm x 10mm x 10mm. The samples were deposited on the square faces with the heaters directly opposite the detectors. The square faces were cut perpendicular to the c-axis. The phonon signal was thus transmitted from the heater to the detector down the c-axis.

The order of deposition varied depending on whether the glassy film was to be under the heater or the detector. In the former case the glass was deposited first, in the later the heaters were first. The heaters were produced by evaporating constantan wire to produce a 15nm film of constantan on the substrate. Lead bismuth contacts (thickness 200nm) were then evaporated on top, the geometry being shown in figure 3.4. The lead bismuth was superconducting at the temperatures the measurements were made so the resistive heating was restricted to a well defined area. After this had been completed the evaporator was opened up to air. The substrate was either mounted in the sputterer for the deposition of the glass or simply turned over in the evaporator to allow the detectors to be prepared.

The glass was deposited onto half the substrate face so that it was either under a heater or a detector (see figure 3.4). The silicon monoxide was prepared simply by evaporating powdered polycrystalline silicon monoxide in the evaporator. The arsenic trisulphide was sputtered onto the substrate using argon gas. For the sputtered silicon dioxide a mixture of 10:1 argon : oxygen mixture was used. This ratio was measured by the partial pressure of the gases which were mixed and

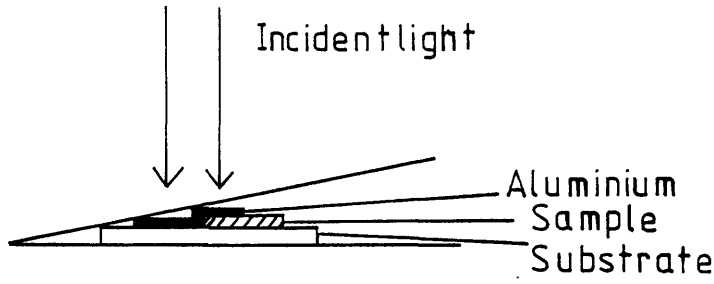

(a)

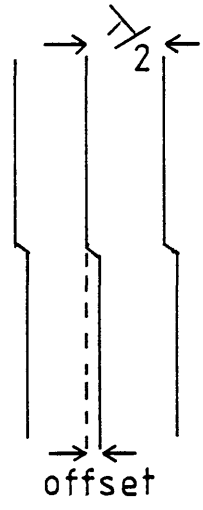

(b)

Figure 3.3 (a) Basic arrangement for measuring the thickness of the samples, (b) The interference fringes observed.

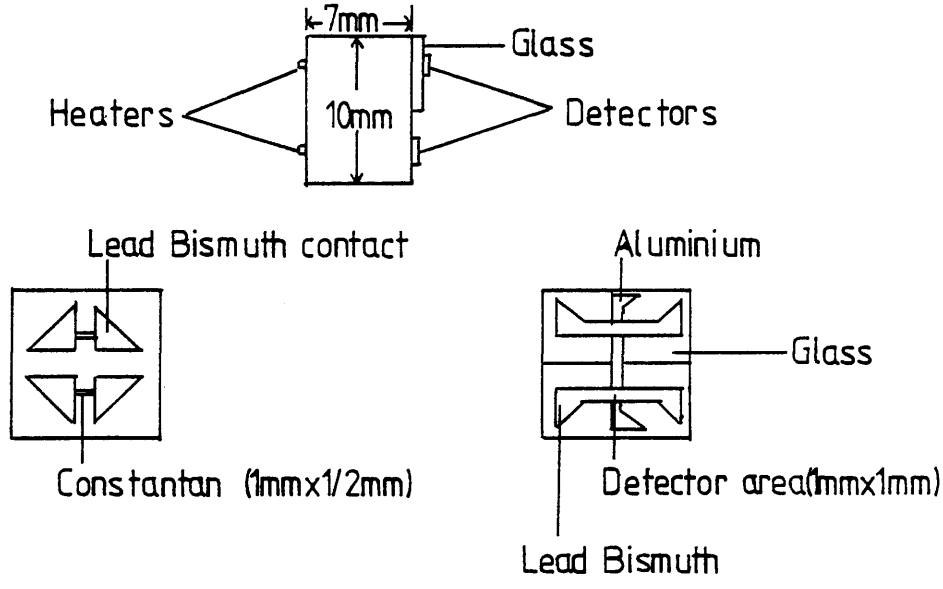

Figure 3.4 The geometry of the thin films.

stored in a reservoir. The atmosphere in the sputterer was sampled before and after sputtering using a V.G. Q4 mass spectrometer to check for possible contaminant gasses. The thicknesses of these samples were measured directly using the Angstromscope.

The detectors were always prepared last in order that they could be cooled as soon as possible to prevent "aging". If the sample was on the heater side of the substrate the sapphire surface was cleaned by oxygen ion bombardment. A layer of aluminium 100nm thick was evaporated first. The mask was then changed to the one needed for the lead bismuth layer before oxidation. This was done to decrease the possibility of damaging the oxide layer between the two metals. The oxidation of the aluminium was achieved by exposing the surface to 10^{-1} torr of oxygen which had been dried by passing it through silica gel. After ten minutes the oxygen was pumped out. When the system had returned to its base pressure the lead bismuth layer of 200nm thickness was deposited (for the geometry see figure 3.4). An alloy of 85% lead and 15% bismuth was used in preference to lead. The scattering in the alloy reduces the anisotropy of the energy gap making it sharper than in pure lead. Therefore the phonon energy values are better defined in the alloy than in lead.

Once this final evaporation was completed the sample was removed from the evaporator and mounted in the insert. To do this first the sapphire substrate was bolted into its copper holder with a solution of bostik glue in acetone. This thin layer of glue improved the thermal contact between the sample holder and the substrate. The electrical connections to the heaters and the detectors were made with pressed indium contacts. Small dots of indium were pressed onto the contact areas of the thin films. This ruptured the oxide layers on the aluminium, tin and lead bismuth. Tinned copper wires were then pressed into the indium. Finally indium was pressed on top. This provided a superconducting contact between the wires and the thin films. The sample and holder were then bolted onto a copper block on the insert, again with a layer of glue. Again the function of the glue was to improve the thermal contact between the sample holder and the insert. The other ends of the wires were soldered onto contact pins on the insert. A can was bolted onto the insert to cover the sample. The seal between the can and the insert was made with indium and had to be leak tight to superfluid helium. The insert was then placed in the cryostat and cooled.

The superconducting phonon generators were also prepared in the evaporator. The first stage was to evaporate on a 200nm layer of tin. It was found that simply exposing the surface of the tin to oxygen did not produce a complete oxide barrier. A good barrier was formed when a discharge current was passed through the oxygen so that the tin surface was bombarded with oxygen ions . The thickness of the barrier depended upon the pressure of the oxygen. The oxidation was monitored by the quartz crystal. After a time the frequency remained steady indicating that the oxidation process had stopped. It was found that a pressure of 0.3 torr and a discharge time of 20 minutes produced a satisfactory oxide layer. The evaporator was again evacuated and a second layer of tin (thickness 200nm) was evaporated across the first in the same configuration as the detectors. As before the detectors were prepared last since the Sn-SnO-Sn junctions appeared to take longer to "age" than the Al-AlO-PbBi detectors.

3.3 The Cryogenic System

In this experiment the scattering of phonons of energy between 0.34 meV and 1.74 meV was being investigated. It was therefore necessary to reduce the number of thermal phonons of this energy present in the sample. This was achieved by reducing the temperature of the samples to below 1K. There were two cryostat systems used. They were basically of the same design. The first was a helium 4 cryostat which had been used by Cattell (1980). This was used for two of the samples discussed in this thesis, samples C9 and C10. A helium 3 cryostat was used for the rest of the experiments. This system was capable of achieving lower temperatures and had better thermal stability. The insert for holding the samples was the same in both cases.

The cryostats had two dewars, a stainless steel one inside which was suspended a glass one. The stainless steel dewar was filled with liquid nitrogen to provide the initial stage of cooling. While there was a sample in the cryostat it was not allowed to empty, this prevented the sample from "aging". The liquid helium and the insert were put into the glass dewar.

The insert was designed to hold the sample so that the heaters and the detectors were exposed to a vacuum and to earth thermally the substrate so that the heat deposited

in the substrate during the measurements was removed (figure 3.5). This was preferred to putting the samples into a bath of liquid helium which would have reduced the phonon signal due to significant phonon losses into the liquid helium at both the heaters and the detectors. The insert was placed in the cryostat and left to cool overnight. The can was pumped out during this time. It was also pumped out when it returned to liquid nitrogen temperature after each cooling to liquid helium temperatures. This was done to ensure that no gaseous helium which would conduct heat from the outer helium bath to the sample collected in the can. The can had three inlets for wires. One for the heaters, one for the detectors and one for the d.c. signals. The wires were guided to the inlets in separate copper nickel tubes to sheild them from one another. These tubes were open to allow the liquid helium to circulate freely around the wires and cool them.

A two stage cooling system was used. The dewar was filled so that the bottom of the insert was submerged in liquid helium. The system took about three hours to cool from liquid nitrogen to liquid helium temperature. A rotary pump was used to reduce the vapour pressure above the liquid helium. This reduced the temperature of the system to about 1.2K. In the middle of the insert was a space which was connected to a reservoir of helium gas. In the first cryostat this was helium 4, in the second the gas used was helium 3. As the insert cooled the helium gas was allowed to condense in this space. When the outer bath had been cooled to its minimum temperature the insert was then isolated from the reservoir. This space formed a smaller, inner helium bath which was thermally connected to the sample holder through a copper block. This bath was then pumped using a diffusion pump. This reduced the vapour pressure in the inner bath and therefore the temperature was also reduced. For helium 3 the vapour pressure is higher at a given temperature than for helium 4. Therefore the helium 3 cryostat could attain lower temperatures than the helium 4 cryostat when using diffusion pumps with similar pumping speeds. The helium 4 gas from this bath was exhausted to the atmosphere. However, due to consideration of cost, the helium 3 cryostat had a closed system for this bath and the exhaust gas from this was pumped back into the reservoir. A small heater was located at the top of the inner bath this was used to evaporate the superfluid helium 4 film which crept up the walls of the inner bath and into the pumping line. By evaporating this film the heat conduction into the bath was reduced. This heater was not used for the helium 3 cryostat since helium 3 does not become superfluid above 3mK. The inner bath was connected to the outer bath with a graphite link.

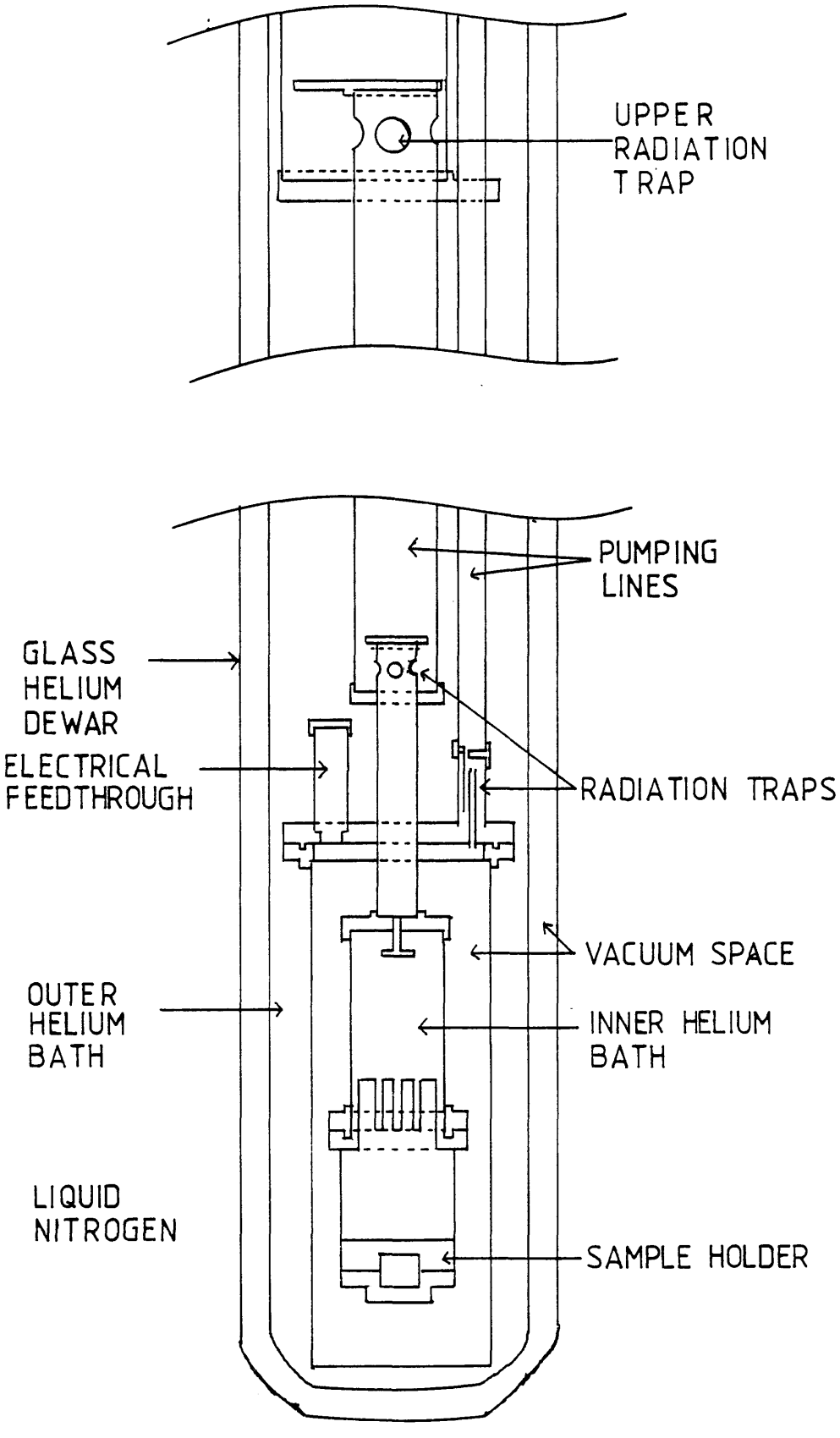

Figure 3.5 The cryostat and insert.

Graphite has a reasonable thermal conductivity at higher temperatures. This enabled the inner bath to cool faster from liquid nitrogen temperatures than it would by radiation alone. The thermal conductivity of graphite decreases with temperature. At the temperature of the experiment graphite is effectively an insulator.The helium 4 system could attain temperatures at the sample of between 0.9K and 1.0K. The helium 3 cryostat cooled the samples to around 0.8K. The temperature was measured in two ways. First there was a solid state germanium thermometer fixed to the copper block. A constant current was supplied to it and the voltage across it was measured. This thermometer had been calibrated by the manufacturers. The detectors themselves acted as thermometers which was in intimate thermal contact with the sample. In chapter 2 it was shown that their d.c. current voltage characteristics are dependent on their temperature. Both systems could maintain their base temperatures for about twelve hours before the level of the helium in the outer bath had dropped below the top of the vacuum space around the sample.

3.4 Generation of the Phonon Pulses

The phonon pulses were generated by passing a current pulse through the thin film metal heaters. To produce the current a Phillips PM5712 pulse generator was used. The pulse passed through a 50Ω attenuator so that the power being fed into the heaters could be varied. The attenuator could reduce the signal over the range 0dB to 100dB in steps of 1dB. The pulse was then changed from single ended to balanced by passing it through a pulse transformer the design for which came from Ruthroff (1959). The balanced signal minimised the capacitive pickup from the pulse on other parts of the system as the signal was transmitted to the heaters. The transmission lines were twisted pairs of 38 gauge copper wire. Despite this the electromagnetic pickup of the generating pulse on the detector transmission lines was about an order of magnitude larger than the detected signal. To reduce the size of this pickup the current in the heaters was driven in one direction for half the time then it was reversed. It was decided to do this by using two pieces of twin cable of equal length. One was connected in the usual manner the other had the connection to one set of pins reversed. This had the effect of changing the sign of the electromagnetic pickup and cancelling it out. The phonon signal had the same sign and therefore added up. This was used in preference to changing the polarity of the

signal emitted by the pulse generator. It had been observed that the positive and negative pulses emitted from the generator were not exactly symmetrical.

The pulse length used was between 100nS and 500nS at a repetition rate of around 30kHz. the rise and fall time of the pulse was 4nS. The pulse height was 1V and was attenuated by values between 0dB and 15dB.

3.5 The Detection System

A schematic diagram of the detection system is shown in figure 3.6. The detectors were biased using a constant current source. The voltage signal was then measured over 10μS around the initiating pulse at different values of the biasing voltage using a signal averaging technique.

The circuit that supplied the current to the detectors is shown in figure 3.7. It used two 9V batteries as its voltage supply in order to eliminate the possibility of mains pickup on the sample. The maximum current it could supply was 10mA at which the output impedance was 1kΩ.

The signals from the detector were around 1μV. This was fed differentially into the front end of a Tektronix 7623A oscilliscope. The oscilliscope was used with a 7A13 differential comparitor. The signal was differentially amplified by the oscilliscope and taken out via a single ended output at the back of the scope. The oscilliscope gave voltage amplification by a factor of 25. The next stage was to amplify the signal further using a Hewlett Packard 461A amplifier. This had a gain of 100. The bandwidth of the oscilliscope was 55 MHz and the input effective noise resistance was 20Ω. Therefore the Johnson noise was about 5μV. This was increased by amplifier noise and the signal was well buried in noise. In order to retrieve the signal it was necessary to do some signal averaging.

There are two ways of performing signal averaging. It can be done either by averaging the signal over some RC time constant or by digitising it and averaging numerically. In this experiment a combination of the two methods was used. A boxcar detector was used to slow the signal down to a frequency suitable for digitising using relatively cheap ADCs. The digital system was designed by Dr. A. M.

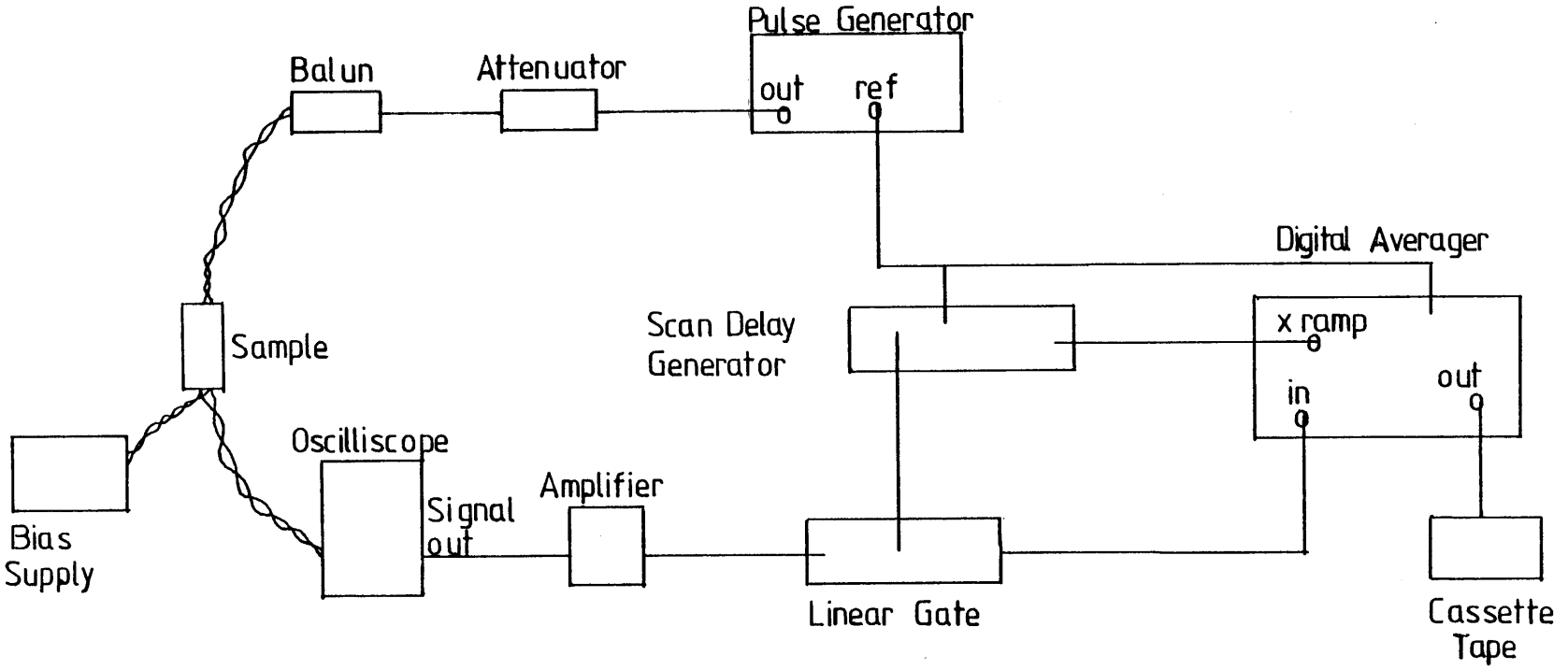

Figure 3.6 A schematic diagram of the electronics of the pulse generation and measurement system.

MacLeod and was built in the department under his supervision (MacLeod and Long 1982). The amplified signal was passed into a Brookdeal 9415 linear gate. This sampled the input for a time t at a time T_1 after a reference pulse supplied by the pulse generator. The reference pulse was emitted a fixed time before the pulse sent to the heaters. The value of t was controlled by a Brookdeal 9425 scan delay generator. It also controlled the range of possible T_1 values, 0 to 10μS. The value of T_1 within this range was set by the output of the xramp on the digital acquisition system. This system was designed to collect 1024 data points so it needs 1024 values of T_1. This produced a value of 10nS for t which provided the necessary resolution. At first T_1 was set to zero. For the next N pulses the signal was sampled at this time and the result was added to channel 1 in the digital acquisition system's memory. T_1 was then increased by 1/1024 of its maximum value (10/1024 μS). The next N pulses were then sampled at the new value of T_1 then digitised and added to channel 2 of the memory. This process was repeated until the maximum value of T_1 was reached. T_1 was reset to zero and the procedure was repeated M times. Both M and N were controlled by switches on the data acqusition system. The digitised signal was recorded on cassette tape to be transferred onto floppy disk for analysis using a Motorola Exorset microcomputer.

The detection system was designed to detect and amplify the voltage pulses from the junctions. The quantity of interest in this experiment is the phonon current and this is related to the change in the electron current through the junctions caused by the phonon pulse. Therefore the relationship between the current and voltage pulses needed to be known. Figure 3.7 shows the equivalent circuit of the amplifier input. R_o is the output of the bias supply, R_ℓ is the lead resistance and R_i is the input impedance of the amplifier. The d.c. current through , I, and the voltage across, V, the junction are related by:-

$$V_o = \{I + V/(R_i + 2R_\ell)\}(R_o + 2R_\ell) + V \qquad (3.3)$$

A similar equation can be written for the enhanced tunneling current, I', and the voltage, V', when a phonon pulse has been absorbed by the junction. By subtracting

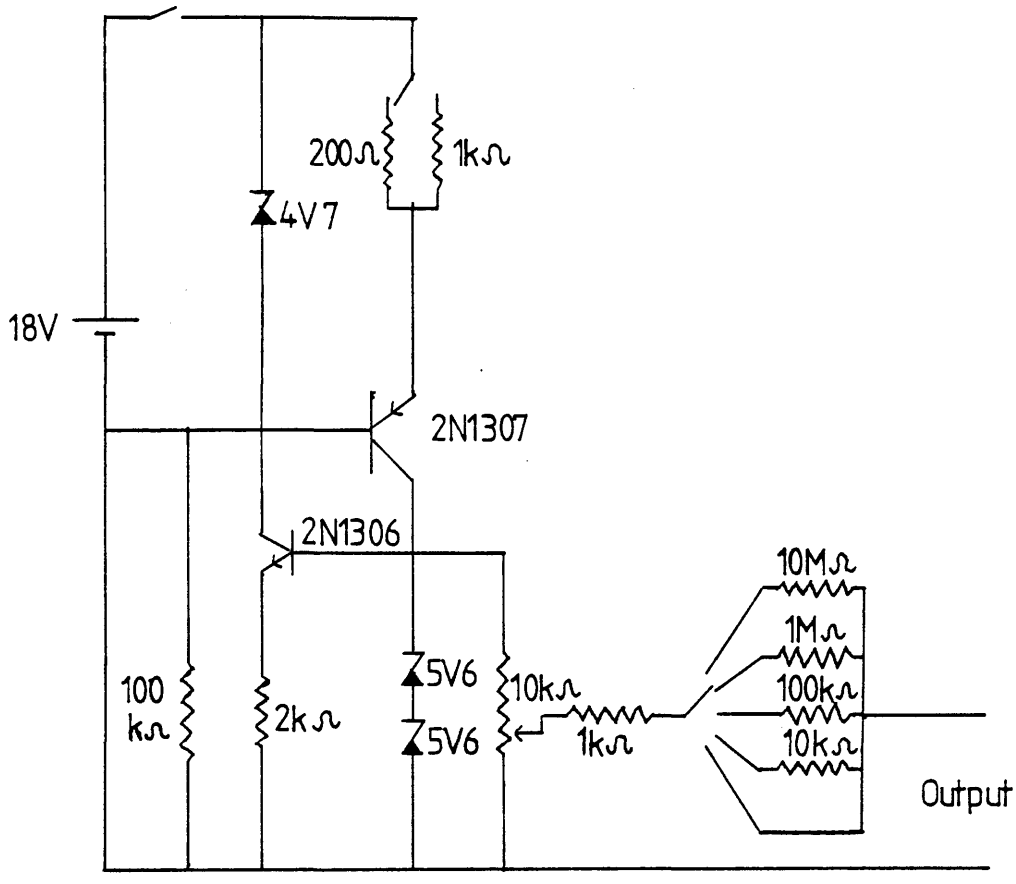

Figure 3.7 The detector biasing circuit.

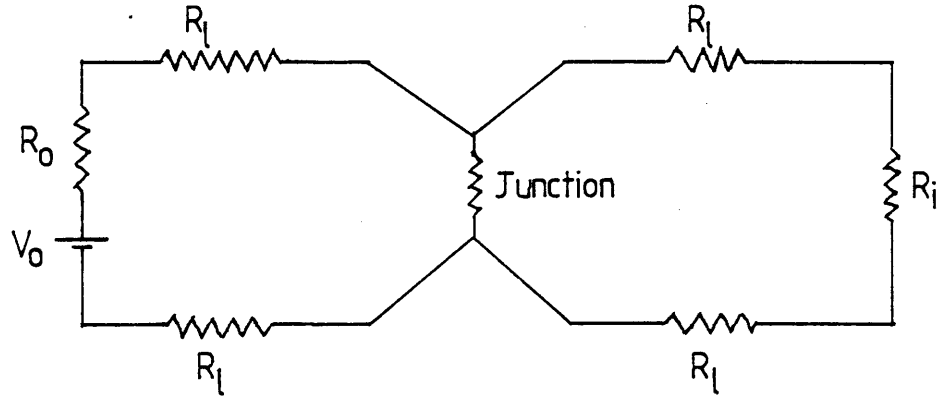

Figure 3.8 The equivalent detector circuit.

these two equations it is found that:-

$$\{\Delta I' + \Delta V'/(R_i + 2R_\ell)\}(R_o + 2R_\ell) + \Delta V' = 0 \qquad (3.4)$$

where $\Delta I' = I' - I$ and $\Delta V' = V' - V$.

Rearranging this equation gives:-

$$\Delta V'/\Delta I' = -R_{out} \qquad (3.5)$$

where

$$R_{out} = (R_i + 2R_\ell)^{-1} + (R_o + 2R_\ell)^{-1} \qquad (3.6)$$

This represents the load line applied to the junction externally. Figure 3.9 shows the I-V characteristics of the junction with and without the phonon pulse. It is assumed that the curves are parallel since the heat pulse induces a very small change in the temperature. The quantity of interest is ΔI, the measured quantity is $\Delta V'$. From figure 3.9 it can be seen that:-

$$\Delta I = \Delta I' - \Delta V'/\delta R \qquad (3.7)$$

where δR is the differential resistance of the junction at this voltage. Substituting for $\Delta I'$ using equation (3.5) gives :-

$$\Delta V' = -\Delta I\ (1/\delta R + 1/R_{out})^{-1} \qquad (3.8)$$

Therefore the voltage pulse across R_i, ΔV_i, is given by:-

$$\Delta V_i = -R_i \Delta I\ .\ (R_i + 2R_\ell)^{-1}.\ (1/\delta R + 1/R_{out})^{-1} \qquad (3.9)$$

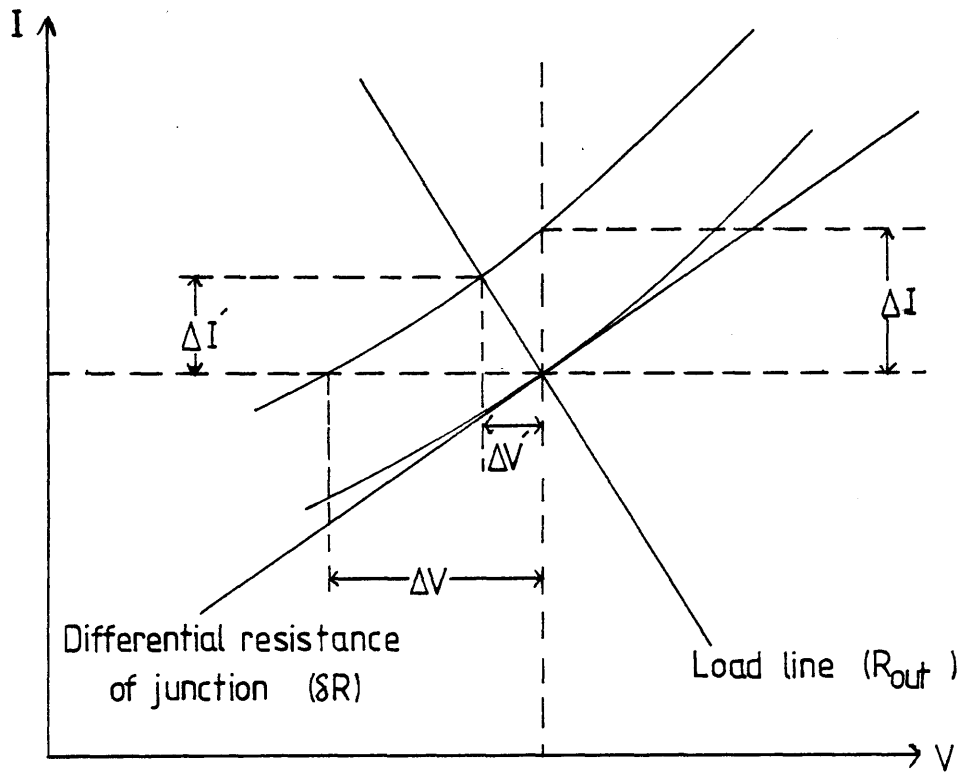

Figure 3.9 The junction characteristics with and without a phonon pulse.

This equation can be simplified by assuming that $R_\ell << R_i$, $R_\ell << R_o$ and $R_i << R_o$. This is reasonable since typical values of R_ℓ, R_i and R_o are 1Ω, 20Ω and 1kΩ respectively. Equation (3.9) can be rewritten:-

$$\Delta V_i = - \Delta I \, . \, (1/\delta R + 1/R_i) \qquad (3.10)$$

Therefore to obtain the excess tunnelling current the voltage pulse needs to be multiplied by $(1/\delta R + 1/R_i)$. This quantity was referred to as the effective resistance, R_{eff}. After this operation had been completed the matrix analysis described in section 2.5 was performed.

4.1 Introduction

In chapter 2 the theory of ideal tunnel junctions as wideband phonon detectors was discussed and a matrix analysis scheme based on this theory was outlined. Using these methods the phonon spectra from thin film constantan heaters are analysed here. At high energies these spectra are expected to have a thermal form (section 2.7) and, therefore, can be used to test the analysis scheme and study its limitations. The analysis scheme is also applied to the output phonon spectrum of tunnel junction generators. The theory of tunnel junctions as phonon generators was also discussed in chapter 2.

The data used here were measured without an amorphous film betweeen the phonon generators and detectors. Due to phonon focussing effects (Taylor et al. (1971)) the analysis is limited to phonons transmitted straight through the sapphire crystal along the c-axis. In an anisotropic material, such as a sapphire crystal, the probability of propagation depends on the direction of propagation and on the mode of the propagating wave. This effect is called phonon focussing. In this experiment symmetric focussing effects on two sets of waves travelling across the crystal from the generators to the detectors are desired. The reason for this is that the analysis technique involves comparing the phonon signals from the two detectors. Symmetric focussing effects are found for waves travelling along the c-axis of a sapphire crystal.

4.2 The d.c. characteristics of the Al-PbBi junctions

Figure 2.4b shows a schematic of the ideal current - voltage characteristics for the superconducting heterojunctions used in our experimental set-up. In figures 4.1 and 4.2 the current- voltage characteristics obtained in this experiment are shown. Both exhibit a current which is in excess of the ideal current. This excess current is particularly noticeable at low biases. Its magnitude varied from sample to sample. It was smallest for the junction of figure 4.1. The excess current generally has the form of the current - voltage characteristics of a junction between a superconducting metal with the gap of aluminium and a normal metal. This has lead to the suggestion that some of the lead-bismuth alloy remains normal opposite an unaffected region of superconducting aluminium even at the low temperatures of the

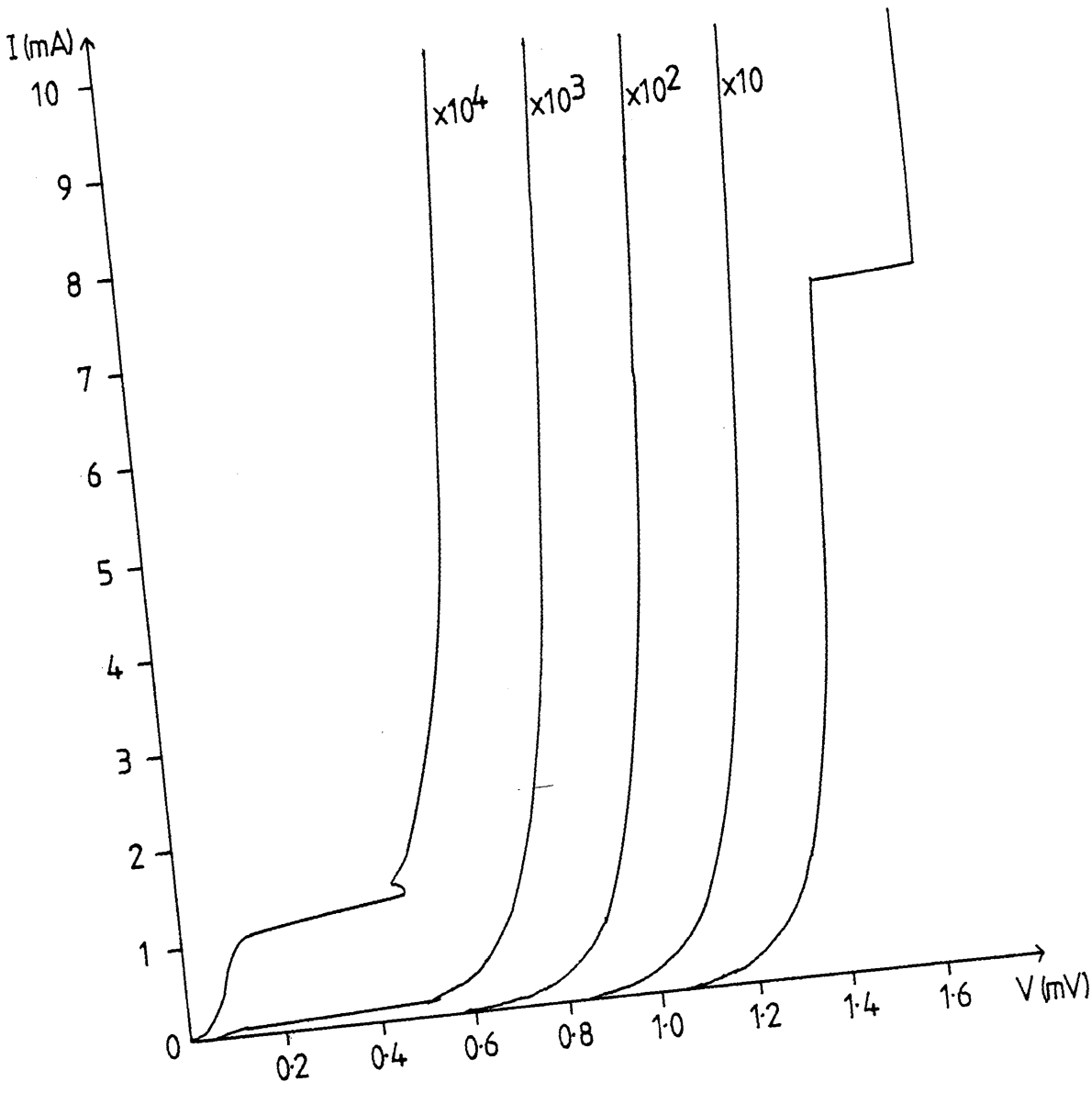

Figure 4.1 The measured d.c. characteristics for the detector in sample C10.

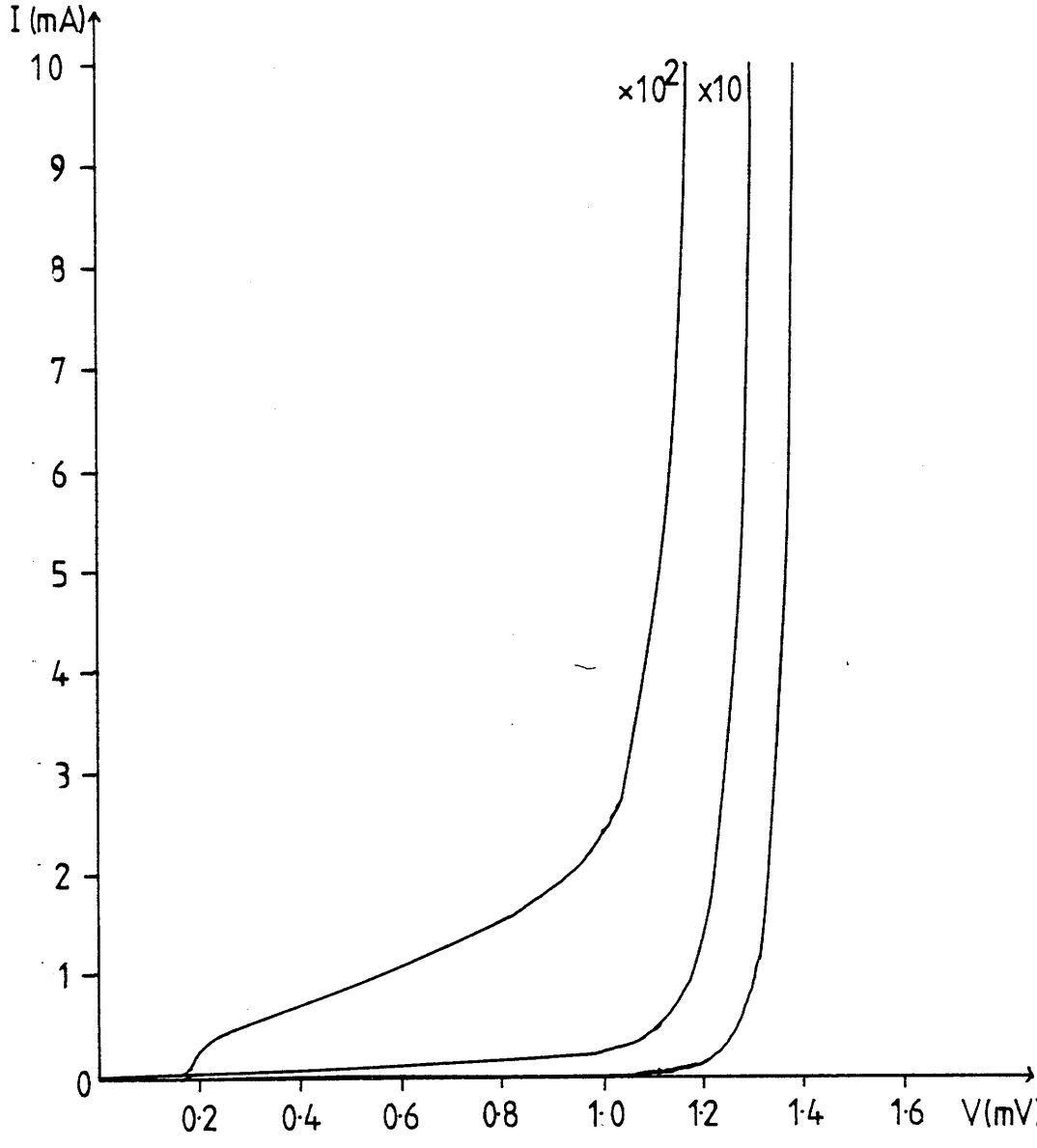

Figure 4.2 The measured d.c. characteristics for the detector in sample C16.

experiment. The reason for this is unclear. The preparation techniques used for the junctions in each sample were standardised as nearly as possible. As previously stated, it is supected that surface scratches on the sapphire substrate may be the cause. In order to remove the aluminium deposited in manufacturing earlier junctions from the sapphire it was necessary to polish the substrate with jewellers' rouge. This left comparitively large scratches on the surface of the sapphire. It was noticed that if a sapphire crystal was used more than once without finer polishing the excess current increased in magnitude. It was also noticed under the same conditions that a superconducting short was likely to appear in the characteristics. After several samples had been deposited and cleaned off in succession, junctions could not be produced, only superconducting shorts were obtained. The aluminium layer deposited was 100nm thick. It is thought that the surface scratches may have caused the surface of the aluminium to be uneven. This could lead to the aluminium not oxidising properly which could produce a superconducting short in parallel with the junction. If the area of the short were large enough, it would dominate the junction characteristics. The Josephson effect was also found in the junctions but this was simply removed by applying a magnetic field in the oxide plane.

From the current - voltage characteristics several quantities that were needed for the analysis of the data were deduced. First the superconducting gaps for both the lead-bismuth, Δ_1, and the aluminium, Δ_2, superconducting films were measured. This was simply done by looking at the region where the current remains constant while the voltage increases (under current bias). The voltage range over which this happens is $\Delta_1 - \Delta_2$ to $\Delta_1 + \Delta_2$ (see section 2.2). The lead-bismuth gap varied from sample to sample. This was probably due to slightly different bismuth contents. The range of values observed was from 1.52meV to 1.59meV. The aluminium gap showed a temperature dependence which can be explained by the fact that the temperatures used in the experiment were relatively close to the transition temperature of the aluminium particularly for the early experiments performed in the helium 4 cryostat. This made it necessary to check the aluminium gap for each set of data collected. Its range of values was between 0.11meV and 0.18meV. When using the helium 3 cryostat, which worked at lower temperatures and had better thermal stability, the aluminium gap was usually 0.17meV or 0.18meV, close to its zero temperature value. This was the case for most of the data presented in this

thesis. The gap values were needed in order to calculate the eleven by eleven matrix to be used in the matrix analysis (see section 2.5). This calculation was performed for each set of junctions used. A typical matrix is shown in table 4.1.

The temperature of the junction was also deduced from its characteristics under many different experimental conditions. Equation (2.7) describes the temperature dependence of the junction current at temperatures less than 1K and voltages such that $eV < (\Delta_1 - \Delta_2)$:-

$$I = KN_2(\Delta_1 - eV). \sqrt{(\Delta_1 \pi kT/2)} . \exp-((\Delta_1 - eV)/kT) \quad (2.7)$$

where

$$N_2(\Delta_1 - eV) = (\Delta_1 - eV).[\sqrt{((\Delta_1 - eV)^2 - \Delta_2^2)}]^{-1} \quad (4.1)$$

So a graph of $\ln(I/N_2)$ versus V should be a straight line of gradient e/kT. Values of current and voltage were obtained from the d.c. characteristics and N_2 values were calculated using equation (4.1). Graphs of $\ln (I/N_2)$ versus V were drawn for each experimental run. Such a graph is shown in figure 4.3. The current and voltage values were taken at high biases in order to minimise the effect of any excess current present in the junction. The temperature of the junction was taken to be the sample temperature since the sample, the junctions and the heaters were in good thermal contact with the substrate. It was found that the junction temperature was about 0.2K to 0.4K higher than the temperature of the germanium resistor. This is to be expected as the germanium thermometer was in closer thermal contact with the helium coolant than the sapphire crystal. This temperature difference did not change significantly when a heat pulse was applied. It was found that the temperature of the germanium thermometer closely followed the temperature of the junctions.The germanium thermometer was used to monitor the changes in temperatureduring the measurement of the data.

The measured temperature was substituted into equation (2.7) along with corresponding values of current and voltage in order to calculate the resistance of

0.0983	0	0	0	0	0	0	0	0	0	0
0.140	0.138	0	0	0	0	0	0	0	0	0
0.197	0.200	0.200	0	0	0	0	0	0	0	0
0.280	0.288	0.296	0.302	0	0	0	0	0	0	0
0.411	0.424	0.440	0.458	0.479	0	0	0	0	0	0
0.638	0.656	0.680	0.712	0.754	0.811	0	0	0	0	0
1.08	1.10	1.13	1.18	1.24	1.34	1.49	0	0	0	0
2.06	2.10	2.14	2.20	2.29	2.43	2.67	3.11	0	0	0
4.82	4.87	4.93	5.01	5.14	5.33	5.66	6.31	7.81	0	0
15.8	16.0	16.1	16.3	16.6	16.9	17.4	18.3	20.4	27.2	0
110	112	114	116	119	121	123	126	130	141	202

Table 4.1

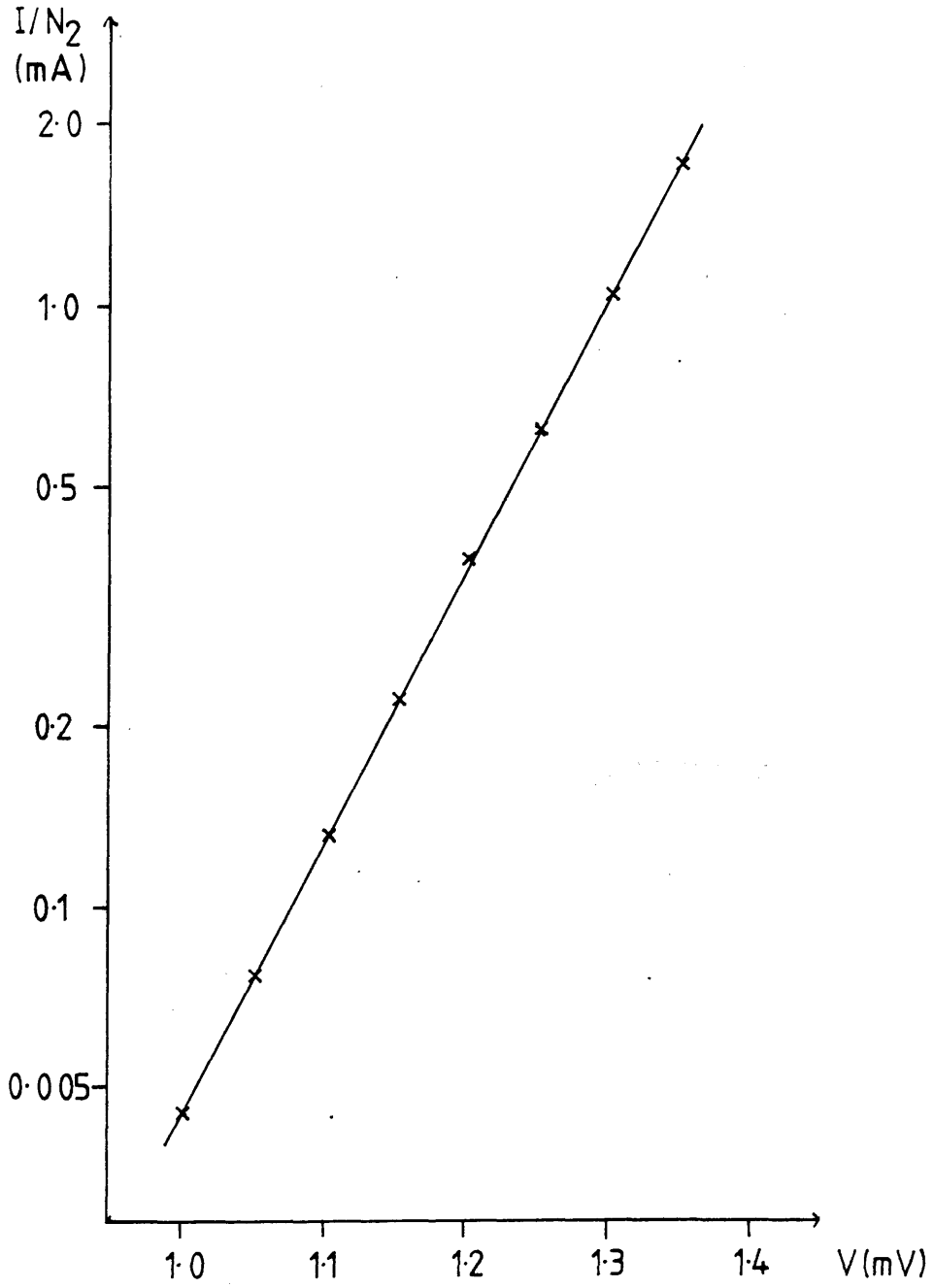

Figure4.3 Graph of $\ln(I/N_2)$ versus voltage at high bias voltage for the detector in sample C10.

the junction ($R = K^{-1}$). This was not measured from the junction characteristics at high voltages since the films were driven normal by the self heating caused by the current through the junctions. The values obtained ranged from 2mΩ to 30mΩ. It was necessary to know these for comparison of data from different junctions. this procedure will be discussed in more detail in chapter 5.

The spectra collected from the junctions are the voltage changes across the junction as it is subject to a changing phonon flux. These spectra are measured as a function of time at different voltage biases. From section 2.4 it is known that it is the changes in the junction current that are related to the phonon currents incident on the junction. In section 3.5 the relationship between the measured voltage changes and the junction current changes was derived:-

$$\Delta V_i' = - \Delta I \, . \, (1/\delta R + 1/R_i) \qquad (3.8)$$

R_i is the terminating resistance at the input of the oscilliscope and was set at 20Ω. δR is the differential resistance of the junction. As can be seen from the d.c. characteristics (figures 4.1and 4.2) the differential resistance of the junction varied with the biasing voltage. To obtain the most accurate value of the differential resistance it was necessary to employ a number of methods. The method used depended on the quality of the junction being examined.

For ideal junctions the differential resistance can be obtained by differentiating equation (2.7) with respect to V. This gives

$$\partial I/\partial V = KN_2 \sqrt{(\Delta_2 \pi/2kT)} . \exp-((\Delta_2 - eV)/kT) \qquad (4.2)$$

Note that this ignores the voltage dependence of N_2. This introduces a negligible error since this dependence is small compared to the exponential term. By taking the reciprocal of this equation the differential resistance can be calculated at different voltages for an ideal junction.

None of the junctions manufactured was completely devoid of leakage currents. For

the junctions in sample C10 (figure 4.1) a graph of $\ln(I/N_2)$ versus V is shown in figure 4.4. This graph is linear from V=0.6mV upwards indicating that this junction was dominated by the tunnelling current in this voltage range. So the differential resistance is given to a good approximation by equation (4.2) for these voltages. Between 0.3mV and 0.6mV the current does not increase exponentially as predicted by equation (2.7). However it increased too rapidly for a good fit to a polynomial in V to be obtained. In order to calculate the differential resistances in this interval the change in the current was measured over a voltage range of 0.01mV around the bias of interest. As the differential resistances at these biases were large (of the order of hundreds of ohms) the error in these measurements had an insignificant effect on the effective detector resistances which were dominated by the terminating resistances at the input of the oscilliscope (R_i).

This method was not suitable for junctions with a large superconducting-normal contribution to the current. It was found that at low biases the current varied sufficiently slowly with voltage for a polynomial function to be fitted to it. It was found that one polynomial could be fitted up to 0.75mV and another between 0.75mV and 1.05mV. The differential resistances were calculated from the derivatives of the polynomials. The current above this voltage varied too rapidly for a good polynomial fit to be obtained. For the voltage range 1.00mV to 1.30mV the methods employed for sample C10 were used. The linearity of a graph of $\ln(I/N_2)$ versus V determined which method was relevant at each bias.

In order to establish the quality of the junction it was necessary to measure the resistance of the S-N junction, R_{SN}. This was done by measuring the resistance of the characteristics at low bias. The S-N and S-S junctions were in parallel with one another and at low biases the differential resistance of the S-S junction was very large. The junction resistance at low bias was therefore dominated by R_{SN} . This is confirmed by the linearity of the junction characteristics at low biases (see figure 4.2). The ratio R_{SS}/R_{SN} gave an indication of how good the junction was. If this ratio was of the order of 10^{-4} or less it was found that no correction was needed for the S-N leakage current in parallel with the S-S junction.

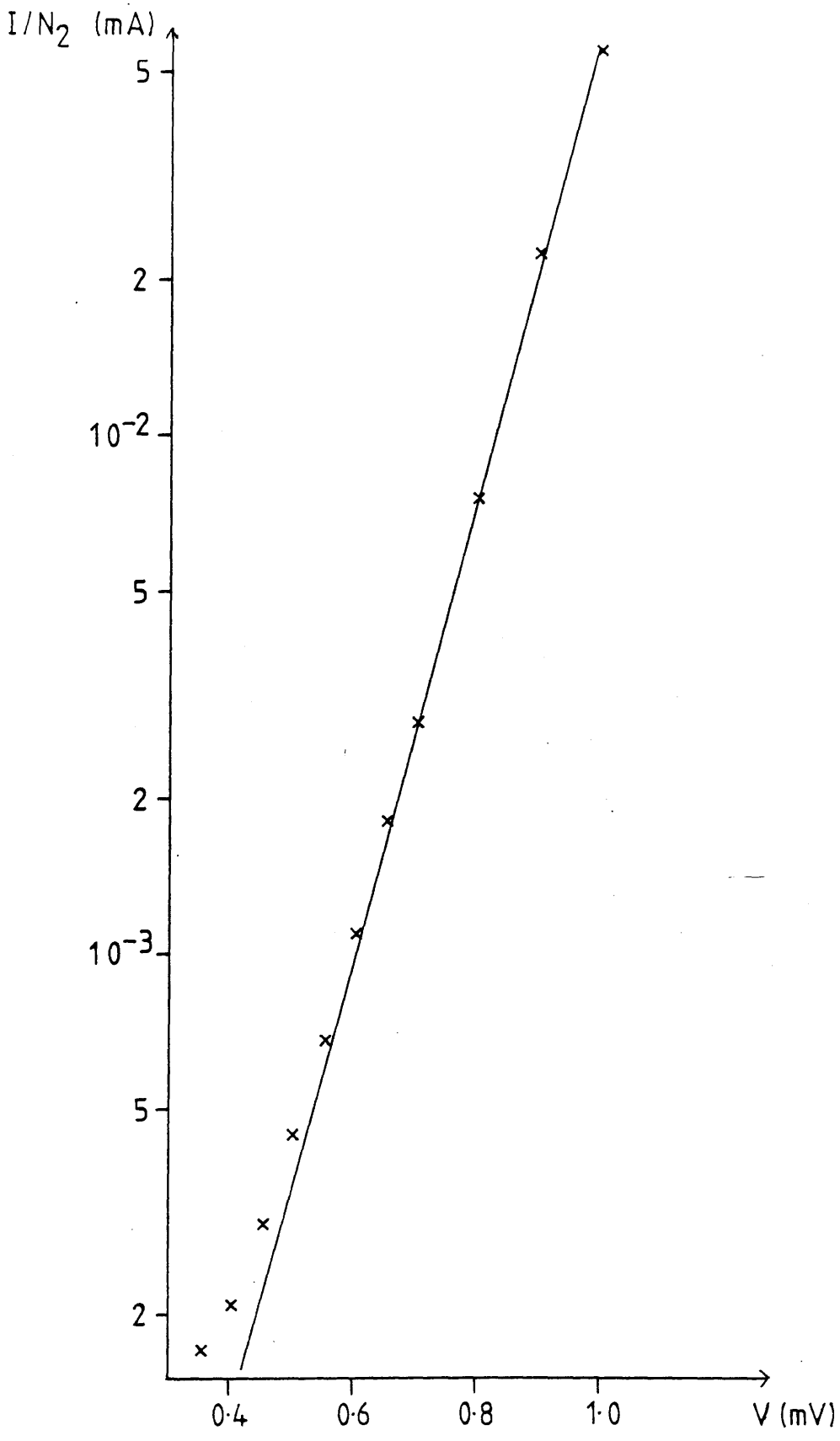

Figure 4.4 Graph of $\ln(I/N_2)$ versus voltage for the detector in sample C10.

4.3 The phonon spectra obtained from the Al-PbBi junctions

As discussed in chapter 2 the phonon pulse enhances the tunnelling current through the junction. In this experiment the effect this phonon enhanced current had on the voltage across the junction was measured at biases of 0.10mV intervals between 0.30mV and 1.30mV. A typical voltage signal pulse is shown in figure 4.5. This was taken at a bias voltage of 1.20mV using the junction whose characteristics are shown in figure 4.1. The phonons were generated by a 250ns pulse of power 4.9mW supplied to a constantan thin film heater. The voltage pulse measured using a junction with a large superconducting-normal current contribution was not discernibly different. The electromagnetic pickup has been suppressed as described in section 3.4.

The first phonons arrive 0.65 ± 0.025μs after the start of the generating pulse. These are the longitudinal phonons. This gives the velocity of these phonons as 10.8 ± 0.4kms^{-1}. The transverse phonons start to arrive 1.15 ± 0.025μs after the start of the generating pulse. Their velocity calculated from this measurement is 6.1 ± 0.2kms^{-1}. These measured values compare well with the calculated values of 11.10kms^{-1} for longitudinal phonons and 6.04kms^{-1} for transverse phonons along the c-axis of sapphire (Weis (1972)).

The voltage spectra were first converted into current spectra by dividing them by the calculated effective resistances. The matrix inversion was then performed using the appropriate Λ_{ij} matrix which had been previously calculated. This produced a series of spectra of phonon current against time at average energies $\bar{\Omega}_j=(\Delta_1-eV_j)+\Delta_2+\varepsilon/2$ where $V_j=1.4-0.1j$ (section2.5). By sampling the spectra at a particular time a phonon energy spectrum can be produced for that time. The signal at the transverse phonon peak was found to be the most useful in constructing such a spectrum since this was always found to be the largest signal in the time resolved spectra. In figure 4.6 is shown an energy spectrum of the phonon currents at the transverse peak taken from the junction shown in figure 4.1. The signal was obtained using a 250ns pulse of power 4.9mW supplied to the heater.

There are several sources of error in such a phonon spectrum. At high energies the

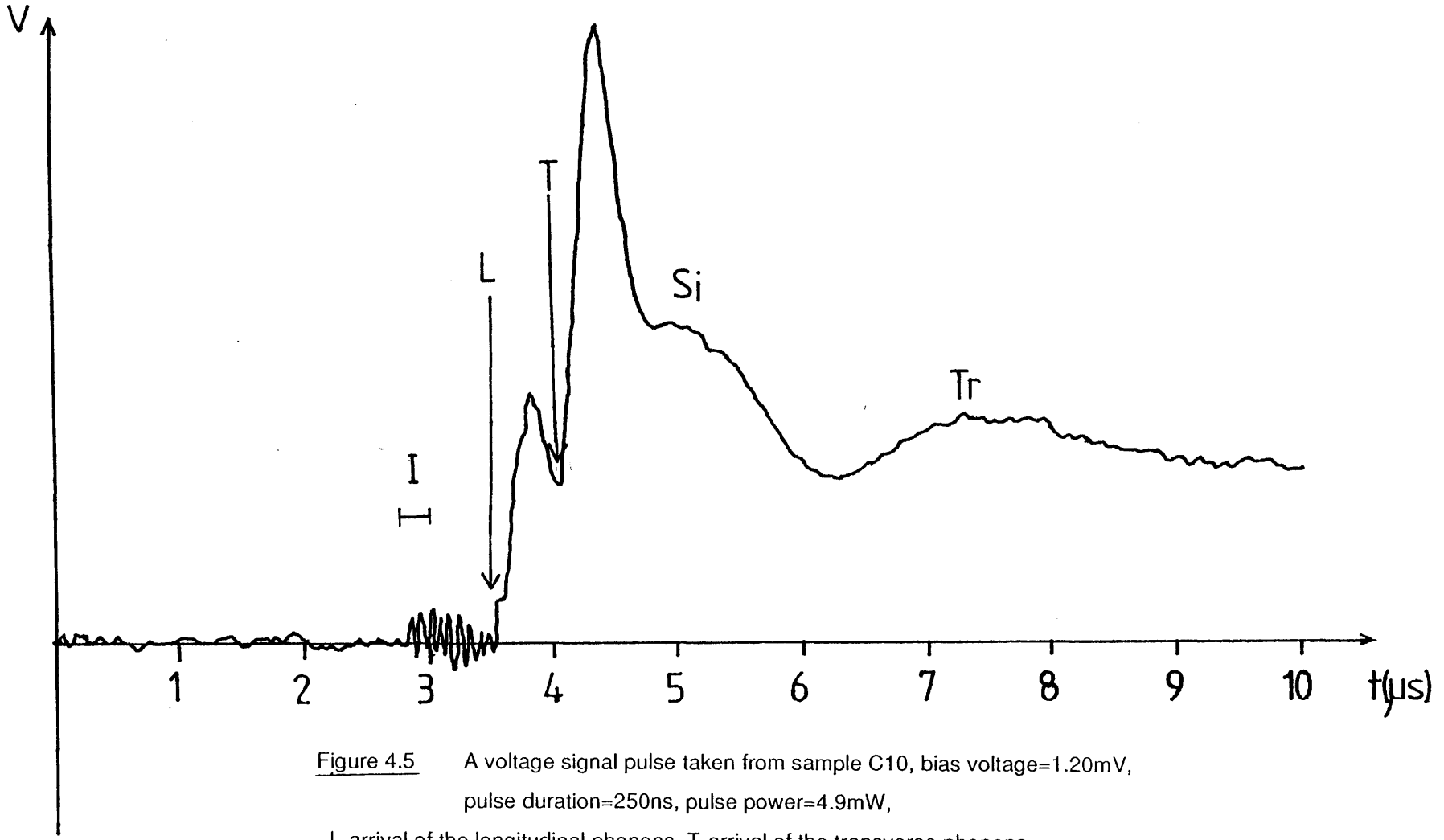

Figure 4.5 A voltage signal pulse taken from sample C10, bias voltage=1.20mV, pulse duration=250ns, pulse power=4.9mW,

L-arrival of the longitudinal phonons, T-arrival of the transverse phonons

I - initiating pulse, Si - peak due to phonons reflected from the crystal sidewall,

Tr - peak due to phonons undergoing triple reflection.

voltage signal from the junction is small and there is a significant error in this signal due to noise. The currents were calculated from the measured voltage signals using the differential resistances. Therefore, any error in the differential resistance will cause an error in the calculated electron current. Errors in the differential resistance arise from the measurement of the quantity itself and from variations in the temperature during the collection of a spectrum. The temperature of the germanium resistor was constantly monitored and if it changed by more than 0.005K while acquiring one voltage spectrum the data were rejected. A typical temperature drift was 0.001K. Both these random errors are amplified by the matrix analysis scheme resulting in larger errors in the phonon currents. Calculations using the matrix analysis with data which had an x% error have shown that the error in the results was 4x%.

At low energy the calculated spectrum is negative. This is probably due to the neglect of recombination of quasiparticles in the matrix analysis scheme. The only process of decay of non-thermal quasiparticles that has been taken into account is relaxation. However, near the gap edge recombination is the more important process. The lowest energy current from the junction is measured near the gap edge and has a contribution from quasiparticles generated by high energy phonons which have relaxed from higher energies. This has been taken into account. However, this current is decreased by the recombination of quasiparticles, this process has been neglected. Therefore the contribution to the quasiparticle current at the gap edge due to high energy phonons is overestimated. When this overestimated current is subtracted from the measured current it can lead to an apparantly negative signal.

The large signal in the top channel of figure 4.6 has two possible sources. There could be a contribution from phonons with energies well above that of the top channel. All these phonons contribute to the current in the top channel but the higher energy contribution is not subtracted since its magnitude is unknown and cannot be measured. Therefore the phonon current at this energy is overestimated. A S-N leakage current would also produce an anomalously large signal in the top channel. It would be measured along with the phonon enhanced current thus overestimating the phonon current. It is likely that both these effects contribute to the large top channel phonon current in figure 4.6.

The phonon energy spectrum shown in figure 4.7 was calculated from data measured

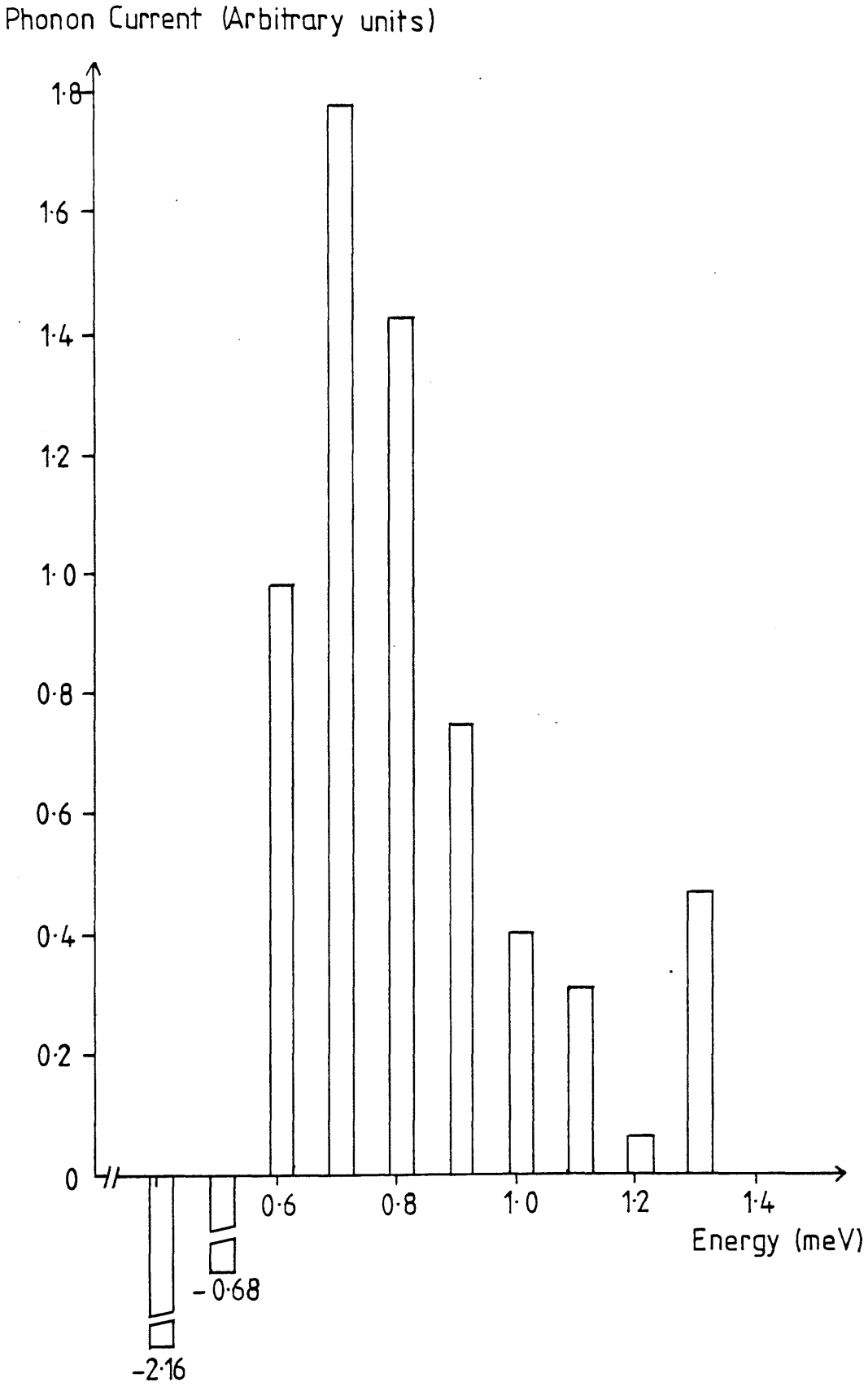

Figure 4.6 Phonon current versus energy measured from sample C10. Input pulse duration=250ns, input pulse power=4.9mW.

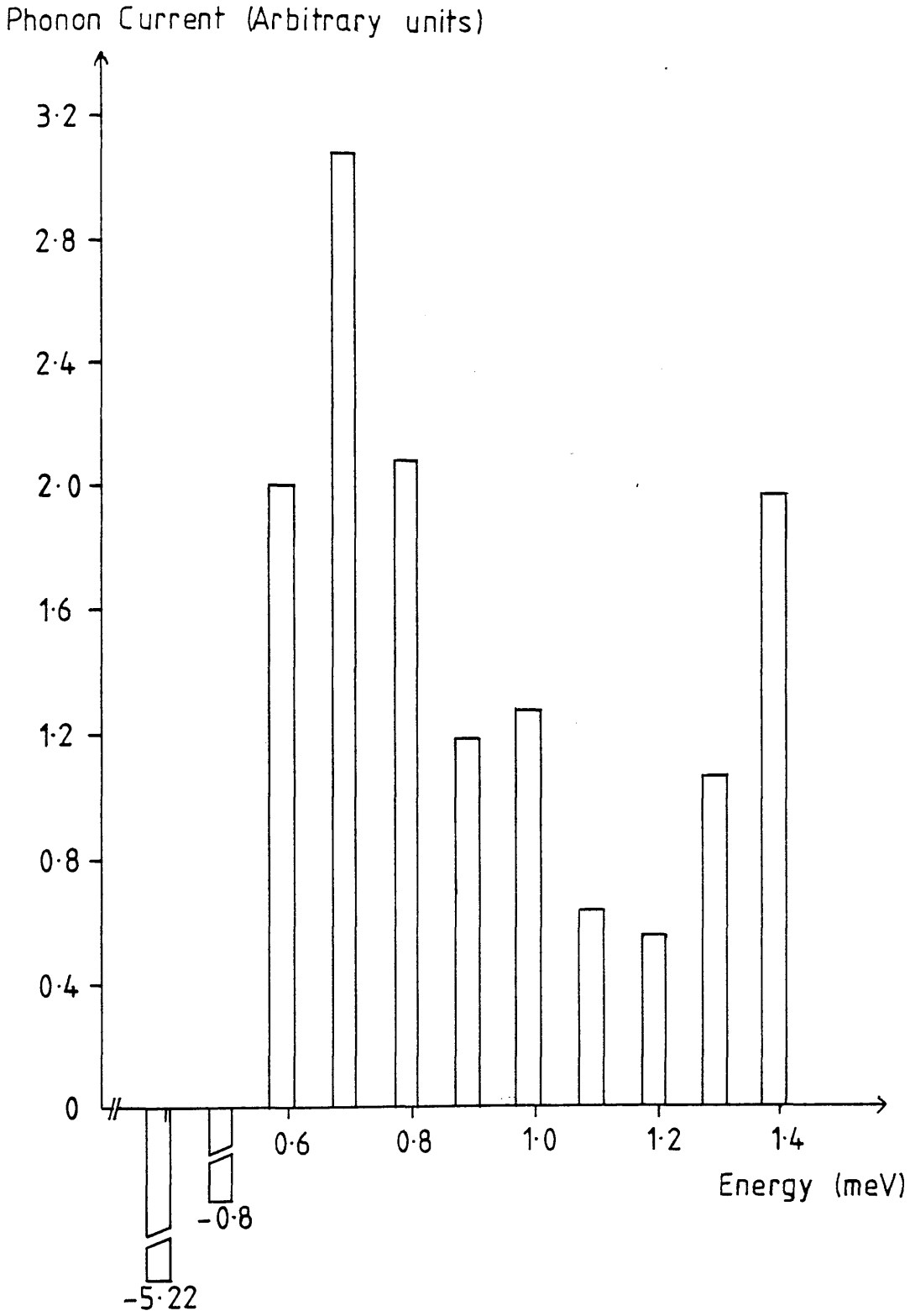

Figure 4.7 Phonon current versus energy measured from sample C16. Input pulse duration=250ns, input pulse power=5.5mW.

using the junction whose d.c. characteristics are shown in figure 4.2. As before the pulse width was 250ns, the pulse power was 5.5mW. The difference in the power was due to differing heater resistances. It can be seen that the high energy signal is relatively much larger than that in figure 4.6. This second spectrum was calculated from enhanced tunnelling currents measured at bias voltages from 0.30mV to 1.30mV inclusive. There is the possibility that the phonons incident on these junctions had energies higher than that measured by these junctions. Later in this chapter it will be shown that this effect is too small to account for such a large signal at high energies as found in figure 4.7. Although this possibility cannot be ignored completely. It can be seen by comparing figures 4.1 and 4.2 that the S-N leakage current is larger for the junction used in the measurement of the data in figure 4.7 as compared to that of figure 4.6. Therefore a larger contribution to the top channel signal from the S-N leakage current should be expected.

Attempts were made to correct for the superconducting-normal excess current. In chapter 2 an expression for the voltage due to this current was derived

$$V_{SN} = K\,[K^{-1}.dI_{SN}/dT].\,(d\,\Delta/dT)^{-1}.\delta.R_{eff} \qquad (2.29)$$

The change in the aluminium gap, δ, during the phonon pulse was measured from the time resolved voltage spectrum taken at a bias voltage of $(\Delta_1 + \Delta_2)/e$. Using equation (2.29) the V_{SN} were calculated for the transverse phonon peak. These were then subtracted from the relevant signal voltages which have been measured from the time resolved voltage spectra. These adjusted voltages were analysed using the matrix technique. The phonon energy spectrum thus produced is shown in figure 4.8. It can be seen that the overall signal is decreased particularly at high energies. This is to be expected since the superconducting-normal signal has a relatively larger effect on the smaller high energy signal. This correction appears to have produced a reasonable result in this case. In many other cases, however, with larger leakage currents more serious problems arose. In some cases the calculated superconducting-normal voltages were larger than the measured voltages. In other cases the correction left a spectrum in which almost all the phonon currents were negative. This implies that this simple form for the leakage current change in the

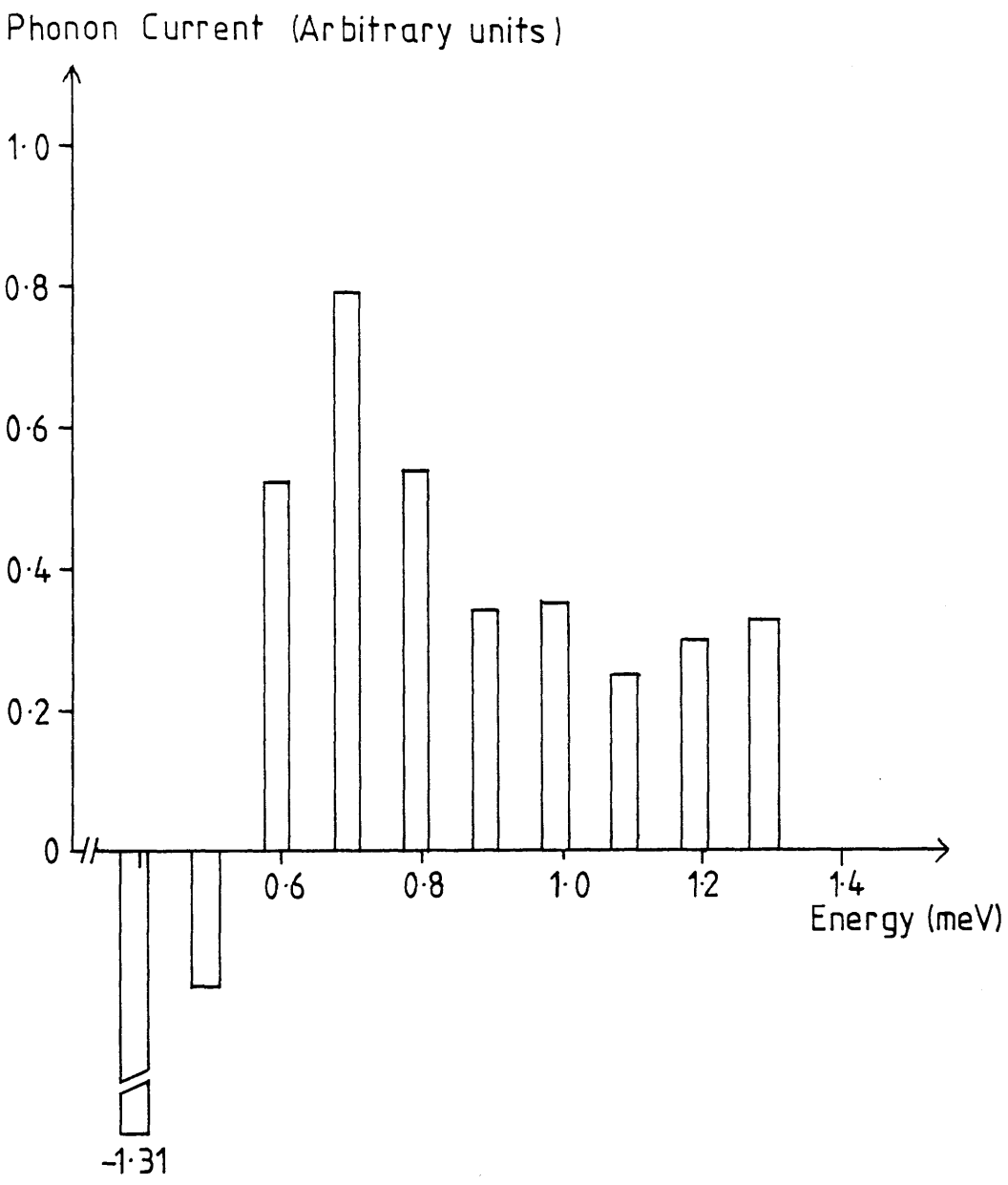

Figure 4.8 Phonon current versus energy calculated from the signal from sample C16 corrected for S-N contribution. Input pulse duration=250ns, input pulse power=5.5mW.

junctions based on thermal equilibrium principles is inadequate. Therefore, this correction could not be applied. This gave further reason for neglecting data from junctions with large leakage currents.

As discussed above, phonons of higher energy than the top channel energy of the junctions are included in the signal measured in the top channel. This produces an erroneously high phonon current at the highest energy in the calculated spectrum. A calculation cannot be performed to correct for this effect since there is no information available about the higher energy phonons. However, we should be aware of this source of error and any possible effects it may have on the measured phonon energy spectrum. By considering the analysis technique it should be possible to obtain some information about the latter.The analysis technique involves the subtraction of a corrected high energy signal from the enhanced current at the next, higher, bias to produce the phonon current at the next energy. From chapter 2 the enhanced tunnelling current in channel i, $\Delta I(\Omega_{oi})$, is given by

$$\Delta I(\Omega_{oi}) = \sum_{j=1}^{i} \Lambda_{ij} I_{Pj} \qquad (2.25)$$

where I_{Pj} is the phonon current at energy $\bar{\Omega}_j$.This leads to the lowest bias, highest energy, enhanced current

$$\Delta I(\Omega_{o1}) = \Lambda_{11} I_{P1} \qquad (4.3)$$

At the next bias the enhanced current is given by

$$\Delta I(\Omega_{o2}) = \Lambda_{21} I_{P1} + \Lambda_{22} I_{P2} \qquad (4.4)$$

Using equation 4.3 this can be rewritten as

$$I_{P2} = [\Delta I(\Omega_{o2}) - \Lambda_{21} I_{P1}] \Lambda_{22}^{-1} \qquad (4.5)$$

So if I_{P1} has been overestimated, such as when an the phonon flux contains phonons of energies greater than the top channel energy, then I_{P2} is underestimated. The measured signal in the second top channel is less than its true value. The third enhanced current is

$$\Delta I(\Omega_{03}) = \Lambda_{31} I_{P1} + \Lambda_{32} I_{P2} + \Lambda_{33} I_{P3} \qquad (4.6)$$

So the phonon current at this energy is given by

$$I_{P3} = [\Delta I(\Omega_{03}) - \Lambda_{32} I_{P2} - \Lambda_{31} I_{P1}] \Lambda_{33}^{-1} \qquad (4.7)$$

Depending on the relative signs of Λ_{32} and Λ_{31} then I_{P3} could either be underestimated or overestimated. This effect can be present throughout the spectrum. From the results of the measurement of the output of the constantan heaters it is believed that this effect is small in this experiment. This is dicussed in the next section of this chapter.

4.4 The phonon spectrum emitted by the constantan heaters

In section 2.7 two theories about the output of constantan heaters were outlined, the acoustic mismatch theory for bulk constantan and the theory of Frick et al. (1975) for thin film constantan. These theories predicted very different spectra. Comparing the measured spectrum shown in figure 4.6 with the two theoretical spectra shown in figures 2.10 and 2.11 it can be seen that the form of the measured spectrum is closest to that produced by the theory of Little (1959). It does not show the form predicted and measured by Frick et al (1975). Using equation (2.31) the equivalent heater temperatures, T^*, were calculated for all the experimental conditions. They varied between 1.67K and 4.04K. In their model Frick et al. (1975) assume that the frequency position of the spectral maximum is given by Wien's law, i.e. $h\nu_{max} \approx 2.8kT$. They also assume that the total radiation power

follows the T^4 law of Stephan-Boltzmann. The output of thin film constantan heaters on sapphire was measured and found to fit a model in which the heater boundaries were weakly coupled. In this model the wavelength of the lowest energy phonon which can be emitted perpendicular to the interface is twice the heater thickness. This cut-off wavelength occurs at the spectral maximum. The heater temperature below which this effect would become significant can be estimated by equating the maximum in the spectral radiant energy curve (at 2.8kT) to the energy of the transverse phonons at the cut-off wavelength. For the heater used in this experiment the calculation indicates that for a T^* greater than 1.5K this model is invalid. So it should not be expected that the measured spectrum in this experiment follow the form predicted by Frick et al (1975).In order to investigate the theory of Frick et al. (1975) it would be necessary to go down to lower input powers so that the effective heater temperature would be less than 1.5K. In order to be able to detect such small signals reliably lower resistance detector junctions would be needed. No high quality junctions were produced at a lower resistance, they all had excess S-N currents. So it was not possible to verify the Frick et al. (1975) theory.

As discussed in section 4.1 only the phonon spectra which have been transmitted perpendicularly to the heater-sapphire boundaries and down the c-axis of the sapphire crystal will be considered. The spectra were measured using sample C10, the details of which are listed in table 4.2. Figures 4.9 to 4.12 show phonon current spectra obtained from the transverse phonon peak at input puwers of 15.4mW, 4.9mW, 1.54mW and 0.49mW respectively. Figures 4.13 to 4.15 show the longitudinal peaks at the three corresponding higher powers. The signal at the longitudinal phonon peak is smaller than at the transverse phonon peak. The 0.49mW signal for the longitudinal phonons is very small and, therefore, subject to large errors, for this reason it has not been included. The heater equivalent temperature was calculated for each of these powers. These were then used to calculate the corresponding theoretical spectra using the theory of Little (1959). The results of these calculations have been superimposed on the measured spectra as broken lines in figures 4.9 to 4.15. These have been fitted to the measured spectra by multiplying them by a correction factor. The correction factors used were the same for the transverse phonon spectra as were the correction factors for the longitudinal phonon spectra with the exception of the 15.4mW spectra (figures 4.9 and 4.13). These had a larger correction factor. The reason for this is unclear but it

Aluminium thickness (nm)	200 ± 10
Lead bismuth thickness (nm)	200 ± 10
Junction normal resistance (R mΩ)	34 ± 2
Junction capacitance (nF)	33 ± 3
R_{SN}/R	10^5

Table 4.2

Aluminium thickness (nm)	150 ± 5
Lead bismuth thickness (nm)	220 ± 20
Junction normal resistance (R mΩ)	7 ± 1
Junction capacitance (nF)	20 ± 2
R_{SN}/R	10^4

Table 4.3

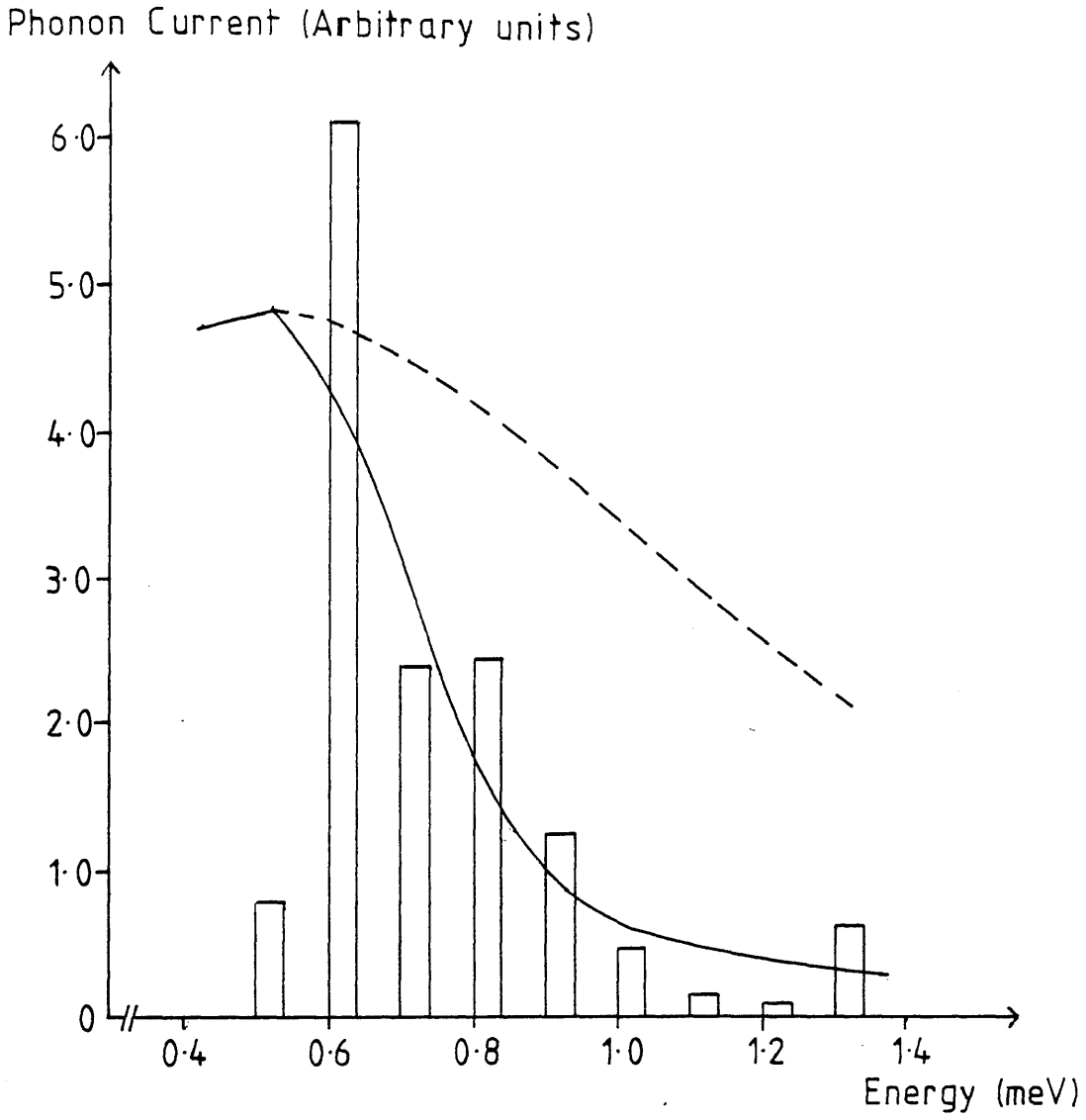

Figure 4.9 Phonon current versus energy measured from sample C10, transverse phonon signal. Input pulse duration=100ns, input pulse power=15.4mW.

– – – phonon current calculated from Little (1959),

——— corrected for junction time constant.

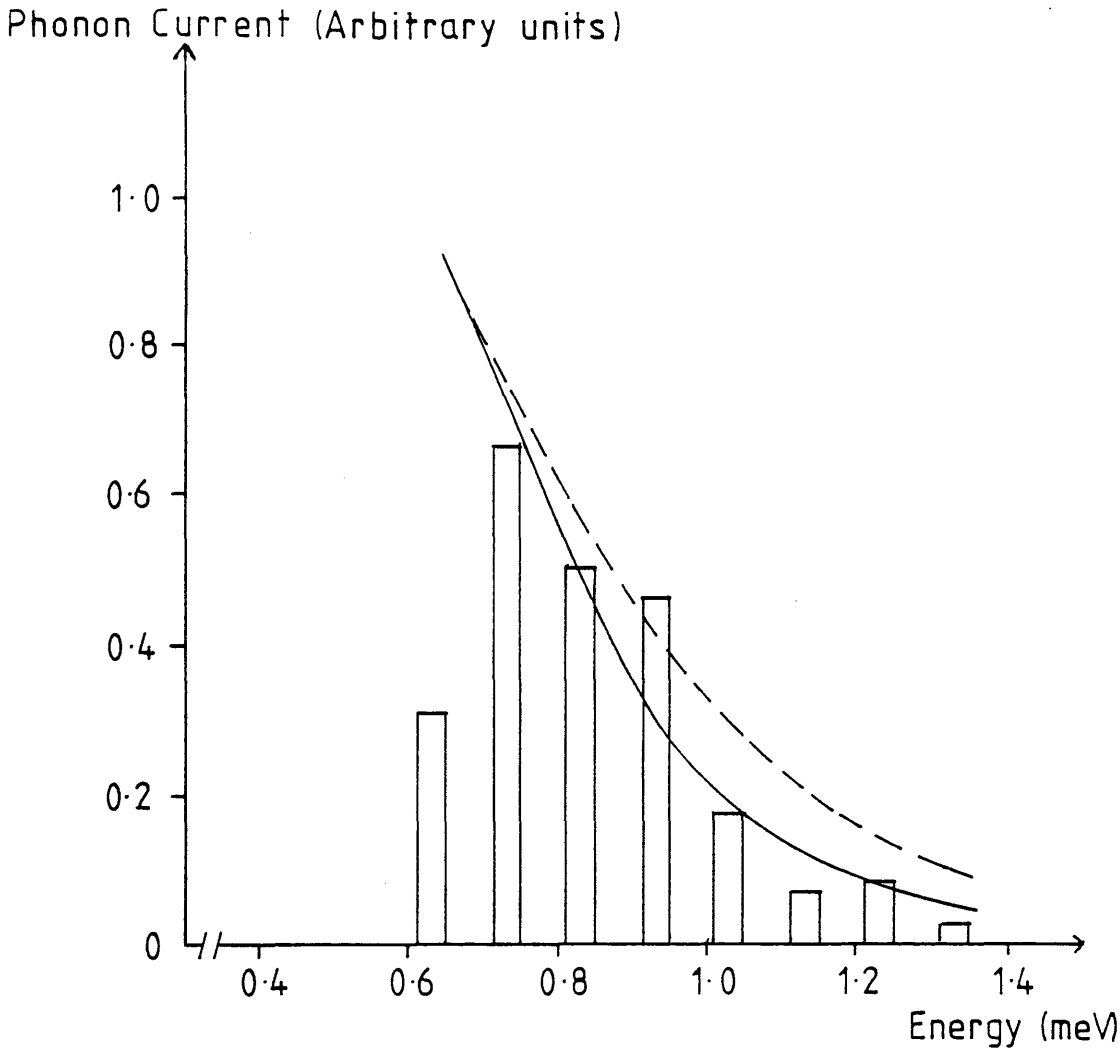

Figure 4.11 Phonon current versus energy measured from sample C10, transverse phonon signal. Input pulse duration=500ns, input pulse power=1.54mW.

– – – phonon current calculated from Little (1959),

——— corrected for junction time constant.

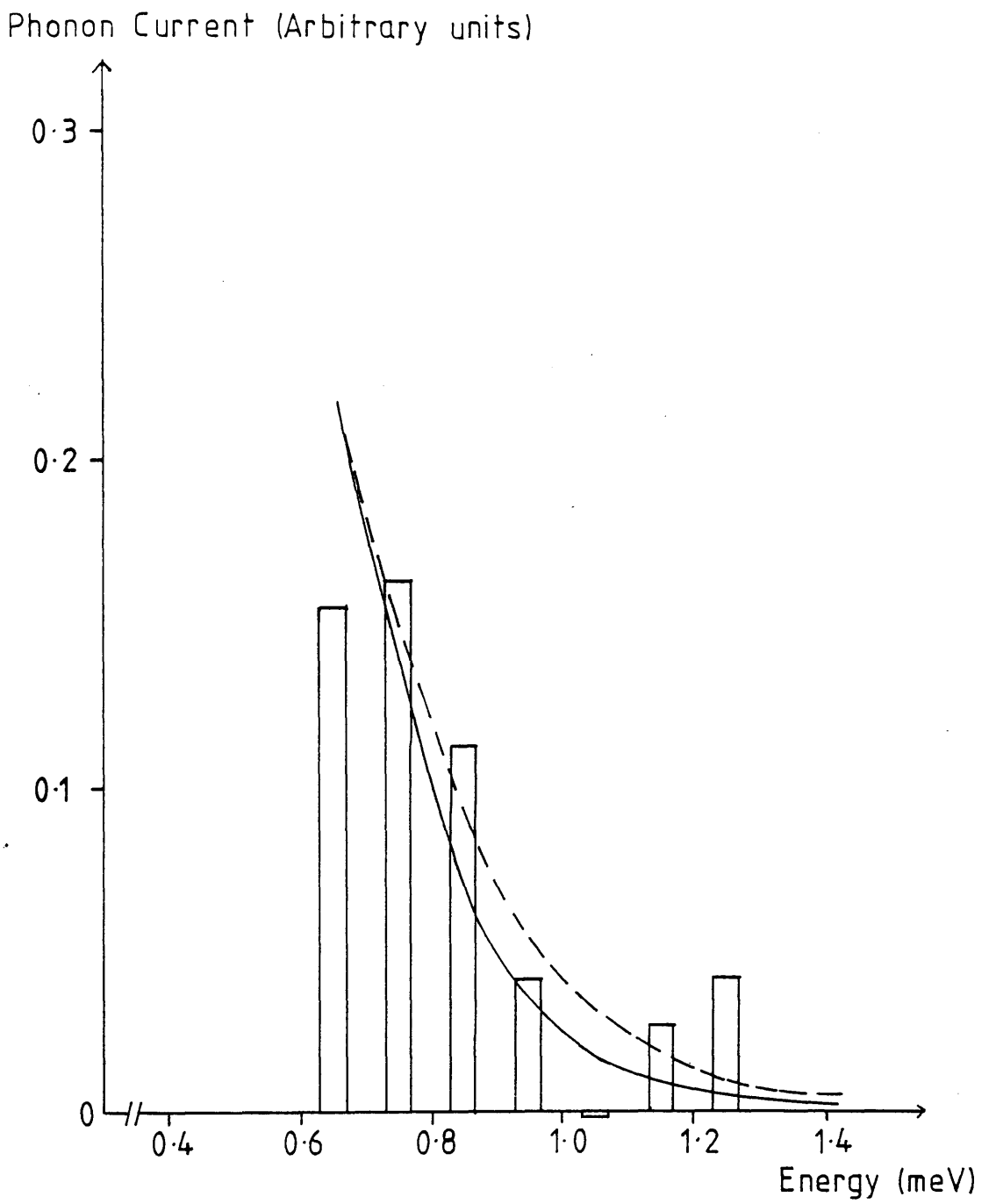

Figure 4.12 Phonon current versus energy measured from sample C10, transverse phonon signal. Input pulse duration=500ns, input pulse power=0.49mW.

– – – phonon current calculated from Little (1959),

——— corrected for junction time constant.

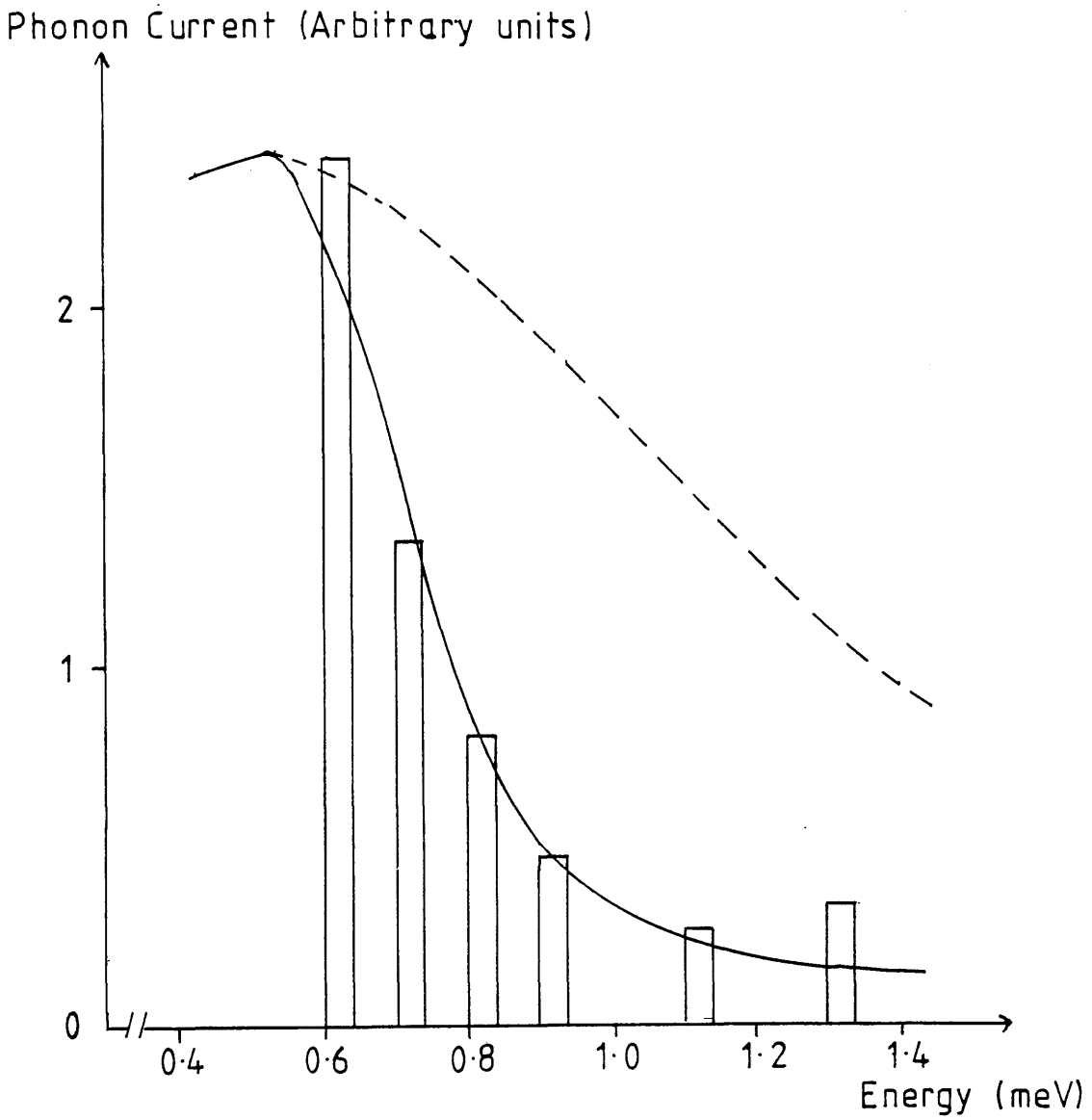

Figure 4.13 Phonon current versus energy measured from sample C10, longitudinal phonon signal. Input pulse duration=100ns, input pulse power=15.4mW.

– – – phonon current calculated from Little (1959),

——— corrected for junction time constant.

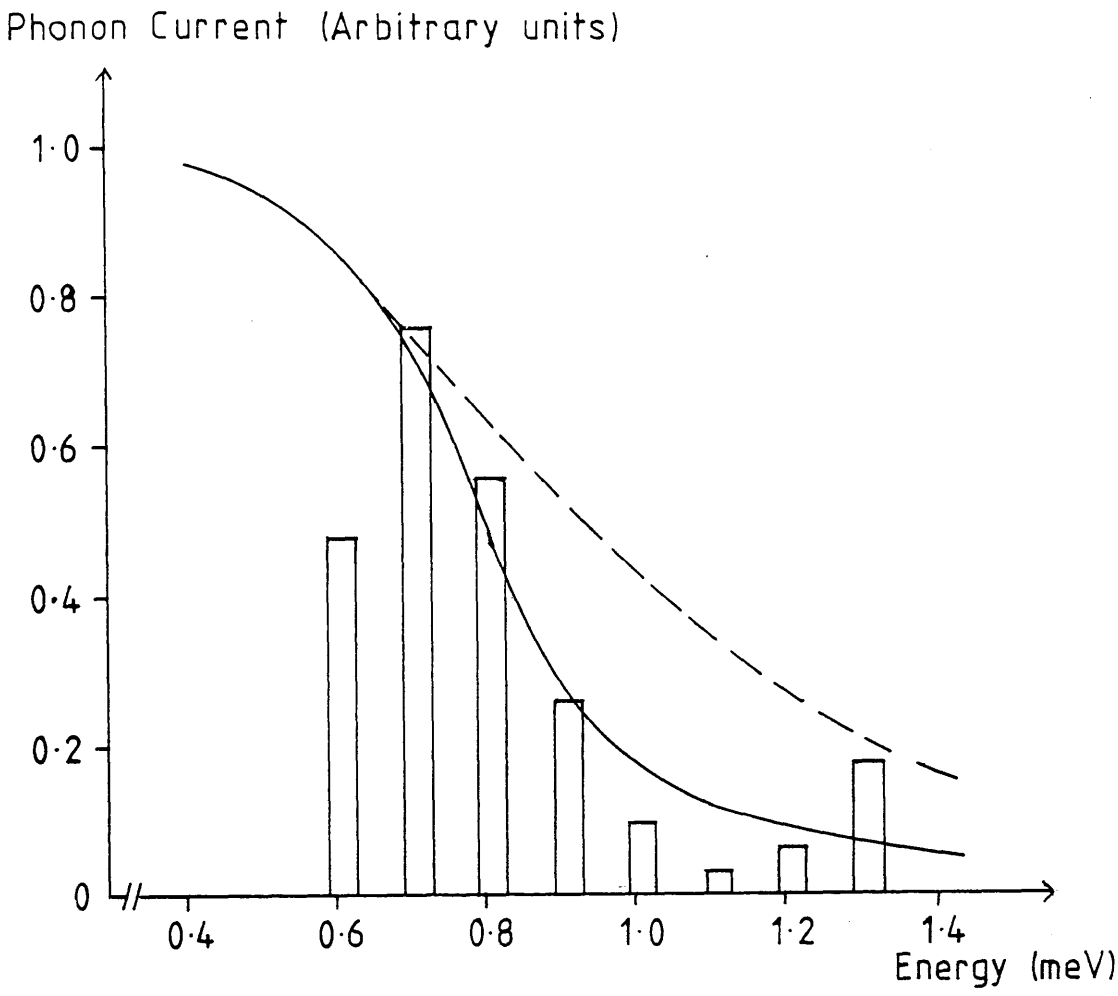

Figure 4.14 Phonon current versus energy measured from sample C10, longitudinal phonon signal. Input pulse duration=250ns, input pulse power=4.9mW.

– – – phonon current calculated from Little (1959),

——— corrected for junction time constant.

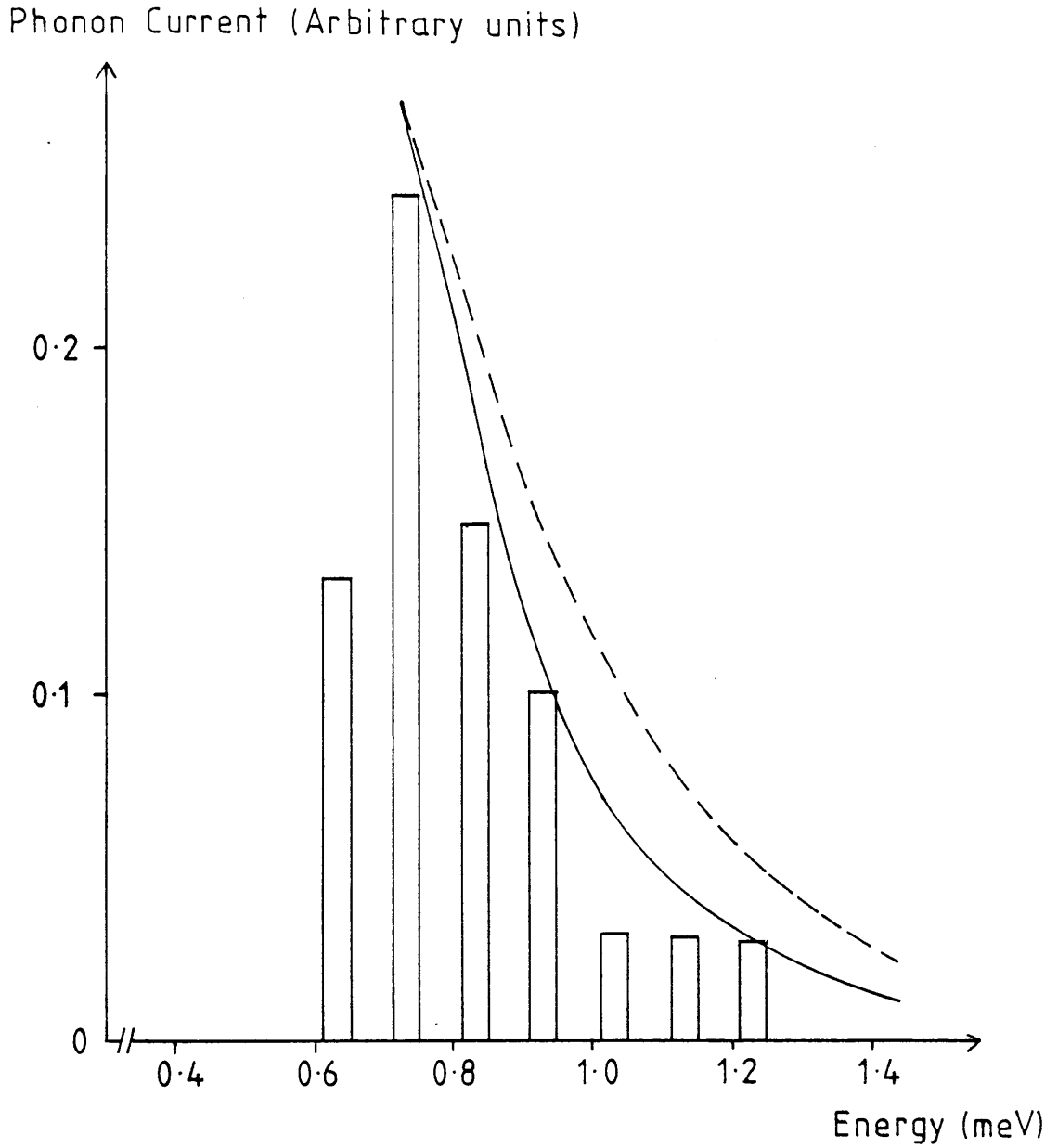

Figure 4.15 Phonon current versus energy measured from sample C10, longitudinal phonon signal. Input pulse duration=500ns, input pulse power=1.54mW.

— — — phonon current calculated from Little (1959),

——— corrected for junction time constant.

is suspected that it could have been due to the temperature in this experimental run being unusually high owing to the high mean power being dissipated in the crystal. The fit for the two lowest powers, 1.54mW and 0.49mW, was reasonable. However, as the input power increased the fit became less good. The agreement at the two lowest powers suggested that this effect was not due to the difference in input powers but had other origins. It was noted that the current pulse supplied to the heater for the measurements at 1.54mW and 0.49mW lasted 500ns. Whereas, the pulse duration was 100ns for the 15.4mW data, and 250ns for the 4.9mW data. The fit appeared to deteriorate as the duration of the input pulse decreased. It was also noted that the agreement deteriorated as the phonon energy increased. This implied that the junction had a time constant that varied with bias and was significant compared to the pulse length.

In order to confirm this the junction capacitance was measured. A voltage pulse was applied across the detector junction of amplitude very much smaller than the energy gap ($\Delta_1 + \Delta_2$). Using the detection system the voltage across the detector was measured as a function of time. It was noticed that the voltage across the junction did not fall to zero immediately the pulse was removed. A graph of lnV versus time was plotted. Figure 4.16 shows such a graph for sample C10. It was found to be a straight line. It was assumed that the voltage was proportional to $(1-\exp-(t/\tau_o))$ where $\tau_o$was the RC time constant of the system, the capacitance being that of the junction. The equivalent circuit is shown in figure 4.17. From this it can be seen that

$$R = (1/R_o + 1/R_v + 1/\delta R)^{-1} \qquad (4.8)$$

$R_o = 50\Omega$ and $R_v = 20\Omega$. At the measurement voltage ($eV \ll \Delta_1 - \Delta_2$) δR was much larger than R_o and R_v and (4.8) simplifies to

$$R = (1/R_o + 1/R_v)^{-1} = 14.3\Omega \qquad (4.9)$$

Using this value the junction capacitance was calculated. This varied between 10nF

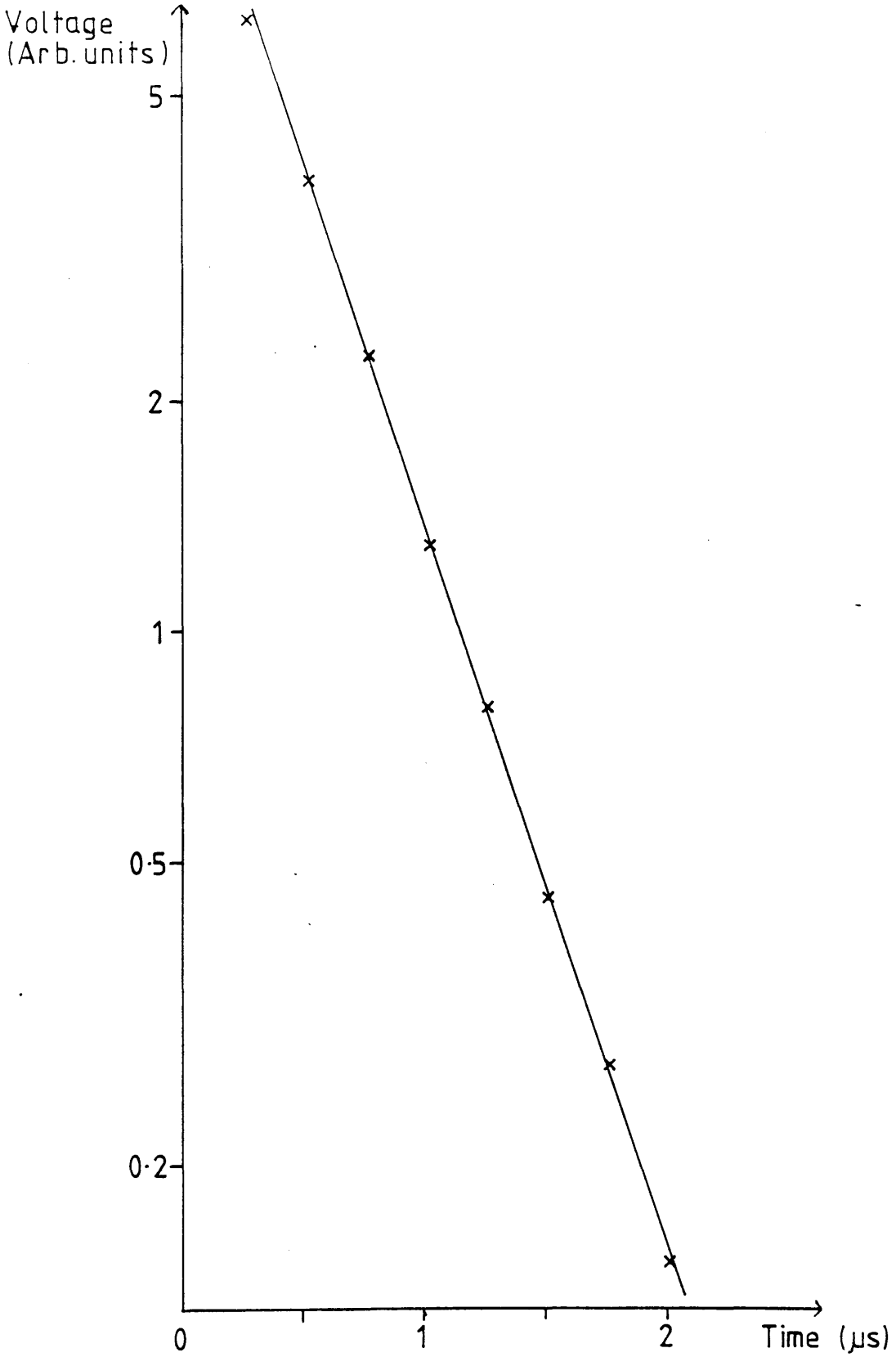

Figure 4.16 A graph of lnV versus time for the detector in sample C10.

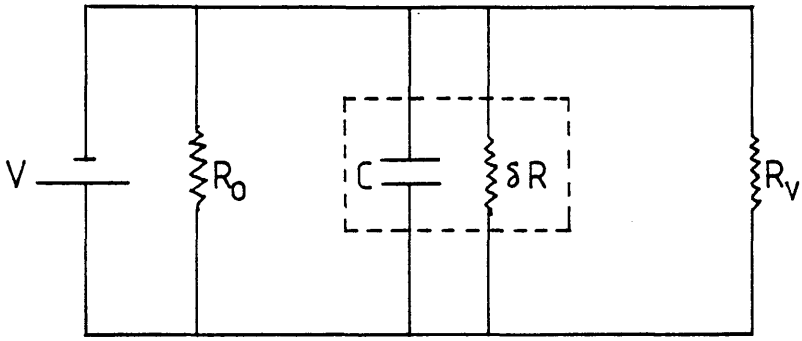

Figure 4.17 The equivalent detector circuit.

and 60nF. For sample C10 it was measured as 33 ± 3 nF.

The effective time constant as a function of bias was calculated using the calculated capacitance and the effective resistance. It was assumed that the phonon current at a particular energy was mainly derived from the signal from the corresponding bias voltage. Therefore only a fraction $(1-\exp-(t_o/\tau))$ of the current will be developed during a pulse of length t_o. The theoretical spectra were corrected for this. The results are shown as solid lines in figures 4.9 to 4.15. The correction had a larger effect at higher powers. This was expected since the pulse duration was shorter. Within each of the spectra there was only a small reduction in the theoretical signal, if any, at low energies. Again, this was expected since the effective resistances and, hence, the effective time constants were small at these energies. The correction produced a reasonable agreement between the theoretical ouput predicted by Little (1959) and the measured output of the constantan heaters used in this experiment. From this agreement it can be concluded that there were very few phonons emitted by the heaters that were above the energy range of the detectors.

In figures 4.9, 4.10, 4.13 and 4.14 there is a larger signal in the top energy channel than that predicted by theory. As discussed in section 4.3 the origin of this large top channel signal is unclear. It was noted that the detectors could not be used at the lowest bias, 0.30mV. The highest energy in the analysis scheme was set to zero. Whereas it can be seen from the graphs that the theory of Little (1959) predicts a measurable signal. This signal will indeed have been measured but it will have been included in the next highest energy channel, that is the top channel of the measured spectra, thus overestimating the size of this signal. This signal was about the same magnitude as the excess signal in the top channel which is an indication that it could be the main cause of the excess signal. To establish the origin of the excess signal it would be necessary to use detectors which respond down to lower bias voltages. We were not able to manufacture such junctions.

Figures 4.18 and 4.19 show the energy spectra obtained from sample C16 at powers of 5.5mW and 1.75mW respectively. The details of the constantan heater and the detector are shown in table 4.3. Superimposed on the measured spectra are the

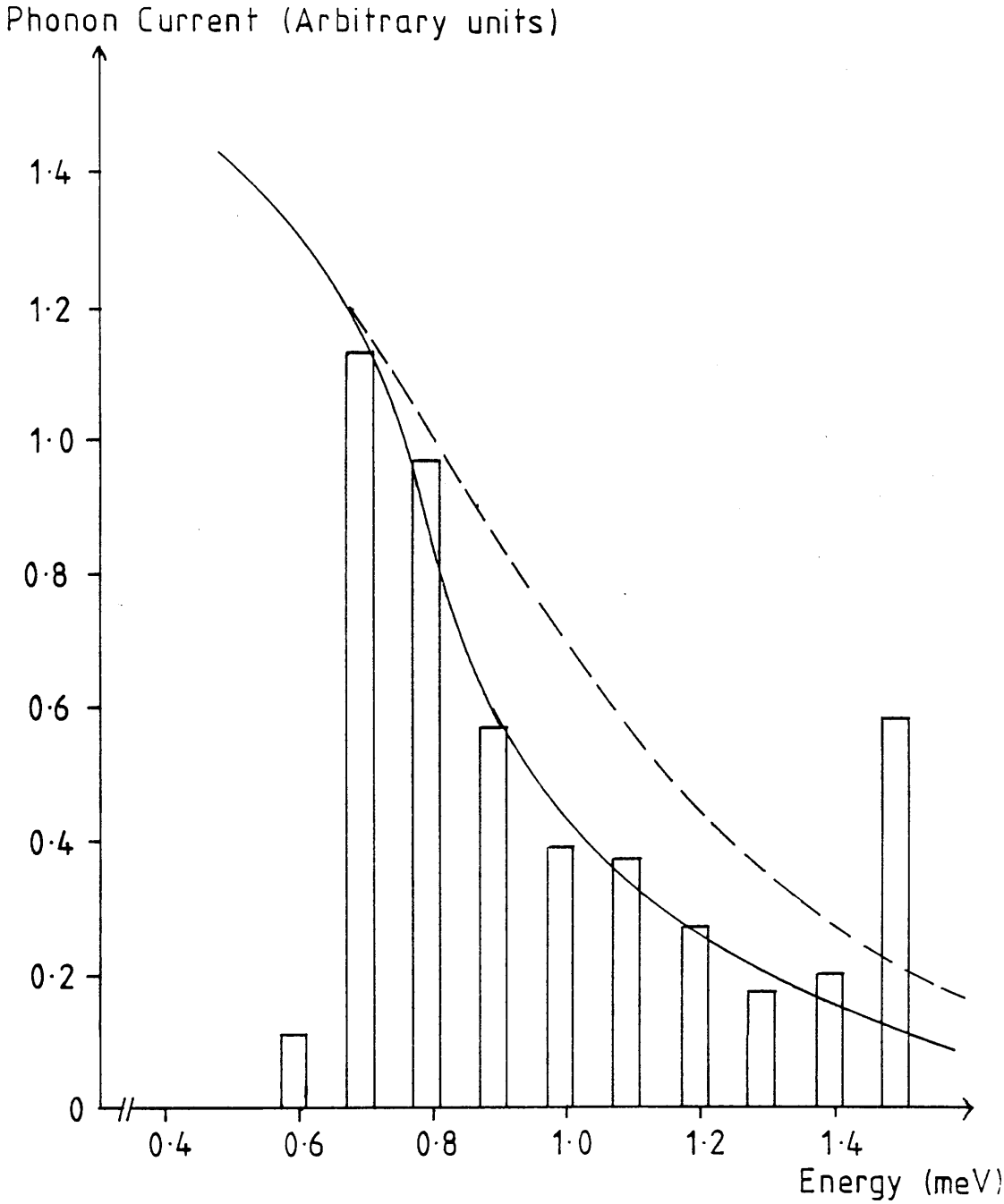

Figure 4.18 Phonon current versus energy measured from sample C16, transverse phonon signal. Input pulse duration=250ns, input pulse power=5.5mW.

— — — phonon current calculated from Little (1959),

——— corrected for junction time constant.

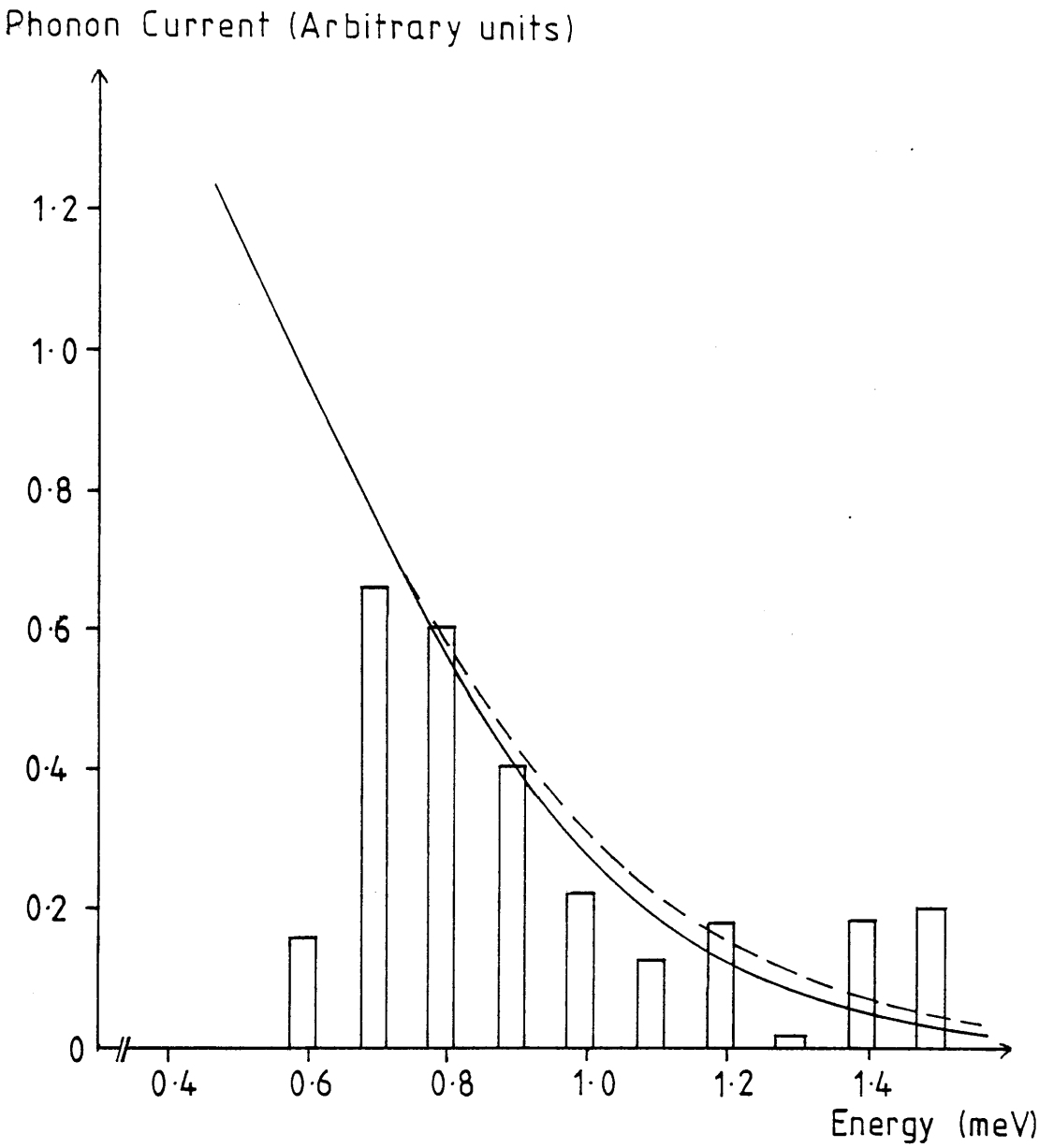

Figure 4.19 Phonon current versus energy measured from sample C16, transverse phonon signal. Input pulse duration=500ns, input pulse power=1.75mW.

– – – phonon current calculated from Little (1959),

——— corrected for junction time constant.

theoretical spectra predicted by Little (1959). It can be seen that the excess signals in the top channels were relatively larger than in sample C10. In this sample the excess signal cannot be explained using the theoretical signal at energies above the top channel. The excess signal was much larger than these theoretical signals. It is believed that this excess signal was derived mainly from the superconducting-normal contribution to the junction, as explained in section 4.3.

4.5 The output of the Sn-Sn superconducting junctions

As discussed in chapter 2 the output of the Sn-Sn superconducting junctions is within the energy range of the Al-PbBi detectors. Several attempts were made to measure this spectrum with very little success. Two sets of junctions had to be manufactured, generators and detectors and it proved very difficult to obtain a sample in which both sets of junctions were usable. Only sample C9 was a limited success; details of the junctions in this sample are listed in table 4.4. The current-voltage characteristics of the Sn-Sn junctions are shown in figure 4.20. There was some evidence of a conduction path in parallel with the junction. This was probably caused by holes in the oxide layer. The effect was small and could be neglected as it would not affect the phonon output of the junctions greatly. The Sn-Sn junctions had a large resistance, 0.5Ω, which meant that in order to obtain a suitable output a large voltage pulse was needed. In these conditions the junctions act as thermal sources and the spectrum is not necessarily dominated by the gap edge phonons. An attempt at the measurement was made, an output voltage pulse from the pulse generator of 1.20V and 500ns duration was applied to the generators and the spectrum shown in figure 4.21 was produced.

The effect of the detection system time constant has not been corrected for since the pulse was of 500ns duration this effect would be small. There was a large superconducting-normal current present in the detector therefore the signal at the highest energy was likely to have been much larger than that emitted by the generators. Due to this only a qualitative comparison with theory was made. The arrow in figure 4.21 indicates the energy of the 2 Δ phonons, 1.15meV, emitted by the Sn-Sn generators. There is a peak in the measured spectrum around this energy. However, the rest of the spectrum is negative and shows no evidence of the "bremsstrahlung" effect (section 2.3).

Generators

Tin thickness	
- lower electrode (nm)	200 ± 10
- upper electrode (nm)	200 ± 10
Junction normal resistance (Ω)	0.48 ± 0.01

Detectors

Aluminium thickness (nm)	100 ± 10
Lead bismuth thickness (nm)	200 ± 10
Junction normal resistance (mΩ)	30 ± 3
R_{SN}/R	600

Table 4.4

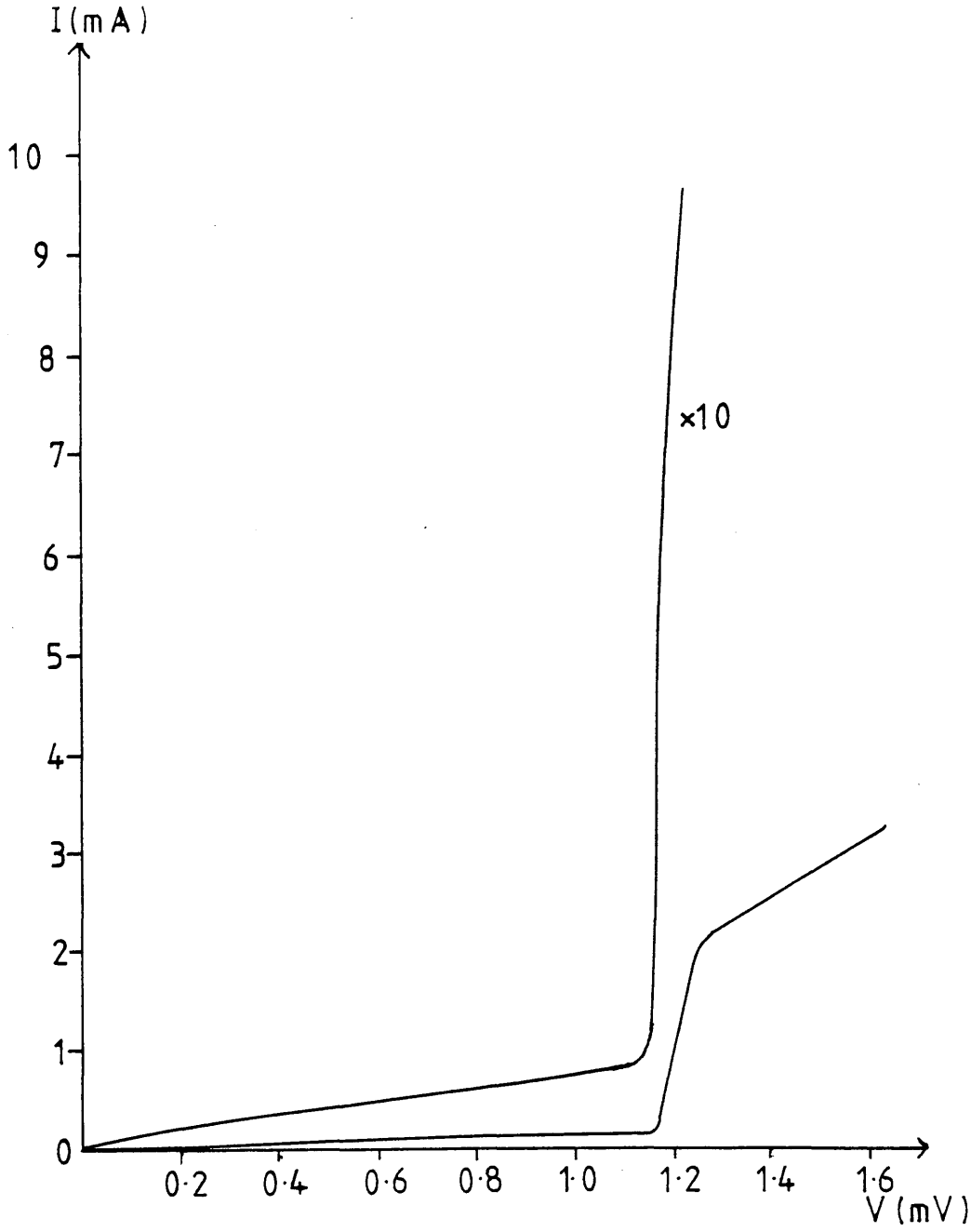

Figure 4.20 The d.c. characteristics of the phonon generators in sample C9.

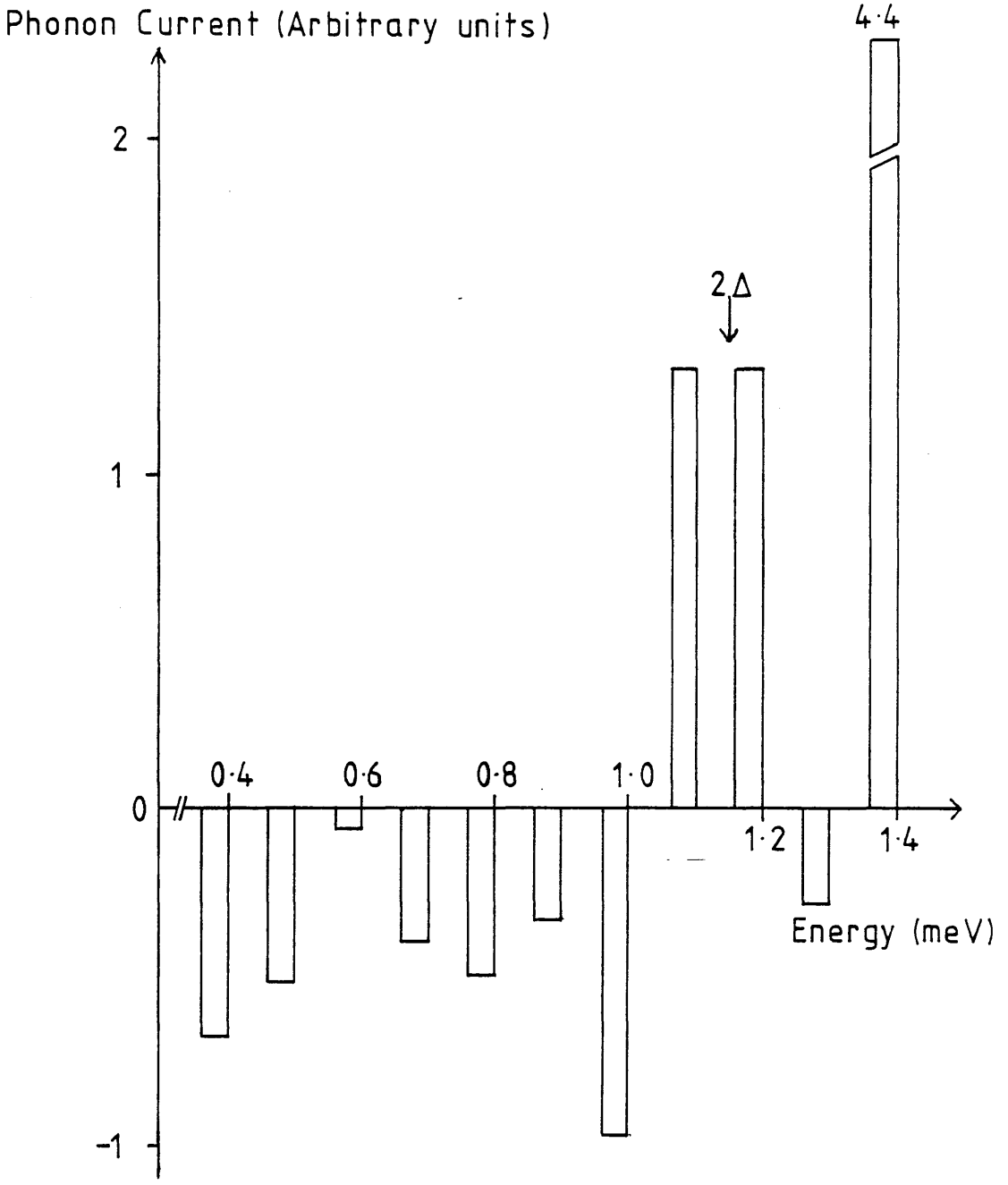

Figure 4.21 Phonon current versus energy measured from sample C9.

This experiment is of limited validity because of the poor quality of both the detectors and the generators. Also the possibility of self heating by the generators cannot be ignored. Ideally the experiment would have been repeated with better quality detectors and lower resistance generators, the output of which would be dominated by gap edge phonons, but the constraints of time prevented this.

5.1 Introduction

In this chapter the data from the measurements on the glasses are presented and analysed. The original phonon matrix analysis scheme was not used, despite the success with it reported in chapter4. There were two main reasons for this. Firstly, the detectors were almost always non-ideal. Secondly the matrix analysis scheme had an amplifying effect on the random error of the measurements (see chapter 4). For these reasons the analysis scheme was reversed. The expected signal current ratio from the detectors under the influence of theoretical phonon currents with and without the glassy film was calculated. For the detector side experiment the phonon currents as a function of energy reaching the detector side of the substrate were calculated from the acoustic mismatch theory. The phonon scattering in the glass was taken into account by calculating the probability of loss from a given energy band using simple physical models. (These models are discussed in sections 5.2 and 5.3.) From this the phonon current as a function of energy reaching the detector on top of the glass can be calculated. Applying the matrix analysis in reverse produces the enhanced tunnelling current as a function of bias voltage caused by such a phonon flux being absorbed by the detector. This calculation is performed for the phonon current with and without the glass. The ratio of the theoretical enhanced tunnelling currents can then be calculated and compared to the ratio of the measured enhanced tunnelling currents. For the generator side the phonon current as a function of energy reaching the detector side without travelling through the glass is again given by the acoustic mismatch theory. For the heater on top of the glass it has been assumed that phonons backscattered into the heater by the glass are reabsorbed by the heater. This has the effect of raising the effective heater temperature and changing the energy distribution of the emitted phonon current. This new energy distribution was calculated. (This is discussed in sections 5.2 and 5.3.) As in the detector side experiment the enhanced tunnelling currents as a function of bias in the detectors are calculated using the matrix analysis in reverse. The ratios of the theortical and measured enhanced tunnelling currents with and without the glass are compared.This analysis scheme is discussed in the fourth section of this chapter. Only the silicon dioxide data has been analysed fully using this scheme. The other two sets of data were unsuitable for this type of analysis for various reasons.

The experiment was designed to use a comparison technique. For this reason there were two heaters symmetrically disposed opposite two detectors as described in

chapter 3. There was a glass sample deposited under either one of the heaters or one of the detectors. This is shown in figure 5.1. It was decided to use the notation heater 1 and detector 1 for the heater and detector involved in the phonons travelling straight across the substrate without travelling through the glass film (path 1). Heater 2 and detector 2 are involved in the phonons travelling straight through the substrate and through the glass (path 2). The signal in path 2 could be compared with the unaffected signal in path 1, with only the influence of the glassy film being important. As before the cross shoot signal, paths 3 and 4, is not analysed because of the uncertainty of the orientation of the sapphire crystal and therefore the uncertainty in the possible phonon focussing effects. For this reason also the signal after the onset of the sidewall peak (see figure 4.5) in the straight through data is not analysed as phonons arriving after this have not travelled straight along the c-axis of the sapphire crystal. In general the two heaters in each sample had resistances which were within one percent of each other, typically. The detectors were also very similar, typically within 10%, needing only a small correction for differences in the junction resistances. The arsenic trisulphide samples were the only exception to this. They will be discussed in the last section of this chapter.

5.2 Elastic Scattering

The detector side experiment is considered first. It was decided to use a one dimensional model for simplicity. Moving through the amorphous film is a forward phonon flux, p, and a backward moving flux, q. It is assumed that, on average , the scattering events reverse the direction of travel of half the phonons, the direction of the other half remains unchanged. for this situation differential equations describing the steady state of p and q can be written

$$dp/dx = -p/2\ell + q/2\ell \qquad (5.1a)$$

$$dq/dx = p/2\ell + q/2\ell \qquad (5.1b)$$

where ℓ is the elastic mean free path of the phonons. The boundary conditions appropriate to the experiment are as follows. There is an incident initial phonon flux, p_o, from one side of the film, at x=0. There are no phonons incident from the

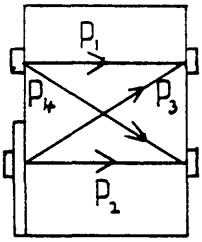

Figure 5.1 The possible paths between the heaters and the detectors.

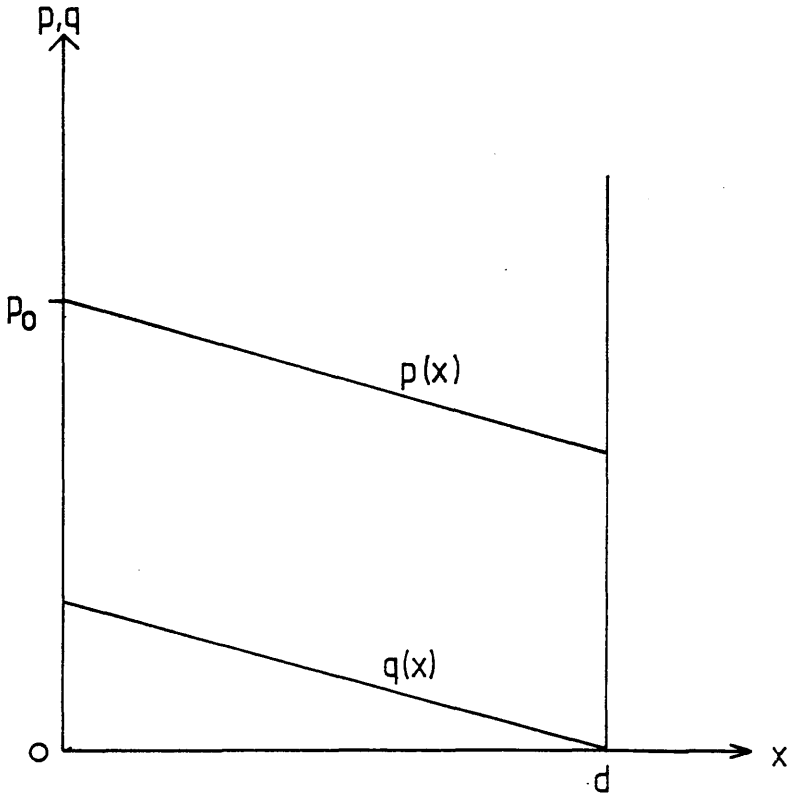

Figure 5.2 The variation of the forward moving phonon flux,p(x), and the backward flux, q(x). in an amorphous film of thickness d.

other side of the film, q(d) = 0 where d is the film thickness. This is because the detectors act as a sink for high energy phonons, absorbing the phonons incident upon them (Dietsche 1978). Under these circumstances the differential equations can be solved for the phonon fluxes transmitted through the film, p(d) and q(0),

$$p(d)/p_0 = 1/(1 + d/2\ell) \qquad (5.2a)$$

$$q(0)/p_0 = d/2\ell \,.\, (1 + d/2\ell)^{-1} \qquad (5.2b)$$

Note, $p(d) + q(0) = p_0$. There are no phonons lost in the material as expected for elastic scattering. This solution is shown in figure 5.2. q(0) is transmitted back into the sapphire substrate and is effectively lost. If it does reappear at the amorphous film it is at a much later time and is not measured.

This is not an exact solution to a complex situation, it is only an approximation. Strictly a three dimensional calculation should be performed. However, in this situation, it is difficult to do such a calculation. Very little is known about the angular distribution of the incident phonon flux. Whereas Davison (1957) shows that, for thermal neutrons, the fraction of incident flux penetrating a slab in which scattering occurs depends on the angular distribution of the incoming particles. So it is difficult to find an analytic solution. Davison solves the slab problem in the case of isotropic illumination over a half space. The solution looks like equations 5.2 but has a factor of 3/4 instead of 1/2. In the light of this it is felt that adopting the linear approximation (equations 5.2) is justified in this experiment. A more rigorous approach would not realise significantly more accurate results due to the error inherent in the experimental measurements. It must be remembered that any mean free path derived using this approximation will have an uncertainty of the same order of magnitude as the mean free path itself.

Two other assumptions have been made. Firstly, no distinction has been made between the scattering of the different polarisations. This is discussed later in this chapter along with the silicon dioxide data. Secondly, steady state solutions have been used. This assumes that the time the phonon pulse takes to cross the amorpous film is small compared to the exciting pulse length. It will be seen that this

assumption is justified when the data is discussed later in this chapter.

If there is only elastic scattering in an amorphous film then the different phonon energies are decoupled from one another. The energy of a phonon does not change when it is scattered. It is therefore simple to derive from equation 5.2a the phonon transmittance for the amorphous film as a function of energy, P(E), by writing :-

$$P(E) = p(d)/p_o = (1 + d/2\ell(E))^{-1} \qquad (5.3)$$

This is equivalent to the ratio of the phonon current absorbed by the detector on the top of the amorphous film to that absobed by the detector directly on top of the substrate, R(E). This ignores any difference in transmission coefficients between the two cases. However, the phonons being considered here have been transmitted along the c-axis of the sapphire. The phonons are incident perpendicular to the interfaces so the transmission coefficients are close to unity in both cases. Therefore this is a reasonable approximation. Figure 5.3 shows P(E) as a function of energy, for the different energy dependencies of the mean free path with the mean free path at 1meV being equal to 2.2μm and a sample thickness of 0.91μm. Above 1meV the higher the energy dependence the faster P(E) decreases with energy , as expected. The dependence of P(E) on the magnitude of the mean free path at 1meV is shown in figure 5.4 for $\ell \propto E^{-4}$. As the mean free path increases P(E) increases and becomes a much weaker function of energy.

The situation on the generator side is more complex. The analysis scheme has been developed specifically for the thin film heaters used in this project. In chapter 4 it was shown that these heaters emitted the broad band spectrum predicted by Little (1959). According to this theory the output power of the heaters per unit area, W/A, is given by:-

$$W/A = 1/(8\pi^2\hbar^2).\{\Sigma\alpha_i/c_i^2\}.\int_o^\infty E^3 dE/(\exp(E/kT_1) - 1) \qquad (5.4)$$

where α_i are the transmission coefficients for the phonons of polarisation i from the emitting film into the substrate. Since the scattering model does not take into account the different phonon polarisations the term involving the transmission

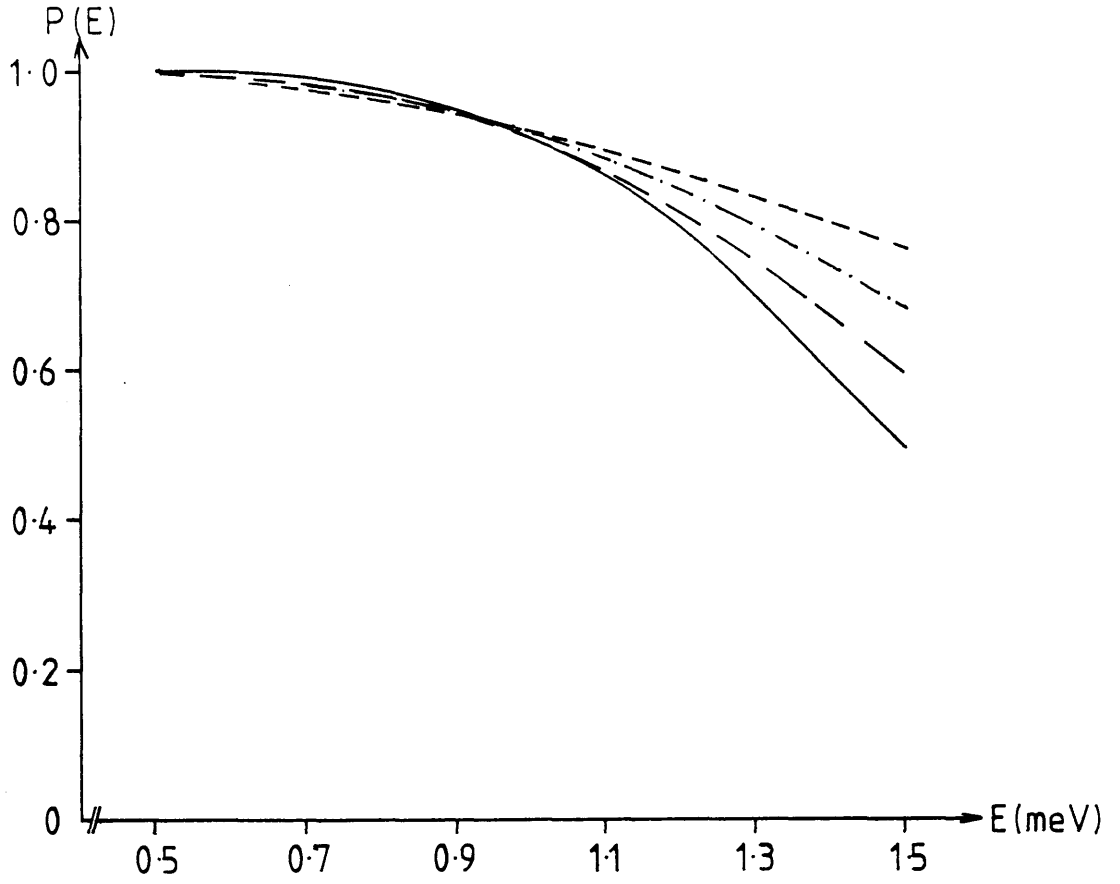

Figure 5.3 Graph of P(E) over the energy range of our detectors for elastic scattering. The mean free path at 1meV being 2.2μm, d=0.39μm.

——— $\ell \propto E^{-6}$

— — $\ell \propto E^{-5}$

– · – · – $\ell \propto E^{-4}$

– – – – $\ell \propto E^{-3}$

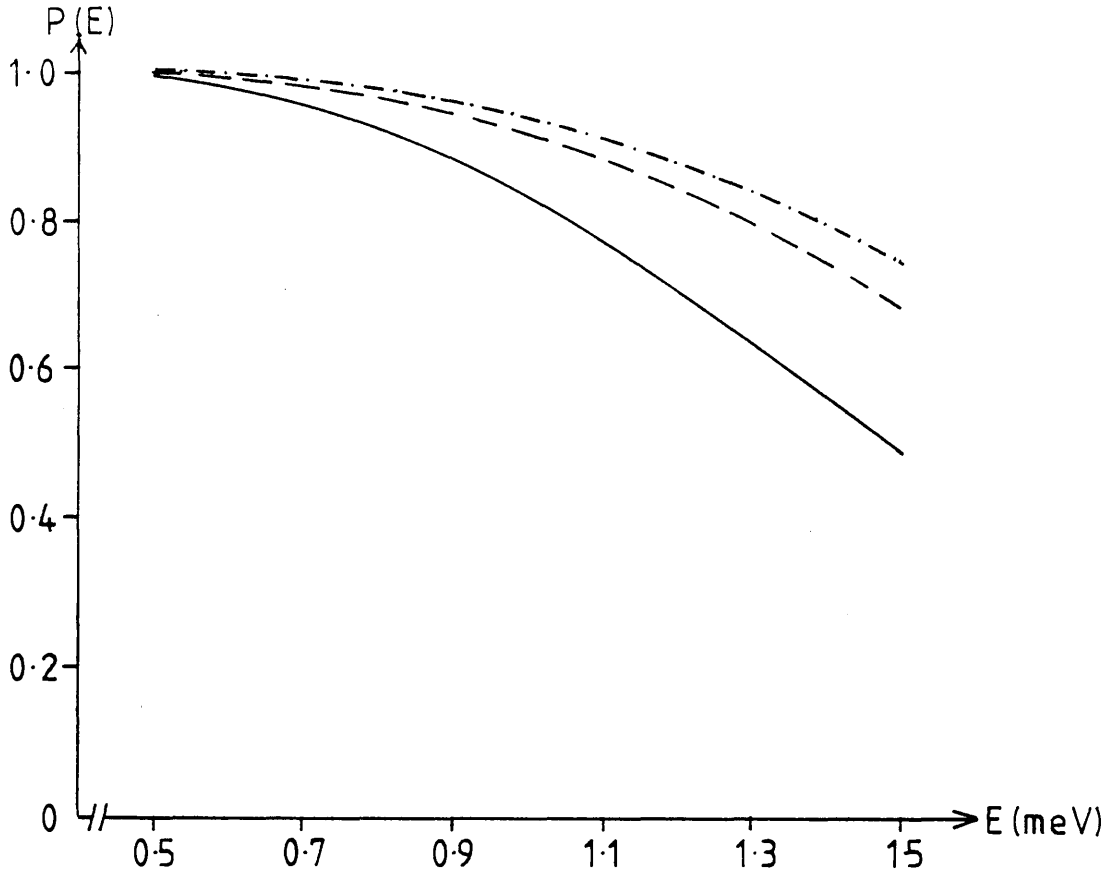

Figure 5.4 Graph of P(E) over the energy range of our detectors for elastic scattering. $\ell \propto E^{-4}$, d=0.39μm.

——— ℓ(1meV)=1.0μm

— — — ℓ(1meV)=2.2μm

—·—·— ℓ(1meV)=3.0μm

coefficients and the phonon velocities is simplified using :-

$$\Sigma \quad \alpha_i/c_i^2 \;=\; 3\bar{\alpha}/\bar{c}^2 \qquad (5.5)$$

where $\bar{\alpha} = 0.18$ and $\bar{c} = 3.05$ kms^{-1} for constantan on sapphire (Weis 1972).

When there is a thin film of glass on top of the heater some of the phonons are backscattered into the heater. If the same assumptions are made as when deriving the phonon output of the heaters, that the heaters are thick, then these phonons are reabsorbed. Thus the effective heater temperature increases. The phonons that reach the other side of the glass are transmitted into the substrate and effectively lost to the generator side. So the boundary conditions used in the elastic scattering model can be applied. Therefore, the calculation for the elastic scattering model can be used. The transmission coefficient, $\bar{\alpha}$, is modified to $\bar{\alpha}P$. Using this in equation 5.4 and taking into account that P is a function of energy gives :-

$$W/A \;=\; 3/(8\pi^2\hbar^3).\bar{\alpha}/\bar{c}^2\int_0^\infty P(E)E^3dE/(\exp(E/kT_2) - 1) \qquad (5.6)$$

where T_2 is the increased effective heater temperature. It must be remembered that, again, this does not take into account the scattering at the different film interfaces. To do this the angular distribution of the phonons in the amorphous film would need to be known. The same power was put into the heater in both cases, with and without the glass on top of the heater. So the same power must be transmitted into the sapphire substrate in both cases since there is no other escape path for the phonons. By equating the right sides of equations 5.4 and 5.6 this condition is taken into account. Evaluating the integrals produces T_2/T_1.

The phonon current from the heater without the glass is :-

$$n_{wo}(E) \;=\; A \,.\, E^2 \,/\, (\exp(E/kT_1) - 1) \qquad (5.7)$$

where A is a constant. The phonon current from the heater and the glass is given by

$$n_w(E) = A \cdot P(E)\, E^2 / (\exp(E/kT_2) - 1) \qquad (5.8)$$

Combining these two equations gives the transmission ratio

$$R(E) = P(E) \cdot (\exp(E/kT_1) - 1)/(\exp(E/kT_2) - 1) \qquad (5.9)$$

Assuming that the phonons propagate to the detectors and are absorbed there in the same manner, this is the ratio of the phonon currents absorbed by the two detectors.

Figure 5.5 shows the transmission ratio as a function of energy for elastic scattering in the generator side experiment with a sample of thickness 0.49μm. The mean free path at 1meV used in the calculations was 2.2μm and the energy dependence was varied as stated. It can be seen that the transmission ratio is greater than one at low energies. In the model the high energy phonons are more likely to be backsattered into the heater than the low energy phonons. So the low energy phonon current is enhanced resulting in a transmission ratio which is greater than one. The stronger the scattering the greater this enhancement. This is reflected in a greater low energy transmission ratio when the mean free path is a stronger function of energy. As in the detector side calculation R decreases more rapidly with energy when the scattering is stronger. The effect of varying the magnitude of the mean free path on R(E) is shown in figure 5.6. The smaller the mean free path the stronger the scattering. So R is larger at lower energies for the shorter mean free path and decreases faster with increasing energy.

5.3 Inelastic Scattering

The situation for inelastic scattering is more complex than that for elastic scattering. The most important process for a high energy phonon is the spontaneous process which splits it up into two phonons of lower energy. The energy of the two secondary phonons is determined by the scattering mechanism. In this case the scattering mechanism is unknown. The approximation is made that the incident phonon is split into two phonons of energy equal to half that of the incident phonon. Again this approximation does not give an exact answer but tells us what form of transmission ratio to expect. It is also assumed that one phonon is scattered forward

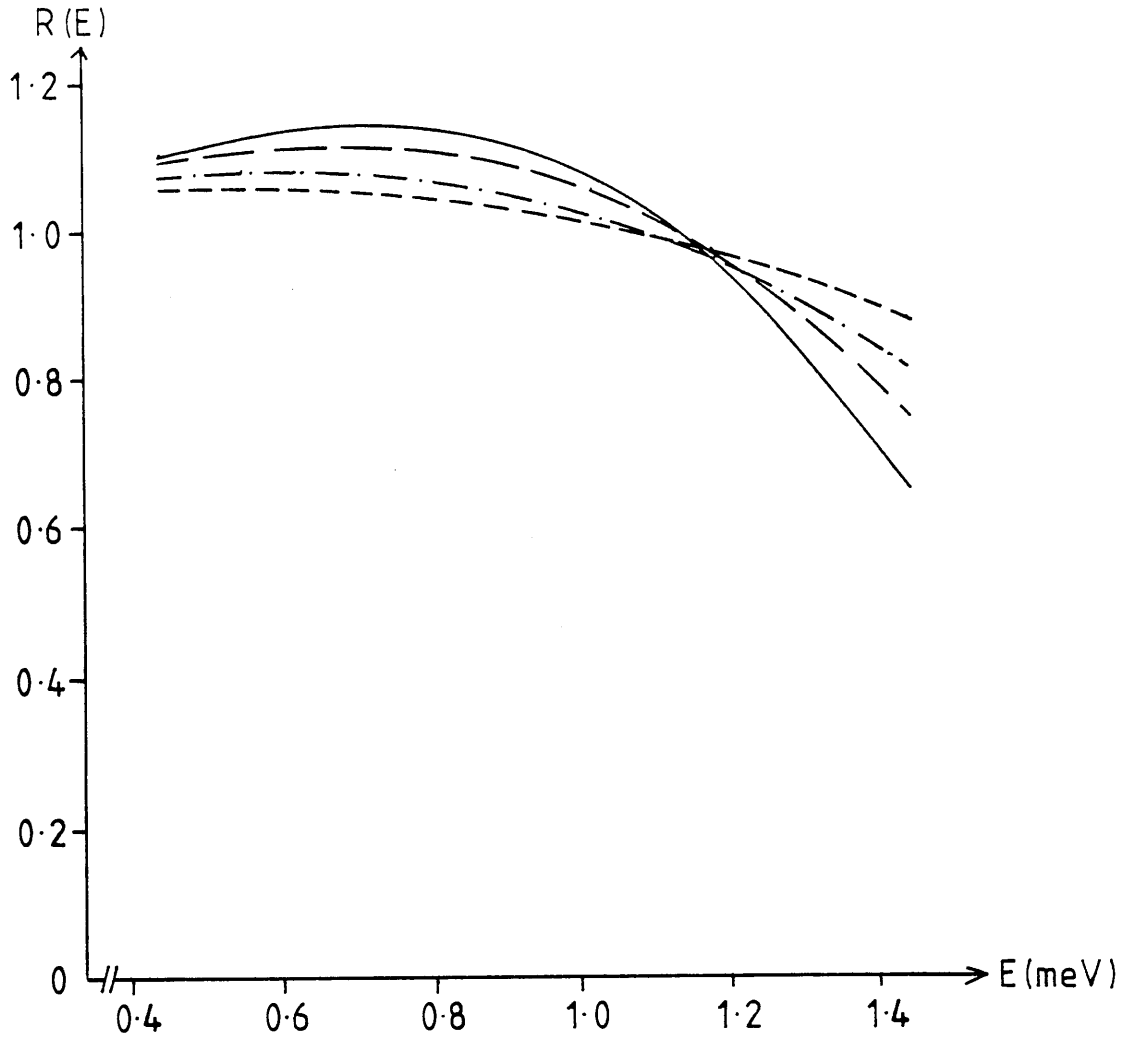

Figure 5.5 The transmission ratio as a function of energy for the generator side experiment with elastic scattering. d=0.49μm, ℓ (1meV)= 2.2μm.

——— $\ell \propto E^{-6}$

— — $\ell \propto E^{-5}$

— · — · — $\ell \propto E^{-4}$

— — — — $\ell \propto E^{-3}$

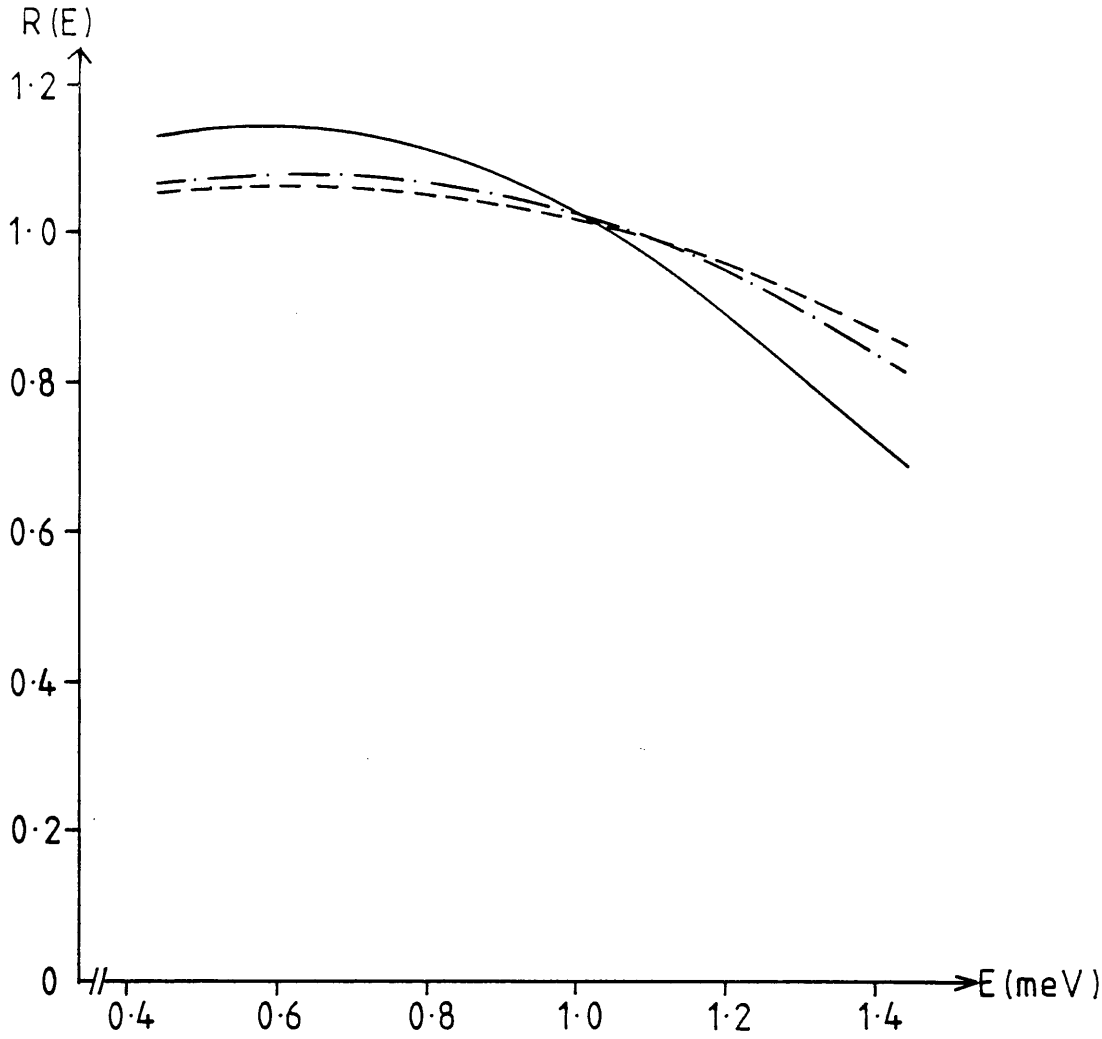

Figure 5.6 The transmission ratio as a function of energy for the generator side experiment with elastic scattering. d=0.49μm, $\ell \propto E^{-4}$.

——— ℓ(1meV)=1.0μm

—·—·— ℓ(1meV)=2.2μm

— — — — ℓ(1meV)=3.0μm

and one backward. Scattering of the secondary phonon is neglected since the scattering mean free path is a strongly decreasing function of energy and thin glass films are being considered. So the mean free path of the secondary phonon is large compared to the film thickness. Also ignored is the possibility of two low energy phonons combining to give a higher energy phonon, i.e. inverse three phonon processes. This model is of limited use. It would be no good if strong inelastic scattering were occuring throughout the whole energy range. It is only useful for the high energy tail of a spectrum such as that found in this experiment. In these circumstances it is expected to give a good guide to the behaviour of the transmission ratio.

As in the elastic scattering case there is a phonon flux with a thermal distribution characterised by T_1 incident on one side of the glass. For random inelastic scattering the proportion of phonons penetrating a slab of material of thickness d is $\exp(-d/\ell(E))$. It is necessary to take into account that the phonons of energy 2E are scattered to energy E and that half are scattered forwards and half backwards. So the phonons emerging from the other side of the material have an energy distribution :-

$$\exp(-d/\ell(E)) \cdot E^2 / (\exp(E/kT_1) - 1) + (1-\exp(-d/\ell(2E))) \cdot (2E)^2 / (\exp(2E/kT_1)-1) \qquad (5.10)$$

The first term represents the phonons of energy E which pass through the material without being scattered. The second term represents the phonons of energy 2E that are scattered down to energy E and continue through the material in the forward direction. Dividing 5.10 by the input phonon flux produces the transmission ratio, R(E) :-

$$R(E) = \exp(-d/\ell(E)) + (1 - \exp(-d/\ell(2E))) \cdot 4 \cdot (\exp(E/kT_1)-1)/(\exp(2E/kT_1)-1) \qquad (5.11)$$

Figure 5.7 shows the calculated form of R(E) for different energy dependencies of the mean free path. In all cases, at low energies the transmission ratio increases to a peak which is greater than one. This is due to more phonons being scattered from energy 2E to energy E than being scattered from E to E/2. The higher the energy

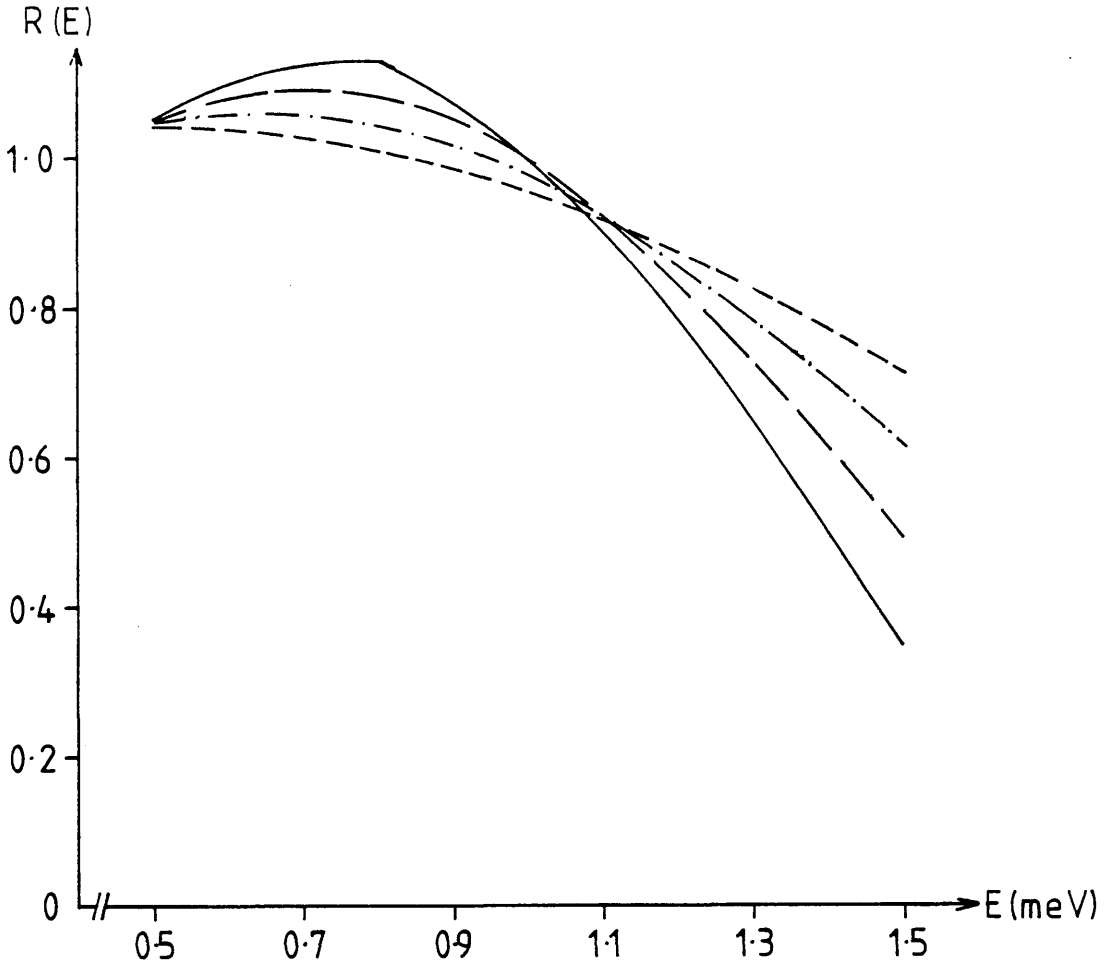

Figure 5.7 The transmission ratio, R(E), as a function of energy for inelastic scattering. d=0.39μm, ℓ (1meV)= 4.0μm.

———— $\ell \alpha E^{-6}$

—— —— $\ell \alpha E^{-5}$

—·—·— $\ell \alpha E^{-4}$

— — — — $\ell \alpha E^{-3}$

dependence of the mean free path the more pronounced is this peak and the faster the transmission ratio decreases with increasing energy. Figure 5.8 is a graph of the transmission ratio where ℓ is proportional to E^{-4} for various values of ℓ at 1meV.The smaller the value of ℓ at 1meV the larger the low energy value of the transmission ratio and the faster it decreases with energy.

For the generator side experiment the same assumptions are made as in the elastic case. Namely that the phonons which are transmitted through the glass into the substrate are lost to the heater side and those phonons which are backscattered are absorbed by the heater and change the heater temperature. For the phonons of energy E the proportion of their energy which is transmitted through the glass into the substrate is give by :-

$$P(E) = \exp(-d/\ell(E)) + 1/2(\ 1 - \exp\ (-d/\ell(E)) \qquad (5.12)$$

The first term is due to those phonons that travel through the glass without being scattered. The second term is due to the scattered phonons and takes into account that on scattering half the energy goes forward and half goes backward. Using this form of P(E) in equation 5.6 allows the raised effective heater temperature, T_2, to be calculated. R(E) is then given by :-

$$R(E) = \exp(-d/\ell(E)) \ .\ (\exp(E/kT_1)-1)/(\exp(E/kT_2)-1) + (1-\exp(-d/\ell(2E))).4.(\exp(E/kT_1)-1)/(\exp(E/kT_2)-1) \qquad (5.13)$$

Figure 5.9 shows R(E) for ℓ=4.0μm at 1meV with different energy dependencies of the mean free path. At low energies the transmission ratio is greater than one and is largest for the strong scattering. As the energy increases the stronger the scattering the faster the decrease in the transmssion ratio. Figure 5.10 shows the dependence of the transmission ratio on the magnitude of the mean free path. The shorter the mean free path the stronger the scattering is. This produces a larger transmission ratio at low energy compared to the weaker scattering plus a more rapid decrease of the transmission ratio as energy increases.

So far it has been assumed that the secondary phonons have no correlation with the

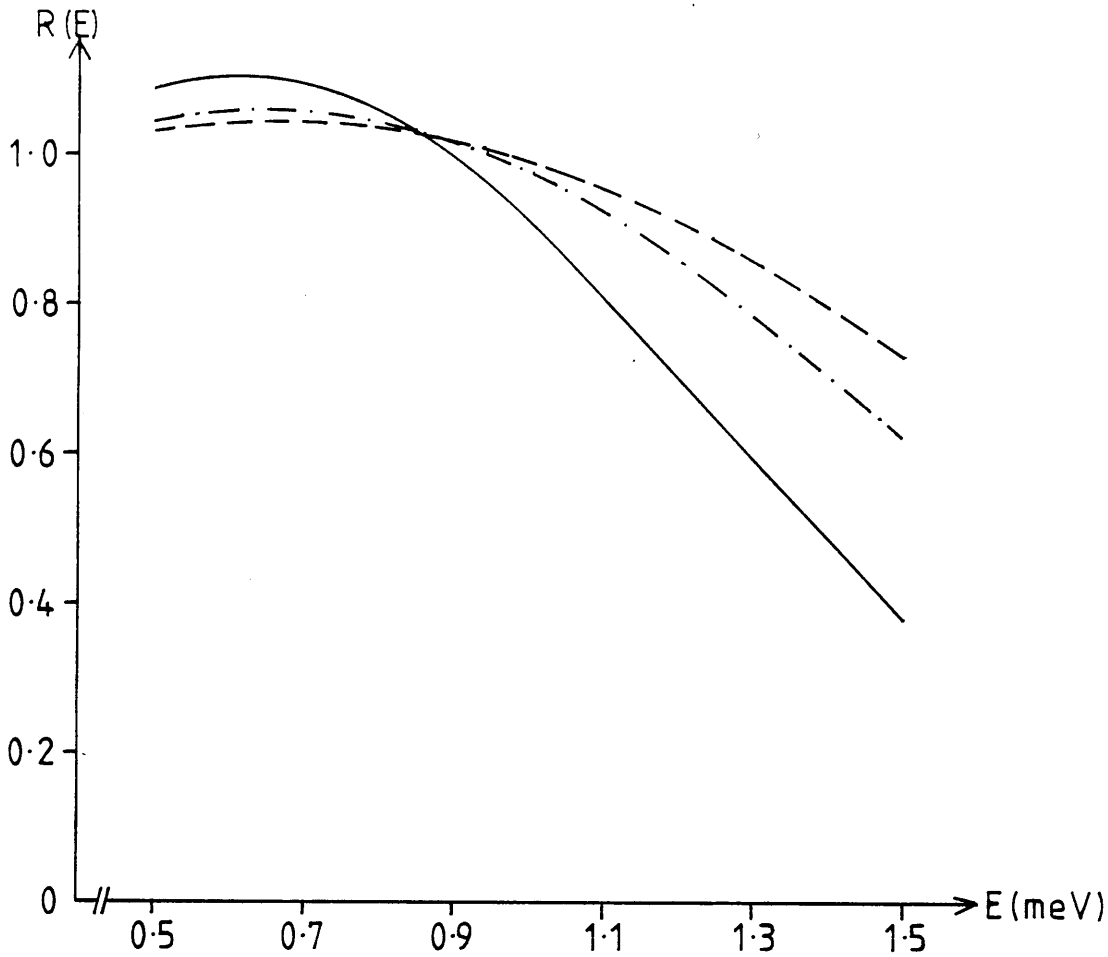

Figure 5.8 The transmission ratio, R(E), as a function of energy for inelastic scattering. d=0.39μm, $\ell \propto E^{-4}$.

——— ℓ(1meV)=2.0μm

— · — · – ℓ(1meV)=4.0μm

— — — - ℓ(1meV)=6.0μm

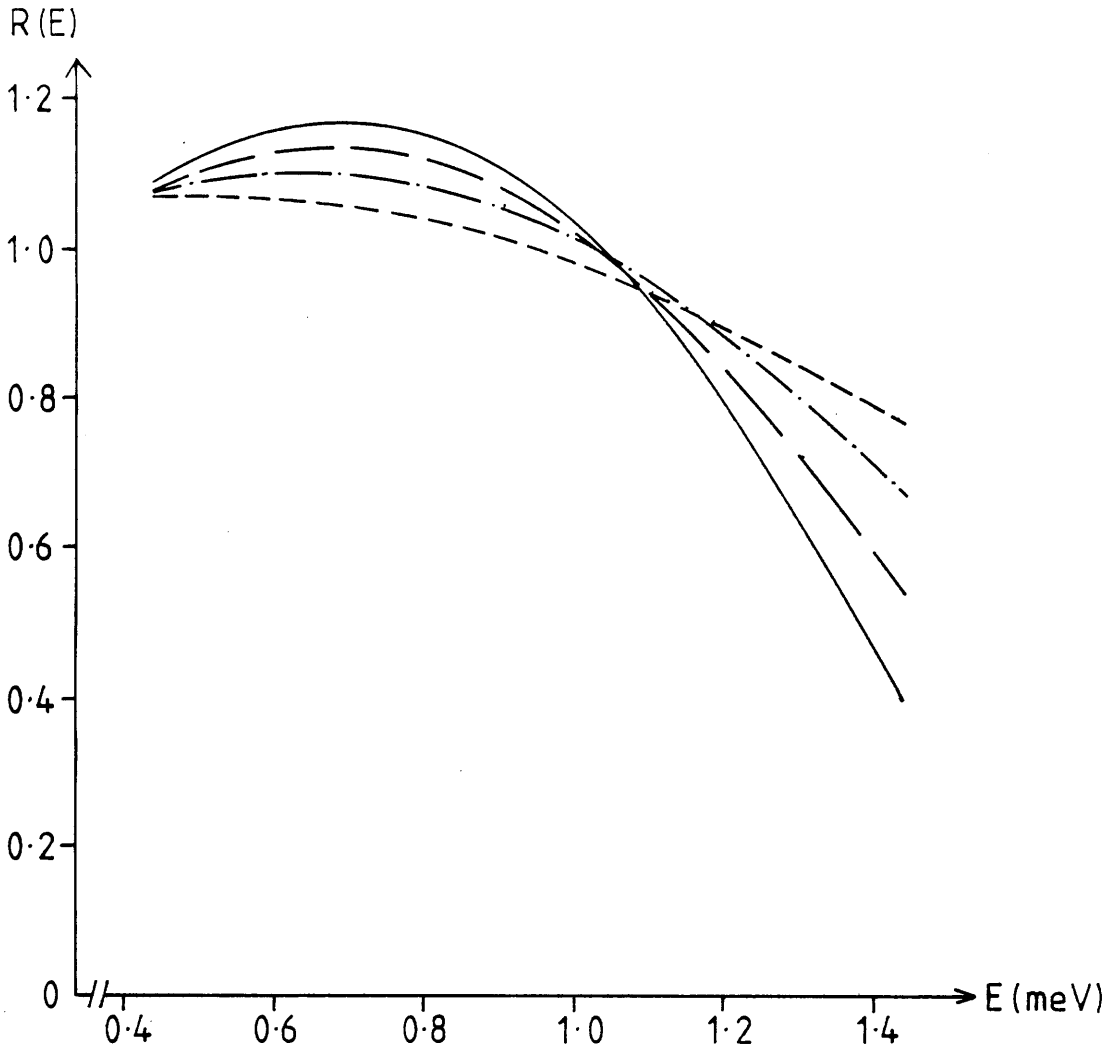

Figure 5.9 The transmission ratio, R(E), as a function of energy for inelastic scattering in the generator side experiment. d=0.49μm, ℓ = 4.0μm. at 1meV.

——— $\ell \propto E^{-6}$

— — $\ell \propto E^{-5}$

— · — · – $\ell \propto E^{-4}$

— — — — $\ell \propto E^{-3}$

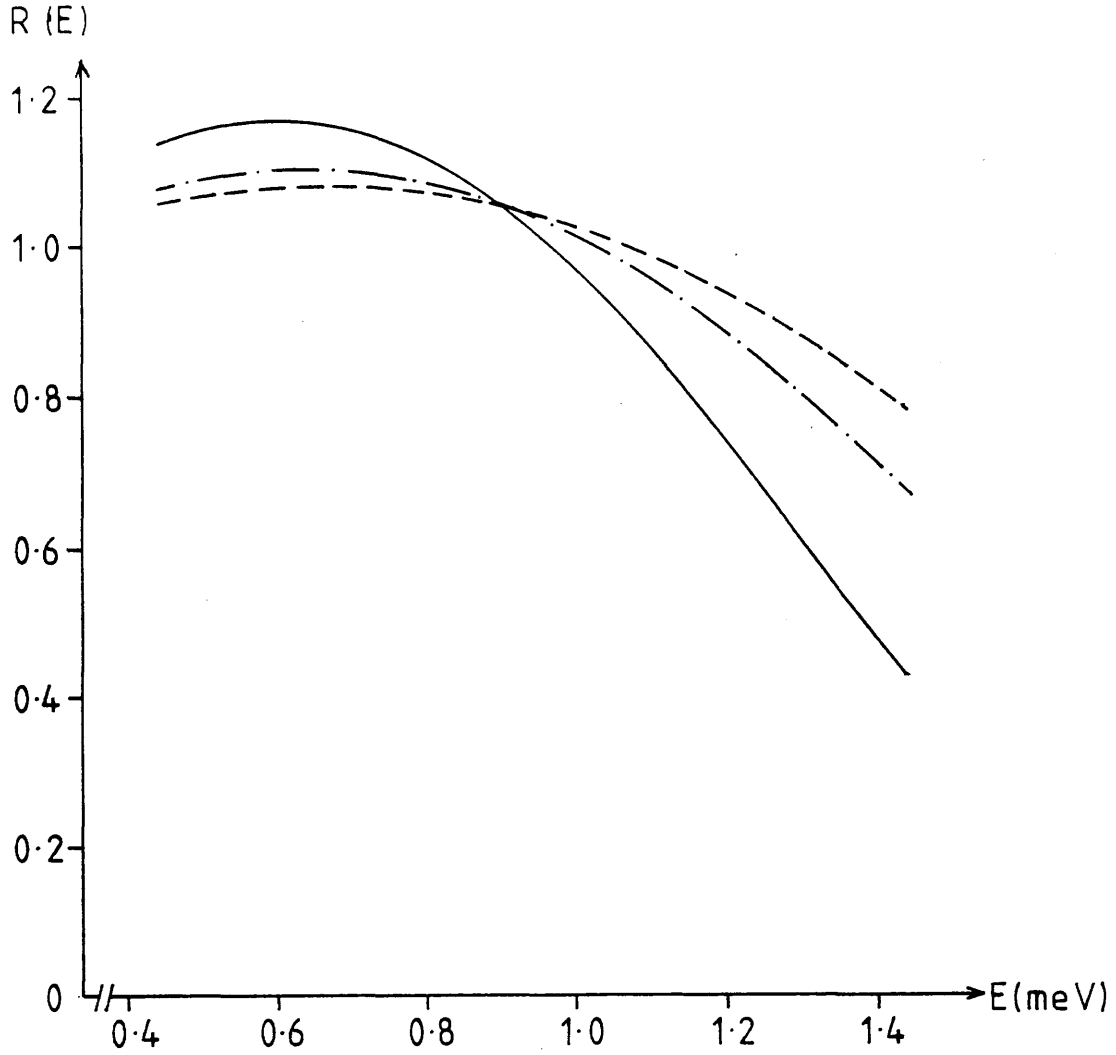

Figure 5.10 The transmission ratio, R(E), as a function of energy for inelastic scattering in the generator side experiment. d=0.49μm, $\ell \propto E^{-4}$.

——— ℓ(1meV)=2.0μm

— · — · — ℓ(1meV)=4.0μm

– – – – ℓ(1meV)=6.0μm

primary phonons. Although the wave vector is not an accurately defined parameter in a disordered material, at these frequencies the waves are expected to be close to plane waves. For a 3-phonon anharmonic process in a crystal the wave vector is conserved and the direction of the secondary phonons are correlated with that of the primary. It is possible to envisage a similar scattering process in an amorphous film in which case the energy composition of the phonon flux is affected but not its direction of propagation. The effect on the detector side experiment is to increase the second term of equation 5.11 by a factor of two. From figure 5.11 it can be seen that this produces an enhanced peak in the transmission ratio. In the generator side experiment there are no phonons backscattered into the heater. So the effective heater temperature is not increased, it remains at T_1. Putting this into equation 5.13 and increasing the second term by a factor of two produces a transmission ratio identical to that for the detector side under these conditions. So the generator side transmission ratio has the form shown in figure 5.11.

5.4 The Modified Matrix Analysis Scheme

In the previous two sections of this chapter the transmission ratio has been calculated for both elastic and inelastic scattering. This could be directly compared to the transmission ratio calculated from the phonon currents obtained from the experimental data using the matrix analysis scheme. However, as previously discussed, the matrix analysis increases the error in the measurements by a factor of approximately 4. Therefore any transmission ratios calculated from the data are subject to large errors. This renders the experimentally measured transmission ratio difficult to interpret. For this reason it was decided to use the ratio of the electron current signals from the detectors, S.

In chapter 4 the phonon output of the heaters was established. The phonon current from the heater at discrete energies can be calculated. By multiplying these values by a calculated transmission ratio for the particular energy the possible phonon current of that energy emerging from the glass can be produced. These phonon currents can then be used to calculate the electron currents through tunnelling junctions absorbing such phonon fluxes using equation (2.25)

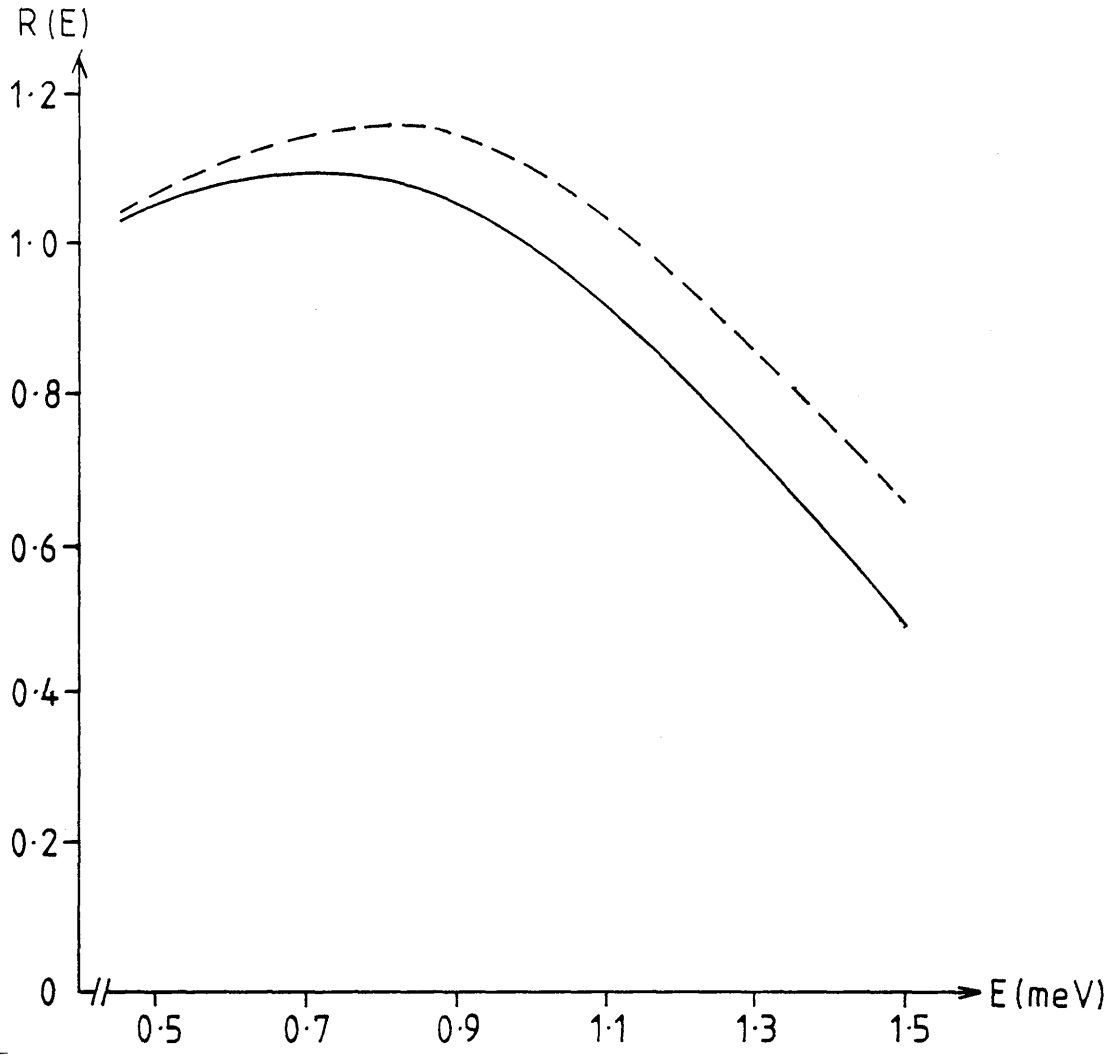

Figure 5.11 The transmission ratio, R(E), as a function of energy for inelastic scattering. $\ell=4.0\ E^{-5}\mu m$, $d=0.39\mu m$.

——— one phonon scattered forward per scattering event

— — — two phonons scattered forward per scattering event

$$\Delta I(\Omega_{oi}) = \Sigma_{j=1} {}^{i}\Lambda_{ij} I_{pj} \qquad (2.25)$$

From these the theoretical values of the current signal ratio, S, can be obtained as a function of bias.

As discussed in chapter 2 the electron current in the junctions at a particular bias, V_B, is determined by the phonons with energies from $\Delta_1 + \Delta_2 - V_B$ upwards. So the current signal ratio, S, has contributions from energies corresponding to the bias voltage upwards. At a particular bias the higher energy contributions have the effect of reducing the current signal ratio in comparison to the transmission ratio. This can be seen from figure 5.12 which shows both the transmission ratio and the current signal ratio for elastic scattering with a mean free path at 1meV of 2.2μm and varying as E^{-6}. At the highest energy they have the same value but at lower energies the current signal ratio is smaller.

5.5 The silicon dioxide data

Three different silicon dioxide samples were successfully prepared. For two of them, samples C13 and C16, the glass was on the detector side of the sapphire crystal. In the third, sample C12, the glass was under one of the heaters. The details of these samples are shown in table 5.1.

Figure 5.13 shows the voltage signal as a function of time for sample C16. The top trace shows the signal without the glass between the heater and the detector. The lower trace shows the signal with the glass. As can be seen the pulse shapes of the two traces are similar, therefore no discernible time delay was caused by the glass. This allows the application of the analysis procedure developed earlier in this chapter.

Figure 5.14 shows the current signal ratio data as a function of time, calculated from the data shown in figure 5.13. The points before the longitudinal phonon pulse have been omitted since these are mainly due to noise and fluctuate wildly. The onset of the various ballistic peaks are marked on the figure. The

Sample number	C12	C13	C16
Sample thickness (μm)	0.49 ± 0.01	0.39 ± 0.005	0.91 ± 0.01
Resistance of detector 1 (mΩ) (R_1)	1.9 ± 0.2	30 ± 3	11 ± 1
R_2/R_1	0.95 ± 0.01	0.83 ± 0.01	0.68 ± 0.01
R_{SN}/R_{SS}	10^4	200	7000
Heater resistance (Ω)	55.0	14.3	24.0

TABLE 5.1 The silicon dioxide samples.

Sample number	C10
Sample thickness (μm)	0.59 ± 0.01
Resistance of detector 1 (mΩ) (R_1)	32 ± 3
R_2/R_1	1.08 ±0.01
R_{SN}/R_{SS}	$>10^5$
Heater resistance (Ω)	17.6

TABLE 5.2 The silicon monoxide sample.

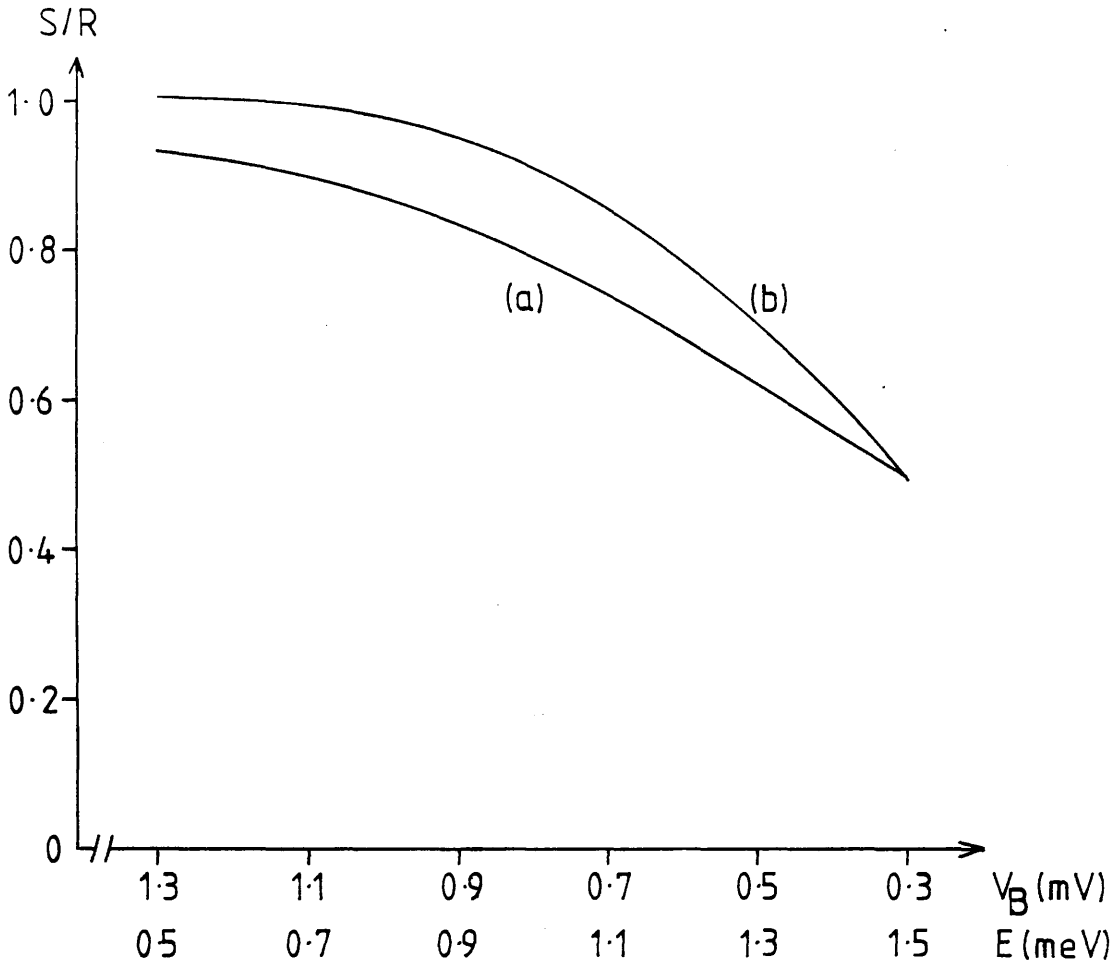

Figure 5.12 (a) S and (b) R calculated for a sample of thickness 0.39μm and a mean free path of $2.2E^{-6}$μm and elastic scattering.

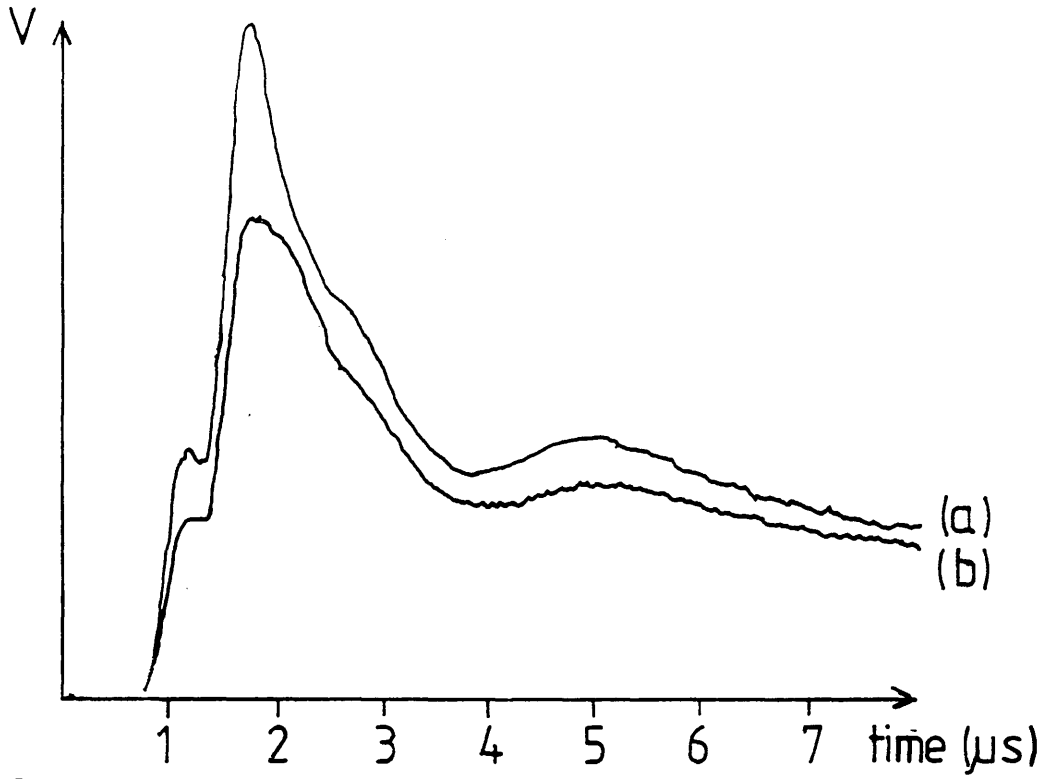

Figure 5.13 Sample C16 voltage signal as a function of time for an input power of 5.53mW and bias voltage of 1.0mV. (a) without and (b) with the glassy film.

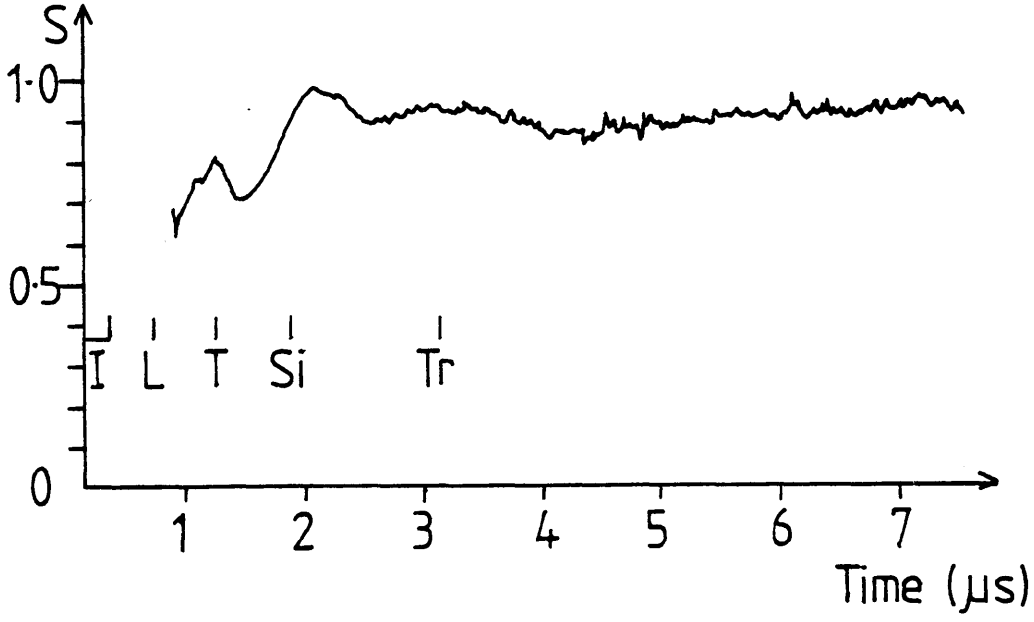

Figure 5.14 The transmittance as a function of time for the data shown in figure 5.13.

I - initiating pulse, arrival of longitudinal phonons - L, transverse phonons - T, phonons reflected from the sidewall - Si, triple reflection phonons -Tr.

transmittance remains relatively constant over the longitudinal and transverse peaks. This allows the calculation of the current signal ratio for the longitudinal and transverse phonon fluxes. After the multiple reflection signal it tends to unity indicating that the junctions are acting as thermometers monitoring the background temperature of the crystal.

For the quantitative analysis it was decided to concentrate on the transverse phonon ballistic peak. This was the largest signal and therefore could be analysed with the greatest accuracy. The current signal ratio was averaged over the transverse peak. The position of this peak was determined from the measured data as shown in figure 5.13. The experimental values of the current signal ratio were then compared to the theoretically calculated form. In the following figures the expermental values of the current signal ratio, S, are displayed as bars and the theoretical values are shown as curves.

The detector side experiment is considered first. In figure 5.15 the values of S calculated for the data from samples C13 and C16 are shown. Superimposed on these values are the theoretical curves for a mean free path of 1.0μm at 1 meV varying as E^{-4} , 2.2μm varying as E^{-6}. It can be seen that the stronger energy dependence fits the data better than the Rayleigh type (E^{-4}) scattering. However, it was found that the index does not need to be exactly -6. This can be seen in figure 5.16 which shows that E^{-5} and E^{-7} could also fit the data within experimental error. Therefore any value around -6 will do just as well. From figure 5.17 it can be seen that a mean free path at 1meV between 1.5μm and 3.0μm give a reasonable fit to the data. This justifies the use of the simple model in the analysis since a more sophisticated model could not produce greater accuracy about the form of the scattering because of the error in the experimental measurements. So far only the highest heater input power data has been considered. The lower power data is more difficult to analyse since the signal is smaller and, therefore, more inaccurate. This is demonstrated in figure 5.18 which shows the exprimental values of S for sample C16 at lower input powers. It can be seen that at low biases that S is larger than the theoretically calculated value. This is due to the signal being so small that it is dominated by the superconducting-normal current. The ratio of these effects between the junctions is approximately one and therefore they lead to an artificially high value of S. At higher biases the data fits the E^{-6} scattering with a mean free path of 2.2μm at 1meV as before. At these biases the signal is larger and the effect of the

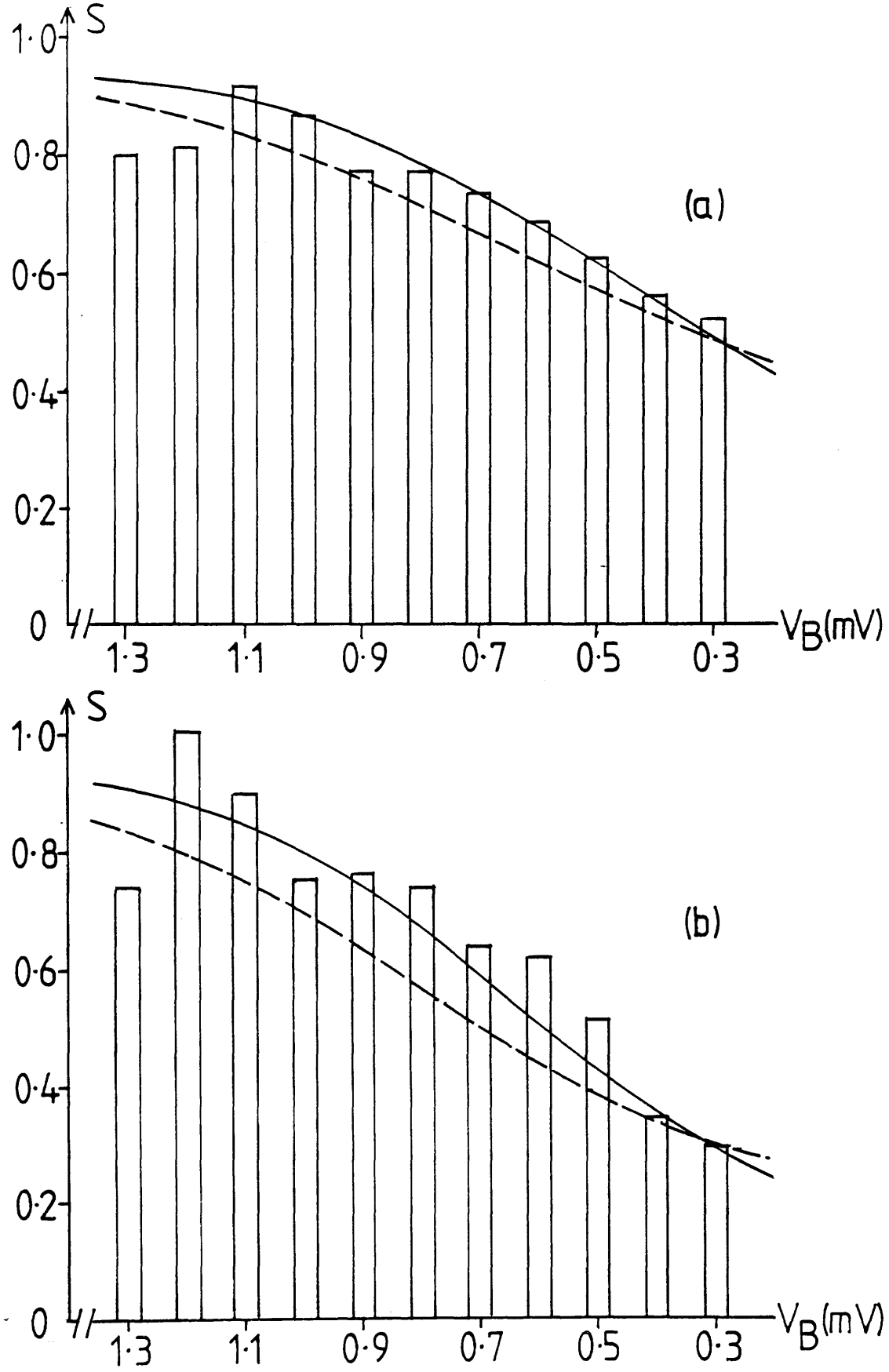

Figure 5.15 The transmittance for (a)C13, p=13.8mW, and (b)C16, p=5.53mW. The theoretical values were calculated for elastic mean free paths of ———— $2.2E^{-6}\mu m$ and — — — $1.0E^{-4}\mu m$.

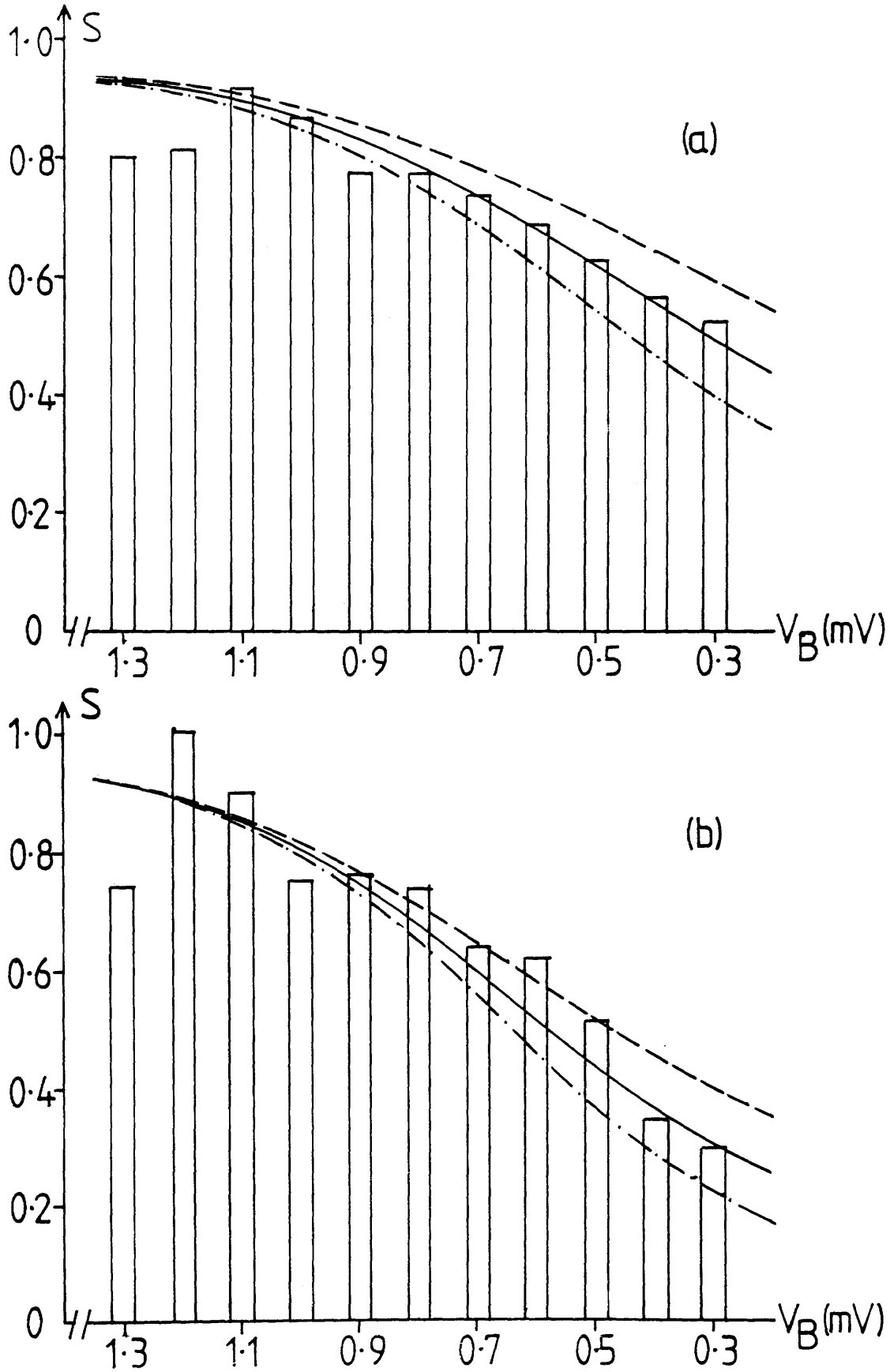

Figure 5.16 The transmittance for (a)C13, p=13.8mW, and (b)C16, p=5.53mW. The theoretical values were calculated for elastic mean free paths of — — — $2.2E^{-5}\mu m$ ——— $2.2E^{-6}\mu m$ — · — · — $2.2E^{-7}\mu m$

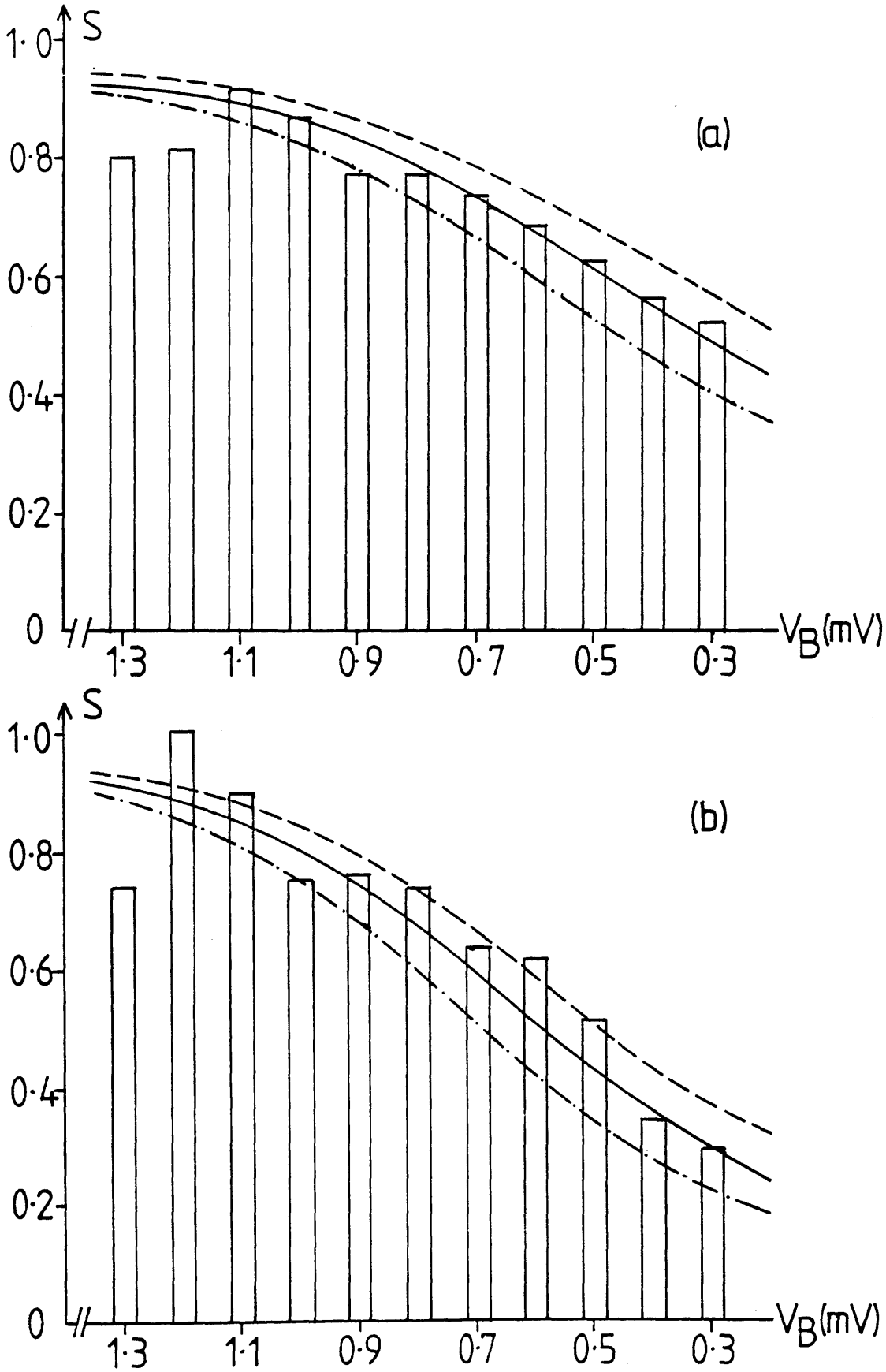

Figure 5.17 The transmittance for (a)C13, p=13.8mW, and (b)C16, p=5.53mW. The theoretical values were calculated for elastic mean free paths of
– · – · – $1.5E^{-6}\mu m$ ——— $2.2E^{-6}\mu m$ – – – $3.0E^{-6}\mu m$

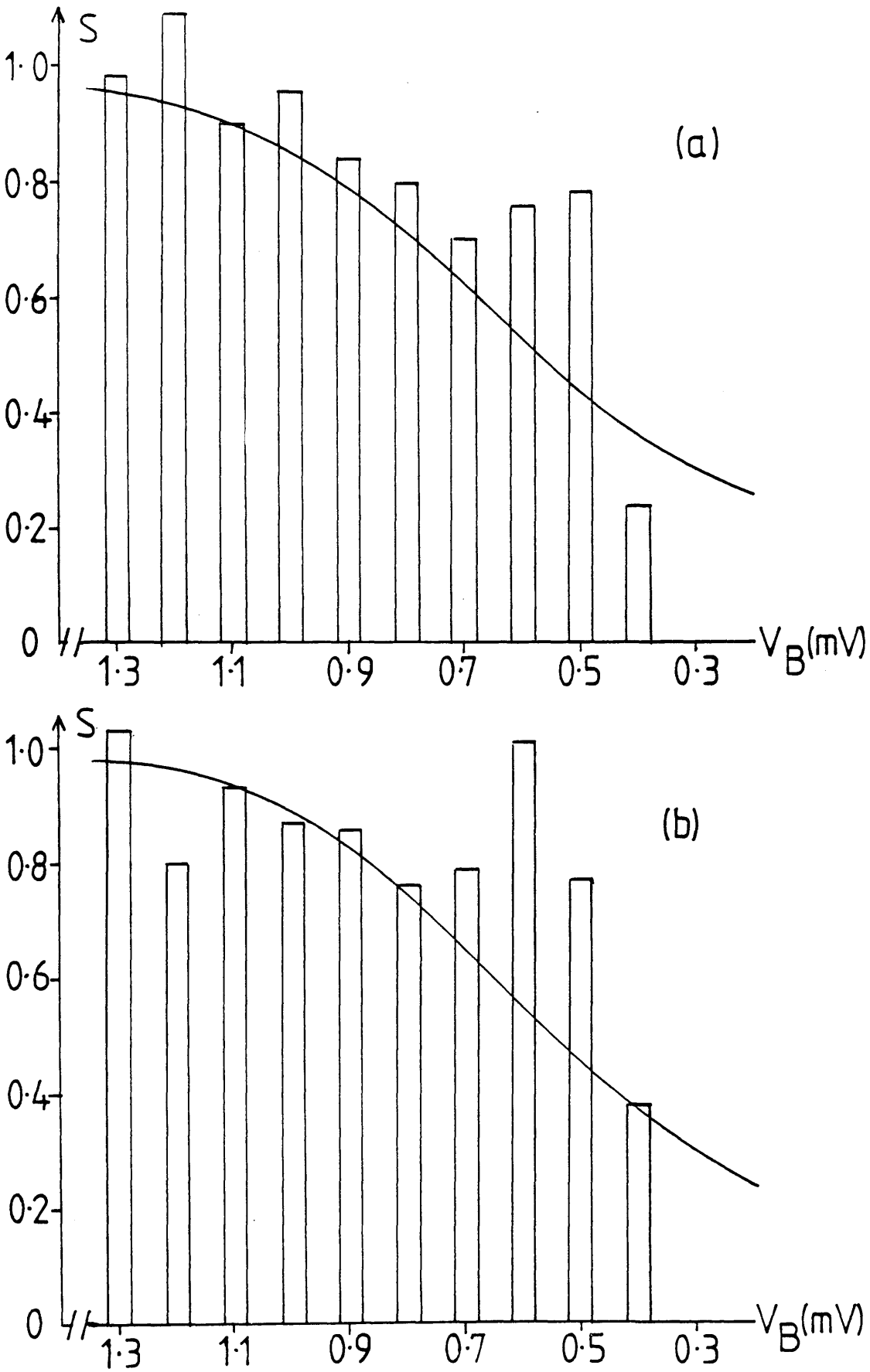

Figure 5.18 The transmittance for C16 (a)p=1.75mw and (b)p=0.55mW. The theoretical values were calculated for elastic mean free path of $2.2E^{-6}\mu m$.

superconducting-normal current is negligible. The data for sample C13 shows this problem even more markedly. The junctions for this sample had a higher superconducting resistance than those in sample 16 therefore the tunneling current is smaller for the same phonon flux. The simple answer to this would have been to increase the input power. However, this would cause the crystal and, therefore, the junctions to heat up continously. Introducing errors in the measurement as the change in the tunnelling current is more dependent on the background temperature at high temperatures.

The experimental data can also be fitted with an inelastic scattering model. Figure 5.19 shows the high input heater power data of samples C13 and C16 with the theoretical S curves for inelastic scattering with an energy dependence of E^{-5}. The fit to the data from sample C16 is as good as that for elastic scattering. For sample C13 the fit is not quite so good, the theoretical values are consistently higher than the experimental. Two phonons being scattered forward per inelastic scattering event appears to be very unlikely (figure 5.20). This model produces values of S which are too large to fit the data.

In sample C12, the generator side experiment, the detector junctions had a low resistance (see table 5.1). This enables one to analyse more than one input power. The comparison of the theoretical and experimental values of S are shown in figures 5.21 to 5.28. First the data has been compared to the elastic scattering models that fitted the detector side data (figures 5.21 to 5.24). It was found that these models also fit this data. The fit is good at both heater input powers. The inelastic scattering models (figures 5.25 to 5.28) also show a fairly good agreement with the data. Again the assumption that two phonons are scattered forward per scattering event (figures 5.27 and 5.28) gives a poorer fit to the data compared to one phonon scattered forward per scattering event. However it should be noted that there is very little difference between the transmission ratios for elastic and inelastic scattering in the heater side experiment, and thus the generator side experiment is not good at distinguishing between elastic and inelastic scattering.

All the experimental data can be fitted for elastic scattering with an energy dependence of around E^{-6} and a mean free path of around 2.2μm at 1 meV. They can also be fitted with an inelastic scattering model with an E^{-5} dependence and a mean free path at 1meV of about 5.0 μm. The fit for the elastic scattering appears to be

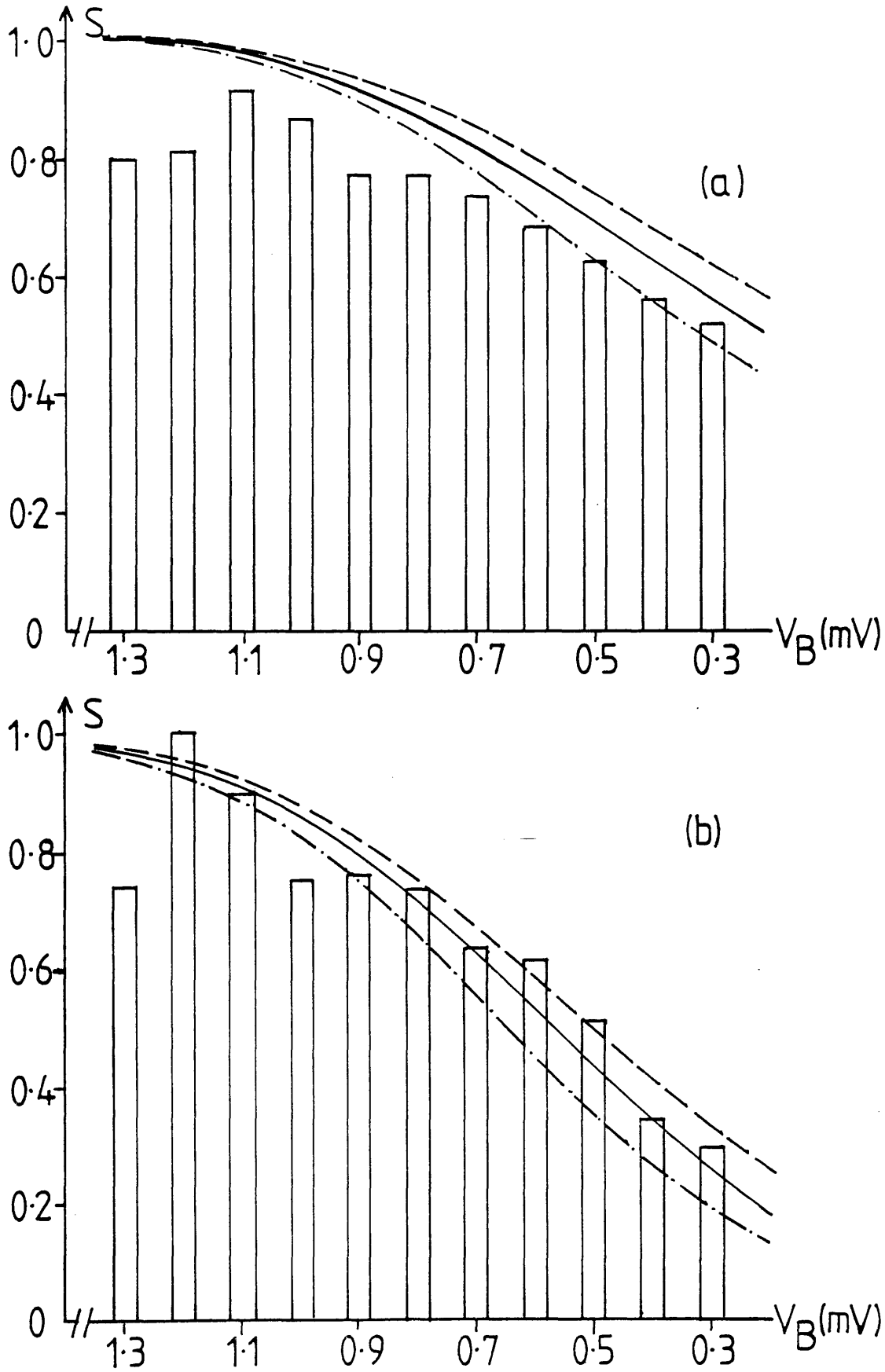

Figure 5.19 The transmittance for (a)C13, p=13.8mW, and (b)C16, p=5.53mW. The theoretical values were calculated for inelastic mean free paths of
— · — · —4.0E^{-5}μm ——— 5.0E^{-5}μm – – – 6.0E^{-5}μm

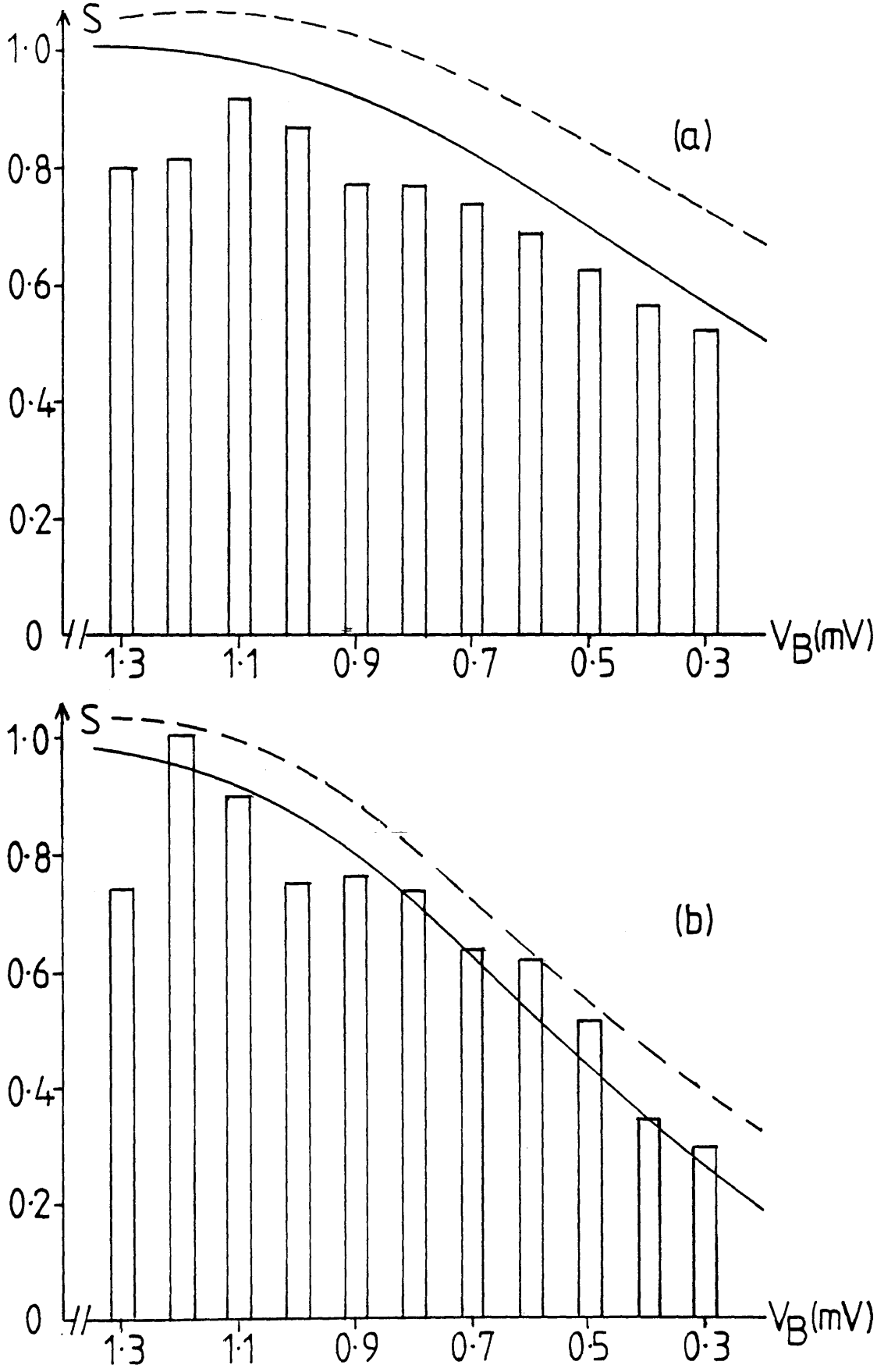

Figure 5.20 The transmittance for (a)C13, p=13.8mW, and (b)C16, p=5.53mW. The theoretical values were calculated for inelastic mean free path of $4.0E^{-5}\mu m$. —— one, – – – two phonons scattered forward per event

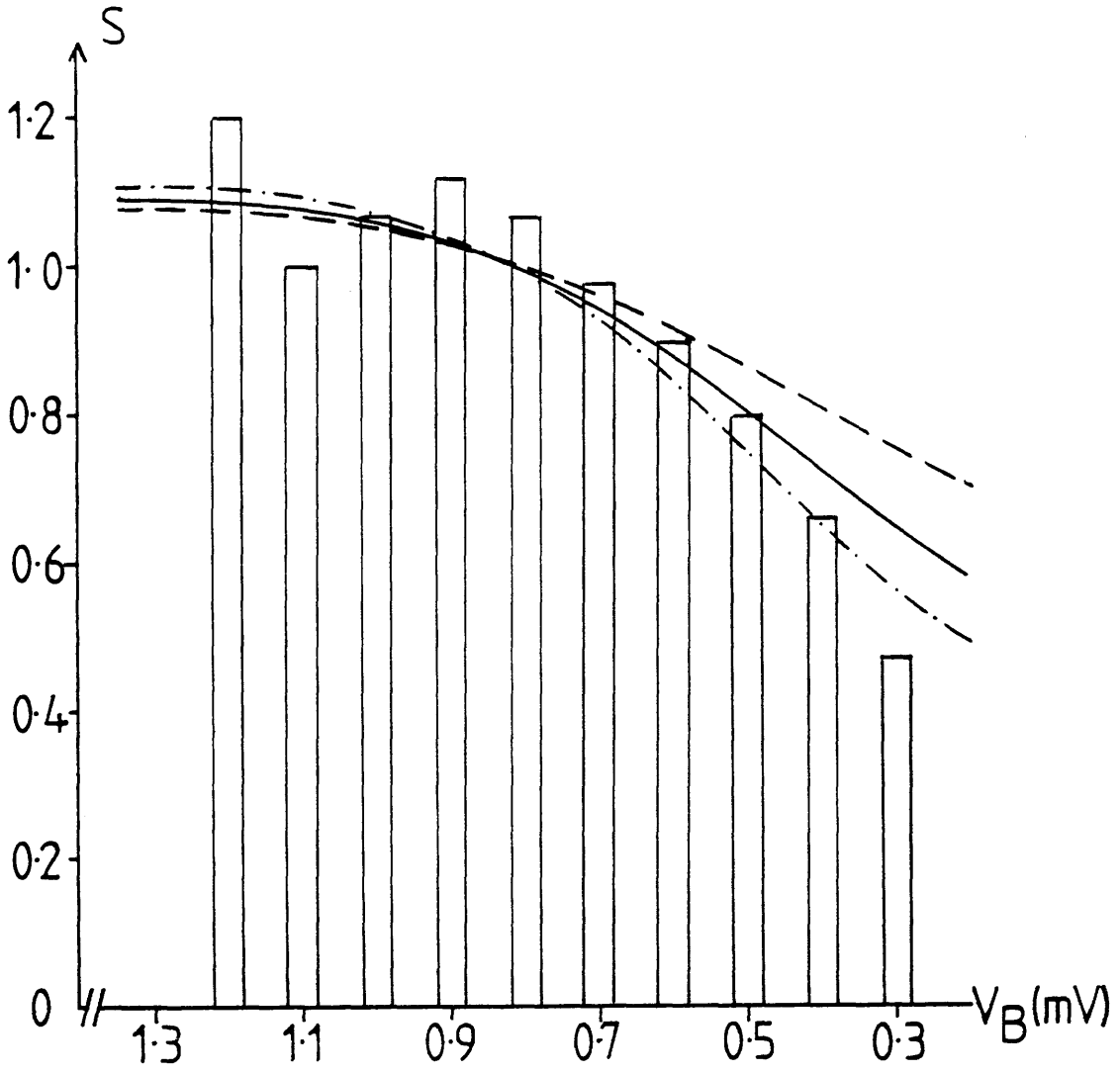

Figure 5.21 The transmittance data for sample C12, p=6.29mW.
The theoretical values were calculated from elastic mean free paths of
—·—·— $2.2E^{-5}\mu m$ ———— $2.2E^{-6}\mu m$ — — — $2.2E^{-7}\mu m$

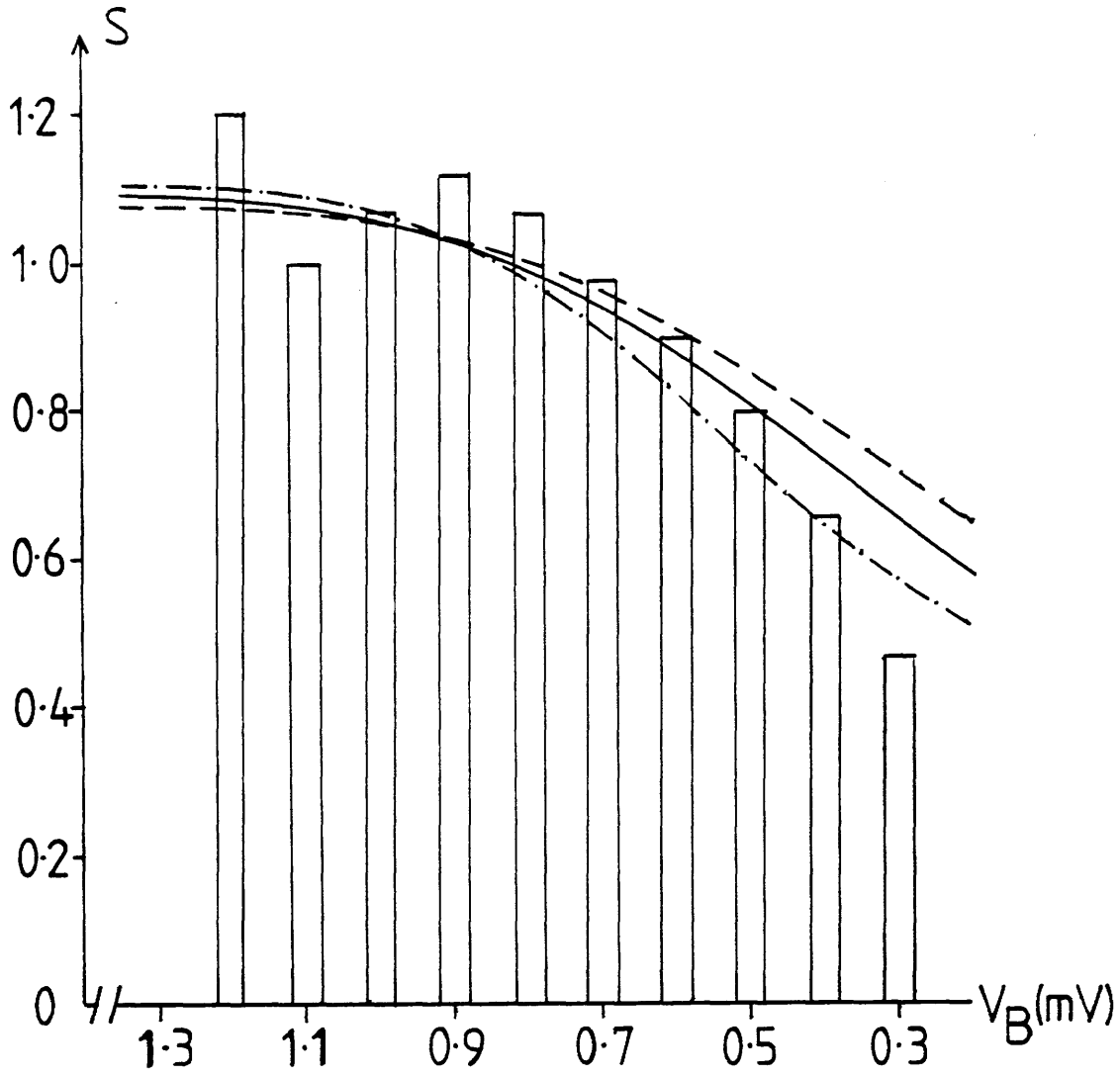

Figure 5.22 The transmittance data for sample C12, p=6.29mW.
The theoretical values were calculated from elastic mean free paths of
— · — · — $1.5E^{-6}\mu m$ ——— $2.2E^{-6}\mu m$ — — — $3.0E^{-6}\mu m$

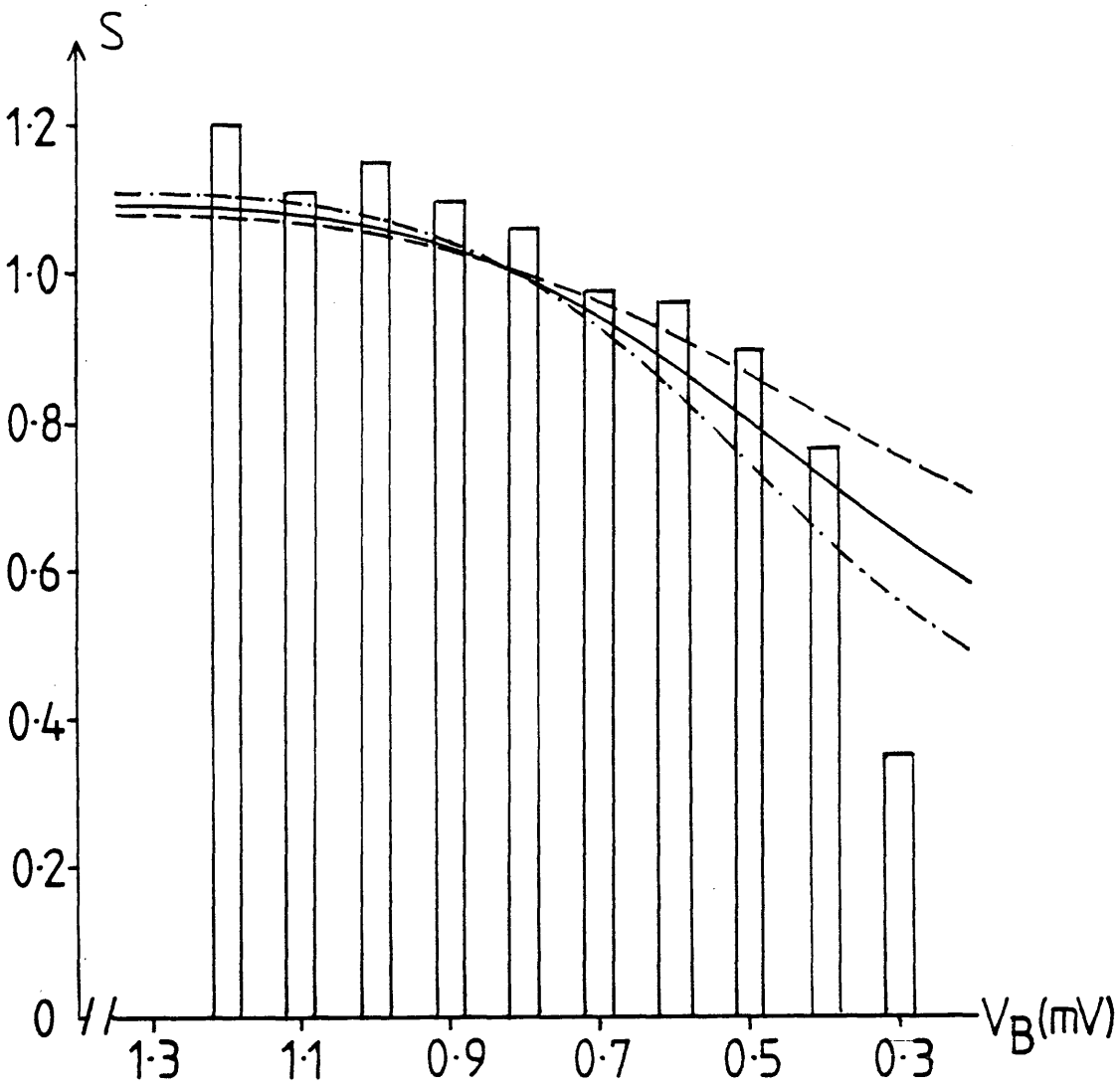

Figure 5.23 The transmittance data for sample C12, p=1.99mW.

The theoretical values were calculated from elastic mean free paths of

— · — · — $2.2E^{-5}\mu m$ ——— $2.2E^{-6}\mu m$ — — — $2.2E^{-7}\mu m$

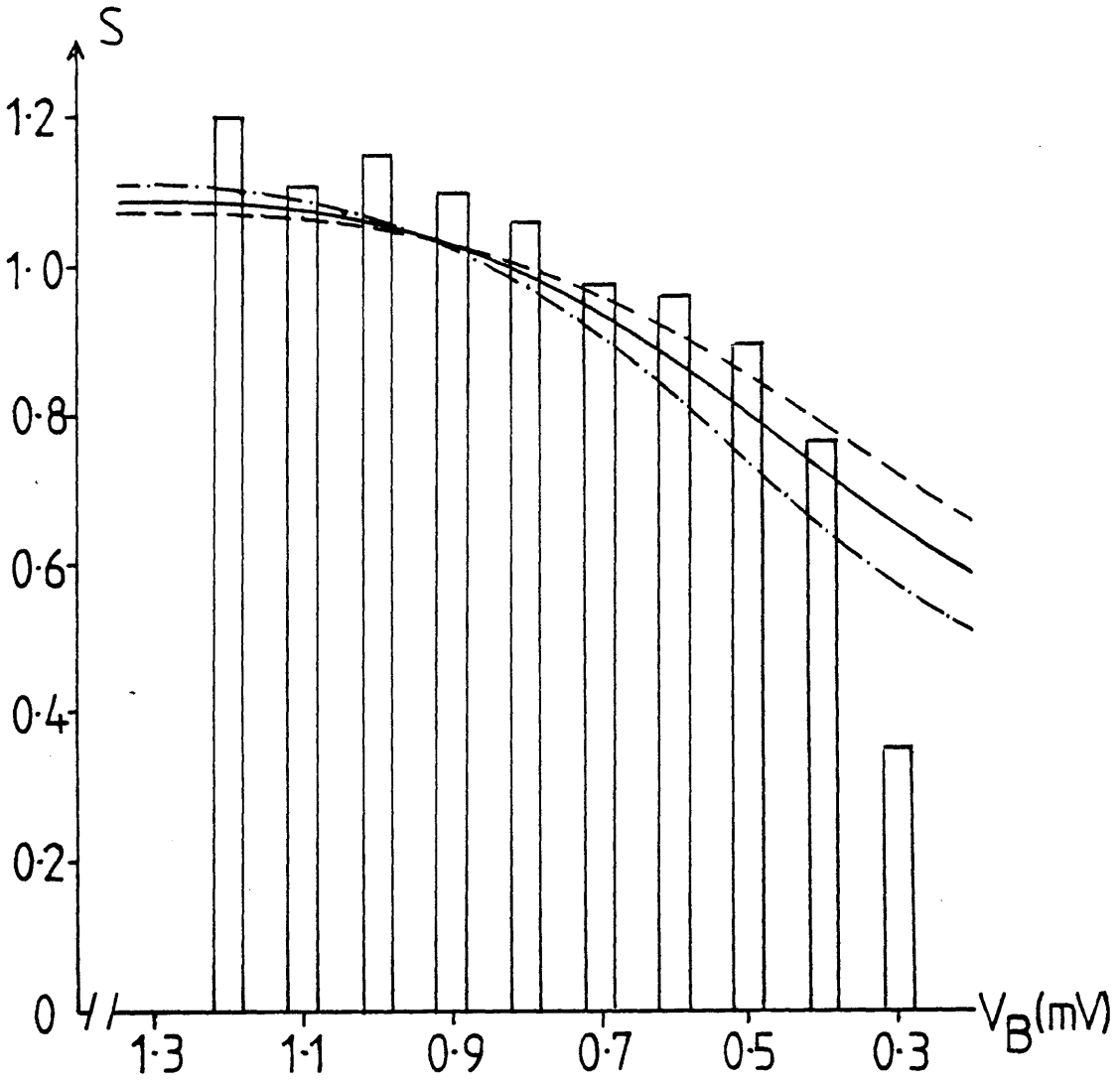

Figure 5.24 The transmittance data for sample C12, p=1.99mW.
The theoretical values were calculated from elastic mean free paths of
– · – · – $1.5E^{-6}\mu m$ ——— $2.2E^{-6}\mu m$ – – – – $3.0E^{-6}\mu m$

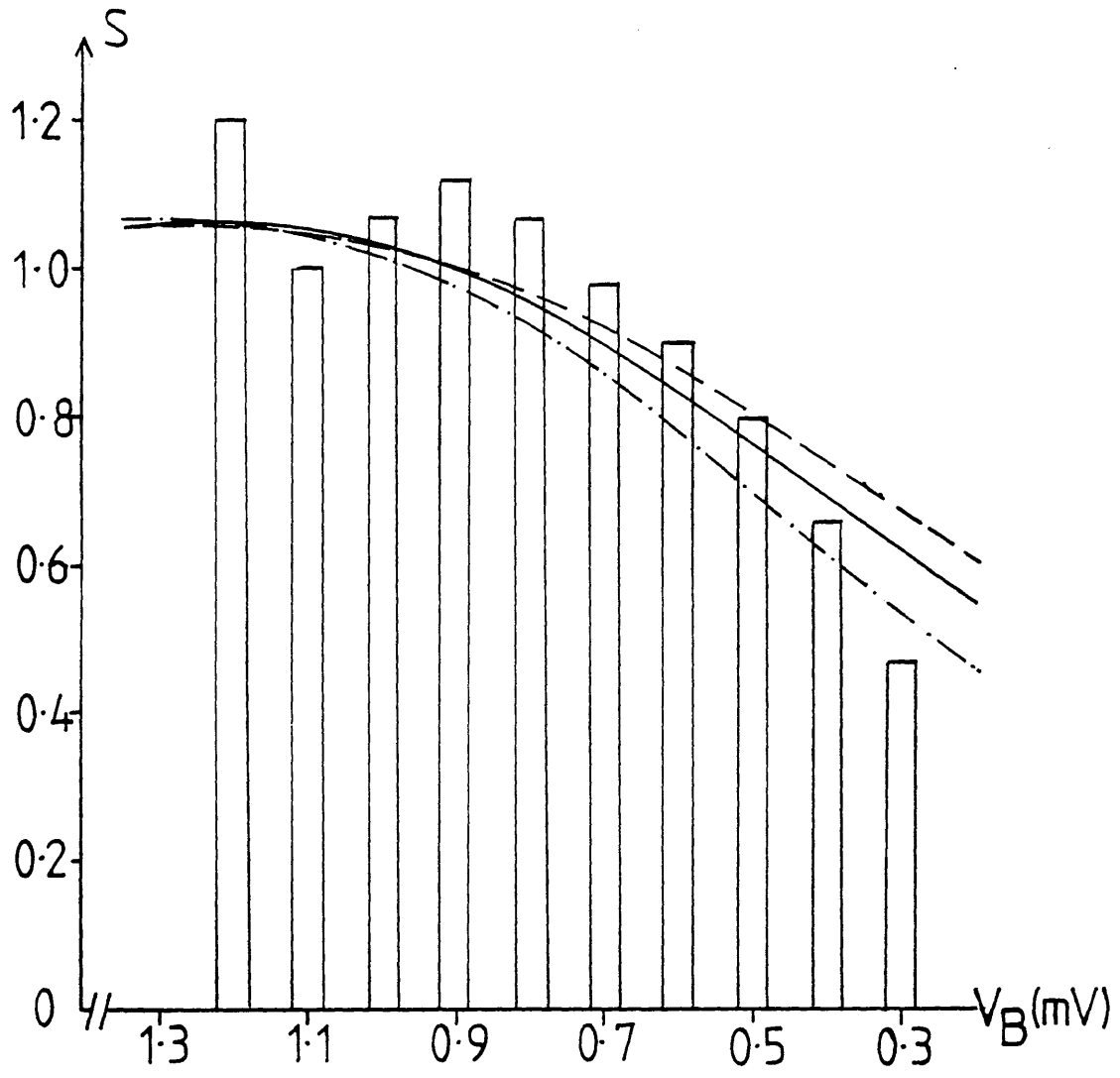

Figure 5.25 The transmittance data for sample C12, p=6.29mW.The theoretical values were calculated from inelastic mean free paths of
— · — · — $4.0E^{-5}\mu m$ ——— $5.0E^{-5}\mu m$ — — — — $6.0E^{-5}\mu m$

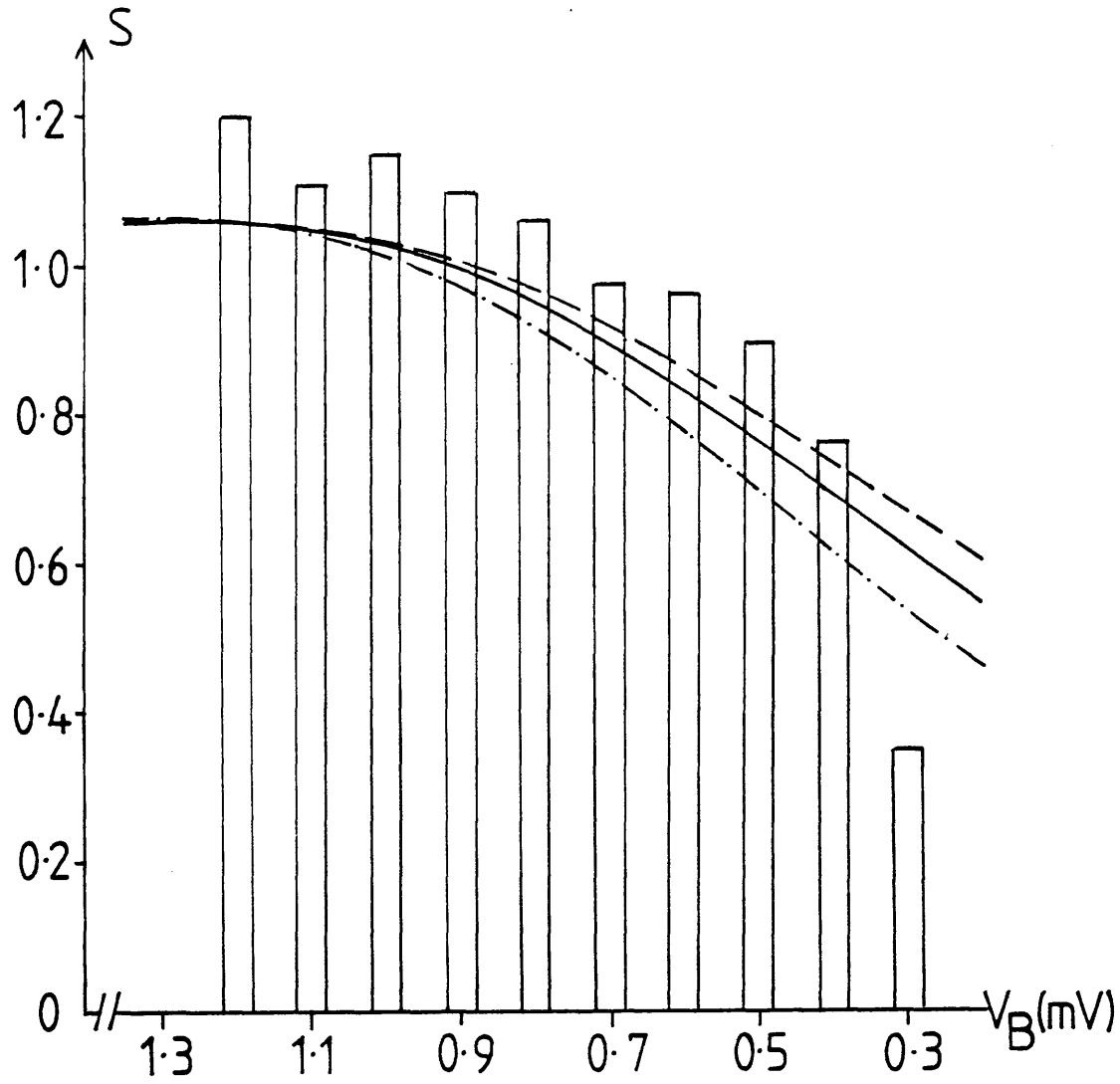

Figure 5.26 The transmittance data for sample C12, p=1.99mW.The theoretical values were calculated from inelastic mean free paths of
— · — · — $4.0E^{-5}\mu m$ ——— $5.0E^{-5}\mu m$ - - - - $6.0E^{-5}\mu m$

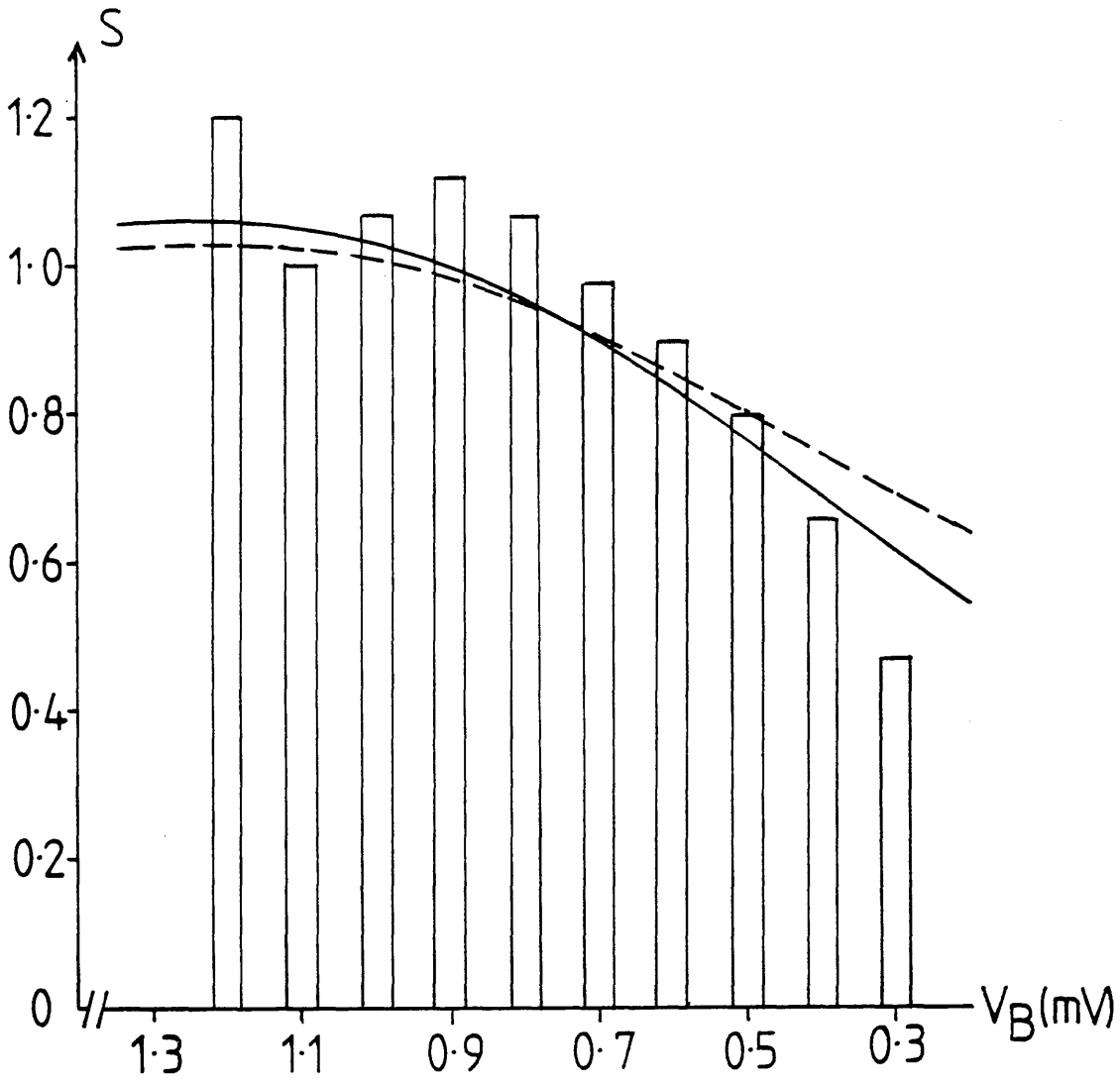

Figure 5.27 The transmittance data for sample C12, p=6.29mW.The theoretical values were calculated from inelastic mean free path of $5.0E^{-5}\mu m$

———— one phonon scattered forward per scattering event

– – – – two phonons scattered forward per scattering event

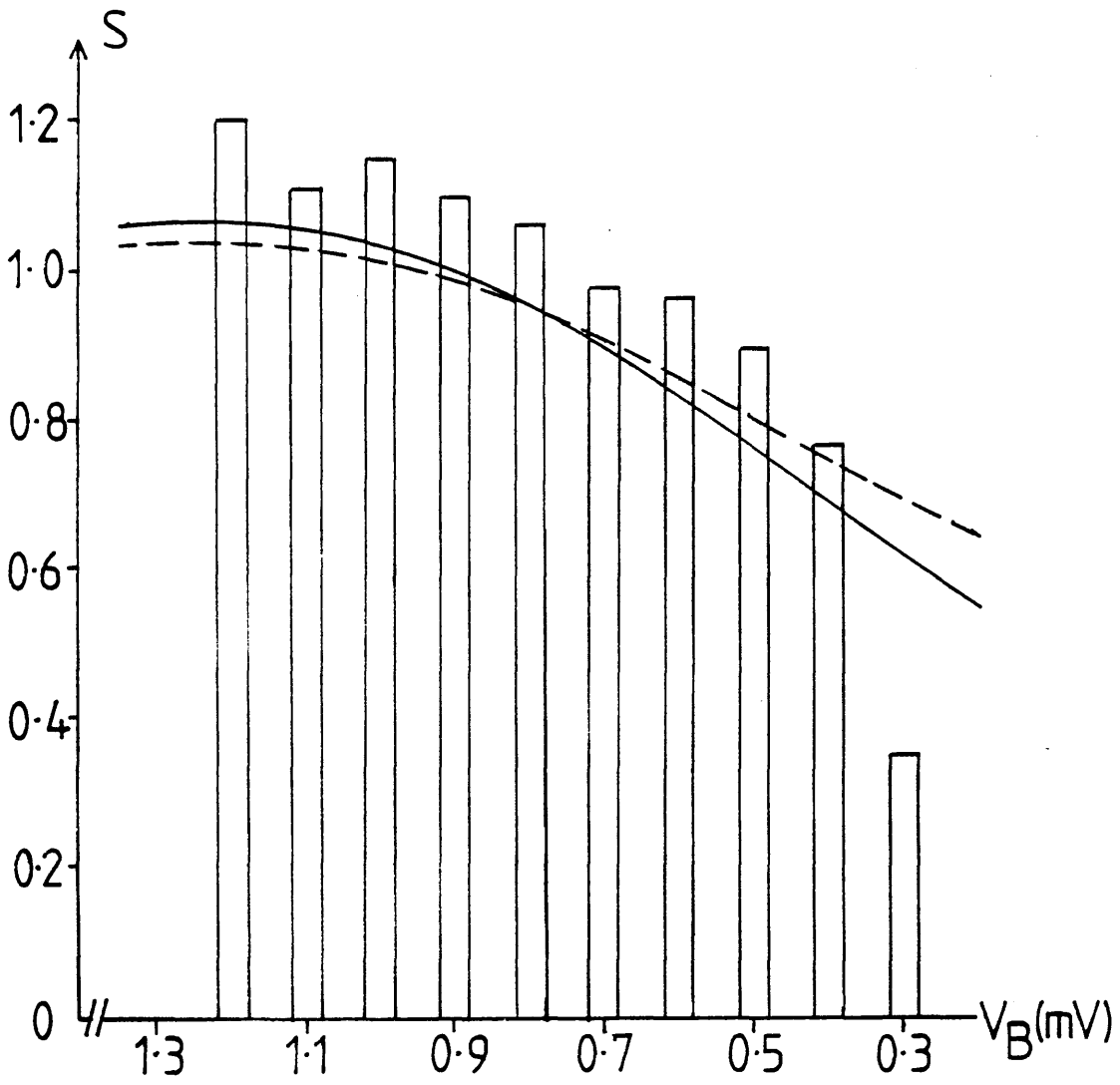

Figure 5.28 The transmittance data for sample C12, p=1.99mW.The theoretical values were calculated from inelastic mean free path of $5.0E^{-5}\mu m$

——— one phonon scattered forward per scattering event

— — — — two phonons scattered forward per scattering event

the best. However, it is impossible to rule out the inelastic scattering, because of the magnitude of the experimental error and the uncertainties introduced by the analysis technique. The samples studied were of different thicknesses (Table 5.1) and can be fitted with the same scattering models. This suggests that the boundaries between the glass and the sapphire crystal and the evaporated films do not have a significant effect on the scattering, in accord with our assumptions.

The longitudinal pulse was much smaller than the transverse pulse so there were only two measurements with large enough signal to be analysed. Figure 5.29 shows the transmittance for sample C16 at the highest heater input power. This shows very similar behaviour to the transverse phonon signal. There is, however, some tenuous evidence of higher transmittance at low energy, though this is not conclusive. The signals in the highest energy channels were too small to recover.

The heater side sample, C12, shows very different behaviour (figure 5.30). The transmittance is much higher at low energies and drops off more rapidly at high energies. This difference between the longitudinal and transverse phonons is not expected to be due to differences in the boundary transmission coefficients. The phonons being examined have been transmitted perpendicular to the boundaries and all the transmission coefficients are expected to be close to unity. Also the longitudinal and transverse phonons in the glass are expected to couple to longitudinal and transverse modes, respectively, in the substrate. The output of the heaters is assumed for phase space reasons to be mainly transverse phonons. Therefore the number of longitudinal phonons is small compared to the number of transverse in the glass. It would only need a small proportion of transverse phonons to scatter inelastically to longitudinal phonons to enhance the low energy longitudinal signal significantly. This is the most likely source of the extra longitudinal phonons.

5.6 The Silicon Monoxide Data

Measurements were performed on only one sample, C10. The glass was under one of the heaters. The details of this sample are shown in table 5.2. The helium 4 cryostat was used so the temperatures were slightly higher and less stable than for the other experiments. This was a particular problem for the higher input powers

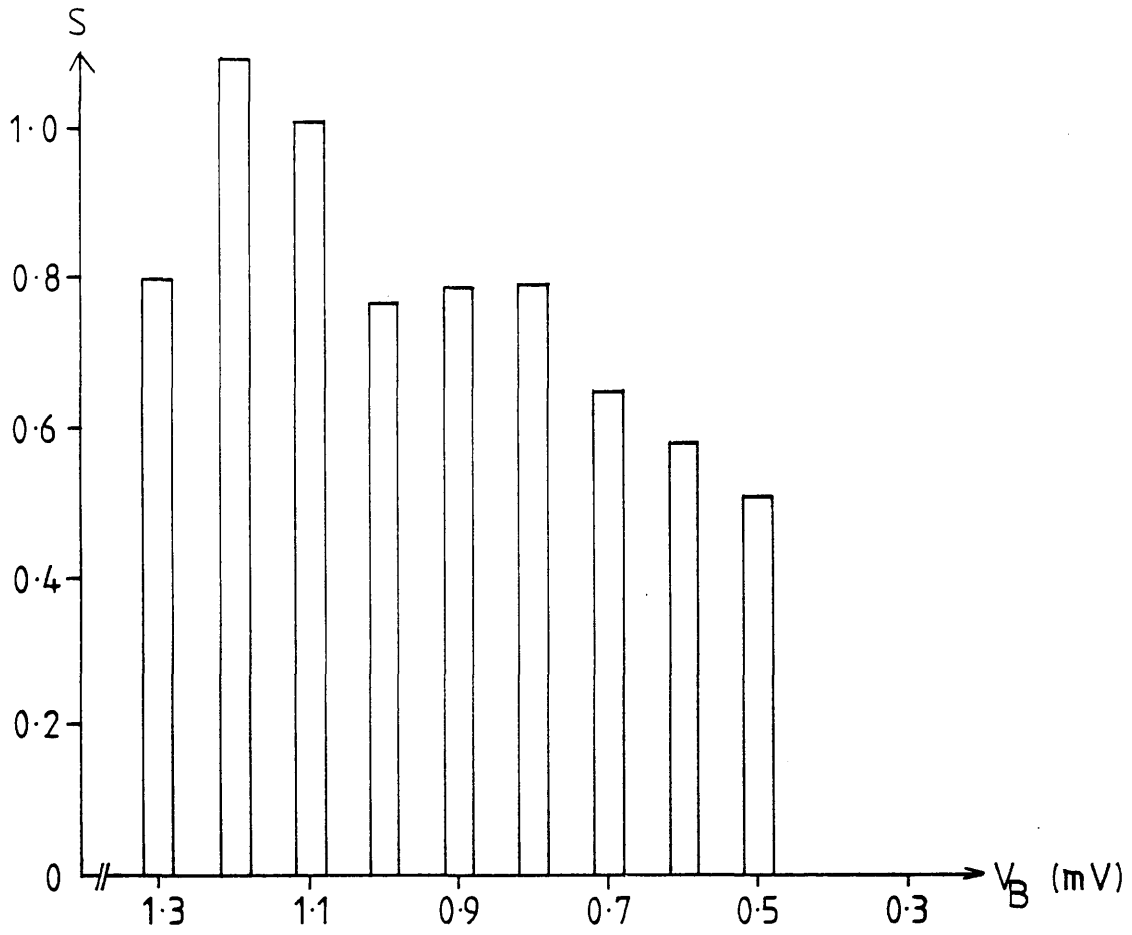

Figure 5.29 The transmittance data for C16, longitudinal phonons. p=5.53mW.

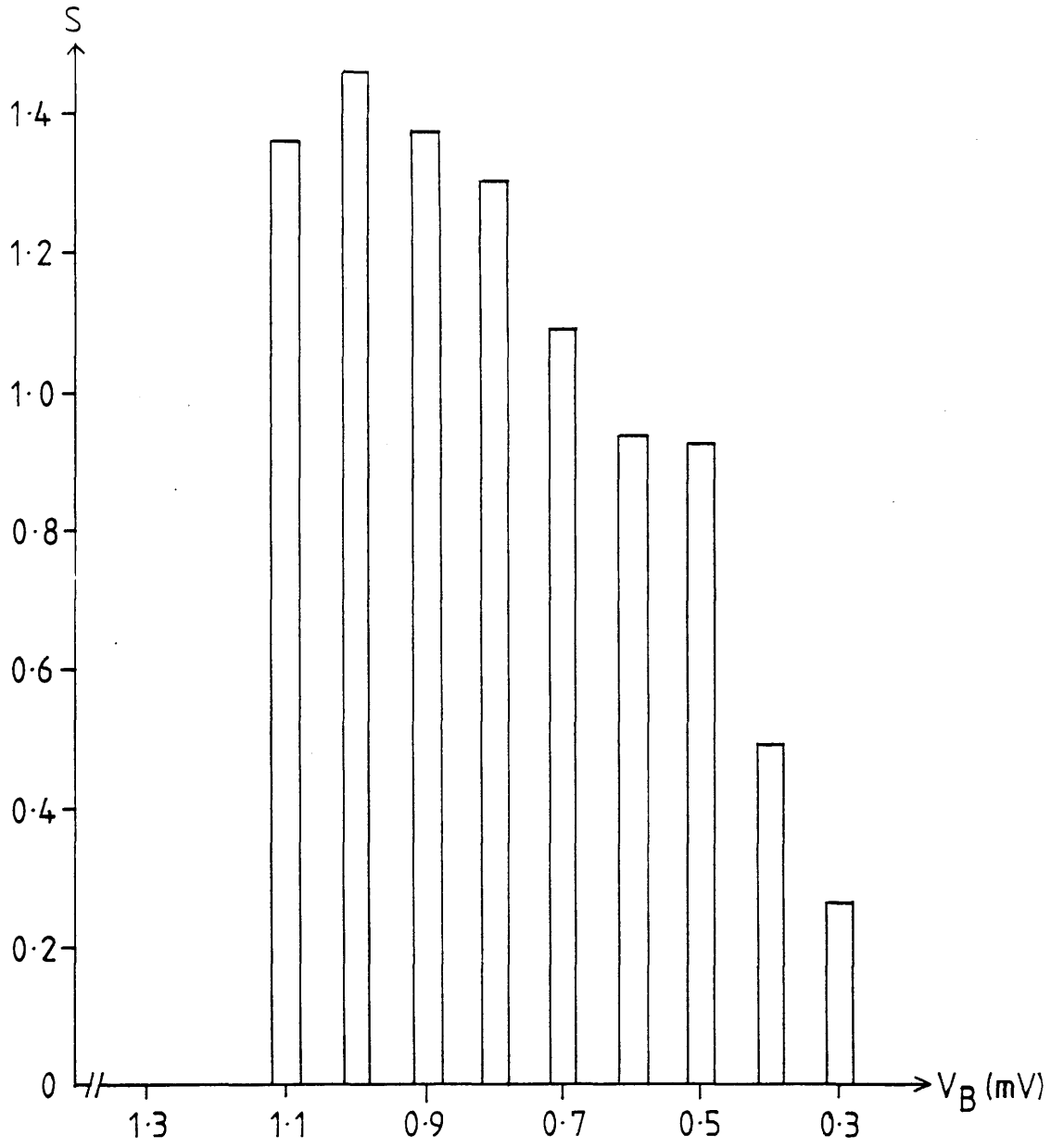

Figure 5.30 The transmittance data for C12, longitudinal phonons. p=6.29mW.

used and as a result some of the measurements were unsatisfactory. As before the cross shoot signal was not used since the orientation of the crystal around the c-axis was not known. This left three sets of data to be analysed.

This glass showed quite different scattering behaviour from the silicon dioxide glass. This is obvious from an examination of the voltage signal. Figure 5.31 shows the signal at a bias voltage of 0.70mV and an input power of 1.54mW both with and without the glass. There is an enhancement of the signal in the presence of the glass which only occurs at low bias, high phonon energy. This is clear when the signal transmittance is plotted as a function of bias (figure 5.32) . At low bias S is greater than one and decreases as the bias increases. This suggests very strong elastic scattering, much stronger than that observed in the silicon dioxide samples. The back scattering into the heaters appears to substantially increase their temperature causing increased phonon output at high energies and an apparant depletion of the low energy signal. If the scattering were inelastic the signal at low energies would be expected to increase also. Figure 5.33 shows the voltage signal at a bias of 0.70mV and an input power of 4.87mW. The enhancement of the signal is still present but much weaker than at the lower power. This is reflected in the signal transmittance (figure 5.34) which has smaller values of S at low bias values. On increasing the power to 15.4mW (figure 5.35) the effect of this elastic scattering becomes insignificant and a much weaker process dominates. This weaker scattering mechanism is thought to be inelastic however, since this was a generator side sample, the possibility that it is elastic cannot be ignored. In the previous section it was shown that it was difficult to differentiate between elastic and inelastic scattering of this magnitude on a heater side sample. Obviously a comparable detector side sample needs to be measured and analysed using the current technique.

It is obvious that more than one mechanism is operating in this glass, this renders quantitative analysis difficult. Also only one measurement of the scattering has been made and the transmittance could be fitted to more than one pair of values of mean free path and energy dependence. For these reasons further discussion of this data, along with the measurements of other workers, is left until chapter 6.

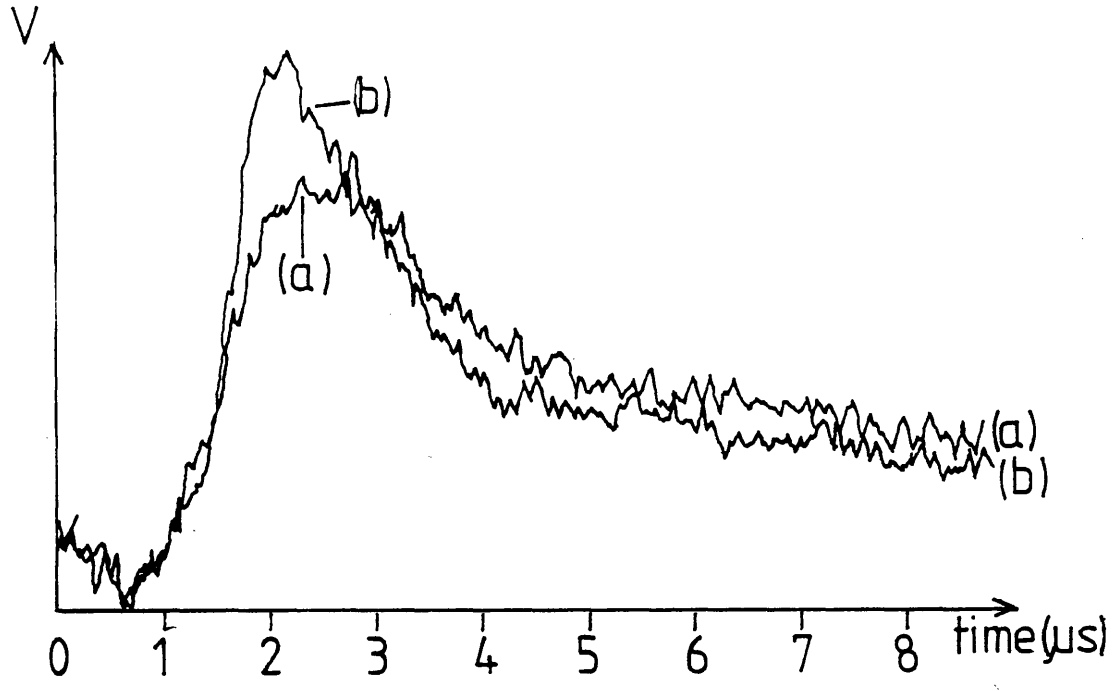

Figure 5.31 Sample C10 voltage signal as a function of time for an input power of 1.54mW and bias voltage of 0.7mV. (a) without and (b) with the glassy film.

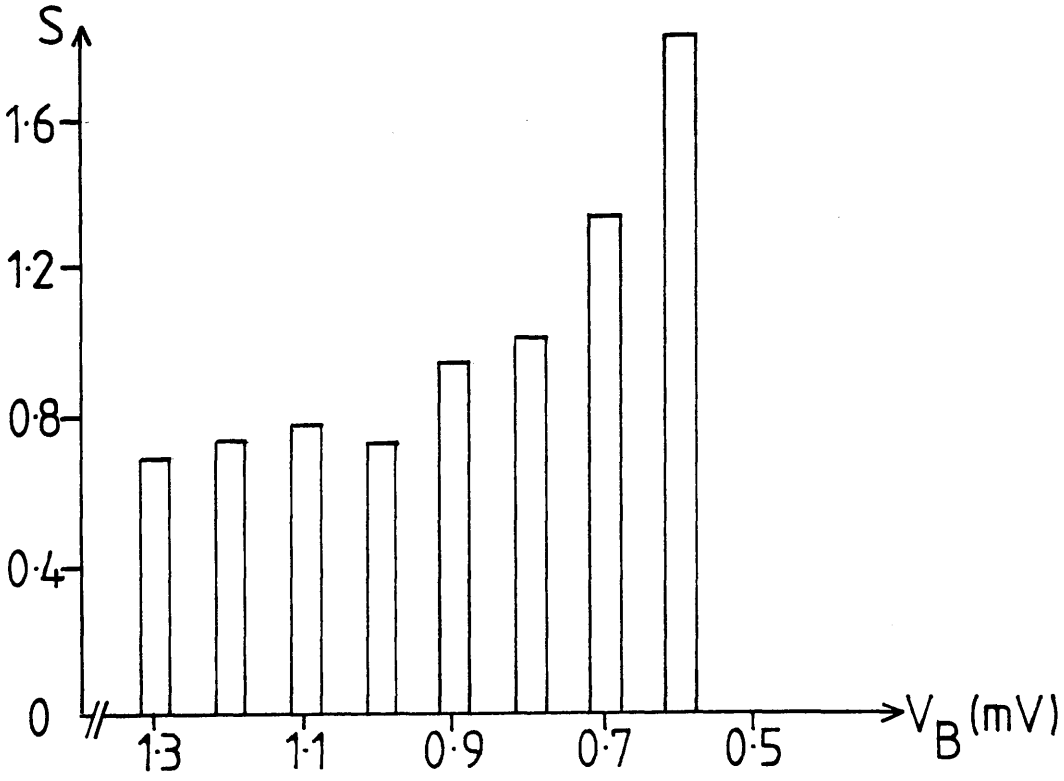

Figure 5.32 The transmittance data for C10, p=1.54mW.

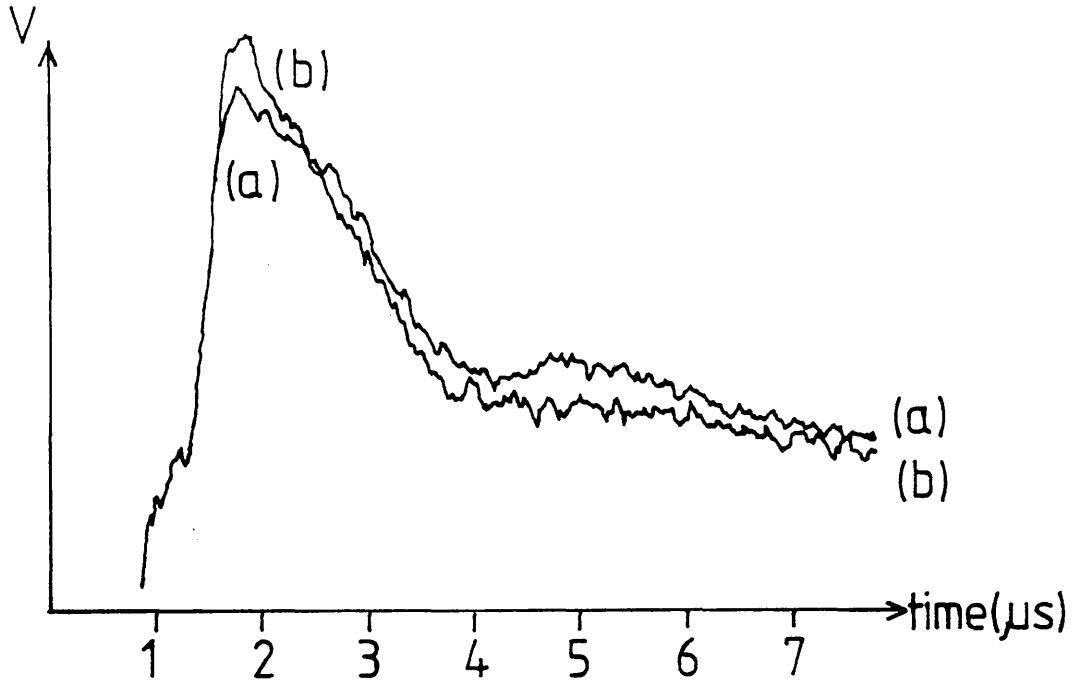

Figure 5.33 Sample C10 voltage signal as a function of time for an input power of 4.87mW and bias voltage of 0.7mV. (a) without and (b) with the glassy film

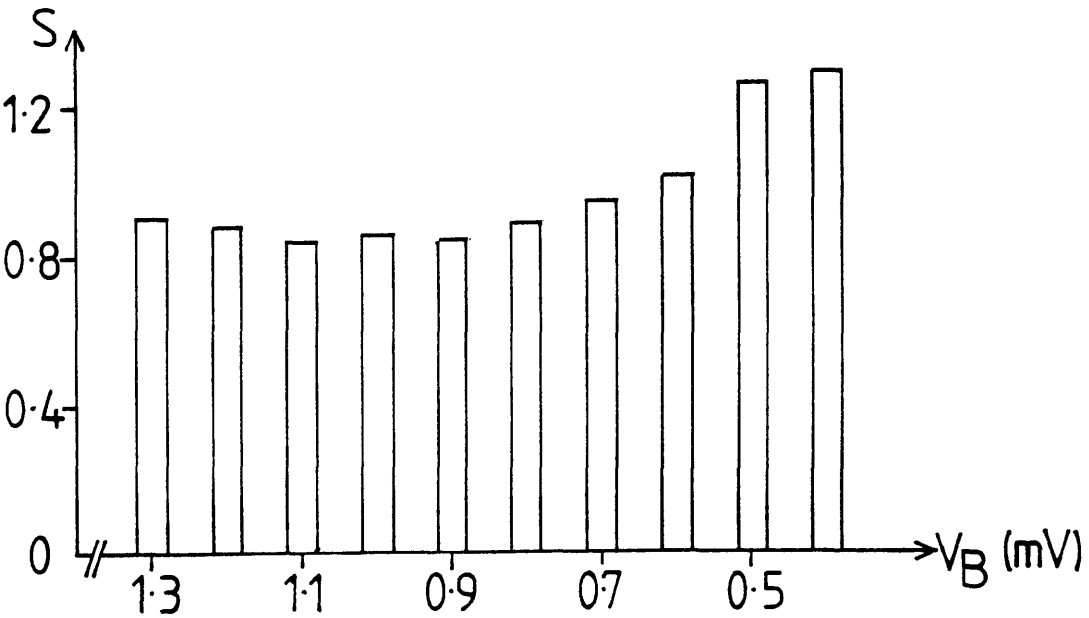

Figure 5.34 The transmittance data for C10, p=4.87mW.

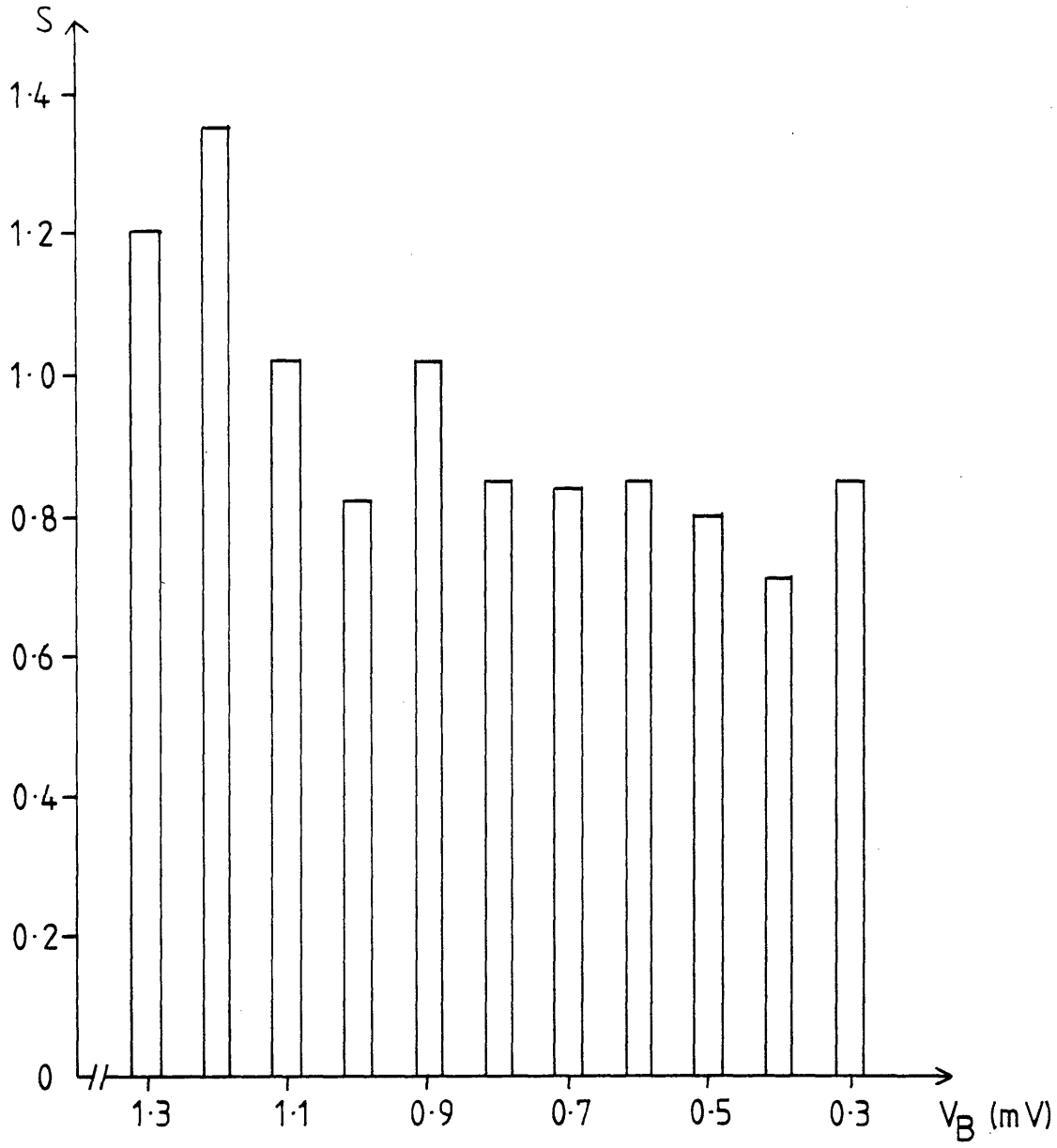

Figure 5.35 The transmittance data for C10, p=15.4mW.

Two samples of this glass were prepared, samples C18 and C20. The details can be seen in table 5.3. The data from these samples are of very limited use mainly due to the poor quality of the detectors.

C18 was a detector side experiment. The detectors had low resistances and, consequently, it was found to be impossible to maintain a stable bias voltage below 0.7mV. There was also a short acting in parallel with the insulating layer which caused the voltage signal at the lowest usable biases to be negative. So only the data from a bias of 0.8mV upwards was meaningful. Therefore there was no high energy data available for this sample. It is this "missing" energy range that cantains most information about the phonon scattering. It is very difficult to distinguish between different forms of scattering using only the low energy transmission ratio. From the measured spectra at high bias it can be seen that there is a time delay of the phonon signal that has passed through the glassy film (figure 5.36). The delay is $0.14\pm0.02\mu s$. Otherwise the pulse shape has not been changed significantly. From figure 5.37 it can be seen that the time delay has changed the shape of the transmission ratio. Instead of being relatively constant over the transverse phonon pulse, as in the silicon dioxide measurement, S begins to increase sharply at the time of the transverse phonon peak in the signal without the glass and reaches a maximum after it. In these circumstances it is difficult to calculate a true transmission ratio.

C20 was a heater side sample. The detectors had very different R_{SS}/R_{SN} values. To correct for this difference it is necessary to use the technique of calculating V_{SN} as described in section 2.6 which was shown in section 4.3 to be very inaccurate. It was not considered worthwhile performing calculations to correct for this because of the unreliability of this correction and because of the lack of high energy data for quantitative analysis. One of the detectors had a short in parallel with it which produced a negative signal up to a bias of 0.6mV. Thus, as in sample C18, only low energy data was available for analysis. Moreover the heaters were of very different resistances in this sample, presumably because of the difference in the underlying surface. This was compensated for by calculating the voltages that produced the same input power in each. In section 4.4 it was shown that the phonon output spectrum is

Sample number		C18	C20
Sample thickness (μm)		2.2 ±0.2[1]	0.824 ± 0.006
Resistance of detector 1 (mΩ) (R_1)		2.9 ± 0.2	12 ± 1
R_2/R_1		1.39 ± 0.01	1.08 ± 0.01
R_{SN}/R_{SS}	Det. 1	200	700
	Det. 2	200	3000
Heater resistance (Ω)	Htr. 1	23.2	430
	Htr. 2	22.9	2000

TABLE 5.3 The arsenic trisulphide samples.

(1) The thickness of this sample was not measured. This thickness was calculated from the sputtering time and rate.

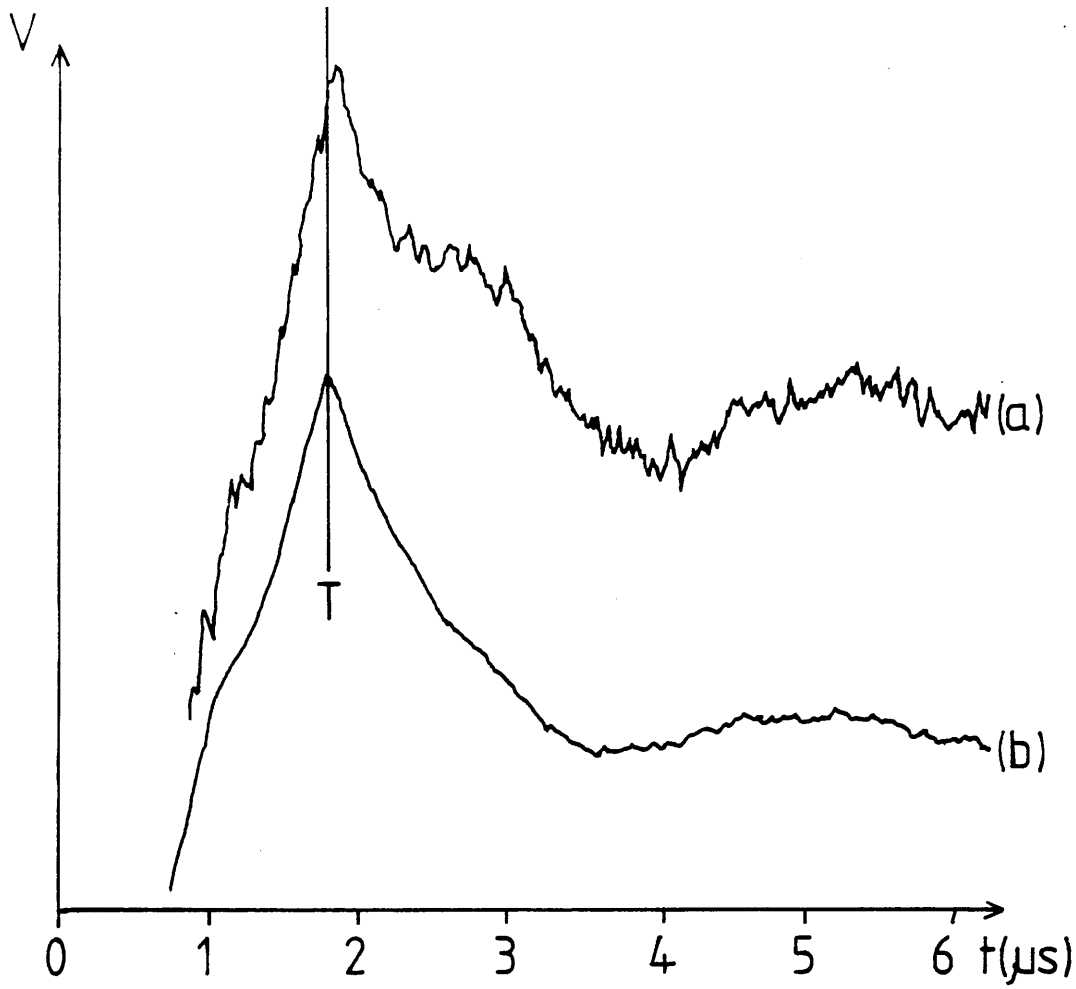

Figure 5.36 Sample C18 voltage signal as a function of time and bias voltage of 1.2mV. (a) without and (b) with the glassy film.
T - the transverse phonon peak.

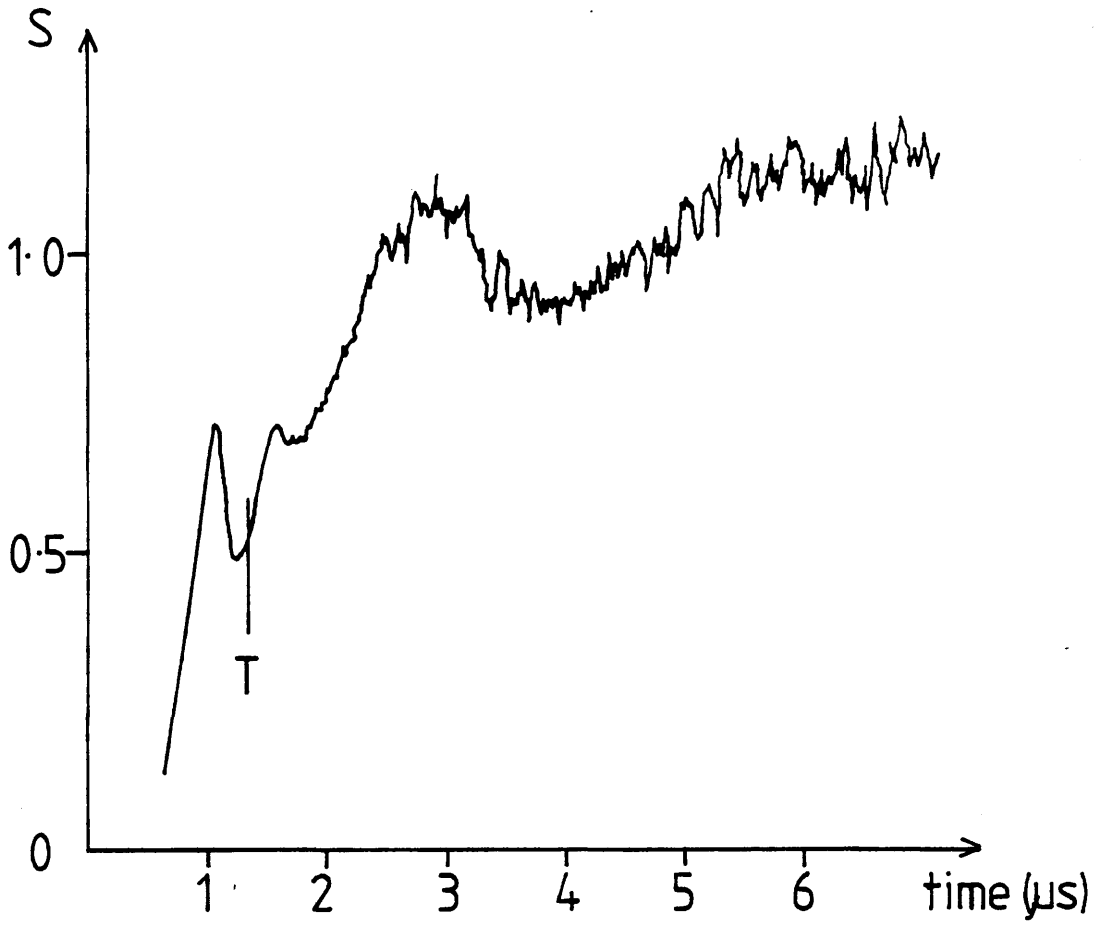

Figure 5.37 The transmittance as a function of time for the data in figure 5.36.
T - the transverse phonon peak.

determined by the temperature of the heaters and this in turn is controlled by the input power. By ensuring that the input power to each heater was the same the phonon output spectra should be identical. Again a time delay in the phonon signal with the glass was observed (figure 5.38). It was measured to be 0.16±0.02μs.

In both samples it was only possible to measure the electron current through the junctions at high bias. Therefore there is only infromation for the low energy part of the spectra and very little information on the energy resolved scattering. There is also a time delay of the signal that has travelled through the glassy film. This time delay is about the same size for both the samples whereas the thicknesses differ by a factor of two. This delay also has an effect on the calculation of the transmission ratio. Not all the scattered phonons reach the detector simultaneously therefore any calculation of the transmission ratio will be an underestimate. This causes the scattering strength to be overestimated. Therefore the analysis technique in its present form is inadequate for the quantitative analysis of this data.

In this chapter we have discussed our measurements and their analysis. As stated in section 1.8 there have been other phonon scattering measurements made in this temperature range on silicon dioxide and silicon monoxide. In chapter 6 the results of the other measurements are compared to our results.

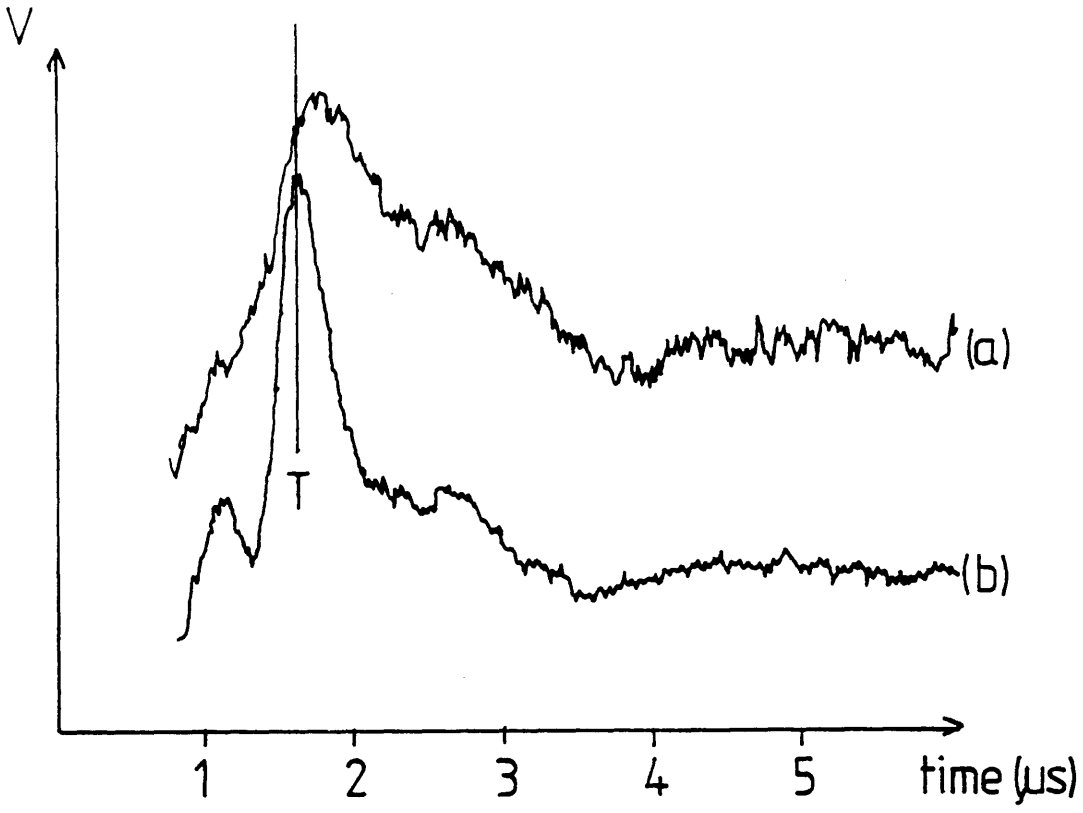

Figure 5.38 Sample C20 voltage signal as a function of time and bias voltage of 1.2mV. (a) without and (b) with the glassy film.
T - the transverse phonon peak.

6.1 Introduction

There have been very few measurements made on glasses of the energy resolved phonon scattering in the plateau region of the thermal conductivity. The results of these experiments are not in total agreement. In this chapter we compare our measurements to others and discuss the possible reasons for the differences observed in the scattering.

6.2 Silicon dioxide

It was shown in section 5.5 that the silicon dioxide data was best fitted by an elastic scattering mechanism with a phonon mean free path of 2.2μm at 1meV and varying as E^{-6}. However the possibility of inelastic scattering cannot be ignored, it was also shown that the data can be fitted with an inelastic scattering model. The only other phonon scattering measurements on silicon dioxide are those made by Deitsche and Kinder (1979). They fit their data using an inelastic model with a mean free path of 0.71μm at 1meV and proportional to E^{-3}. As can be seen from figure 6.1 this scattering is too strong to fit our data. The scattering observed in our measurements is different from the scattering observed by Dietsche and Kinder (1979). This could be caused by differences between the two experiments. The glasses were grown by different methods. In our experiment the film was deposited by sputtering whereas Dietsche and Kinder (1979) evaporated their silicon dioxide. The difference in scattering strength between the two measurements suggests that there is a difference at a microscopic level between films grown by sputtering and those grown by evaporation. Von Haumeder et al. (1980) have also noted that sputtered silicon dioxide shows slightly different acoustic properties from the bulk material. This difference in measurements suggests that care should be taken when comparing measurements made on silicon dioxide prepared by different methods.

In Dietsche and Kinder's experiment the glass was under the phonon generator which was a Sn-Sn tunnel junction and the samples were surrounded by liquid helium. The liquid helium provides an additional escape path for the phonons which are backscattered from the glass into the generators thus reducing the overall signal. It has also been shown that phonons reflected at an interface with liquid helium are detuned from their original energy (Dietsche and Kinder (1976)). This would

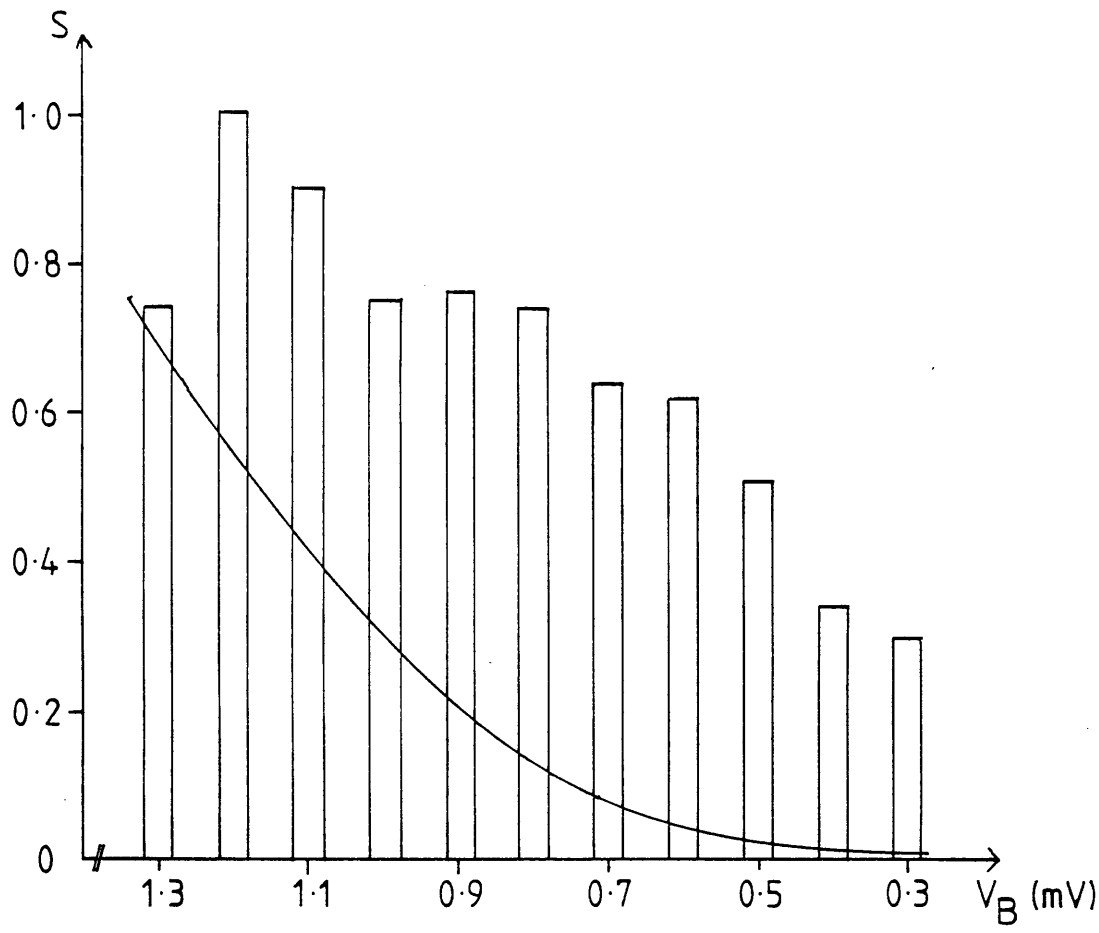

Figure 6.1 The current transmission ratio for sample C16.
Input pulse duration = 250ns, input pulse power = 5.5mW.
The curve is for the current transmission ratio calculated for inelastic scattering with a phonon mean free path of 0.71μm at 1meV and varying as E^{-3} (as obtained by Dietsche and Kinder (1979)).

produce lower energy phonons similar to inelastic scattering in the glass. Dietsche and Kinder (1979) have ignored both these effects in the analysis of their data. In their third measurement there was no covering of liquid helium, inelastic scattering was still observed. They noted that the recombination phonon output from the phonon generator was broader than expected. This broadening could be caused by inelastic scattering in the junction itself, the possibility of such events was discussed by Long and Adkins (1973). In this case elastic scattering in the glass followed by inelastic scattering in the junction is a possible explanation for their data.

Neither our meaasurements nor those of Dietsche and Kinder have determined with absolute certainty whether the scattering mechanism is elastic or inelastic. In order to do this further measurements would need to be made. These are discussed in section 6.5.

6.3 Silicon Monoxide

In section 5.6 it was shown that there are at least two different scattering mechanisms present in silicon monoxide. A stronger, probably elastic, one which dominates at low powers. This mechanism saturates and the scattering is dominated by a much weaker mechanism which is thought to be inelastic.

Long et al. (1980) measured the energy resolved phonon scattering in this material using the same experimental set-up with detector side samples. They fitted their data with elastic scattering with a mean free path of 0.5μm at 0.9meV and varying as E^{-3}. The magnitude and energy dependence is similar to that found in evaporated silicon dioxide by Dietsche and Kinder (1979). In figures 6.2 to 6.4 both these models are compared to our data. Neither of them can be used to describe either of the scattering mechanisms present in this sample.

Figures 6.2 and 6.3 show the data collected at the two lower powers, 1.5mW and 4.9mW respectively. Both these graphs show that at high energies the transmission ratio is greater than one. This is unlikely to be a detector effect since they were very good detectors, sample C10 which was discussed in chapter 4, the S-N leakage current was very small. Even if this was not the case then the maximum value of

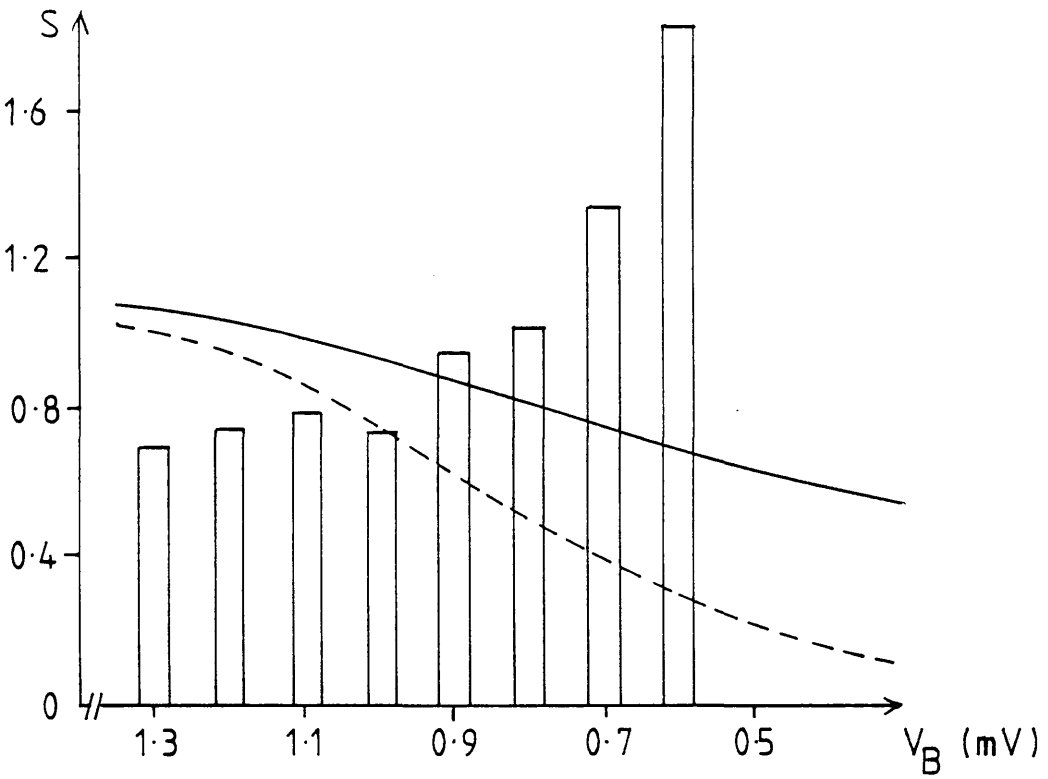

Figure 6.2 Transmittance data for sample C10, input power = 1.54mW.

Theoretical values ——— elastic scattering $\ell = 0.365E^{-3}\mu m$

– – – – inelastic scattering $\ell = 0.71E^{-3}\mu m$

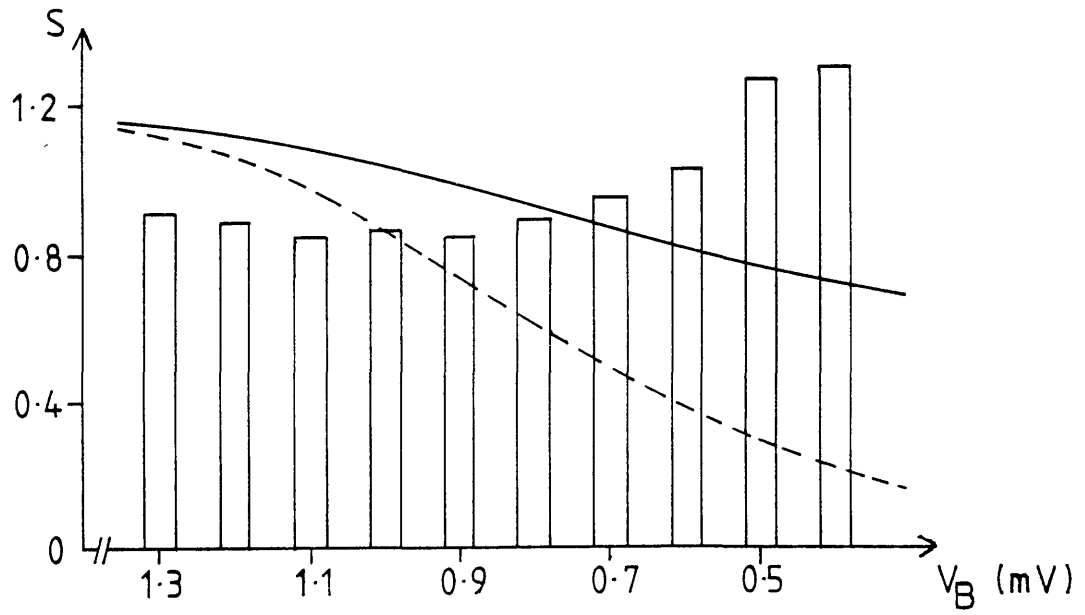

Figure 6.3 Transmittance data for sample C10, input power = 4.9mW.

Theoretical values ——— elastic scattering $\ell = 0.365E^{-3}\mu m$

– – – – inelastic scattering $\ell = 0.71E^{-3}\mu m$

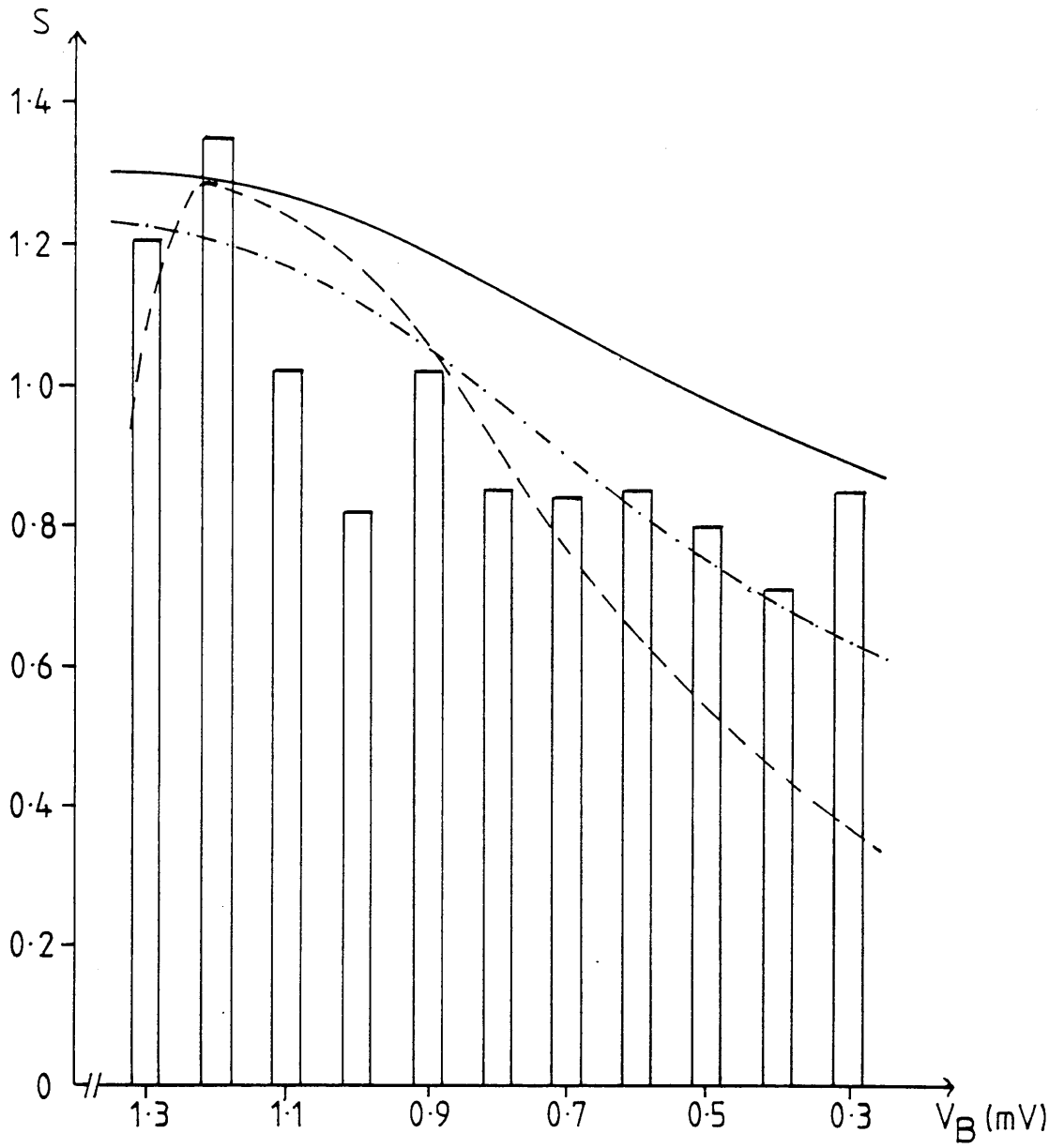

Figure 6.4 Transmittance data for sample C10, input power = 15.4mW.

Theoretical values ———— elastic scattering $\ell = 0.365E^{-3}\mu m$

– – – – – – inelastic scattering $\ell = 0.71E^{-3}\mu m$

—·—·— inelastic scattering $\ell = 1.0E^{-2}\mu m$

transmission ratio that this leakage current would produce is unity since the detectors were identical to within one percent. Using the theoretical model developed for the generator side experiments it was not found possible to find a scattering model which would fit this low power data. In section 5.2 it was assumed that for generator side samples the backscattered phonons were reabsorbed by the heater. This raised the heater temperature and increased the output of the low energy phonons by the heater. It is thought that with this strong scattering mechanism that this assumption is no longer valid. To establish the form of this scattering a detector side sample should be investigated.

The highest input power used in this measurement was 15.4mW. This data is shown in figure 6.4. As can be seen from the figure inelastic scattering with a mean free path of 1.0μm at 1meV varying as E^{-2} fits the data. However this result is considered to be unreliable since the stronger scattering mechanism found at lower powers probably has a significant contribution to the energy resolved transmission ratio at this power. In order to estabish the correct form of this weaker scattering it is necessary to go to higher input pulse powers.

It should be noted that only one sample of this glass was measured. These measurements were performed in the helium 4 cryostat which had a less stable background temperature than the helium 3 cryostat therefore the systematic errors in the measurements are larger than for the silicon dioxide data. More measurements should be performed on this glass in a helium 3 cryostat in order to verify these conclusions.

6.4 Arsenic Trisulphide

Our attempts to measure the energy resolved phonon scattering in arsenic trisulphide were unsuccessful. The junctions manufactured for these two samples were among the poorest quality of those made during the duration of this experiment. It was noticed that for the detector side samples the two junctions were quite different. Also the heaters in the generator side sample had very different resistances. In all other samples the heaters were nearly identical, this was also true for the detectors. This suggests that the arsenic trisulphide causes contamination of the layers evaporated on top of it. It would be necessary to

manufacture more samples in order to verify this. If this is found to be the case then it will not be possible to investigate the phonon scattering in arsenic trisulphide using this particular experimental technique.

These preliminary measurements have shown however that at least some of the scattering has a time delay associated with it which is independent of the thickness of the glass. This indicates that there is a scattering mechanism in this material which has a significant dwell time. The existence of such slow scattering states is a prediction of the atomic tunnelling model. Their observation suggests that tunnelling states significantly contribute to the phonon scattering arsenic trisulphide.

6.5 Further work

It has been shown in chapter 5 that with wideband phonon sources elastic and inealstic scattering mechanisms cannot be differentiated in a totally satisfactory manner. The detector side experiments provided the most information about the scattering mechanism but there was still some doubt. In order to determine whether or not there is inelastic scattering present in the material a monochromatic phonon source should be used in a detector side sample held in a vacuum (see section 6.2). Tunnel junctions can be used as a near monochromatic source of phonons. By biasing a tunnel junction at the gap edge and applying a small voltage pulse phonons of energy about twice the gap energy can be generated. By observing the energy distribution of the phonons transmitted through the glass elastic and inelastic scattering can easily be distinguished. Some experiments using Sn-Sn tunnel junction generators were attempted (section 4.5). However it did not prove possible to manufacture them with low enough resistance to obtain a detectable signal with our time-resolved experiment for generator voltages less than 4Δ. Therefore they could not be used with signal voltages in the region where the phonon output of the generators can be predicted.

It should be possible to investigate samples at lower phonon energies, corresponding to temperatures below the plateau in the thermal conductivity-temperature curve, by using superconducting-normal junctions which, in theory, have no lower limit to the detectable phonon energy. This would extend the range of energies over which

information about the phonon scattering is known. It would reveal whether or not there is a change in the scattering mechanism between the T^2 region and the plateau in the thermal conductivity curve.

It was suggested by Phillips (1972) that an open structure is necessary for the existence of tunnelling systems. Therefore tunnelling states should not exist in four fold coordinated materials, such as amorphous silicon and germanium, since their networks are thought to be too tight for large atomic motions. By measuring the phonon scattering in these materials and comparing them to measurements on other materials some insight into this suggestion may be gained. Measurements on amorphous germanium have been performed by Long et al. (1980). However, these measurements are probably subject to errors caused by S-N leakage currents in the detectors. Further phonon scattering measurements should be made on these four fold coordinated materials.

The arsenic trisulphide measurement had a scattered signal which was delayed in time. This data was not analysed quantitatively since there was only low energy data available. However, if this material is to be investigated thoroughly an analysis technique which deals with a delayed signal will need to be developed.

References

P.W. Anderson, B.I. Halperin and C.M. Varma, Phil. Mag. 25, 1, (1972)

W. Arnold and S. Hunklinger, Solid State Commun. 17, 883 (1975)

H.D. Bale, R.E. Shepler and G.W. Gibbs, J. Appl. Phys. 41,241 (1970)

H.P. Baltes, Solid State Commun. 13, 225 (1973)

P. Berberich and H. Kinder, J. de Physique C 6, 374, (1981)

J.L. Black, Phys. Rev. B 17, 2740 (1978)

J.L. Black and B.I. Halperin, Phys. Rev. B 16, 2879 (1977)

V.M. Bobetic, Phys. Rev. A 136, 1535, (1964)

U. Buchenau, Solid State Commun. 56, 889 (1985)

A.F. Cattell, A.R. Long, A.C. Hanna and A.M. MacLeod, J. Phys. F 13, 855 (1983)

G.K. Chang and R.E. Jones, Phys. Rev. 126, 2055 (1962)

A.F. Cohen, J. Appl. Phys. 29, 591 (1958)

M.H. Cohen and G.S. Grest, Solid State Commun. 39, 143 (1981)

B. Davison, Neutron Transport Theory (Oxford: OUP) (1957)

A.H. Dayem, B.I. Miller and J.J. Wiegand, Phys. Rev. B 3, 2949, (1971)

A.H. Dayem and J.J.Wiegand, Phys. Rev. B 5, 4390, (1972)

J.Y. Dequesne and G. Bellessa, J. Physique 46, C10-449 (1985)

A.J. Dianoux, U. Buchenau, M. Prager and N. Nucker, Physica 138B, 264 (1986)

W. Dietsche, Phys. Rev. Lett. 40, 786, (1978)

W. Dietsche and H. Kinder, Phys. Rev. Lett. 43, 1413 (1979)

W. Eisenmenger, Physical Acoustics XII, Edited by W.P. Mason and R.N. Thurston (Academic Press, 1976), p135

W.Eisenmenger and A.H. Dayem, Phys. Rev. Lett. 18, 125, (1967)

W. Frick, D. Waldman and W. Eisenmenger, Appl. Phys. 8, 163, (1975)

P. Fulde and H. Wagner, Phys. Rev. Lett. 27, 1280 (1971)

I. Giaever and K. Megerle , Phys. Rev. 122, 1101, (1961)

B. Golding, J.E. Greabner, B.I. Halperin and R.J. Schutz, Phys. Rev. Lett.30, 223 (1973)

B. Golding and J.E. Greabner, Phys. Rev. Lett. 37, 852 (1976)

B. Golding, J.E. Greabner and R.J. Schutz, Phys. Rev. B 14, 1660 (1976)

W.M. Goubau and R.A. Tait, Phys. Rev. Lett. 34, 1220 (1975)

J.E. Greabner and B. Golding,Phys. Rev. B19, 964 (1979)

J.E. Greabner, L.C. Allen, B. Golding and A.B. Kane, Phys. Rev. B 27, 3697 (1983)

K. Handrich, Phys. Stat. Sol. (b) 116, 533 (1983)

M. von Haumeder, U. Strom and S. Hunklinger, Phys. Rev. Lett. 44, 84 (1980)

P. Herth and O. Weis, Zeit. Angew. Physik 29, 101, (1970)

S. Hunklinger, W. Arnold, S. Stein, R. Nava and K. Dransfeld,
Phys. Lett. 42A, 253 (1972)

S. Hunklinger, W. Arnold and S. Stein, Phys. Lett. 45A, 311 (1973)

S. Hunklinger and L. Piche, Solid State Commun. 17, 1189 (1975)

S. Hunklinger, L. Piche, J.C. Lasjuanias and K. Dransfeld,
J. Phys. C 8, L423 (1975)

S. Hunklinger and M. von Schickfus, Amorphous Solids Low Temperature Properties
Edited by W.A.Phillips, (Springer-Verlag 1981), p81

J. Jackle, Z. Phys. 157, 212 (1972)

J. Jackle, L. Piche, W. Arnold and S. Hunklinger,
J. Non-crystalline Solids 20, 365 (1976)

D.P. Jones, N. Thomas and W.A. Phillips, Phil.Mag. B 38, 271, (1978)

D.P. Jones, J. Jackle and W.A. Phillips, Phonon Scattering in Condensed Matter
Edited by H.J. Maris (Plenum, New York, 1980), p49.

D.P. Jones, W.A. Phillips, and J.C. Lasjuanias,
Solid State Commun. 41, 255 (1982)

R.B. Kummer, R.C. Dynes and V. Narayanamurti, Phys. Rev. Lett. 40, 1187 (1978)

J.C. Lasjuanias, Solid State Comm. 10, 215, (1972)

J.C. Lasjuanias, A. Ravex, M. Vandorpe and S. Hunklinger,
Solid State Comm. 17, 1045, (1975)

W.A. Little, Can. J. Phys. 37, 334, (1959)

H. von Lohneysen and F. Steglich, Phys. Rev. Lett. 39, 1420 (1977a)

A.R. Long, J. Phys. F 3, 2040, (1973)

A.R. Long and C.J. Adkins, Phil. Mag. 27, 865, (1973)

A.R. Long, A.F. Cattell and A.M. MacLeod,
J. Non-crystalline Solids 59-60, 1149 (1980)

A.R. Long, A.C. Hanna and A.M. MacLeod, J. Phys. C 19, 467 (1986)

M.T. Loponen, R.C. Dynes, V. Narayanamurti and J.P. Garno,
Phys. Rev. B 25, 1161 (1982)

A.M. MacLeod, and A.R. Long, J. Phys. E : Sci. Instrum. 15, 1231, (1982)

D.S. Matsumoto, C.L. Reynolds, and A.C. Anderson, Phys. Rev. B 19, 4297 (1979)

M. Meissner and K. Spitzmann, Phys. Rev. Lett. 46, 265 (1981)

K.K. Mon, Y.J. Chabal and A.J. Sievers, Phys. Rev. Lett. 35, 1352 (1975)

G.J. Morgan and D. Smith, J. Phys. C 7, 649 (1974)

B. Muhschlegel, Z. fur Physik 155, 313, (1959)

L. Piche, R. Maynard, S. Hunklinger and J. Jackle,
Phys. Rev. Lett., 32, 1426 (1974)

W.A. Phillips, J. Low Temp. Phys. 7, 351, (1972)

W.A. Phillips, J. Non-crystaline Solids 77+78, 1329 (1985)

R.O. Pohl, W.F. Love and R.B. Stephens, Proc. of the 5th Int. Conf. on Amorphous and Liquid Semiconductors (Garmisch), Taylor and `Francis (1974) p. 1121

A.K. Raychaudhuri and R.O. Pohl, Phys. Rev. B 25, 1310 (1982)

H.B. Rosenstock, J. Non-crystaline Solids 7, 123 (1971)

C.L. Ruthroff, Proc. of the I.R.E. 47, 1337 (1959)

M. von Schickfus, S. Hunklinger and L. Piche, Phys. Rev. Lett. 35,876 (1975)

T.L. Smith, P.J. Anthony and A.C. Anderson, Phys. Rev. B 17, 4997 (1978)

R.B. Stephens, Phys. Rev. B 8, 2896 (1973)

R.B. Stephens, Phys. Rev. B 13, 852 (1976)

S. Takeno and M. Goda, Prog. Theor. Phys. 48, 1468 (1972)

B. Taylor, H.J.Maris and C.Elbaum, Phys. Rev. B3, 1426 (1971)

D. Walton, Solid State Commun. 14, 335 (1974)

O. Weis, J. Physique Coll. 33 C4, 49, (1972)

M.P. Zaitlin and A.C. Anderson, Phys. Rev. B 12, 4475 (1975)

R.C. Zeller and R.O. Pohl, Phys. Rev. B 4, 2029, (1971)

J. Zimmerman and G.Weber, Phys. Rev. Lett. 46, 661 (1981)